UNIVERSITY OF ALBERTA

DISCRETE FINITE ELEMENT METHOD FOR CONTINUUM-DISCONTINUUM ANALYSIS

by

GURPREET SINGH BALA ©

A THESIS
SUBMITTED TO THE FACULTY OF GRADUATE STUDIES AND RESEARCH
IN PARTIAL FULFILMENT OF THE REQUIREMENTS FOR THE DEGREE
OF DOCTOR OF PHILOSOPHY
IN
GEOTECHNICAL ENGINEERING

DEPARTMENT OF CIVIL AND ENVIRONMENTAL ENGINEERING

EDMONTON, ALBERTA

FALL 2008

Library and
Archives Canada

Published Heritage
Branch

395 Wellington Street
Ottawa ON K1A 0N4
Canada

Bibliothèque et
Archives Canada

Direction du
Patrimoine de l'édition

395, rue Wellington
Ottawa ON K1A 0N4
Canada

Your file Votre référence
ISBN: 978-0-494-46279-9
Our file Notre référence
ISBN: 978-0-494-46279-9

NOTICE:
The author has granted a non-exclusive license allowing Library and Archives Canada to reproduce, publish, archive, preserve, conserve, communicate to the public by telecommunication or on the Internet, loan, distribute and sell theses worldwide, for commercial or non-commercial purposes, in microform, paper, electronic and/or any other formats.

The author retains copyright ownership and moral rights in this thesis. Neither the thesis nor substantial extracts from it may be printed or otherwise reproduced without the author's permission.

AVIS:
L'auteur a accordé une licence non exclusive permettant à la Bibliothèque et Archives Canada de reproduire, publier, archiver, sauvegarder, conserver, transmettre au public par télécommunication ou par l'Internet, prêter, distribuer et vendre des thèses partout dans le monde, à des fins commerciales ou autres, sur support microforme, papier, électronique et/ou autres formats.

L'auteur conserve la propriété du droit d'auteur et des droits moraux qui protège cette thèse. Ni la thèse ni des extraits substantiels de celle-ci ne doivent être imprimés ou autrement reproduits sans son autorisation.

In compliance with the Canadian Privacy Act some supporting forms may have been removed from this thesis.

While these forms may be included in the document page count, their removal does not represent any loss of content from the thesis.

Conformément à la loi canadienne sur la protection de la vie privée, quelques formulaires secondaires ont été enlevés de cette thèse.

Bien que ces formulaires aient inclus dans la pagination, il n'y aura aucun contenu manquant.

Canada

TO MY BELOVED MOTHER **KULDIP KAUR BALA**

With love and gratitude

ABSTRACT

The developed discrete finite element method is used here to analyze hybrid/coupled problems with continuum and discontinuum properties. Research in geomechanics usually focuses on the development of methods to capture deformation and failure behaviour of geotechnical structures. These methods analyze interactions between multiple deformable bodies discritized into a single element or numerous finite elements and are applied as such to geotechnical problems of soil and rock. When used to predict the behaviour of geo-mechanical materials, these methods require unrealistic idealizations; however, interest in the use and development of these techniques is increasing rapidly.

The present research employs well-developed finite element formulations and incorporates techniques of the discrete element method and the elasto-plastic constitutive relationship into the developed method. Theoretical aspects of the problem are considered and then the solutions for practical applications are obtained.

Solutions for discrete finite element analysis are developed based on solutions for the equation of motion for finite element components. Solutions are obtained within the framework of existing theories and modified to fit the present approach. Existing finite element methods lead to excessive distortion of the elements; this limitation is overcome by splitting the elements and progressing into discrete element analysis. The present research uses two-dimensional quadrilateral discrete elements to generate finite element solutions. Individual

deformable elements are constrained against nodal/contact movements. Two approaches related to displacement and velocity constraints are considered. The developed scheme generates solutions equivalent to a finite element continuum. Knowing the stress state of the elements, a transition from continua to discontinua is achieved through fracture and fragmentation processes by adopting suitable failure criteria. Realistic distributed contact models verified by other research programs were considered and a suitable contact model is applied. The movement and interaction of each discrete element captures the motion, while the finite element meshes employed capture the deformation and stress-strain states. Examples of block toppling, bearing capacity, retaining wall earth pressures verify the schemes presented.

In an analysis of the Carsington Dam failure, the developed technique produces a failure plane comparable to earlier research results. Failure progresses as the elements move and develop further contacts. The Carsington Dam failure involved many parameters and material variations; therefore, the success of the technique presented here in simulating the failure validates the developed methodology. The method proves to be effective in simulating the failure mechanism of various complex engineering structures, although conclusions are necessarily case dependent.

ACKNOWLEDGEMENTS

This investigation was conducted in the Department of Civil Engineering of the University of Alberta under the supervision of Professor Dave H. Chan. The author is grateful to Dr. Chan for continuous and patient guidance in completing this THESIS. Dr. Chan's orientation, ideas, timely encouragement, benevolence, and discussions throughout the research are very much appreciated.

The author thanks the Department of Civil Engineering for research assistantships and fellowships.

The author is grateful to Dr. Ante Munjiza of Swansea University, Dr. Jamshid Ghaboussi of the University of Illinois, and Srba Masala of Klohn Crippen Ltd. for help with different aspects of the research. The author also acknowledges the help of his friend Garry Deol in development of the computer code in Visual Studio C++ and for his initial stay in Canada.

The author dedicates this THESIS to his beloved mother Kuldip Kaur Bala who died on 27 April 1991 but whose hope, wishes, and aspirations motivated the author to pursue higher studies abroad and to overcome many obstacles during graduate study. The love of the author's father Balwinder Singh Bala and his spirit in pursuing knowledge have been a source of strength during the research. Special thanks are given to the author's wife Manpreet for her understanding and endurance. Love for his children Upneet and Jasjot motivated and helped the author throughout the study.

TABLE OF CONTENTS

RELEASE FORM

ABSTRACT

ACKNOWLEDGEMENTS

TABLE OF CONTENTS

LIST OF TABLES

LIST OF FIGURES

LIST OF SYMBOLS

1 INTRODUCTION 1

- 1.1 GENERAL 1
- 1.2 OVERVIEW OF PREVIOUS STUDIES 2
- 1.3 OBJECTIVES AND SCOPE OF THE THESIS 3
- 1.4 ORGANIZATION OF THE THESIS 4

BIBLIOGRAPHY 6

2 LITERATURE REVIEW 7

- 2.1 INTRODUCTION 8
- 2.2 CONTINUUM BASED METHODS 8
- 2.3 DISCRETE ELEMENT METHOD 12
- 2.4 COMBINED FINITE DISCRETE ELEMENT METHOD 16
  - 2.4.1 Discrete Finite Element Method 17
  - 2.4.2 Hybrid DEM/FEM Methods 19
  - 2.4.3 Combined Finite Discrete Element System 20
  - 2.4.4 Discontinuous Deformation Analysis 21
- 2.5 MANIFOLD METHOD 23
  - 2.5.1 Formulation of the Manifold Method 23
  - 2.5.2 Limitations of the Manifold Method 26
  - 2.5.3 Applications 28
- 2.6 MATERIAL POINT METHOD 28

BIBLIOGRAPHY 30

3 ANALYSIS FOR CONTINUUM SOLUTIONS 34

- 3.1 INTRODUCTION 35

3.2 APPROACH OF THE PROPOSED METHOD....36
3.3 METHOD OF ANALYSIS....37
  3.3.1 Displacement Constraints—Step by Step Procedure....38
  3.3.2 Velocity Constraint Formulation....43
  3.3.3 Computational Scheme....44
3.4 VALIDATION EXAMPLES....50
  3.4.1 Development of a Uniform Stress Field in a Body under UDL....50
  3.4.2 Principal Stresses under a Foundation....54
  3.4.3 Free Fall of a Group of 16 Elements....57
  3.4.4 Stress Distribution for a Slope....61
3.5 PARAMETRIC STUDY FOR NUMERICAL STABILITY....61
  3.5.1 Time Steps....64
  3.5.2 Global Damping Effects....66
  3.5.3 Comparison of Mass Matrices....68
3.6 CONCLUDING REMARKS....70
BIBLIOGRAPHY....70
4 DISCRETE ELEMENT MODEL....71
4.1 INTRODUCTION....72
4.2 CONTACT DETECTION....73
4.3 CONTACT RESOLUTION....76
  4.3.1 Normal Contact Force....76
  4.3.2 Tangential Contact Model....80
4.4 STRESS CALCULATIONS WITHIN DISCRETE ELEMENTS....83
4.5 DISASSEMBLY CRITERIA....88
4.6 REDEFINITION OF CONTACTS....91
4.7 NUMERICAL DAMPING....92
4.8 SOLUTION STABILITY....93
  4.8.1 Time Steps....93
  4.8.2 Contact Formation....94
  4.8.3 Memory Allocations....95
4.9 VALIDATION EXAMPLES FOR DISCRETE ANALYSIS....95
  4.9.1 Validation of the Contact Model....96

4.9.2 Discrete Contact Formation with a Finite Element Assembly 99
4.9.3 Toppling of a Block Assembly 102
4.10 CONCLUDING REMARKS 107
BIBLIOGRAPHY 107
5 ELASTO-PLASTIC CONSTITUTIVE MODEL 110
5.1 INTRODUCTION 111
5.2 REVIEW OF APPLIED MODELS IN PREVIOUS ANALYSES 111
5.3 ELASTO-PLASTIC MODEL 115
5.3.1 Mohr-Coulomb Yield Criteria 116
5.3.2 Finite Element Formulation 118
5.3.3 Displacement Constraints 121
5.3.4 Variable Stiffness 122
5.3.5 Time Steps 123
5.4 EXAMPLES 123
5.4.1 Bearing Capacity of a Footing 124
5.4.2 Retaining Wall 134
5.5 CONCLUDING REMARKS 147
BIBLOGRAPHY 147
6 CARSINGTON DAM—A CASE STUDY 149
6.1 INTRODUCTION 150
6.2 DETAILS OF CARSINGTON DAM 151
6.2.1 Geology and Site Description 151
6.2.2 Construction of the Carsington Dam 153
6.2.3 Material Properties 157
6.2.3.1 Yellow Clay 157
6.2.3.2 Foundation 159
6.2.3.3 Core Material 159
6.2.3.4 Zone I Fill 162
6.2.3.5 Zone II Fill 162
6.2.3.6 Mudstone Deterioration 163
6.2.4 Description of Failure of the Carsington Dam 164
6.2.5 Material Models 168

6.2.6 Mesh used in Analysis of the Carsington Dam Failure 171
6.3 RESULTS AND DISCUSSION 172
6.3.1 Finite Element Analysis of the Carsington Dam 173
6.3.1.1 Staged Construction 173
6.3.1.2 Displacement Profiles 178
6.3.2 Discrete Finite Element Analysis of the Carsington Dam 182
6.4 CONCLUDING REMARKS 188
BIBLIOGRAPHY 188
7 CONCLUSIONS 189
7.1 SUMMARY AND CONCLUDING REMARKS 189
7.2 SUGGESTIONS FOR FURTHER RESEARCH 191
APPENDIX A 193
Intersection Points 193
APPENDIX B 196
Areas of Overlap 196
BIBLIOGRAPHY 198
APPENDIX C 199
Resolving Contact Forces in the Global Coordinate System 199
APPENDIX D 205
Mohr-Coulomb Elasto-Plastic Model 205
APPENDIX E 215
Interval Halving Technique 215
BIBLIOGRAPHY 216
APPENDIX F 217
Radial Return Method 217
BIBLIOGRAPHY 219

LIST OF TABLES

Table 3.1: Input parameters 51

Table 4.1: Input parameters used in the examples 96

Table 5.1: Parameters used in the analysis of the bearing capacity of a footing . 126

Table 5.2: Parameters used for discrete element analysis of active and passive earth pressures 135

Table 6.1: Index properties of the materials at the Carsington Dam site 159

Table 6.2 : Strength properties of materials at the Carsington Dam site 161

Table 6.3: Material parameters used in analysis of the Carsington Dam failure . 171

LIST OF FIGURES

Figure 2.1: Domain discretization for (a) the finite difference method and (b) the boundary element method 10
Figure 2.2: Different shapes of particles used in DEM 13
Figure 2.3: Nature of particle-particle contact in DEM, Cundall [27] 14
Figure 2.4: Motion of a deformable body in a stationary Cartesian coordinate system, modified from Bathe [4] 18
Figure 2.5: Distribution of vertical stress under an inclined load at the top of a slope, Barbosa [36] 19
Figure 2.6: Blocks and FEM discretizations by DDA—for three blocks Shi [44] 22
Figure 2.7: Three covers C_1, C_2, and C_3 have a common area E, Shi [47] 24
Figure 2.8: Different covers of the manifold method of splitting elements..........28
Figure 3.1: Independent degrees of freedom for each node sharing the same coordinates 38
Figure 3.2(a): Under the application of external loads element 1 deforms........... 41
Figure 3.2(b): History from the substep of element 1 carried onto element 2...... 41
Figure 3.3(a): Flow chart for finite element solutions using velocity constraints 48
Figure 3.3(b): Flow chart for finite element solutions using displacement constraints 49
Figure 3.4: Two-dimensional section of the ground and its discretization...........50
Figure 3.5: Horizontal, vertical, and shear stress convergence.............................52
Figure 3.6: Displacement history of node 16 53
Figure 3.7: Discrete element mesh for a smooth flexible footing..........................54
Figure 3.8: Ground surface settlement profile 55
Fig. 3.9: Developed stresses and displacement vectors..56
Figure 3.10: Regular grid of elements in freefall, and self-weight contributions to the nodal force 57
Figure 3.11: Velocity X distribution over time steps for elements 1, 6, 11, and 16 (node 1) 58
Figure 3.12: Vertical velocity distribution over time steps 59

Figure 3.13: Net nodal Y force distribution over time steps for zero damping 60
Figure 3.14: Stress distribution within a slope at 0.009 seconds..........................62
Figure 3.15: Stress distribution within a slope after 5 seconds 63
Figure 3.16: Convergence of Y-stress at time steps (a) $\Delta t = 0.01$, (b) $\Delta t = 0.02$ seconds 65
Figure 3.17: Stress convergence with heavy damping, $\alpha = 20 \text{ sec}^{-1}$.......................67
Figure 3.18: Nonconvergence under a small damping coefficient of $\alpha = 0.01 \text{ sec}^{-1}$ 67
Figure 3.19: Consistent mass matrix applied to the scheme 68
Figure 4.1: Grid cell decomposition of the domain, modified from Hopkins [5]..74
Figure 4.2: Detection of a contacting node N within the home element H...........75
Figure 4.3: Definitions of the angles between the local and global coordinate systems used in the model..79
Figure 4.4: Tangential force model 82
Figure 4.5: Reference configurations representing the motion of a deformable body within a stationary Cartesian coordinate system..85
Figure 4.6: Vertical stress distribution of a 2D iso-parametric element falling under gravity (example 1)..97
Figure 4.7(a): Simulations of an element falling on base elements at different equilibrium points (example 1, points A, B, C, D) 98
Figure 4.7(b): Simulations of an element falling on base elements at different equilibrium points (example 1, points E, F) 99
Figure 4.8: Vertical stress developments as discrete-finite elements interact (example 2).. 101
Figure 4.9: Vertical stress and time step plots for elements 5 and 6 in example 2 102
Figure 4.10: Multi-block toppling for finite and discrete simulations (example 3) 106
Figure 5.1: Mohr-Coulomb yield surface in principal stress space, Chan, [13]....117
Figure 5.2: Flow chart showing the steps for elasto-plastic computations 120
Figure 5.3: Comparison of element shapes...121

Figure 5.4: (a) 100 element mesh, (b) 800 element mesh ... 125
Figure 5.5: Load-Displacement curves for a circular footing ... 125
Figure 5.6: Surface displacements for different loading conditions ... 127
Figure 5.7: Spread of yielded zone under different loading conditions ... 128
Figure 5.8: Simulation extracts at different time steps ... 131
Figure 5.9: Stress-strain variation within an element at the edge of a footing ... 132
Figure 5.10: Stress-strain variation within an element at 0.8 m depth below a footing ... 133
Figure 5.11: Mesh comprised of 520 elements used in retaining wall analysis ... 134
Figure 5.12: Developed pressures for corresponding displacements computed from nodal forces and element stresses. ... 136
Figure 5.13: Translation of a wall and corresponding earth pressure coefficients ... 137
Figure 5.14: Degree of convergence in terms of horizontal and vertical stresses behind a retaining wall. ... 138
Figure 5.15: Failure for active condition—Simulation with 520 elements ... 140
Figure 5.16: Stress-strain plots for elements 25 and 248 during continuum and discontinuum analyses for the active earth pressure case ... 141
Figure 5.17: Developed plastic zones and yielded elements ... 142
Figure 5.18: Stress-strain plots during finite and discrete analyses for elements 33 and 105 ... 143
Figure 5.19: Mobility of the elements; Passive earth pressure ... 146
Figure 6.1: Location plans for the Carsington Dam, Skempton [3] ... 152
Figure 6.2: Plan of the Carsington Dam, Chen [8] ... 154
Figure 6.3: Longitudinal profile of the Carsington Dam, Chen [8] ... 155
Figure 6.4: Typical cross-section of the Carsington Dam, Chen [8] ... 156
Figure 6.5: Peak shear strength data (Carsington Dam) ... 158
Figure 6.6: Stress-Displacement curves for yellow clay (Carsington Dam), Skempton [3] ... 160
Figure 6.7: Post peak behaviour of the core (Carsington Dam), Skempton [3] ... 161
Figure 6.8: Zone II fill strength on slip surfaces (Carsington Dam), Skempton [3] ... 163

Figure 6.9: Plan of the Carsington Dam during failure, Skempton [3] 165
Figure 6.10: Sudden reduction of pore pressure in the Carsington Dam after failure, Skempton [3] 166
Figure 6.11: Investigative section at Ch. 725 of the Carsington Dam, Skempton [3] 167
Figure 6.12: Yield criteria and definition of terms (Carsington Dam), Potts [4] 170
Figure 6.13: Mesh used in the analysis of the Carsington Dam failure, chainage 725 172
Figure 6.14: Vertical stress contours as different stages of elements are added to the Carsington Dam 175
Figure 6.15: Contour plots of the Carsington Dam at the end of construction ... 177
Figure 6.16: Displacement vectors over the upstream slope (Carsington Dam) 178
Figure 6.17: Vertical displacements (in meters) (Carsington Dam) 179
Figure 6.18: Horizontal displacements (in meters) (Carsington Dam) 180
Figure 6.19: Horizontal displacement in the core versus elevation (Carsington Dam) 180
Figure 6.20: Comparison of vertical strains in the core (Carsington Dam) 181
Figure 6.21: Stages of failure of the Carsington Dam 187
Figure A-1: Illustration of the calculation of the intersection point between two lines 194
Figure B-1: Comparison of area of overlap and depth of penetration 197
Figure C-1: Definition of local coordinate system 199
Figure C-2: Near element approaching from top right direction 200
Figure C-3: Near element approaching from bottom left side 201
Figure C-4: Near element approaching from top left direction 201
Figure C-5: Near element approaching from bottom right direction 202
Figure C-6: Special cases for the calculation of angle γ 203
Figure C-7: Local coordinate system for 4 intersection points 204
Figure D-1: Elastic perfectly-plastic Mohr-Coulomb constitutive relationship. 205
Figure E-1: Solution procedure for interval halving technique, Chan [1] 216

Figure F-2: Radial return for Mohr-Coulomb plasticity, two dimensional stress space 218

LIST OF SYMBOLS

i, j	coordinates for grid
u, v	displacements in the X and Y directions
a_i, b_i	constants for defining displacement fields
N_{ij}	interpolation shape function
$\mathbf{[K]}$	stiffness matrix
$\mathbf{\{f\}, [F]}$	force matrix
N	total number of elements
$\mathbf{[B]}$	strain displacement matrix
$\mathbf{[C], D}$	constitutive matrix
Ω	domain for the integral (surface or volume)
t	time
Γ	boundary of the domain
t_{ij}	traction vector
$\int$	integration
∂	incremental form (/variation) of a term
c_{ij}	constant for boundary element method
Δ	incremental variation of any quantity
k_n, K_n	normal stiffness
k_t, K_t	tangential stiffness
X, Y	coordinate system
$\mathbf{[m], m_i}$	mass matrix
c	cohesion intercept of the Mohr-Coulomb criterion
ϕ	angle of internal friction
C_n	normal damping coefficient
C_s	tangential damping coefficient
D_n	normal damping force
D_s	tangential damping force
n^*	normal component of velocity

s^*	tangential component of velocity
τ_s	shear strength
ω	frequency
L	length of any side of element
A, B, C, D, E, F	constants of a displacement field
T	tangential force component
N	normal force component
μ	frictional component
f	friction coefficient
a	radius of contact
R	radius of sphere
G_s	elastic constant
v_s	displacement response—Mindlin's solution
$\{d\}$	mass proportional damping
$\{s\}$	stiffness proportional damping
$\{\dot{u}, \dot{U}\}$	velocity matrix
$\{\ddot{u}, \ddot{U}\}$	acceleration matrix
α, β	damping constants
σ_{ij}	stress components
ε_{ij}	strain components
$\ddot{u}_i$	acceleration
$\ddot{\theta}$	rotational acceleration
δ	small variation of any referenced quantity
$I, [\mathbf{I}]$	internal resisting force vector (/matrix)
$P, [\mathbf{P}]$	external force matrix
Φ	shape function
φ	penalty function
U_c	contact force (penalty function)
dA	incremental area
$\mathbf{A}$	area matrix
γ	shear strain and unit weight (interchangeable)

Π	strain energy
d	penetration of the contact of two elements
$\mathbf{B_p}$	displacement function for manifold method
$\mathbf{T_i}$	cover displacement function
C_i	covers of manifold method
Σ	summation over the given number of terms
V	volume of the referenced domain
$\mathbf{J}$	Jacobian matrix
E	modulus of elasticity
ρ	density of material
ν	Poisson's ratio
${}_0\nabla$	partial differentiation
$\boldsymbol{X}$	deformation gradient
I_1	first invariant of stress tensor
J_2	second invariant of stress tensor
λ	scalar constant of proportionality
π	PI constant
θ	lode angle
M	slope of critical state line
q, p	critical state stress parameters
S	first Piola-Kirchhoff stress tensor
F	yield function
G	plastic potential function

1 INTRODUCTION

1.1 GENERAL

Discretizations of engineering systems, including geotechnical applications, are based on the idealization of continuity. The versatile and valuable finite element method and the finite difference method incorporate continuum constitutive models. Since the microstructure of geological materials is small, continuum approaches are successful. However, for simulating jointed rock problems, masonry, ice plates, and problems related to granular materials, continuum methods are severely limited.

The discrete/particulate nature of granular materials makes it difficult to capture their behaviour with continuum models. During the last two decades, efforts have been made to model the behaviour of these materials under large deformations and to overcome the limitations of continuum methods in situations approaching failure. Discrete element methods simulate discrete body interactions, capturing motion and irrecoverable deformations. Attempts have been made to simulate discrete behaviour by introducing discontinuities into continuum methods and to model a discontinuum with continuum incorporated as a special case.

In this thesis a hybrid technique is developed to deal with problems of excessive displacements in the field of geomechanics. Finite element and discrete element methods are coupled and the results are validated by applying the developed technique to few practical examples. A case history of the Carsington Dam failure is back-analyzed.

1.2 OVERVIEW OF PREVIOUS STUDIES

Geotechnical engineering analysis plays an important role in the design of many engineering structures. Various analyses of the mechanisms of soil-structure interactions and the stability of soil structures are carried out by using various available methods. For continuum solutions, empirical approaches, closed form solutions, the finite element method, and the finite difference method are applied. The concepts of the discrete element method are introduced based on an idealization of geological/geotechnical materials as comprising of individual discrete bodies. In order to capture the states of large displacements and deformations within the soil medium, the coupled approaches of discrete and finite element methods were developed.

The finite element method has found applications in many fields of engineering and has been incorporated into geotechnical engineering, as reviewed by Potts [1] and Desai [2]. The constitutive models idealizing the behaviour of geotechnical materials are applied within the method and their limitations appreciated. Some software's based on this approach and used in geotechnical industry are SIGMA-W, Phase2, etc. However, because of the nonlinearity involved in soil behaviour, these methods are numerical in nature. As computing costs decrease, the trend to apply these methods to analyses of geotechnical structures is likely to increase.

Some of the other available software's, e.g., UDEC, PFC, are based on the discrete element method of analysis; that is, the generic behaviour of geological materials and earth structures are simulated using multiple interacting bodies and suitable constitutive relations to define the contacts formed. The conventional discrete element model (DEM) uses the process of dynamic relaxation by integrating Newton's law over time, Cundall [3]. Since, DEM simulations are computer resource intensive and involve numerous bodies and time steps, current research in this field is focused on the development of options for parallel processing and chaos management. Another limitation of DEM is the difficulty in determining the material properties of the soil models.

As analysis methods evolved, researchers attempted to integrate the capabilities of the finite element method and the flexibility of the discrete element method to model interactions among multiple bodies. These approaches include the discrete finite element method (DFEM), discontinuous deformation analysis (DDA), material point method (MPM) and others, Munjiza [4], and have been applied to the problems of progressive fracturing and fragmentation and in the transient dynamics of systems involving large numbers of deformable bodies. DDA method based on decoupling constant deformation modes from rigid body modes led to computation of spurious stresses. Methods using joint elements were limited to small displacements and unchanging topology as they are not designed to handle large block movements.

A literature review of the methods considered in this thesis is presented in chapter 2.

1.3 OBJECTIVES AND SCOPE OF THE THESIS

This study develops an approach to model the progression from a continuum state to a discontinuum state of geological materials under various loading and displacement conditions. The methodology is based on the finite element method for continuum analysis and the discrete element method for discontinuum analysis. These methods were selected because each has a unique capability to solve engineering problems.

A numerical method is introduced to effectively simulate the computations of displacements, strains and stress states, splitting of the elements, and element mobility over time. The highlights of the research are described below:

- A new strategy is presented to use independent discrete elements and apply displacement/velocity nodal constraints to obtain solutions equivalent to finite element solutions.

- For contact detection and its subsequent force computations, physical and numerical issues are identified and discussed.
- Specific material constitutive relation is applied and verified using conventional examples.
- A case history of the failure of the Carsington Dam is analyzed.

1.4 ORGANIZATION OF THE THESIS

The thesis is organized into seven chapters.

A review of literature is presented in Chapter 2. Well-established approaches to the finite element and discrete element methods are described. Similar coupled techniques based on these two basic approaches are also discussed eg discontinuous deformation analysis, the manifold method, material point method and the discrete finite element method. The strengths and deficiencies of each method are discussed and related applications are presented.

The present investigation is divided into three parts, each one with specific objectives. In part one, presented in Chapter 3, a numerical procedure is developed by using individual discrete elements, each having independent degrees of freedom and solutions equivalent to those of the finite element method were obtained. The use of iso-parametric quadrilateral elements representing geological material is considered. Specific constraints are applied to the nodes in terms of either displacements or velocities to obtain the continuum solution.

The results obtained for the finite element continuum are from the solution of the equation of motion, which is the basic equation for the discrete element procedures. This provides the foundation to generate solutions for the discrete element method in continuation of the finite element solutions. The discrete finite element method can thus analyze multiple deformable bodies and overcome the limitations of either of the methods.

In Chapter 4, techniques required for the development of discrete element analysis are reviewed and appropriate schemes are applied to the present research. This includes models that represent contacts among different interacting elements along with the associated contact detection procedures. To check the reliability of the computer code and the techniques applied, several simple examples involving the movement of discrete elements are solved and discussed.

In the second part of the study presented in Chapter 5, a relevant constitutive relation representing the generic behaviour of the geological material is incorporated. The elasto-plastic Mohr-Coulomb relation with a non-associated flow rule is applied to the in-built constitutive behaviours of the contact models. Compatibility of the yield criteria with the dynamic time stepping solution scheme is recognized and checked. Two conventional examples of bearing capacity of a strip footing and earth pressures generated behind the retaining wall are solved in order to check the incorporation of the elasto-plastic constitutive relation incorporated into the developed discrete finite element scheme.

In the third part of the thesis, a case history of the Carsington Dam failure is analyzed in Chapter 6. Previous work on this case history is described and parameters applied in the present analysis are reviewed and summarized. The advantage of using staged construction procedures to perform the analysis is discussed. Results obtained from previous analyses and from current simulations are amalgamated to define the problem up to the continuum part. The developed technique is useful in identifying the probable slip surface and the mobility of the failed mass to capture.

In Chapter 7, conclusions and recommendations for further research are presented.

BIBLIOGRAPHY

1. Potts, D. M., and Zdravkovic, L., *Finite element analysis in geo-technical engineering: Theory*. 1999, London, U.K.: Thomas Telford Publishing. 440.
2. Desai, C. S., and Siriwardane, H. J., *Constitutive laws for engineering materials*. 1984: Prentice Hall Inc. 468.
3. Cundall, P. A., and Hart, R. D., *Numerical modeling of discontinua*. Comprehensive Rock Engineering, Ed. Hudson, J. A., 1993. **2**: p. 231–243.
4. Munjiza, A., *The combined finite-discrete element method*. 2004, West Sussex: John Wiley & Sons Ltd. 333.

2

LITERATURE REVIEW

It has long been recognized that geotechnical modeling problems are data limited. While it is not uncommon in the civil engineering environment to devote several percent of the project budget to soil mass characterization, in various situations this figure is normally several orders of magnitude smaller. According to Wiles [1], this necessitates a very different modeling approach from that developed in, e.g., civil (structural), electrical, or aerospace engineering.

Nevertheless for a selected modeling approach, it is necessary to verify the reliability of model predictions if designs based on these are also to be reliable. Here, it is considered that back analysis is the basis of model calibration for reliable failure prediction. Although back analysis cannot guarantee unique solutions since different constitutive laws, numerical methods, and boundary conditions may reach the same result, prediction reliability can be established by comparing results based on back analysis of multiple predictions. Agreement in a few isolated cases is at best anecdotal. Reliability can be established only by using statistical techniques to compare the difference of many individual predictions with their average behaviour. Well clustered results under a wide range of conditions would indicate reliable modeling predictions.

Chapter 2

2.1 INTRODUCTION

Many disagreements and ambiguities arise in civil engineering due to the fact that soil is inelastic, anisotropic, and rarely homogeneous. Subjecting the soil medium to loading in the field gives rise to large deformations. Traditionally, geotechnical problems have been treated in terms of small-strain elasticity and limit analysis with variable results.

Considerable effort has been expended on the numerical solution of problems involving large deformations or strains. Finite element formulations, discrete element modeling, discontinuous deformation analysis, discrete finite element methods, manifold method, material point method and other techniques have been employed for problems dealing with large deformations and are reviewed in this chapter. This thesis develops a hybrid approach to continuum and discontinuum analysis based on some of the reviewed methods.

2.2 CONTINUUM BASED METHODS

The ability to evaluate large deformations, displacement vectors, stresses, and strains enhances the potential to evaluate the effects of load and find solutions for problems involving failure and mobility of the soil mass. In engineering simulations of failure, the geometry of the geological model results in a continuously evolving nonlinear interaction of the discretized structure, Dufour [2].

The developed discrete finite element method models the continuum behaviour of a given soil profile under various loading conditions until failure and after failure the mobility of the disintegrated soil mass is analyzed by discrete or discontinuum methods. A review of continuum-based models provides insight into selection of computational procedures for the continuum part of the method developed in this thesis.

The finite difference method (FDM) — arguably the oldest numerical method of continuum analysis—replaces the partial derivatives of the field functions with differences defined over certain spatial intervals in the coordinate directions. The set of simultaneous algebraic equations and proper boundary constraints obtained are used to solve for the values of unknowns.

The displacement of one node can be represented in terms of the neighboring nodes for an incompressible solid in 2-D by:

$$u_x^{i,j} = a_1 u_x^{i-1,j} + a_2 u_x^{i,j-1} + a_3 u_x^{i,j+1} + a_4 u_x^{i+1,j} \qquad 2.1$$

$$u_y^{i,j} = b_1 u_y^{i-1,j} + b_2 u_y^{i,j-1} + b_3 u_y^{i,j+1} + b_4 u_y^{i+1,j} \qquad 2.2$$

where u_x and u_y represents displacements in the x and y directions respectively for any node position (i,j) in terms of coefficients a_i and b_i, Figure 2.1(a). Finite difference methods can also be applied to time domains with properly chosen time steps, so the function values at time t can be inferred from the values at t-Δt. The finite difference method is applied to FLAC computer software developed by Itasca Engineering Consultants, Minneapolis, USA [3].

The grid system is used to generate the function values at sampling points; no local trial functions or interpolation functions are defined as in finite element method (FEM). The FDM suffers from shortcomings in dealing with complex boundary conditions, fracture, and material inhomogeneity.

In contrast to the finite difference method, the finite element method discretizes the domain into a finite number of internal contiguous elements with fixed number of nodes and regular shapes. The unknown function is then approximated using trial functions of the nodal values, which form the basic unknowns in the equations of the finite element method and must satisfy the governing equations and equilibrium.

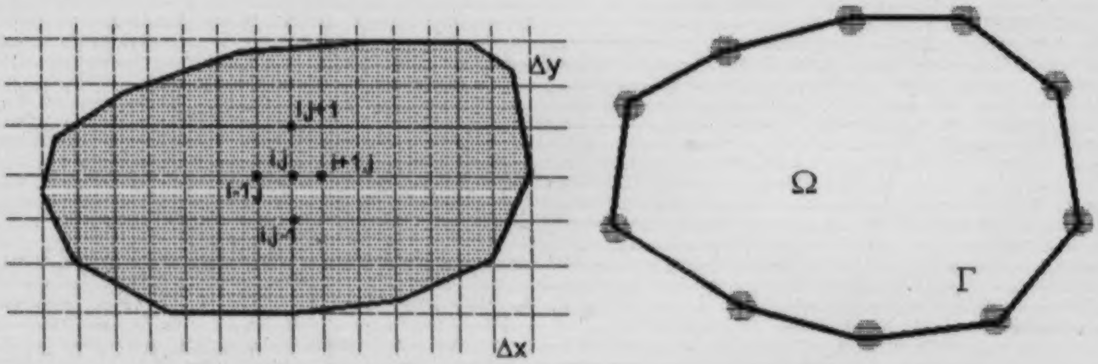

(a) (b)

Figure 2.1: Domain discretization for (a) the finite difference method and (b) the boundary element method

These trial functions for displacements *u* for any element *e* can be of the form:

$$u_i^e = \sum_{j=1}^{m} N_{ij} u_i^j \qquad 2.3$$

where N_{ij} are shape functions, *i* represents displacement index for either x or y direction and j represents number of total nodes of an element *e*.

In most of the finite element formulations it is assumed that the displacements are infinitesimally small and the boundary conditions remain unchanged during the application of the loads on the assemblage of the elements. The assumption that the displacements are small goes into the formulation of the stiffness matrix for small deformation problems. The strain displacement matrix is assumed constant and independent of element displacements. For elastic solutions, linearity is maintained by the use of a constant stress strain matrix, with constant constraint relations being used, as the boundary conditions remain unchanged. However, if the displacement boundary conditions change during loading, the response becomes nonlinear, Bathe [4].

For large deformation problems the Eulerian, total Lagrangian, updated Lagrangian, and arbitrary Lagrangian Eulerian formulations are the main approaches to continuum mechanics problems, Hu [5]. The softwares Sigma/W, Phase 2, ADINA, ABAQUS and many more developed with the finite element approach are available commercially.

Another continuum approach, the boundary element method (BEM), seeks a weak solution for the global domain through a boundary integral statement. The main advantage of the boundary element method is a reduction in the computational model dimensions by one. In this method discretization is carried out over the boundary and not over the domain of the problem, and boundary elements are approximated as in the finite element method. For a linear elastic problem with domain Ω (Figure 2.1 b), a boundary Γ of a unit normal vector n_i, and a constant body force f_i, the integral is written as:

$$c_{ij}u_j + \int_\Gamma t^*_{ij}u_j d\Gamma = \int_\Gamma u^*_{ij}t_j d\Gamma + \int_\Gamma \frac{\partial u^*_{ij}}{\partial n} f_j d\Gamma \qquad 2.4$$

where u_j and t_j are displacement and traction vectors on the boundary and u^* and t^* are displacement and traction kernels. The term c_{ij} is determined from the geometry of the system.

Finite element and finite difference procedures are used in geomechanics to analyze slope stability problems, excavation sequences, bearing capacity, and for tunnel construction. The finite element method is an accurate and versatile alternative requiring fewer prior assumptions regarding failure mechanisms. The advantages of finite element methods include not having to make assumptions about the failure surface and inter-slice forces and the ability to monitor progressive failure, Griffiths [6].

As summed by Duncan [7] and reported by Benko [8], Brown [9], Chen [10], Hassan [11], Jeremic [12], Potts [13], Wong [14], Fairhurst [15], Snitbhan [16] and many more researchers, the finite element method in the geotechnical field has been used to calculate movements (deformations), stresses, strains, and pore pressures in embankments and slopes.

2.3 DISCRETE ELEMENT METHOD

Development of the discrete element method (DEM) by Cundall [17] led to an upsurge of applications to the solution of load deformation problems. The basic difference between discrete element methods and continuum-based methods is that contact patterns between components of the system continuously change with the deformation for the DEM, whereas they remain fixed for the FEM. Cundall and Strack [18] employed idealized particles such as cylinders, spheres, and ellipsoids to study the constitutive behaviour of granular materials, Figure 2.2. The method is based on the use of an explicit numerical scheme in which the interaction of the particles is monitored contact by contact and motion is modeled particle by particle. In this method, repeated solution of Newton's second law of motion and the force displacement law is processed over number of timesteps to simulate the interaction between particles. The cycle of the formulation involves the following steps:

- Newton's second law of motion is applied to each particle and acceleration for each particle is computed.

  $$\text{Acc.} = F_{(x)1} / m_{(x)} \qquad 2.5$$

- These accelerations are then integrated to obtain the velocities and displacements of the particles.
- For the next timestep the values of the inter-particle contact forces are determined using the contact laws.

  $$\Delta F_n = k_n \, v \, \Delta t \qquad 2.6$$

  where ΔF_n is the incremental normal contact force, k_n is normal stiffness, v is relative velocity and Δt is the timestep.

- Locations of the particles are updated, formation of new contacts are determined, existing contacts are deleted, and the cycle is repeated until either equilibrium is obtained or to the point of interest.

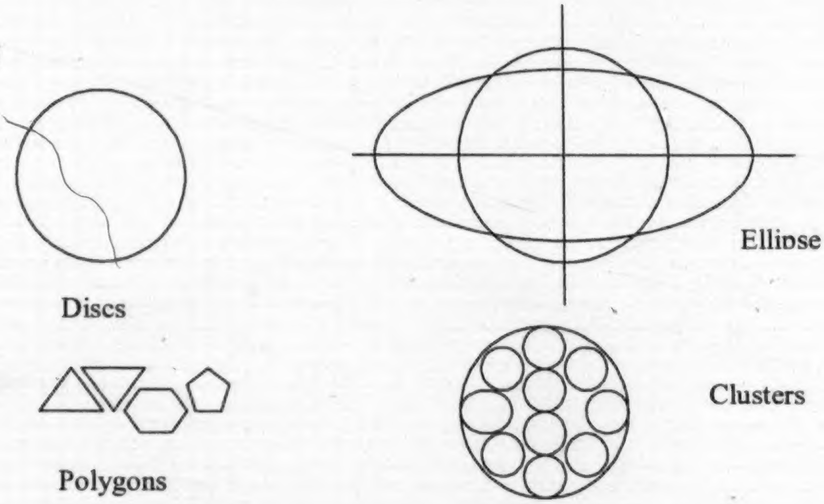

Figure 2.2: Different shapes of particles used in DEM

Timesteps for the above dynamic behaviour are chosen such that velocities and accelerations are assumed to be constant during each timestep. Chosen timesteps should be so small that during a single timestep disturbances cannot propagate from any disc further than its immediate neighbors, Cundall and Strack [18]. A Coulomb type friction law is incorporated such that when the magnitude of the shear force exceeds the maximum possible value, the shear force is assigned that value. Whenever the absolute value of the shear force is maximum, friction damping occurs either by local contact damping or global damping. Damping can be envisioned as normal or shear with the use of stiffness springs and dashpots as shown in Figure 2.3.

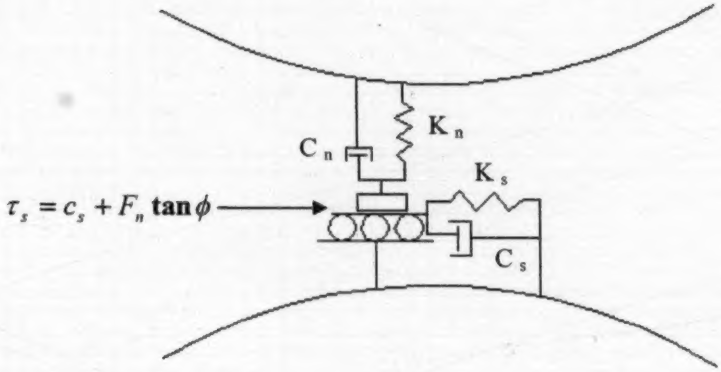

Figure 2.3: Nature of particle-particle contact in DEM, Cundall [27]

The related damping forces in the normal and tangential direction are calculated respectively by the following set of equations:

$$D_n = C_n n^* \qquad D_s = C_s s^* \tag{2.7}$$

where C_n and C_s are damping coefficients and n^* and s^* are the normal and tangential components of the relative velocities.

A central difference scheme is used to integrate equations whereby velocities are evaluated halfway through the timestep. The numerical scheme will be stable if the timestep Δt is taken as a fraction less than one of the critical timesteps. The instability is a result of the explicit nature of the model and to stabilize computations a mass damping is used to maintain the system of conditions close to static equilibrium. The critical timestep is estimated based on the single degree of freedom system of mass m connected to the ground by a spring of stiffness k, for which the critical timestep equals $2\sqrt{(m/k)}$.

Another important feature of discrete element analysis is contact detection. As reported by Williams [19], contact detection is done either by graph based or cell based decomposition models. A contact detection based on no binary search (NBS) is presented by Munjiza [20] with the detection time proportional to N, i.e., the number of contacting bodies, but with a limitation that this is only applicable to bodies of similar size. This approach is based on space decomposition with each disc and cell in the space being assigned an identification number and a linked list being continuously updated. As no loops over the cells are performed for any operation, the total CPU time needed to perform detection is considerably reduced.

The contacts are based on either a soft contact approach or a hard contact approach. In the soft approach, a finite normal stiffness is taken to represent the measurable normal stiffness that exists at contacts, while for the hard contact, interpenetration is considered nonphysical and the computational schemes prevent overlaps or interpenetration. Cundall [21] suggests that choice of the contact assumption should be based on physics rather than on numerical convenience or mathematical elegance. Further, the material can be represented either as rigid or deformable. If, however, deformation of the solid material cannot be neglected, deformability can be incorporated either by subdividing the body into elements or by mode superposition schemes, Williams [22].

Once contacts are established, primarily four types of contact models have been used for normal and tangential stiffness by various researchers. The simplest of all is the linear contact law, Rothenburg [23], and at the extreme is Mindlin's complete solution for contacts. In Mindlin's solution, for identical elastic rough spheres of radius R and elastic constants G_s and ν_s and radius of contact a, the normal load displacement response is nonlinear elastic:

$$K_n = 2\,G_s\,a/(1-\nu_s) \qquad 2.8$$

The discrete element method finds application in analyzing slopes, underground excavations, surface mining of rocks having multiple joint sets, geologic materials having discrete nature (soils), and for intact rocks. A good database is yet to be generated where numbers of slopes or other structures have been simulated using distinct element techniques.

The discrete element method has been applied in the field mainly for slope stability analysis and excavations, as presented by Williams [19], Hocking [24], Kishino [25], Coggan [26], Choi [27], Hamajima [28], Hsu [29], Potyondy [30], Wang [31], and others for geological material involving rocks. It is concluded that the use of discrete element analysis, UDEC, or PFC [3], eliminates the need for a constitutive material model for rock (intact or fissured) as is normally required for finite element analysis. In turn, PFC uses micro-parameters to create an assembly that exhibits the same deformational behavior as rock samples in laboratory tests. Thus, this excludes the inaccuracy of the stress-strain relation hypothesis.

It is worth mentioning the remarks made by Peter Cundall about the future of the discrete element method:

> *"The elimination of discrete element methods? If we could develop continuum formulations that successfully reproduce the effects of a discontinuum (such as micro-rotation, interlocking, etc.), we could use more efficient continuum programs for modeling."*

2.4 COMBINED FINITE DISCRETE ELEMENT METHOD

Incorporation of deformation kinematics into discrete element formulations has led to a combined finite/discrete element approach in which a problem is analyzed by a combination of the two methods. This solution methodology is suited well to problems in which progressive fracturing takes place, Munjiza [32]. In considering fracturing media, starting from a continuum representation by finite elements of the solid domain, progressive fracturing is allowed to take place according to some fracturing criteria, thereby giving rise to a discontinuum, eventually leading to discrete elements that can be either rigid or deformable. Te main issues are, Bicanic [33]:

- *Finite element formulation capable of capturing the strain localization and eventually leading to fracturing;*
- *Fracturing criteria and models;*
- *Remeshing algorithm (applied locally) for fully fractured zones;*
- *Contact detection procedures; and*
- *Representation of frictional contact conditions.*

The complex geometrical changes that take place during the transition from finite elements to discrete elements can be better appreciated with the use of visualization techniques which facilitate the interpretation of results and help to validate the procedures for contact penetration conditions.

2.4.1 Discrete Finite Element Method

Barbosa [34] proposed a method to analyze deformable bodies, idealized as finite elements, using an explicit finite element formulation based on an updated Lagrangian approach. The equation of motion for the system of finite elements representing each deformable body is expressed as:

$$M^t\ddot{U} + \alpha M^t\dot{U} = P^t - I^t \tag{2.9}$$

The motion continues until the out of balance force $({}^tP - {}^tI)$ tends to zero as the solutions are obtained using the explicit second central difference integration scheme over a number of time steps. The Cauchy stress tensor and the Almansi strain tensor are updated after each time step by updating the 2nd Piola-Kirchoff stress tensor and Green's strain tensor, respectively. Motion of the deformable body is shown in Figure 2.4.

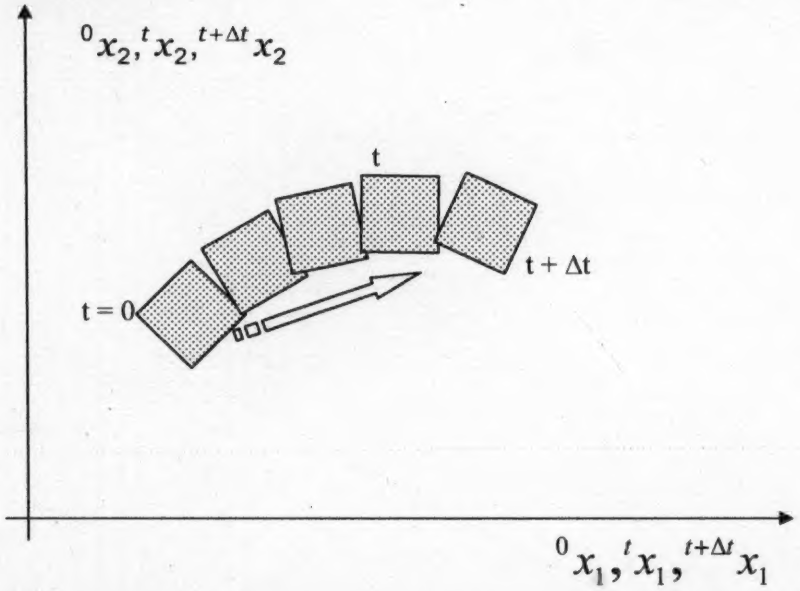
${}^{0}x_2, {}^{t}x_2, {}^{t+\Delta t}x_2$
t
t + Δt
t = 0
${}^{0}x_1, {}^{t}x_1, {}^{t+\Delta t}x_1$

Figure 2.4: Motion of a deformable body in a stationary Cartesian coordinate system, modified from Bathe [4]

In his study based on a similar approach, Ghaboussi [35] assembles the discrete elements by enforcing the contact laws and the analysis is similar to the nonlinear finite element method. The nonlinearity in the contact law applied by Ghaboussi is due to the separation and sliding of the blocks, with material nonlinearity being the other source along with geometric nonlinearity. The contact stresses are transformed into energy equivalent nodal forces and the contact shear stresses are determined from a simple elastic, perfectly plastic material model.

Barbosa [36], in the method DBLOCKS, uses only face-to-face contacts, and a simplified linear relation between contact stresses and contact deformations is assumed. Due to the nonlinearity, an explicit second central difference method is used which does not require formation of the tangent stiffness matrix. The DFEM as proposed for DBLOCKS is applied to the modeling of jointed rock, to the analysis of slope stability in rock slopes, and to the bearing capacity analysis of the rock slope face. The vertical stress distribution as evaluated by this approach for the rock slope is shown in Figure 2.5.

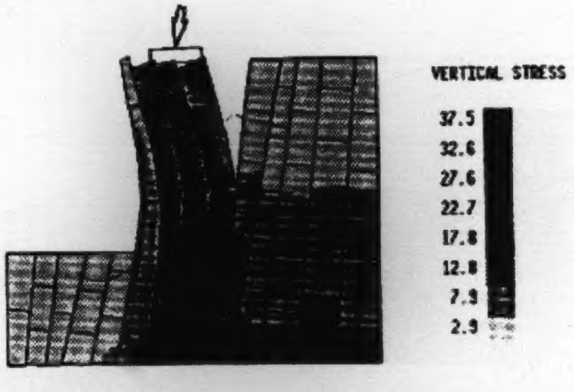

Figure 2.5: Distribution of vertical stress under an inclined load at the top of a slope, Barbosa [36]

2.4.2 Hybrid DEM/FEM Methods

Pan [37], Ishibashi [38], and Mohammadi [39] described a hybrid numerical method of modeling delamination and rock fracture, in which the DEM and FEM are coupled with distinct elements used in the part of the mesh where failure is likely and the remainder of the mesh is composed of finite elements. The hybrid analysis experiences relatively large deformations, including slips at the interface. The interface between the two domains includes points common to both regions and is modeled with seven noded iso-parametric elements. During the analysis, displacements from the FEM are fed into the DEM domain as displacement boundary conditions. The test program developed has been applied to tunnel roof problems and the excavation of a square tunnel through fractured rock.

In a similar approach followed by Liao [40], the domain of the particles is defined by a suitable number of nodal points. This reduces the degrees of freedom of the discrete system to the number of nodal points. This is achieved by using a continuum shape function Φ to represent the field of discrete kinematic variables. However, in this formulation particle displacement u and rotation $\boldsymbol{\omega}$ are considered independently, with the displacement of the contact point on the surface given by:

$$\{ u^{ac} \} = \{ u^{a} \} + [\Phi^{ac}] \{\omega^{a}\} \qquad 2.10$$

The principle of virtual work is used to obtain a relationship between the forces and displacements at the nodal points. Mamaghani [41] uses the finite element method, incorporating concepts of discrete elements to model masonry structures. The difference is in the contact model which is based on a direct shear test and is represented as stress-strain type modeling (i.e., band type modeling), where contacts are considered as bands of finite thickness. The secant stiffness method together with an updated Lagrangian scheme is employed to deal with the nonlinear behavior.

2.4.3 Combined Finite Discrete Element System

Munjiza [42] uses the penalty function method for a combined finite-discrete element system in which the algorithm assumes discretization of individual elements into finite elements to deal with fracture and fragmentation. The penalty function method in its classical form assumes that two bodies in contact penetrate and this penetration results in contact force and it takes the form:

$$U_c = \int_{\Gamma} \frac{1}{2} p \, (r_t - r_c)^T (r_t - r_c) \, d\Gamma \qquad 2.11$$

where p is the penalty term, r_i is the position vector for elements bounded by boundary Γ. The penetration of any elemental area dA of a contactor into the target results in an infinitesimal contact force given by:

$$df = [grad\varphi_c(P_c) - grad\varphi_t(P_t)]\,dA \qquad 2.12$$

where φ_i are the potential functions for contactor and target elements for overlapping points P_c and P_t. With transient dynamics, during contact, kinetic energy is transformed into potential energy. Potential energy is transferred back into kinetic energy when contacts are released.

Munjiza [32] demonstrates the dynamic domain decomposition (DDD) strategy for attaining the effective parallelism for the combined discrete/finite element method. The dynamically changing configuration associated with this method makes the parallelism more difficult and challenging. DDD is classified as either geometric or topological, where the geometric domain exploits the location of objects in the simulation and the topological domain deals with the connections of the interactions.

2.4.4 Discontinuous Deformation Analysis

Discontinuous deformation analysis (DDA), proposed by Shi and Goodman [43], is another member of the discrete finite element method family. DDA permits relatively large time steps and closed-form integrations for the stiffness matrices of the elements, two advantages of DDA over the DEM. It is also possible to transform the FEM code into a DDA code while keeping the advantageous features of FEM.

DDA models discontinuum material as a system of individually deformable blocks that move independently without interpenetration. As originally proposed, this method was applied for back analysis, Shi [43], to determine the best fit for a deformed configuration of a block system from measured displacements and deformations. The approach followed did not make use of any material properties as input but was defined as an exercise of geometry, with the formulations based on six basic variables, i.e., three rigid body motions and six strain components. This method was later modified to perform complete deformation analysis, Shi

[44], in which the displacement field was represented as a complete first order approximation, Figure 2.6. The basic simultaneous equilibrium equations are formulated from the concepts of energy minimizations by setting the partial derivatives of the total potential energy equal to zero and the assemblage of the equations is the same as in the finite element method. The displacement field is represented as:

$$\begin{pmatrix} u \\ v \end{pmatrix} = \begin{pmatrix} 1 & 0 & -(y-y_o) & (x-x_o) & 0 & (y-y_o)/2 \\ 0 & 1 & (x-x_0) & 0 & (y-y_o) & (x-x_o)/2 \end{pmatrix} \begin{pmatrix} u_o \\ v_o \\ r_o \\ \varepsilon_x \\ \varepsilon_y \\ \gamma_{xy} \end{pmatrix} \qquad 2.13$$

and the minimization leads to an equations of form [K]{d} = {f}. The kinematic constraints on the system of blocks are imposed using the penalty method. These numerical penalties are analogous to stiff springs and are applied at the contacts to prevent interpenetration of the blocks. Tension and penetration at the contacts results in expansion or contraction of the springs; hence energy is added to the system, defying the concept of minimum energy. Thus, the minimum energy concept is one with no tension or penetration.

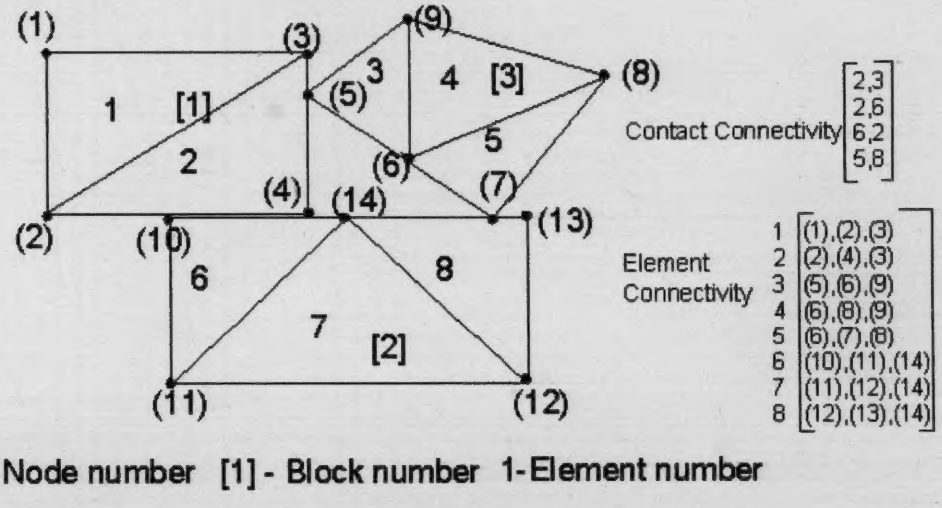
(1)
(2)
(3)
(4)
(5)
(6)
(7)
(8)
(9)
(10)
(11)
(12)
(13)
(14)
1
2
3
4
5
6
7
8
[1]
[2]
[3]
Contact Connectivity
2,3
2,6
6,2
5,8
Element Connectivity
1 (1),(2),(3)
2 (2),(4),(3)
3 (5),(6),(9)
4 (6),(8),(9)
5 (6),(7),(8)
6 (10),(11),(14)
7 (11),(12),(14)
8 (12),(13),(14)
(1)-Node number [1] - Block number 1-Element number

Figure 2.6: Blocks and FEM discretizations by DDA—for three blocks Shi [44]

The strain energy of the spring with stiffness p based on displacement d used for contacts is:

$$\Pi_e = \frac{p}{2}d^2 = \frac{p}{2}\begin{pmatrix}u & v\end{pmatrix}\begin{pmatrix}l_x \\ l_y\end{pmatrix}\begin{pmatrix}l_x & l_y\end{pmatrix}\begin{pmatrix}u \\ v\end{pmatrix} \tag{2.14}$$

and the minimization of energy for the constraints will give the constraint sub-matrix. Sitar [45] employed this technique to analyze the Vaoint landslide using 2, 9, and 105 blocks. The analysis showed the concept of progressive failure with the upper portion of the slide creeping gradually on the lower portion and destabilizing the lower portion. The slide showed a very high rate of movement with the total mass moving over 400 m in 60 seconds.

2.5 MANIFOLD METHOD

In the current research, the manifold method was initially considered for the development of the coupled approach to model continuum and discontinuum behavior. The method is thus discussed in more detail in this section with highlights on the advantages and limitations of the approach from a discrete finite element point of view.

The manifold method, proposed by Shi [46], is an approximate method for solving differential equations defined in a domain with arbitrary shapes. This method provides a unified framework for solving problems that deal with both continuum and jointed materials. The manifold method presented here departs from the traditional method in that the global functions defined for the differential manifold are highly differentiable. The presence of discontinuities in the physical domain makes the function discontinuous on the contact interfaces.

2.5.1 Formulation of the Manifold Method

The manifold method as presented by Shi [46, 47] has separate physical and mathematical meshes where the mathematical mesh defines an appropriate function for the displacement field for fine or rough approximation and the physical mesh defines the domain of the entire material volume and is the integration fields for the mathematical covers. The mathematical cover is defined by the user and these covers are overlapped over the entire material volume such that the global behavior can be defined in terms of the local mathematical cover functions. These mathematical covers (described later) can be viewed similar to interpolation functions of the finite element method. Conventional meshes and regions, e.g., finite element meshes or regular grids can be used, with the mesh being chosen according to the geometry of the problem, the solution accuracy requirements, and the zoning of the physical layout. The physical domain includes the boundaries of the material volume, joints, blocks, interfaces of different material layers, and the variable waterfront. The schematic representation of the physical and the mathematical mesh is shown in Figure 2.7.

To handle a complicated function f(x,y) as defined in field F of Figure 2.7, in the finite element method it is easier to divide the whole field into finite small regions defined as mathematical covers in the manifold method. These regions C_i(i = 1,2,3....,n) can make use of simple local functions u_i(x, y) approximating the function f(x, y) in its small domain.

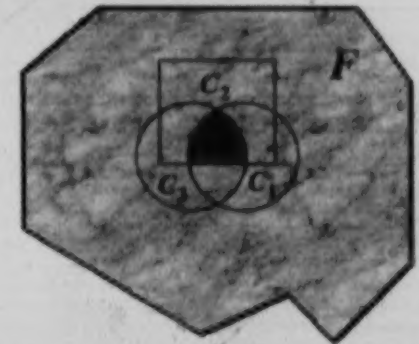

Figure 2.7: Three covers C_1, C_2, and C_3 have a common area E, Shi [47]

These mathematical functions can be either constant, linear, or any other higher order polynomials. As compared with the finite element method in the manifold method, the mathematical covers can overlap each other and the common area forms an element similar to a finite element in the finite element method, Chen [48]. The global displacement functions u(x, y) and v(x, y) over the whole physical domain and the cover system can be defined using the cover displacement functions as under:

$$u(x,y)=\sum_{i=1}^{n} w_i(x,y)\,u_i(x,y) \qquad 2.15$$

$$v(x,y)=\sum_{i=1}^{n} w_i(x,y)\,v_i(x,y) \qquad 2.16$$

where $w_i(x, y)$ is the weighting function and is defined as:

$$w_i(x,y)\geq 0 \;,\quad (x,y)\in U_i \qquad ; \quad w_i(x,y)=0,\,(x,y)\notin U_i \qquad 2.17$$

$$\text{with} \quad \sum_{(x,y)\in U_i} w_i(x,y) = 1 \qquad 2.18$$

The weighting function depends on the shape of the common area formed by the overlapping of the covers and the order of the displacement field. For triangular meshes as used by Chen [48] and Tsay [49], the three weighting functions are the same as the shape functions of the corresponding finite element triangular element. It is important to remember that a manifold cover can span or cover any form of discontinuity and can even be partially out of the physical domain. Thus the same size and shape of material cover can be used for any irregular boundary and complicated shape. The presence of joints inside the physical domain can divide the manifold cover into elements having completely independent nodes and physical cover numbers. Thus the elements move independently of each other and the movement of each separate element is traced as in the discrete element method, knowing the suitable contacts and their interactions. The formulation is based on forward time stepping sequences, and displacements, stresses, and strains are evaluated at the end of each time step, with updating of the possible contacts.

Chen [48] presents a higher order manifold method representing the displacement functions of the covers as:

$$u_p(x, y) = \mathbf{B}_p(x, y)\,\mathbf{U}_p \quad \text{where } p = i, j, k..., \tag{2.19}$$

where $\mathbf{B}_p = (1 \;\; x \;\; y \;\; x^2 \;\; y^2 \;\; ....x^n \;\; ....y^n)$, i.e., the polynomial is of nth order and $\mathbf{U}_p$ are the nodal displacements.

For plane strain small deformation problems, the strain displacement function relation can be expressed similarly to the function defined in the finite element method.

$$\begin{bmatrix} \varepsilon_x \\ \varepsilon_y \\ \gamma_{xy} \end{bmatrix} = \begin{bmatrix} \partial u(x, y)/\partial x \\ \partial v(x, y)/\partial y \\ \partial u(x, y)/\partial y + \partial v(x, y)/\partial x \end{bmatrix} \tag{2.20}$$

This elemental strain can be related to the nodal displacements as $[\varepsilon]=[B_e(x,y)][D_e]$, and can be further related to the stress by the constitutive relation $[\sigma]=[E][\varepsilon]$.

In the manifold method the elements are the integration zones which can be of any general shape, thus the integration becomes difficult. The FEM integrates the complex functions in simple domains using Gaussian integration, whereas the manifold method integrates simple functions in complex domains. As formulated by Shi [47], these integrations are reduced to integrations of the simplex, as presented in the U.S. Army report.

2.5.2 Limitations of the Manifold Method

The most important feature of the manifold method is that it incorporates the independent mathematical cover displacement functions and their contributions to the displacement functions by the applications of the weighted functions. Because of this, discontinuities present in the structure can be easily modeled. If the mathematical covers are partially out of the physical field (shown by shaded portions in Figure 2.9a), then the weight functions are defined to be effective only over the required physical field.

$$w_i(x,y)\geq 0\ ,\quad (x,y)\in\Omega_i \qquad ;\quad w_i(x,y)=0,(x,y)\notin\Omega_i \qquad 2.21$$

The inside part Ω is the effective region of the mathematical cover C_i and any mathematical cover can have only one effective region for a physical domain as shown in Figure 2.9(a).

When the mathematical cover function is divided into two completely disconnected physical domains by a discontinuous boundary, then the overlapping mathematical cover cannot be used for both physical domains. In this case two different cover functions need to be defined for both the discontinuous domains at the same location such that the two disconnected parts can move independently. In this case two mathematical covers C_i and C_m are needed at the same position and of the same shape and size but with different effective regions for the physical domain. The mathematical cover function C_i will be effective for Ω_i and the mathematical cover function C_m is effective for the region Ω_m, as shown in Figure 2.9 (b, c).

In general if the mathematical cover is to be divided into m completely disconnected physical domains by discontinuous boundaries then m completely independent mathematical covers with the same shape will be needed, which can be expensive on the computational time. Each of the mathematical covers will take one domain as its effective region. As is the case for crack growth prediction, shown in Figure 2.10(b), adaptive finite cover approximation schemes are used to construct the remeshing and the refinement is based on locally refined elements, Chiou [50]. As the crack grows to the new one then the previous mesh is abandoned and new physical covers including revised equations are needed for the updated refined mesh.

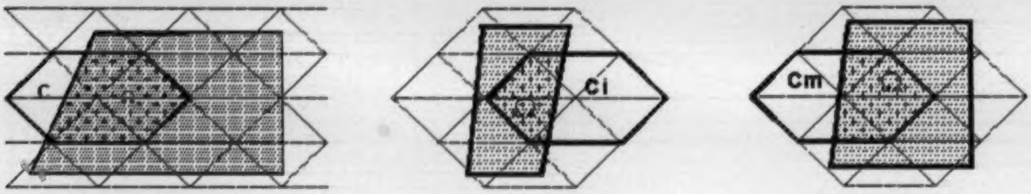

(a) (b) (c)

Figure 2.8: Different covers of the manifold method of splitting elements

2.5.3 Applications

The manifold method has been applied to the analysis of block computations, slope stability, and failure of various structures such as arches and beams by Shi [46, 47]. Crack growth is captured by Tsay [49] by employing mesh refinement techniques and also in the analysis of shear walls, Chiou [50]. Crack growth prediction requires remeshing algorithms, which add further expense to computer time. Lin [51] applied the manifold approach to model discontinuities in tunnels and to explore the difficult issue of scales when modeling a jointed rock system.

2.6 MATERIAL POINT METHOD

In contrast to the conventional mesh based methods such as FEM. FDM and BEM, several meshless methods for spatial discretization have been proposed over the last few decades. Although these meshless methods have been shown to be robust for large deformation analysis, they have not found successful way into practical applications due to some unsolved problems of boundary treatments, large rotations and interactions among different material phases, Chen [52]. One of the forms of spatial discretization, the material point method (MPM) is an extension to solid mechanics the concepts of hydrodynamics.

The MPM method discretizes the domain into a set of finite points to track the deformation process. These material points provides the Lagrangian description of the model and have an associated mass, density, stress, strain and other related parameters attached to them. A computational mesh is used in the background and information is mapped to the mesh nodes from the material points over each time step. The background mesh comprises of four node cells for 2D analysis and interpolation functions are defined to map the required information to the nodes. The description of the problem domain is similar to the Manifold method in which the physical domain is represented in terms of the background mathematical mesh.

An explicit time integrator is used to solve for the nodal accelerations from equation of motion, over a timestep satisfying the stability criteria of the critical timestep for the smallest cell based on wave speed. The boundary conditions are enforced at the cell nodes. The material points are then updated based on the new computed nodal velocities. The strain increments are determined from the gradient of nodal basis function at respective material points and constitutive model is used to compute corresponding stress increments. After updating the material points, the existing mesh may be discarded and a new mesh defined for the next timestep.

In the proposed method the problems dealing with large deformations and displacements are tackled in a different way as opposed to the various methods discussed above.

BIBLIOGRAPHY

1. Wiles, T. D., *Reliability of numerical modelling predictions*. International Journal of Rock Mechanics & Mining Sciences, 2006. 43: p. 454–472.
2. Dafour, E., Morest, L., and Muhlhaus, H. B., *A Lagrangian interpolation point finite element method for large deformation modeling of viscoelastic geomaterials*. Journal of Computational Physics, 2003. 184(2): p. 476–497.
3. FLAC, UDEC, and PFC, *Itasca Engineering Consultants*. 2006: Minneapolis, USA.
4. Bathe, K. J., *Finite element procedures in engineering analysis*. Vol. 1. 1982, New Jersey, USA: Prentice Hall, Inc,. 735.
5. Hu, Y., and Randolph, M. F., *A practical numerical approach for large deformation problems in soil*. International Journal for Numerical and Analytical Methods in Geo-mechanics, 1998. 22: p. 327–350.
6. Griffiths, D. V., and Lane, P. A., *Slope stability analysis by finite elements*. Geotechnique, 1999. 49(3): p. 387–403.
7. Duncan, J. M., *State of art: Limit equilibrium and finite element analysis of slopes*. Journal of Geotechnical Engineering, 1996. 122(7): p. 577–596.
8. Benko, B., and Stead, D., *The Frank slide: A reexamination of the failure mechanism*. Canadian Geotechnical Journal, 1998. 35: p. 299–311.
9. Brown, I., Hittinger, M., and Goodman, R., *Finite element study of the Nevis Bluff (New Zealand) rock slope failure*. Rock Mechanics, 1980. 12: p. 231–245.
10. Chen, W., *Plasticity in soil mechanics and landslides*. Journal of the Engineering Mechanics Division, 1980. 106(EM3): p. 443–464.
11. Hassan, A. M., and Wolff, T. F., *Effect of deterministic and probabilistic models on slope reliability index*. Geo-Technical engineering, Slope Stability 2000, ASCE special publication. 101: p. 194–208.
12. Jeremic', B., *Finite element methods for three dimensional slope stability analysis*. Geo-Technical engineering, Slope Stability 2000, ASCE special publication. 101: p. 224–238.
13. Potts, D. M., Dounias, G. T., and Vaughan, P. R., *Finite element analysis of progressive failure of Carsington embankment*. Geotechnique, 1990. 40: p. 79–101.
14. Wong, F. S., *Uncertainties in FE modeling of slope stability*. Computers & Structures, 1984. 19: p. 777–791.
15. Fairhurst, C., Damjanac, B., and Hart, R., *Numerical analysis as a practical design tool in Geo-Technical engineering*. Slope Stability 2000, ASCE special publication. 101: p. 169–183.
16. Snitbhan, N., and Chen, W. F., *Finite element analysis of large deformation in slopes*. Numerical Methods in Geomechanics, Ed. Desai, C. S., 1976: p. 744–756.

17. Cundall, P. A., *A computer model for simulating progressive large scale movements in blocky rock systems.* Proceedings Symposium International Society of Rock Mechanics, Nancy, 1971. Vol. 1 Paper No. II-8.
18. Cundall, P. A., and Strack, O. D. L., *A discrete numerical model for granular assemblies.* Geotechnique, 1979. 29(1): p. 47–65.
19. Williams, J. R., *Contact analysis of large numbers of interacting bodies using discrete modal methods for simulating material failure on the microscopic scale.* Engineering Computations, 1988. 5: p. 198–209.
20. Munjiza, A., and Andrews, K. R. F., *NBS contact detection algorithm for bodies of similar size.* International Journal for Numerical Methods in Engineering, 1998. 43: p. 131–149.
21. Cundall, P. A., and Hart, R. D., *Numerical modeling of discontinua.* Comprehensive Rock Engineering, Ed. Hudson, J. A., 1993. 2: p. 231–243.
22. Williams, J. R., Hocking, G., and Mustoe, G. W., *The theoretical basis of the discrete element method.* Proceedings of the NUMETA '85 conference, 1985: p. 897–906.
23. Rothenburg, L., and Bathurst, R. J., *Micromechanical features of granular assemblies with planar elliptical particles.* Geotechnique, 1992. 42(1): p. 79–95.
24. Hocking, G., *The discrete element method for the analysis of fragmentation of discontinua.* Engineering Computations, 1992. 9: p. 145–155.
25. Kishino, Y., *Disc model analysis of granular media.* Mechanics of Granular Materials, Eds. Satake, M., and Jenkins, J. T., Elsevier, Amsterdam, 1998: p. 143–152.
26. Coggan, J. S,. and Pine, R., *Application of distinct element modeling to assess slope stability at Delabole Slate Quarry, Cornwall, England.* Trans. Instn. Min. Metall. (Sect.A: Min. Industry), 1996. 105: p. A22–A30.
27. Choi, S. K., *Application of the distinct element method for rock mechanics problems.* Engineering Computations, 1992. 9: p. 225–233.
28. Hamajima, R. et al. *A numerical procedure for the study of deformation and progressive failure of geomaterials.* In the International Symposium on Deformation and Progressive Failure in Geomechanics. 1997. Nagoya, Japan 4–7 October 1997.
29. Hsu, S. C., and Nelson, P. P., *Analysis of slopes in jointed weak rock masses using distinct element method.* Mechanics of Jointed and Faulted Rock, Ed. Rossmanith, H. P., 1995: p. 589–594.
30. Potyondy, D. O., Cundall, P. A., and Lee, C. A., *Modelling rock using bonded assemblies of circular particles.* Rock Mechanics, Eds. Aubertin, Hassani, and Mitri, 1996: p. 1937–1944.
31. Wang, C., Tannant, D. D., and Lilly, P. A., *Numerical analysis of the stability of heavily jointed rock slopes using PFC2D.* International Journal of Rock Mechanics & Mining Sciences, 2003. 40: p. 415–424.
32. Munjiza, A., Owen, D. R. J., and Bicanic, N., *A combined finite-discrete element method in transient dynamics of fracturing solids.* Engineering Computations, 1995. 12: p. 145–174.

33. Bicanic, N., Munjiza, A., Owen, D. R. J., and Petrinic, *From continua to discontinua—A combined finite element/discrete element modelling in civil engineering*. Developments in Computational Techniques for Structural Engineering, 1995: p. 1–13.
34. Barbosa, R. E., and Ghaboussi, J., *Discrete finite element method*. Engineering Computations, 1992. 9: p. 253–266.
35. Ghaboussi, J., *Fully deformable discrete element analysis using a finite element approach*. Computers and Geotechnics, 1988. 5: p. 175–195.
36. Barbosa, R. E. and Ghaboussi, J., *Discrete finite element method for multiple deformable bodies*. Finite Elements in Analysis and Design, 1990. 7: p. 145–158.
37. Pan, X. D., and Reed, M. B., *A coupled distinct element-finite element method for large deformation analysis of rock masses*. International Journal of Rock Mechanics and Mining Sciences and Geomechanical Abstracts, 1991. 28(1): p. 93–99.
38. Ishibashi, I., Agarwal, T. K., and Wang, Y., *Hybrid finite element/discrete element model for large deformation geotechnical engineering problems*. Computation in Civil Engineering, Proceedings 1st congress held in conjuction with A/E/C Systems, 1994: p. 857–864.
39. Mohammadi, S., Owen, D. R. J., and Peric, D., *A combined finite/discrete element algorithm for delamination analysis of composites*. Finite Elements in Analysis and Design, 1998. 28: p. 321–336.
40. Liao, C. L., and Chang, C. S., *A microstructural finite element model for granular solids*. Engineering Computations, 1992. 9: p. 267–276.
41. Mamaghani, I. H. P., Aydan, O., and Kajikawa, Y., *Analysis of masonry structures under static and dynamic loading by discrete finite element method*. Structural Engineering/Earthquake Engineering. JSCE, 1999. 16(2): p. 75s–86s.
42. Munjiza, A., and Andrews, K. R. F., *Penalty function method for combined finite-discrete element systems comprising large number of separate bodies*. International Journal for Numerical Methods in Engineering, 2000. 49(11): p. 1377–1396.
43. Shi, G., and Goodman, R. E., *Two dimensional discontinuous deformation analysis*. International Journal for Numerical and Analytical Methods in Geomechanics, 1985. 9: p. 541–556.
44. Shi, G. H., and Goodman, R. E., *Two dimensional discontinuous deformation analysis*. International Journal for Numerical and Analytical Methods in Geomechanics, 1985. 9: p. 541–556.
45. Sitar, N., and Maclaughlin, M. M., *Kinematics and discontinuous deformation analysis of landslide movement,* Invited Keynote Lecture. II Panamerican Symposium on Landslides, Rio de Janeiro, Nov. 10–14, 1997.
46. Shi, G., *Modeling rock joints and blocks by manifold method*. Rock Mechanics, Eds. Tillerson and Wawersik, Balkema, Rotterdam, 1992: p. 639–648.
47. Shi, G., *Working forum on manifold method of material analysis*. Miscellaneous paper GL-97-17, U.S. Army Corps of Engineers, Waterways Experiment Station, September 1997.

48. Chen, G., Ohnishi, Y., and Ito, T., *Development of high order manifold method.* International Journal of Numerical Methods in Engineering, 1998. 43: p. 685–712.
49. Tsay, R., Chiou, Y., and Chuang, W., *Crack growth prediction by manifold method.* ASCE Journal of Engineering Mechanics, 1999. 125(8): p. 884–890.
50. Chiou, Y., Lee, Y., and Tsay, R., *Mixed mode fracture propagation by manifold method.* International Journal of Fracture, 2002. 114: p. 327–347.
51. Lin, J.-S., and Ku, C.-Y., *Two-scale modeling of jointed rock masses.* International Journal of Rock Mechanics & Mining Sciences, 2006. 43: p. 426–436.
52. Chen, Z. and Brannon, R., An evaluation of the material point method, SandReport 2002, Sandia National Laboratories, Albuquerque, New Mexico, 2002, pp 46.

3 ANALYSIS FOR CONTINUUM SOLUTIONS

The concept of mechanics developed in the eighteenth century was largely empirical. During the first half of the nineteenth century, continuum mechanics and theories of elasticity developed as a branch of mathematical physics. The mathematical analysis was built on the concept of continuous geometrical space, and the Newtonian theory recognized bodies as being composed of discrete media having individual particles connected by forces of attraction and repulsion. The debate of continuum and discontinuum approaches has its origin in the field of mechanics.

There is a large difference between the mathematical analysis of a continuous material and analysis of a body comprising discrete bodies. This gap has been bridged by statistical applications. The scale effects play an important role in defining the type of behavior to be expected for site-specific conditions. Geomaterials are particulate on a micro-scale but may be regarded as a continuum on a much larger scale. Solutions for a continuum having discontinuum assemblies are presented in this chapter. The continuum approach can be derived from proven techniques of the finite element method and applied to discrete assemblies represented by quadrilateral elements. In a number of situations, the finite element description of a domain may not necessarily represent the most appropriate format; a framework allowing some level of discontinuity (strain or displacement) may be better suited to model particular phenomena, Bicanic [1].

Chapter 3

3.1 INTRODUCTION

In an analysis of any engineering system, one needs to idealize the system into a discretized space, formulate governing equations for this system, define solution techniques for the governing equations, and interpret the attained results. The response of this finitely discretized space can be modeled and described by a finite number of state variables. In the standard finite element analysis of a continuous system, a formulation of the exact equilibrium equations is achieved by defining a set of differential equations that govern the response and then discretizing the domain, Bathe [2]. This approach treats the material as a continuum and the idealization of many engineering systems including geo-mechanical materials is based on this universal assumption. However, the continuum approach for rock and soil may need complex constitutive models to represent the behavior. These complex constitutive models may sometimes contain dozens of parameters and internal variables for defining the yield surfaces of the geological materials, Cundall [3].

On the other hand over the past decade, research based on discrete elements for soils and rocks has shown that the complex behavior exhibited by these geological materials, such as continuous nonlinear stress/strain responses, dilation related to mean stress, transition from brittle to ductile, hysteresis, nonlinear strength envelopes, and many more can be implicitly modeled with the explicit discrete analysis approach. Furthermore, discrete elements naturally incorporate localization and banding in granular materials, qualities difficult to reproduce with a continuum mesh approach.

Techniques such as the finite element method and the finite difference method can be applied to a variety of geotechnical problems with complex boundary conditions such as non-homogeneous inelastic materials which may undergo large deformations. But these applications are severely limited because granular media are discrete in nature (for instance, rock mass displays strong discontinuities near the surface) and their complex behavior makes it difficult to represent them with continuum models. Analysis of systems exhibiting grossly discontinuous material and geometrical behavior can be effectively modeled using discrete element methods.

The work in this thesis is guided by the discrete element method to capture mobility but uses the authenticated steps of the reliable finite element method for the deformations and the related stress-strain states. The geometry for any particular problem is modeled as an assemblage of elements having own eight degrees of freedom. Restraints in the form of similar displacements or velocities are imposed at the nodes sharing the same coordinates to ensure compatibility between the elements for continuum analysis. The proposed method of analysis is described in generic terms and examples for validation of this technique are presented.

3.2 APPROACH OF THE PROPOSED METHOD

Coupled approaches for the analysis of a geotechnical system such as a soil/rock mass requires knowledge of the stresses within particles and simultaneously capture the mobility. In order to model this discontinuum soil/rock system, available methods based on the finite element method and the use of joint elements are limited to small displacements and unaltered topology, Barbosa [4]. Further the use of only discrete element methods with constant strain modes or discontinuous deformation based on decoupling the deformation modes from the rigid body modes, sometimes leads to spurious stresses. The proposed method is based on the solution procedures of the finite element method and analyzes the stress states for any geotechnical system using individual elements.

In this approach, the equation of motion is solved for each element sequentially and constraints on the nodal displacements or velocities are imposed to ensure continuity and inter-element compatibility. Even though for each element separate degrees of freedom are defined, the explicit constraints allow the system solution to be computed as a continuum. No contacts with neighboring elements are allowed and the contact forces between elements are not computed for the continuum solution. These constraints will be retained until the individual elements based on any yield/fracture criteria are allowed to split and move independently to create a discontinuum, whereby picking up contact forces and contact stresses.

The first stage of continuum analysis is described in this chapter and the further stages related to splitting of the elements and discrete finite element analysis are discussed in other chapters.

3.3 METHOD OF ANALYSIS

Similar to finite element analysis, the proposed method of analysis consists of idealizing the domain of the problem into a mesh comprising of quadrilateral elements. These elements possess independent degrees of freedom to start with so any interior node of a conventional finite element mesh is equivalent to four different nodes of four individual elements sharing the same nodal coordinates, Figure 3.1. Hence, rather than having two degrees of freedom at a single node, this method computes for eight degrees of freedom at the same location.

a) There are two different ways to apply the nodal constraints. The first is by computing the displacements at the nodal coordinates for each element and then forcing these displacements as constraints on the neighboring elements sharing the same nodal position. The second way is to apply the constraints in the form of computed velocities at the nodes. Both of these techniques result in a solution suitable for a particular scenario. The displacement constraints scheme was found suitable for solving static problems while the velocity constraint scheme was suitable for solving static and dynamic problems.

A group of four elements sharing the same nodal coordinates for a particular node is shown in Figure 3.1.

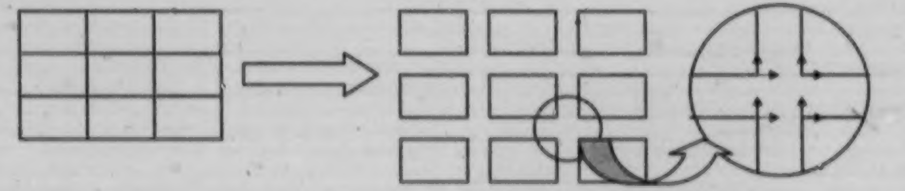

Finite Element Mesh

Mesh comprises of elements with separate degrees of freedom

Figure 3.1: Independent degrees of freedom for each node sharing the same coordinates

In order to apply the nodal constraints, a list of the neighboring elements for each element will be required. In the developed Visual C++ computer program, this list or array of elements was stored in a CONNECT matrix for each element. The CONNECT matrix for any element will include elements starting with the top left element, then other elements sequentially from left to right and then from top to bottom. For the present analysis only quadrilateral iso-parametric elements were considered. As the domain is discretized into iso-parametric quadrilateral elements, each element has a maximum of eight elements in its CONNECT list. If there is no neighboring element connected to a particular element at a node, that array location is given an index value of 0; otherwise the identity number of the neighboring element is stored in the array.

3.3.1 Displacement Constraints—Step by Step Procedure

The computational procedure for this method is a dynamic time stepping incremental scheme. For each time step the following computational steps are followed:

(a) The solution scheme is based on the solution of the equation of motion till the external applied force balances the developed internal resisting force. The applied external force or self weight at any particular nodal coordinate is the sum of the nodal force components from all elements sharing the same coordinate.

(b) The computational scheme progresses like a wave by transferring the displacements and related stress states to the other elements one by one. The computed displacements and internal resisting force vectors for an element during a particular timestep are applied on to the next element.

(c) Starting in the assembly of elements with any element, say top left, the velocities and the corresponding displacements are computed by solving the basic equation of motion for each element individually (the details are described later).

(d) Based on the computed displacements and the corresponding internal stress states, the internal resisting force vectors at the nodes of an element are calculated. This internal nodal resisting force vector will be used for the next time step to find the net external nodal force vector for the next element. During the current timestep, these internal nodal force vectors also contribute as internal force components of the adjoining element nodes.

(e) The computational procedure proceeds to the next element in the specific order chosen. The net external force on the element is computed incorporating the internal force vectors from neighboring element as described in (d) and the equation of motion is solved to compute the displacements.

The term "specific order" refers to the sense in which the analysis is planned to be carried forward from one element to another and the order in which the element's equation of motion is to be sequentially solved.

(f) The equation of motion is solved for all the elements for a particular time step.

(g) After the calculations are completed for a time step for all the elements, the initial parameters for next time step—the nodal coordinates, the internal and external forces, displacements, and velocities—are updated at all nodes.

This method proposed here differs from the finite element method and the method proposed by Ghaboussi [5] in that the global matrices for the elements are not assembled. Instead, the equation of motion is solved for each element in a chosen sequence and induced disturbances are updated in subordinate elements. So, for each time step the formulation can be considered to be divided into a number of additional steps, or sub-step for each element. A sub-step for the one element propagates the effects to the sub-step of the next element.

Retaining the progression of the scheme for an element in sub-steps ensures compatibility and continuity of the stresses and strains between different elements. As is shown in Figure 3.2(a), under the application of an external load, element 1 deforms, i.e., displacements δ occur at the nodes and result in strains, stresses, and internal resisting force vectors within element 1. These displacement disturbances of element 1 are carried forward into the next element(s) as history of this time substep.

During the substeps of a time step the deformations can be viewed as shown in Figure 3.2.

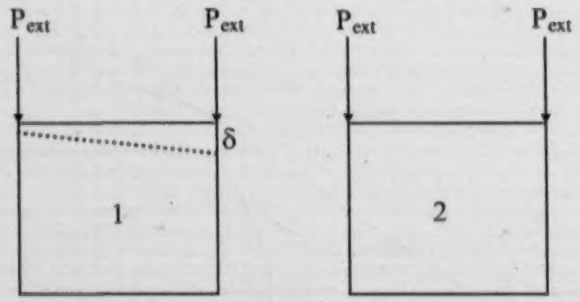

Figure 3.2(a): Under the application of external loads element 1 deforms

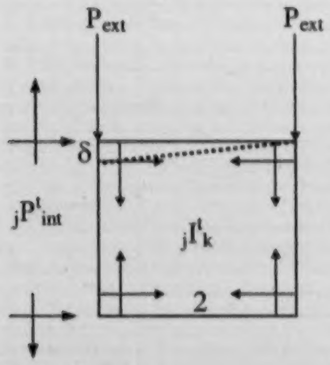

Figure 3.2(b): History from the substep of element 1 carried onto element 2.

To begin with the displacements are computed for element 1 by solving the equation of motion, Figure 3.2(a). The displacements of element 1 are applied as such on the nodes of element 2 that shares the same coordinates. The internal resisting forces developed due to these imposed displacements δ on the nodes of element 2, from all the neighboring elements solved earlier say element 1, are computed and are referred to as $_j\mathbf{I}^{t+\Delta t}_k$ where *k* refers to all the neighboring elements and index *j* is the element for which solutions are being computed for the current timestep, *t+Δt*. This force is used to calculate the net nodal force vectors in the solution of equation of motion for this element. The internal resisting forces of element 1 computed up to timestep *t* also contribute to the internal stress state of element 2 and are thus applied as internal forces on the nodes of adjoining element 2, and are referred to as **${}_jP^t_{int}$** as in Figure 3.2(b). This force vector is the result of disturbance in equilibrium of any element and is responsible for causing displacements on the internal nodes, and propagation of the loads from the external nodes to the internal nodes. The final equilibrium equation for the net unbalanced force is:

$$P_{ext} + {}_jP^t_{int} + \sum {}_jP^{t+\Delta t}_{int} - \sum {}_jI^t_j - {}_jI^{t+\Delta t}_k = 0 \tag{3.1}$$

Terms in the equation of motion are defined below:

P_{ext} - external force vector applied on the nodes including self-weight,

${}_jP^t_{int}$ - internal force vector acting on the shared nodes due to the displacements of the neighboring element, up to time step *t*,

where

$${}_jP^t_{int} = \sum_{k=1}^{n} (-\ {}_jI^t_k) \tag{3.2}$$

Subscript *j* represents the concerned element, *k* sums up over all the neighboring element that is causing this internal nodal force, and *n* is the total number of adjoining elements. This internal force is summed for all the previous time steps on this element.

${}_jI^t_j$ = internal resisting force vector developed within the element up to the present time step *t*,

${}_jI^{t+\Delta t}_k$ = incremental internal resisting force vector developed due to the nodal displacements of all the adjoining elements *k* applied on element *j* during the current time step.

After one complete cycle in a time step, all the coordinates are updated along with internal and external forces, including forces from all neighboring elements. The above cycle then continues and the equation of motion, Equation 3.1, is solved until the required solution is obtained or the required amount of convergence/precision is achieved or up to the point of interest.

3.3.2 Velocity Constraint Formulation

A simpler progression is followed for the formulation based on the velocity constraints, as explained below:

a) During the first time step, the velocities of all the elements are computed using the current net nodal force components.

b) The velocities calculated at various nodes of the elements are averaged such that the node at a particular location has a velocity similar to other nodes at that location. The velocity components to be averaged include the velocities of all the shared nodes in the list of neighboring elements, i.e., from the CONNECT array.

c) The nodal displacements are computed from these averaged velocities. The strains, stresses, and internal resisting force vectors are then computed based on these displacements.

d) The net nodal force components are updated, including the internal resisting force vectors from the element of concern and all the neighboring elements in the CONNECT list. The internal force vectors from the neighboring elements are applied in an opposite sense on to the element of concern and are treated as external forces. These are symbolized as ${}_{j}\mathbf{P}^{t}_{int}$ and are a summation of all the neighboring nodal forces.

e) The cycle is continued over the next time steps.

f) The net unbalanced force for equilibrium of any element in this formulation will be:

$$P_{ext} + {}_{j}P_{\text{int}}^{t} - \sum {}_{j} I_{j}^{t} = 0 \qquad 3.3$$

The terms of equation 3.3 have been explained above and k is the index representing neighboring elements summed over the total elements, n.

3.3.3 Computational Scheme

The computational scheme proceeds by tracking the motion of individual nodes and elements and by looping over the steps of the formulation. The steps of formulation include solving the equation of motion and calculating the velocity, displacement, strain, stresses, and internal nodal force vectors. Subsequent calculations for each step involve updating the various parameters. The incremental velocity and displacements are obtained by integration of the equation of motion. For the solution of the equation of motion, a second order central difference integration scheme is applied as explained later. The equation of motion to be solved is:

$$M\ddot{U} + C\dot{U} + KU = P \qquad 3.4$$

which includes inertial force, damping force, and elastic force components on the left hand side, and applied force components including self-weight on the right hand side.

The term **KU** defines the amount of internal stress developed due to displacements and corresponding strains. This term, when taken on the right side of the equation of motion, results in a net unbalanced force on the element and causes further motion of the element assemblage. Eventually the equation takes the form in equation 3.6 from equation 3.5.

$$M\ddot{U} + C\dot{U} = P - KU \qquad 3.5$$

$$M\ddot{U} + C\dot{U} = P - I \qquad 3.6$$

Using the second order central difference scheme for the integration of equation 3.6 the acceleration component is given as:

$${}^{t}\ddot{U} = \frac{1}{\Delta t^2}\left[{}^{t-\Delta t}U - 2\,{}^{t}U + {}^{t+\Delta t}U\right] \qquad 3.7$$

The error involved in expansion of the acceleration term in equation 3.7 is of the order of $(\Delta t)^2$. With the same order of error, the velocity component can be defined as:

$${}^{t}\dot{U} = \frac{1}{2\Delta t}\left({}^{t-\Delta t}U + {}^{t+\Delta t}U\right). \qquad 3.8$$

By substituting these values in equation 3.6, a general formula for **U** can be defined:

$$\left(\frac{M}{\Delta t^2} + \frac{C}{2\Delta t}\right){}^{t+\Delta t}U = {}^{t}P - \left(K - \frac{2M}{\Delta t^2}\right){}^{t}U - {}^{t-\Delta t}U\left(\frac{M}{\Delta t^2} - \frac{C}{2\Delta t}\right). \qquad 3.9$$

The substitution of the values for acceleration velocity (into equation 3.6) leads to a formulation of the integration scheme for the displacement of the next time step. The damping coefficient C can be related to the nodal lumped mass matrix as αM, where α is the viscous damping proportionality factor and is based on the critical damping values chosen. Damping factors should be selected so that the assembly is neither over damped nor under damped.

However, if the displacements are calculated from the velocity components first evaluated, then for the second order central difference scheme the acceleration is defined in terms of the velocity as:

$$\ddot{U}^{t} = \frac{\dot{U}^{t+\frac{\Delta t}{2}} - \dot{U}^{t-\frac{\Delta t}{2}}}{\Delta t} \qquad 3.10$$

The central difference velocity component is:

$$\dot{U}^{t} = \frac{\dot{U}^{t+\frac{\Delta t}{2}} + \dot{U}^{t-\frac{\Delta t}{2}}}{2} \qquad 3.11$$

Putting these values in equation 3.6, the equation in incremental form for the next time step becomes:

$$\dot{U}^{t+\frac{\Delta t}{2}} = \left(\frac{2-\alpha\,\Delta t}{2+\alpha\,\Delta t}\right)\dot{U}^{t-\frac{\Delta t}{2}} + \left(\frac{2\Delta t}{2+\alpha\,\Delta t}\right)M^{-1}\left({}^{t}R\right) \qquad 3.12$$

The values of displacement in the next time step are given by:

$$\Delta U = \Delta t \cdot \dot{U}^{t+\frac{\Delta t}{2}} \qquad 3.13$$

A better convergence is achieved if the velocity components at the midpoint of two successive time steps are used to calculate the displacement during a time step. Note that **ᵗR** in equation 3.12 is the unbalanced force we are minimizing over number of timesteps, modified from either equation 3.1 or equation 3.3:

$$P_{ext} + {}_{j}P_{\text{int}}^{t} + \sum {}_{j}P_{\text{int}}^{t+\Delta t} - \sum {}_{j}I_{j}^{t} - {}_{j}I_{k}^{t+\Delta t} = {}^{t}R \qquad 3.14$$

The incremental element strains are calculated from the incremental displacements shown above by using the element strain displacement matrix **B**.

$$\Delta\varepsilon = B \cdot \Delta U \qquad 3.15$$

The incremental element strains are combined with the matrix of constitutive relations **D** to compute the incremental element stresses.

$$\Delta\sigma = D \cdot \Delta\varepsilon \qquad 3.16$$

The element strain displacement matrix is evaluated at each Gauss point by using Gauss's integration scheme and correspondingly the stresses and the strains are found at these Gauss points. The internal resisting force vector ***I*** is computed based on the virtual work principle and is evaluated using Gaussian integration as indicated in equation 3.17.

$$_jI_j = \sum \int_V B^T \, \sigma \, dV \qquad 3.17$$

where **B** is the element strain displacement matrix, **σ** is the Cauchy element stress tensor (defined in vector form) and **V** is the element volume at any configuration. As this is based on the principle of virtual work, a consistent relation between the nodal loads and element stresses can be obtained. In this type of formulation, involving an incremental step by step solution, it is assumed that the solution at the next time step corresponding to $t + \Delta t$, where Δt is an appropriately selected small time step increment, is required and the solution corresponding to time t is known.

This formulation is represented by the flow charts shown in Figure 3.3(a) for velocity constraints and in Figure 3.3(b) for displacement constraints.

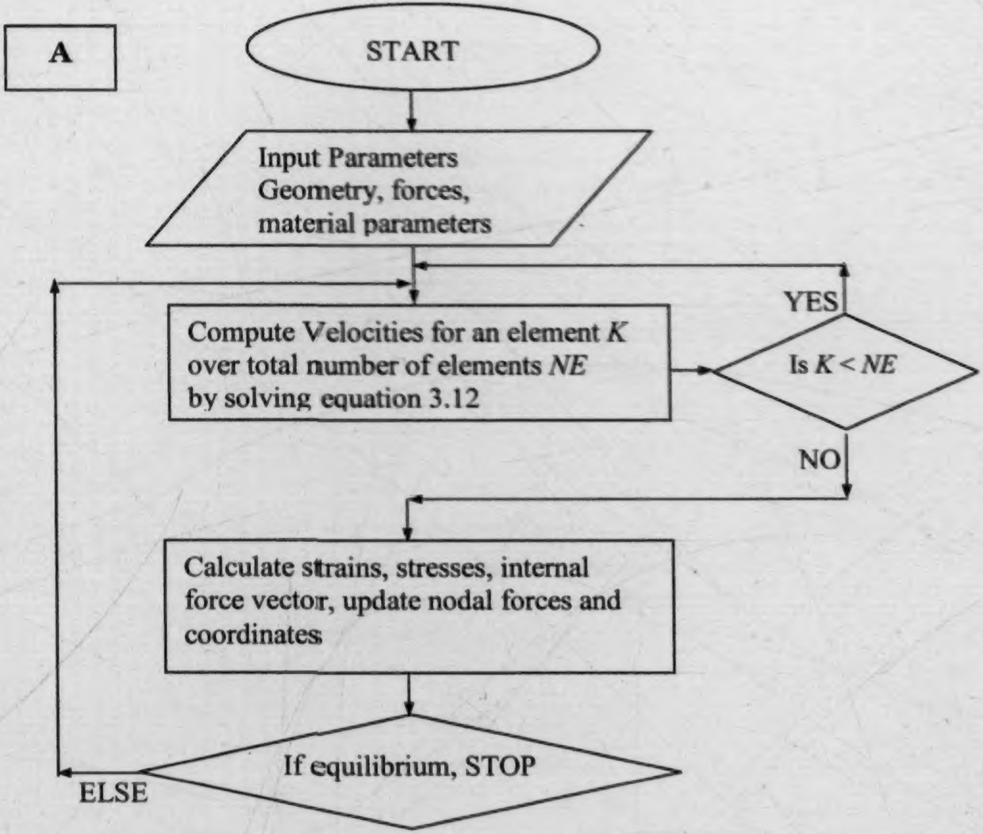
A
START
Input Parameters
Geometry, forces,
material parameters
YES
Compute Velocities for an element K
over total number of elements NE
by solving equation 3.12
Is K < NE
NO
Calculate strains, stresses, internal
force vector, update nodal forces and
coordinates
If equilibrium, STOP
ELSE

Figure 3.3(a): Flow chart for finite element solutions using velocity constraints

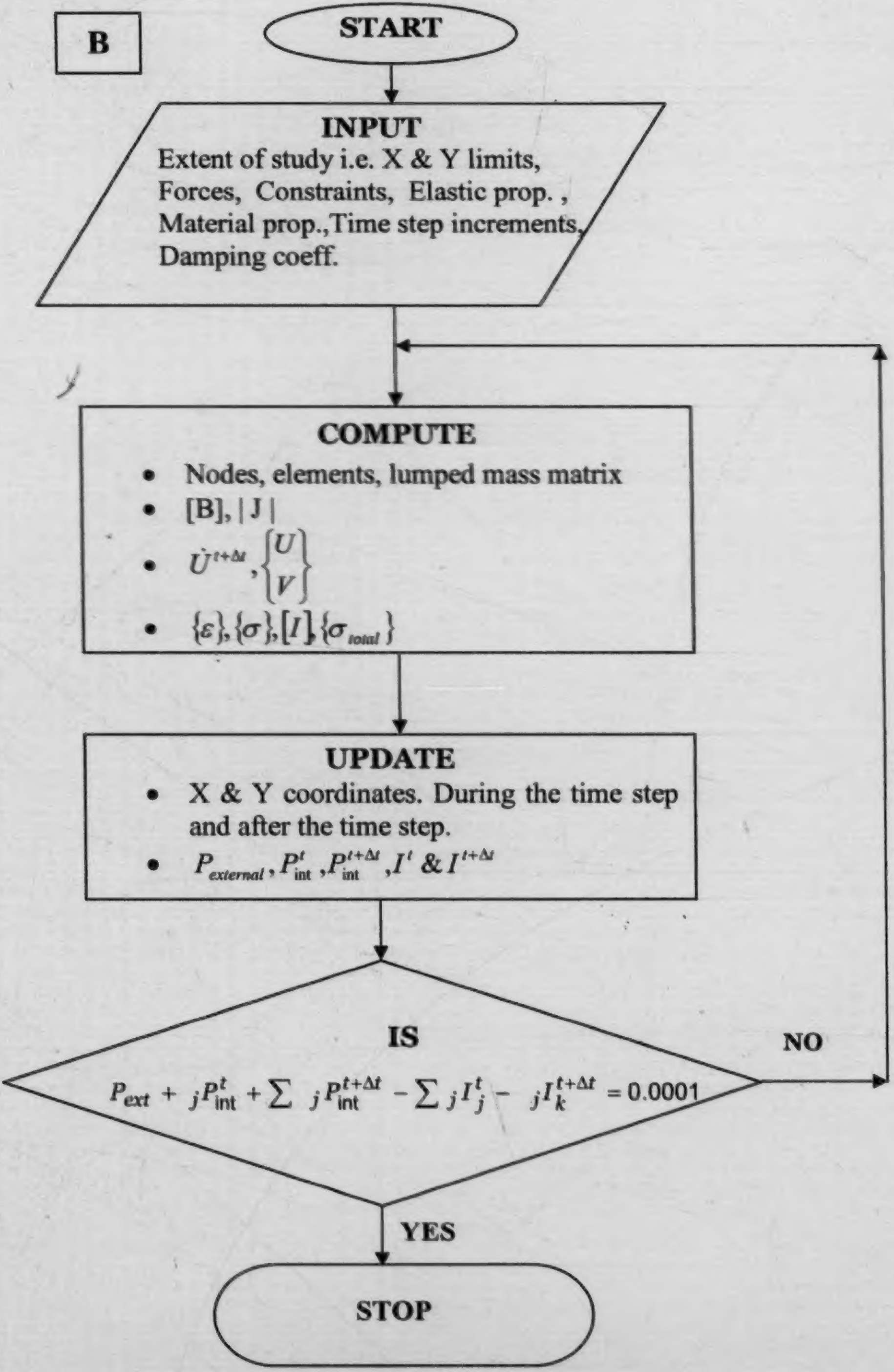
B
START
INPUT
Extent of study i.e. X & Y limits, Forces, Constraints, Elastic prop. , Material prop.,Time step increments, Damping coeff.
COMPUTE
Nodes, elements, lumped mass matrix
[B], | J |
$\dot{U}^{t+\Delta t}, \begin{Bmatrix} U \\ V \end{Bmatrix}$
$\{\varepsilon\}, \{\sigma\}, [I], \{\sigma_{total}\}$
UPDATE
X & Y coordinates. During the time step and after the time step.
$P_{external}, P^t_{int}, P^{t+\Delta t}_{int}, I^t \ \& \ I^{t+\Delta t}$
IS
$P_{ext} + {}_jP^t_{int} + \sum {}_jP^{t+\Delta t}_{int} - \sum {}_jI^t_j - {}_jI^{t+\Delta t}_k = 0.0001$
NO
YES
STOP

Figure 3.3(b): Flow chart for finite element solutions using displacement constraints

3.4 VALIDATION EXAMPLES

The development of the proposed method started with the example given in section 3.4.1, so it is presented here as the basic validation example. The examples described in sections 3.4.1 and 3.4.2 validates the displacement constraint formulation while the examples in sections 3.4.3 and 3.4.4 validates the velocity constraint formulation. Each of the examples involves different checks on the procedure.

3.4.1 Development of a Uniform Stress Field in a Body under UDL

This example demonstrates the validity of the proposed scheme for finite element analysis of discrete elements through an explicit solution scheme for individual elements, hence verifying the continuum response. A case of uniform stress distribution is considered for the validation in which uniformly distributed load is applied on the ground surface.

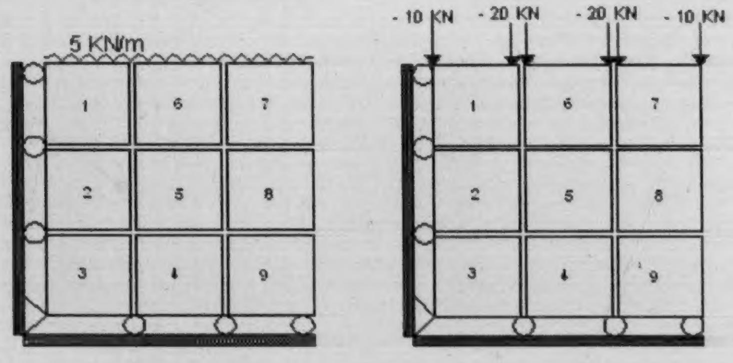

(a) (b)

Figure 3.4: Two-dimensional section of the ground and its discretization

The self-weight of the elements is not considered and no switch–on-gravity condition is assumed. It is assumed that the displacements are infinitesimally small and the material is linearly elastic. The boundary conditions are assumed to be unchanged during application of the load. A two dimensional section of ground is considered, 12 m by 12 m in X and Y directions as shown in Figure 3.4(a). The uniformly distributed force is converted to equivalent nodal forces as shown in Figure 3.4(b).

The standard formulation for the elements is used and a two by two-numerical integration scheme is applied. A uniformly distributed load of about 5 KN/m is assumed to be acting on the ground surface.

INPUT PARAMETERS	VALUES
Element size	4 m × 4 m
Young's modulus	35,000 kN/sq. m
Poisson's ratio	0.3
Density of soil	1650 kg/cu. M
Damping coefficient, α	3.8 per second
Time steps, Δt	0.003 seconds
Number of time steps	4500

Table 3.1: Input parameters

To have a uniform stress distribution within the elements, the essential boundary conditions need to be satisfied. The parameters shown in Table 3.1 are used in the analysis.

The results of this analysis are shown in Figure 3.5, for the stresses at Gauss point 1 corresponding to (-0.577, -0.577) local coordinates, for elements 1, 5, and 9. The plots represent vertical stresses, horizontal stresses, and shearing stresses against time.

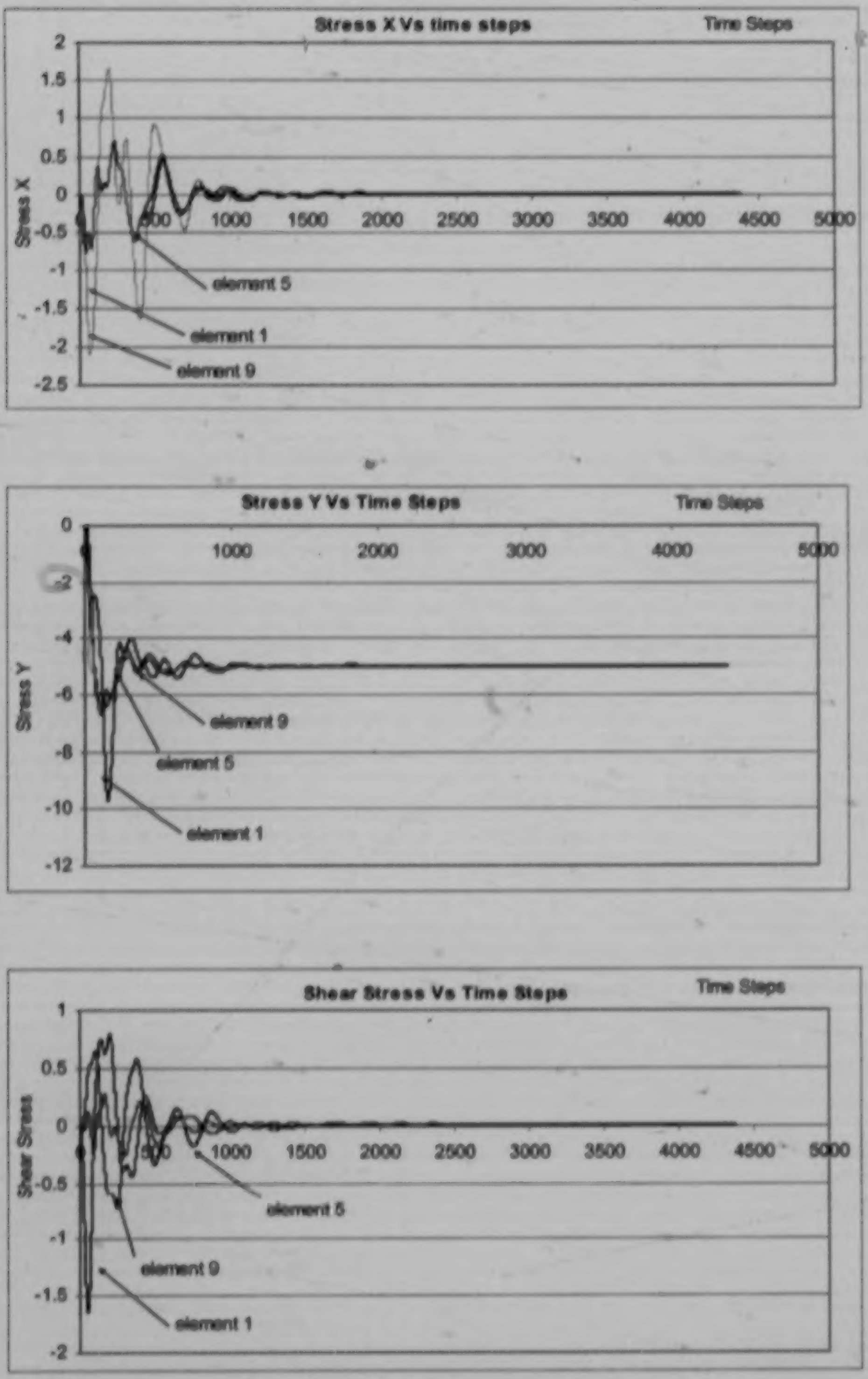

Figure 3.5: Horizontal, vertical, and shear stress convergence

The downward displacement of the nodes induces compressive incremental strain, leading to a compressive stress and an internal resisting force vector. When the wave reaches the bottom, it rebounds and the lower nodes start moving up.

The cycle continues until the external nodal force vector is balanced with the internal resisting force vector and equilibrium or the required convergence is achieved. It can be inferred from the plots in Figure 3.5 that the required vertical stress approaches a constant uniform stress state of 5 kPa (Figure 3.5(b)), and stress in the horizontal direction along with the shear stress achieves a zero value (Figure 3.5 (a, c)).

In this quasi-dynamic process requiring a static solution, the transition of a node to its final equilibrium position from the start point is through a more tortuous path, as shown for node 16 in Figure 3.6.

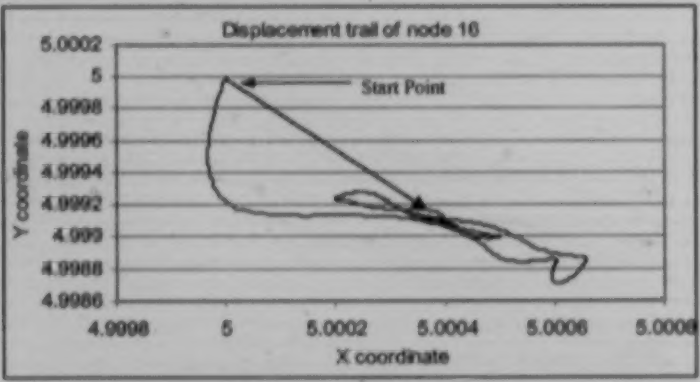

Figure 3.6: Displacement history of node 16

Oscillations continue as in Figure 3.5 and 3.6 until equilibrium is reached, when displacements and oscillations die out completely.

3.4.2 Principal Stresses under a Foundation

The second example is a simulation of the propagation of a stress wave in soil as it is subjected to loading of a superstructure. A finite section of the soil, 20 m deep and 20 m wide from the center of the footing, is analyzed. Only half the footing is considered so the analysis can be symmetric about the central axis of the footing. The size of the footing is 12 m and half of this width is considered for analysis. A uniformly distributed load of 100 kPa is applied to the top of the footing. The soil has a Young's modulus E = 10,000 kN/m^2 and a Poisson's ratio ν = 0.4.

The mesh used in this linear elastic analysis is uniform and comprise of 4 noded quadrilateral elements, shown in Figure 3.7 with mesh origin at (1,1). It should be noted that the soil is discretized into quadrilateral finite elements. The foundation is represented by an appropriate boundary condition.

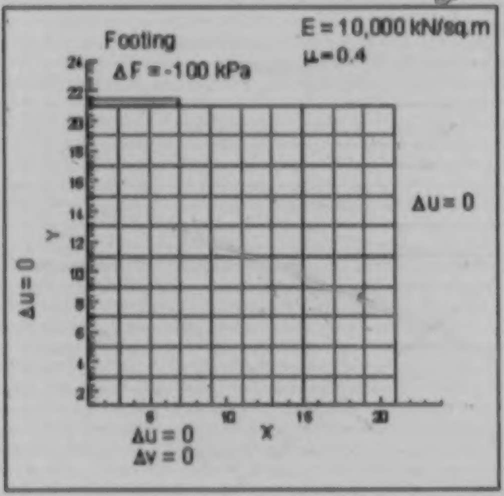

Figure 3.7: Discrete element mesh for a smooth flexible footing

In this analysis, suitable natural and essential boundary conditions specific to the example requirements are applied. The boundary condition on the nodes just below the footing depends on whether the footing is assumed to be rigid or flexible and smooth or rough. For smooth rigid or rough rigid footings a certain amount of displacement is normally specified, whereas for smooth flexible footing, force in the required direction is applied. In this analysis, the footing is assumed to be smooth and flexible, hence nodal forces proportional to the footing pressure of 100 kPa are applied.

The elastic analysis carried out for the footing predicts a vertical settlement of about 0.101 m below the footing edge. The surface settlement profile predicted is shown in Figure 3.8 and has been normalized to the maximum settlement. Irregular settlement profile with a sharp drop can be observed under the footing due to the use of a coarser mesh for analysis. The mesh can be further refined to obtain a smooth settlement profile.

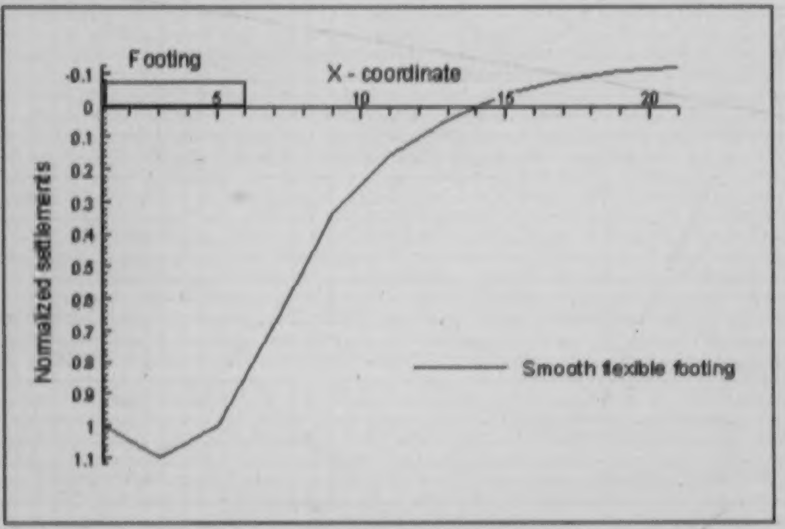

Figure 3.8: Ground surface settlement profile

An advantage of this scheme is that as the computations progress over time steps, the propagation and development of the stresses under the imposed loading can be captured and viewed in real time.

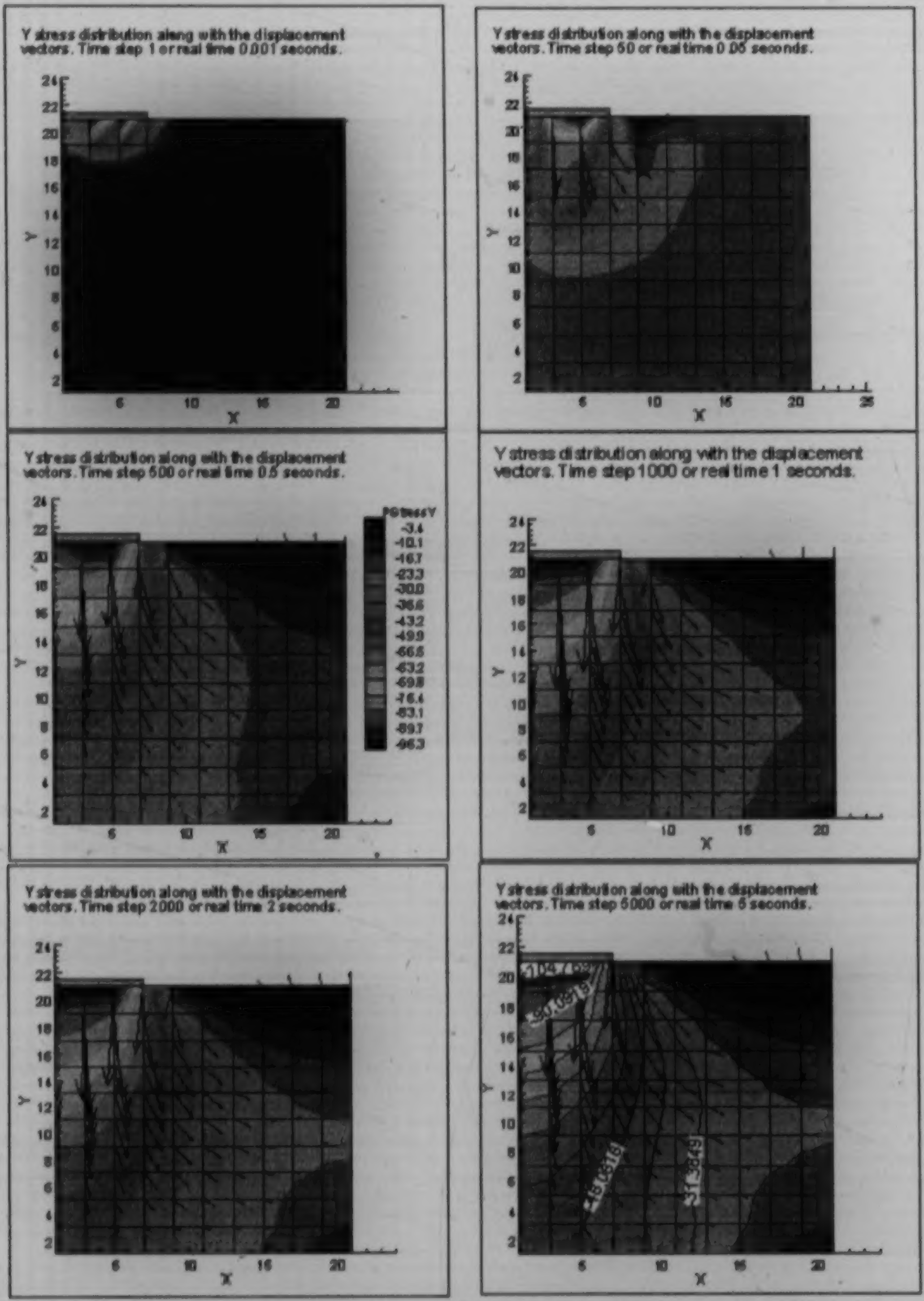

Fig. 3.9: Developed stresses and displacement vectors

In Figure 3.9, the displacement vectors and the vertical stress contours are shown at different time steps. The vectors indicate the transfer of displacement from the exterior disturbed nodes to the interior nodes. The stress contours fairly well represent the development of the pressure bulb under the imposed loading of the footing. The plots are shown at time steps of 1, 50, 500, 1000, 2000, and 5000, depicting the states at 0.001, 0.05, 0.5, 1, 2, and 5 seconds of real time. The progress of the stress wave can be seen at different time steps in Figure 3.9 and in movie format in the attached CD; Chapter 3/Example 2 Foundation Stress Distribution.

3.4.3 Free Fall of a Group of 16 Elements

As mentioned earlier in this chapter, the displacement-constrained formulation is unable to solve for the mobility of multiple elements. The velocity-constrained condition is verified with this example in which a group of sixteen elements is allowed to fall freely under gravity. These sixteen discrete elements are arranged in a 4 × 4 array to form a regular finite element grid, as shown in Figure 3.10.

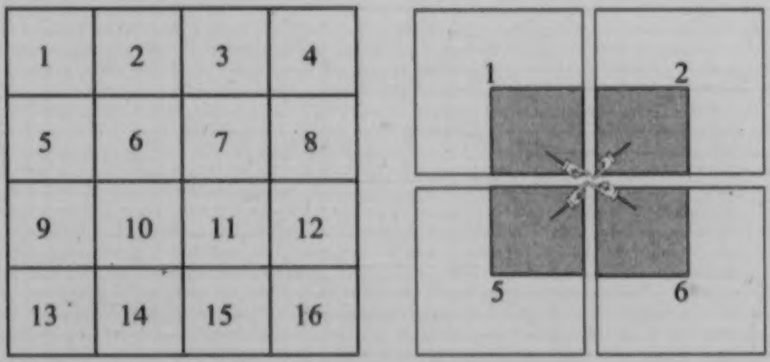

Figure 3.10: Regular grid of elements in freefall, and self-weight contributions to the nodal force

The parameters assumed for this simulation are as follows: modulus of elasticity, 65,000 kN/m²; Poisson's ratio, 0.3; density of material, 16.5 kN/m³; time step, 0.0001 seconds; and damping coefficients, 0 and 3.

The velocity profiles for velocities over time steps for elements 1, 6, 11, and 16 for bottom left hand node 1 in the X and Y directions are shown in Figure 3.11 and 3.12 respectively. As the group of elements is allowed to fall freely under gravity, the velocity in the horizontal direction at the nodes is at the zero mark.

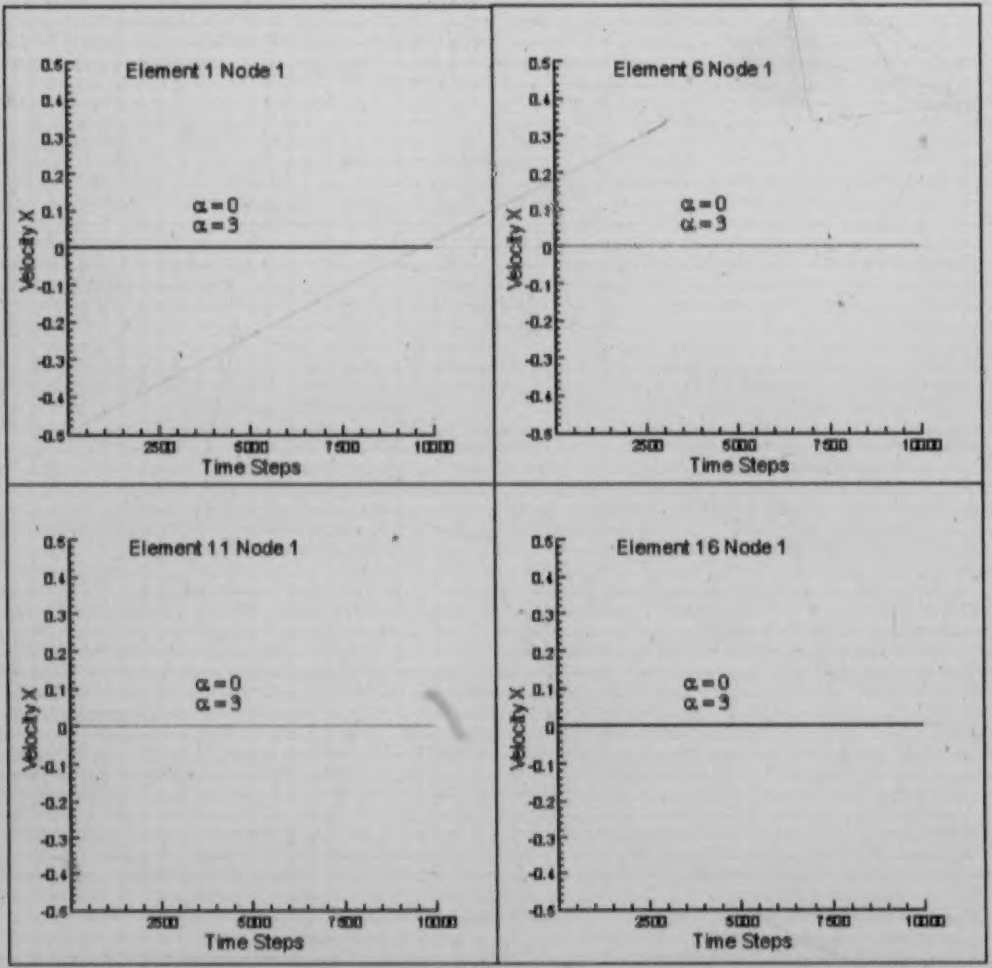

Figure 3.11: Velocity X distribution over time steps for elements 1, 6, 11, and 16 (node 1)

If no damping is applied, then due to the action of gravity g, the vertical velocity keeps on increasing with time. For a damping coefficient of 3 the vertical velocity equalizes to a constant velocity. The slope of the velocity profile with time steps for the elements at the nodes is 9.809 m/s² with no damping, which is similar in value to the g value. The velocity profile plots for the other elements and nodes were similar in distribution and therefore have not been plotted. The formulation developed using velocity constraints results in similar movement of the elements in a group; this cannot be attained using displacement constraints.

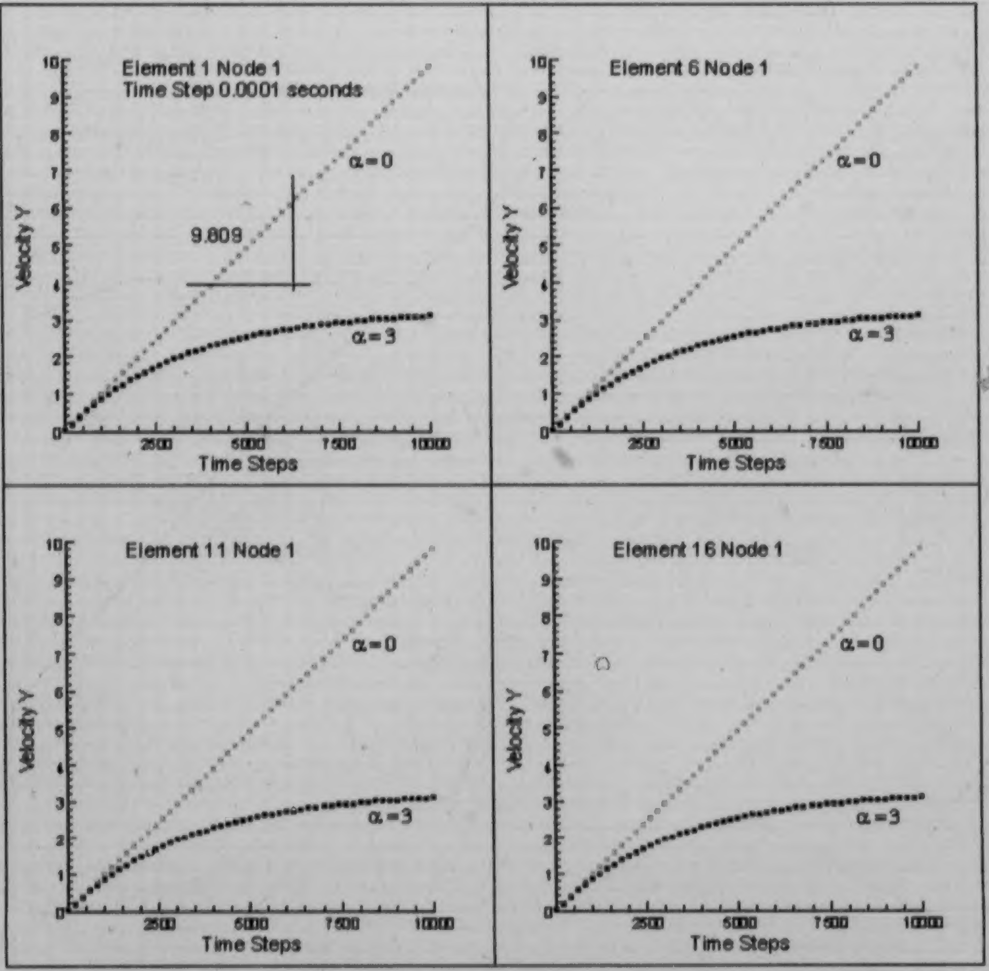

Figure 3.12: Vertical velocity distribution over time steps

The net nodal forces acting on the nodes for elements 1, 6, 11, and 16 are plotted in Figure 3.13. The net total nodal Y forces on all the elements remain constant over time as under the action of gravity; no stresses develop within the elements. Since no horizontal force is applied, the net total horizontal nodal force is zero.

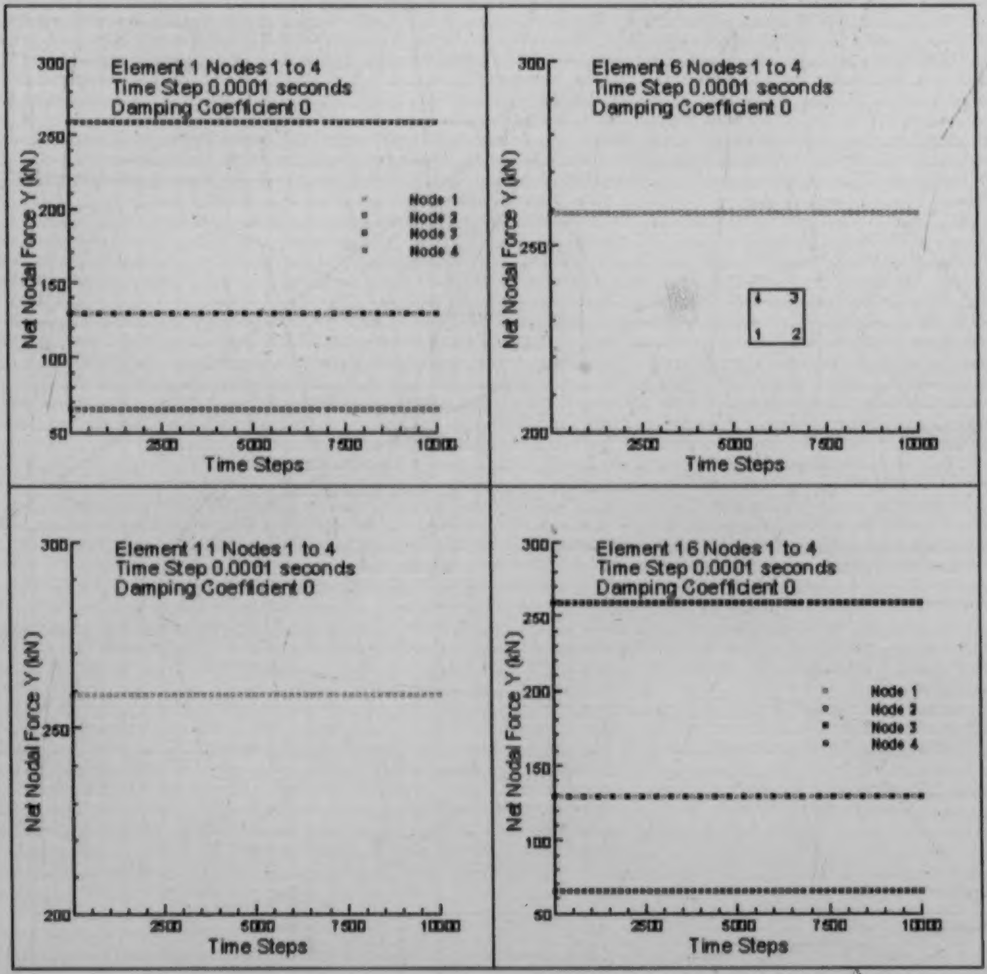

Figure 3.13: Net nodal Y force distribution over time steps for zero damping

Following the sequence of node numbering adopted and as shown in Figure 3.13, the net nodal vertical force on nodes 1 and 3 of element 1 shows contributions from 2 nodes sharing the same coordinates. While for node 2 the contributions are from four nodes and for node 4 the contribution is from one node. Similarly, all the nodes of interior elements 6 and 11 have the same nodal force components at the nodes. For element 16 the pattern of the nodal force distribution is similar to that of element 1.

3.4.4 Stress Distribution for a Slope

This example shows the condition of switch-on-gravity and verification of the developed stresses states within a slope. The formulation developed using the velocity constraints was used to calculate the stress states to validate the procedures for the stress analysis. A 10 m high, 30 degree slope was discretized using 400 iso-parametric quadrilateral elements. The contributions of the self-weight of the elements on the nodes was computed and applied.

A time step of 0.001 seconds was used in the analysis with a damping coefficient of 3 and the solution equilibrates to the static solution within about 5000 time steps. The stress distribution obtained under the slope due to the gravity or self-weight is presented in Figure 3.14 after 0.009 seconds of simulation and is shown in Figure 3.15 after 5 seconds of simulation. The total run time for this simulation was approximately 5 minutes on a Pentium II processor with a RAM of 128 MB.

3.5 PARAMETRIC STUDY FOR NUMERICAL STABILITY

In order to study the effects of the variables involved in the formulations, each variable was varied sequentially and the effects were noted on the scheme applied to example 3.4.1; variable parameters were: time steps, damping coefficients (global), and the choice of using a lumped mass matrix or a consistent mass matrix.

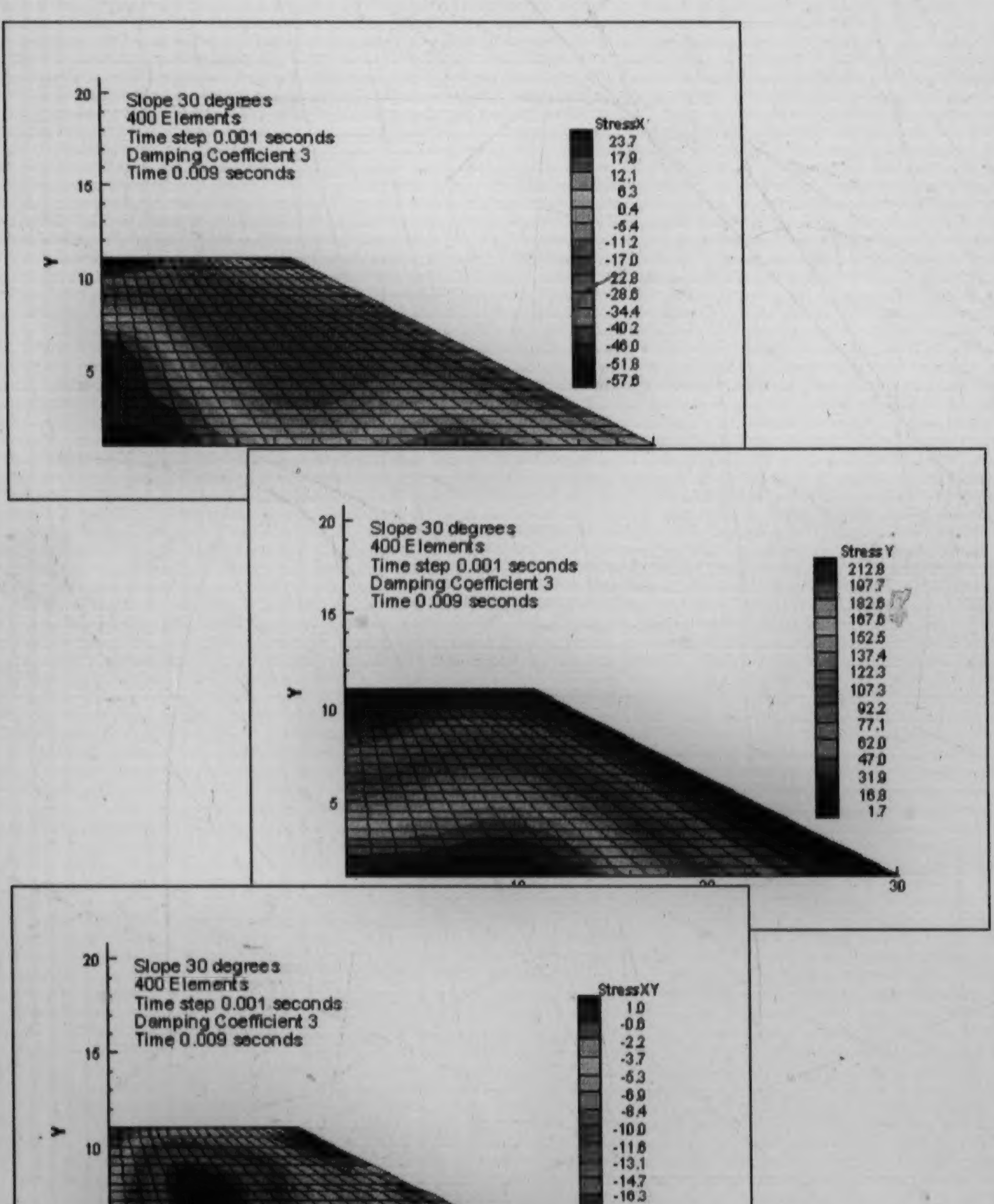

Figure 3.14: Stress distribution within a slope at 0.009 seconds

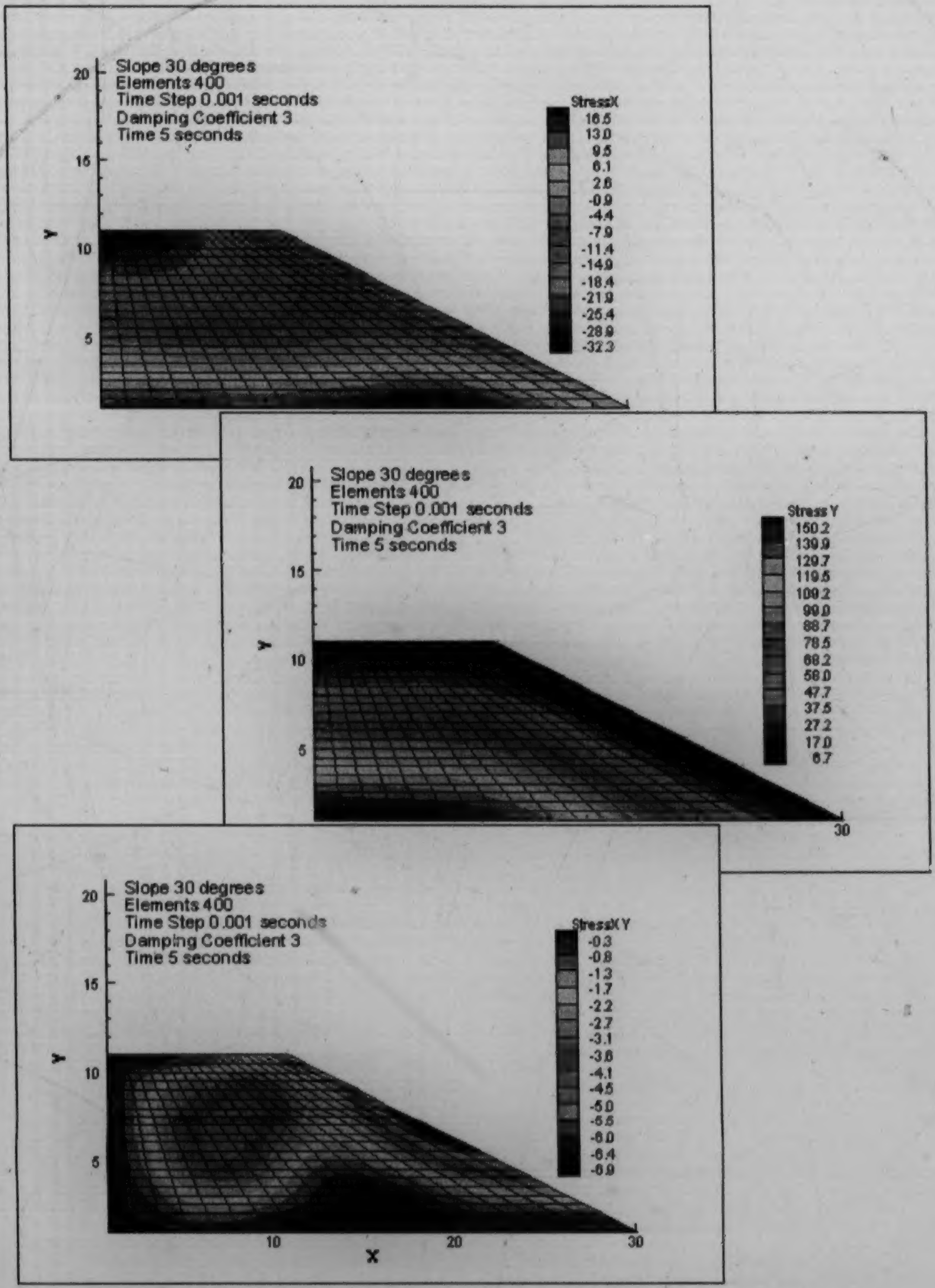

Figure 3.15: Stress distribution within a slope after 5 seconds

3.5.1 Time Steps

Time steps play an important role in this formulation, as the scheme is based on a second order central difference approach, the algorithm is conditionally stable, Bathe [2]. If larger than critical time steps are applied, errors induced by the numerical integration in each time step accumulate, leading to an incorrect solution. The selection of time step depends on the critical time step which is based on the single degree of freedom system of mass connected to the ground by a spring of stiffness k, for which the critical time step is $2\sqrt{m/k}$. The time step selected for the analysis can be assumed a fraction less than the time step calculated from the formula for the critical time step.

Regardless of the above, time step variations were studied from 0.02 to 0.0003 seconds in example 3.4.1. The scheme was stable for time steps up to 0.01 seconds and smaller, but becomes unstable for time steps larger than 0.01 seconds. Figure 3.16(a) shows the convergence of stress in the Y direction in element 5 for a time step of 0.01 seconds, and the required result is obtained in only 400 time steps. For this case a global damping coefficient of 3.8 was used; all other parameters were the same as listed in Table 3.1.

Figure 3.16(b) shows the incremental scheme for a larger time step of 0.02 seconds for a global damping coefficient of 3.8, but for this the solution blows up. However, the scheme seems stable for a time step of 0.01 seconds; thus a smaller time step of 0.003 was used in the analysis to ensure stability; in this case more time steps were needed to converge to the required solution similar to what is observed in the conventional finite element analysis.

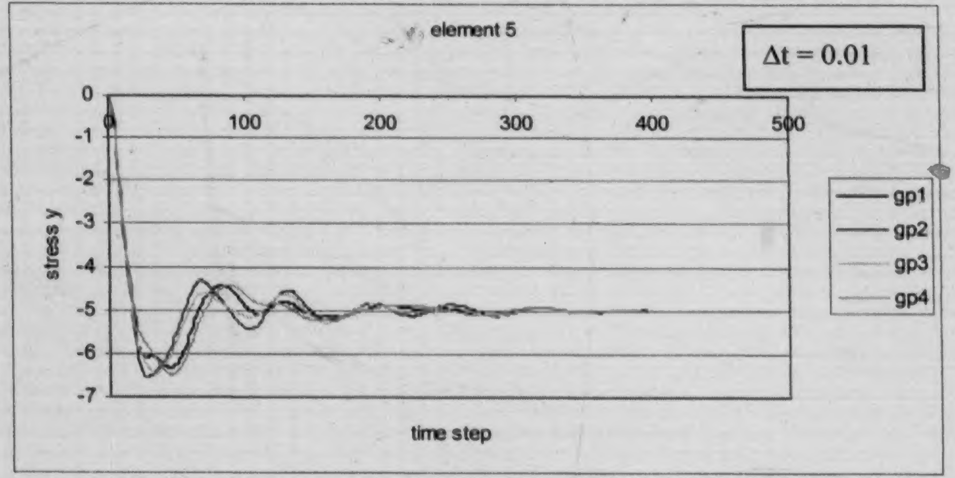

(a)

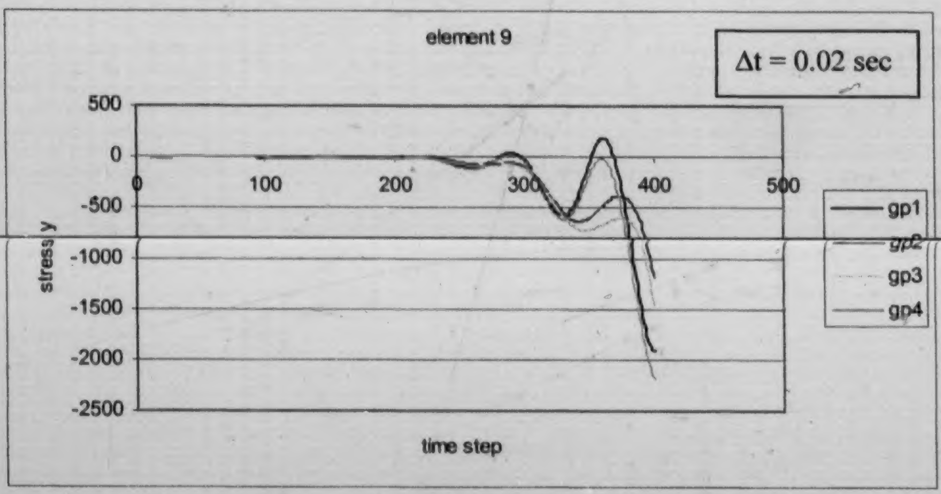

(b)

Figure 3.16: Convergence of Y-stress at time steps (a) Δt = 0.01, (b) Δt = 0.02 seconds

The time steps were chosen on the basis of the velocity of wave propagation through a material medium having modulus of elasticity E and medium density ρ. The velocity is given by:

$$v = \sqrt{\frac{E}{\rho}}\,. \qquad 3.18$$

For the selected parameters the velocity of wave propagation is 460 m/s. Thus it will take about 0.026 seconds for the effects to be transferred to the base of the section. Smaller time steps would be less likely to shock the system.

3.5.2 Global Damping Effects

Damping coefficients were varied from 0.01 to 20 per second to note their effects on the analysis scheme. Values close to 10 or more of damping coefficient α gave the system critical damping; lower values imparted more oscillations to the system and the assembly converged to the required solution more slowly.

Based on the equations of damped harmonic motion the condition for critical damping for a single degree of freedom system is:

$$c \le 2\sqrt{km} \qquad 3.19$$

At $c = 2\sqrt{km}$ the angular frequency of the system is zero.

With critical damping the displacement approaches zero exponentially with no oscillations. The value of C is equal to αM; based on this concept the required value of the damping proportionality coefficient can be decided. A damping coefficient of 20 sec^{-1} resulted in an over-damped system with stresses converging asymptotically to the required solution, as shown in Figure 3.17. The time step selected here is 0.003 seconds with all the other parameters as defined in Table 3.1 for example 3.4.1.

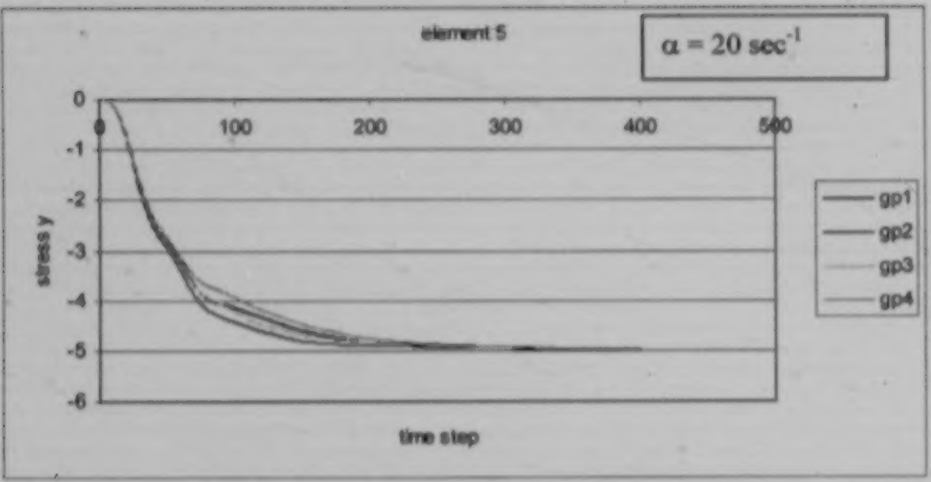

Figure 3.17: Stress convergence with heavy damping, $\alpha = 20\ \text{sec}^{-1}$

A damping coefficient much lower than the critical damping value induces oscillations into the system and can destabilize the entire system as shown in Figure 3.18. This can result from the accumulation of errors and non-convergence over the timesteps.

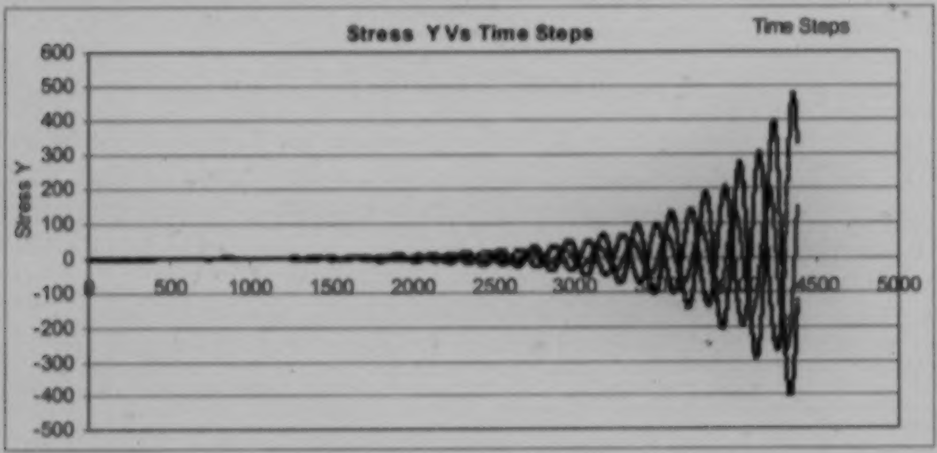

Figure 3.18: Nonconvergence under a small damping coefficient of $\alpha = 0.01\ \text{sec}^{-1}$

3.5.3 Comparison of Mass Matrices

The solutions shown above were obtained using lumped mass matrices to integrate the equation of motion. If instead a consistent mass matrix is used, the solution converges to slightly different values of stresses at the Gauss points.

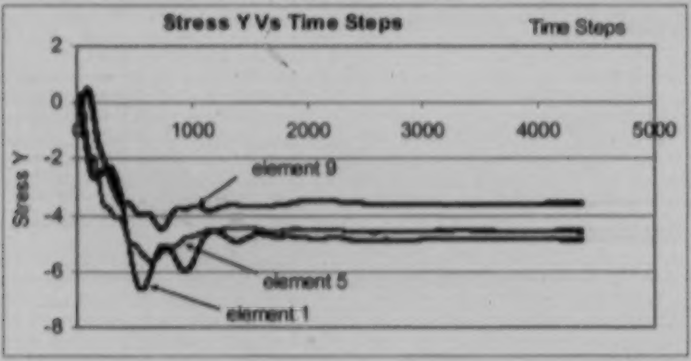

Figure 3.19: Consistent mass matrix applied to the scheme

The lumped mass matrix provided a better convergence than the consistent mass matrix to the exact solution as shown in Figure 3.5. For input parameters with a damping coefficient of 3.8 sec^{-1} and a time step equal to 0.003 seconds, the analysis was performed with a consistent mass matrix and the results are shown in Figure 3.19. It can be observed that for elements 5 and 9 the stress states converge to a different solution. However, for element 1, the required solution was obtained and can be viewed as being outside the boundary effects. This may be due to the use of a coarse mesh for the code development.

The difference in computed solutions between applications of consistent and lumped mass matrixes to the formulation can be explained by the following discussion. In the case of a lumped mass matrix, as the solution converges to equilibrium, the net nodal forces on the internal nodes of the elements tend toward zero. Net nodal forces acting on the boundary nodes are equivalent to the reactions at the supports or the boundary nodes. Based on the boundary conditions, these nodal forces would not be able to produce further displacements on the boundary nodes, will not contribute to the disturbances of the other internal nodes and a final state of equilibrium would be obtained. In contrast, if a consistent mass matrix is used, the net nodal forces on the boundary nodes can result in displacements of the internal nodes because of the use of non-zero diagonal terms. This may result in convergence of the stress states, strains, or displacements to slightly different values from those obtained using a lumped mass matrix. It is expected that this will be more prominent for elements closer to the boundary and required convergence will be obtained for all internal elements. A refined mesh can be applied to reduce the effects of convergence of a consistent mass matrix for the proposed method.

More importantly as pointed out in Bathe [2], the diagonal mass matrices have been effective in analyses using central difference schemes, as the system of equations can be solved without factorizing. If a diagonal mass matrix is used, the number of operations for one time step is roughly 8n for the solution of the equation of motion, where n is the number of elements, while for a consistent mass matrix the number of operations is approximately 512n. If the equation is integrated over a number of time steps, the solution is less costly when the diagonal or lumped mass matrix is used.

The lumped mass matrix was used in the present work to conserve computation time, as the formulation is analyzed by the discrete element method at a later stage. Discrete element computational procedures are themselves time consuming.

3.6 CONCLUDING REMARKS

A computational scheme for the finite element analysis of discrete elements is developed. This can suitably incorporate the effects of discontinuities and will be extended to include deformability and subsequent breakage of the elements/blocks. This method incorporates the defined and tested capabilities of the finite element method and will be extended to include procedures of the discrete element method in order to model the failure of an earth mass and its subsequent movement. In this method the soil mass is idealized as discrete elements and a suitable scheme is used to restrain the movements of these blocks in relation to one another. As far as the assemblage scheme is concerned, this method is significantly different from the standard finite element method in that the matrices are not assembled. This procedure solves explicitly for each element and carries the history of previous time steps on to the next neighboring elements. An example is presented to validate the scheme and it is observed that the system converges to the required solution for stresses within the elements.

BIBLIOGRAPHY

1. Bicanic, N., Munjiza, A., Owen, D. R. J., and Petrinic, *From continua to discontinua—A combined finite element/discrete element modelling in civil engineering*: Developments in Computational Techniques for Structural Engineering, B. H. V. Topping Civil-Comp Press, 1995: p. 1–13.
2. Bathe, K. J., *Finite element procedures in engineering analysis*. Vol. 1. 1982, New Jersey, USA: Prentice Hall, Inc.,. 735.
3. Cundall, P. A., *A discontinuous future for numerical modeling in soil and rock*. In the Third International Conference on Discrete Element Methods. September 23–25, 2002. USA.
4. Barbosa, R., *Discrete element models for granular materials and rock masses in civil engineering*. Ph.D. thesis 1990, University of Illinois: Urbana-Champaign, Illinois USA. p. 140.
5. Ghaboussi, J., *Fully deformable discrete element analysis using a finite element approach*. Computers and Geotechnics, 1988. 5: p. 175–195.

4

DISCRETE ELEMENT MODEL

"Problems of discontinua" represent a class of problems or processes in computational mechanics that continuum based models cannot model reliably. Methods based on the finite element approach are usually limited to small displacements and unchanging topology. If these methods are used for contact problems, the contacts need to be defined a priori and remain unchanged throughout the analysis.

Cundall and Strack [1] proposed a versatile numerical tool, the classical discrete element method (DEM), particularly suitable for the simulation of particulate and granular materials. The DEM needs few material properties in comparison to continuum methods, which require complex constitutive models containing dozens of parameters for yield surfaces, etc. Further, the DEM naturally exhibits localization and it is difficult to capture such localization in a continuum model that uses a mesh.

However, many industrial and scientific problems are characterized by a transformation from a continuum to a discontinuum state. This situation can be governed by appropriate constitutive models that control the material separation and follow inter-particle interactions in the motion of the particles.

Chapter 4

4.1 INTRODUCTION

Discrete element computational procedures are important tools in the development of a coupled approach to discrete finite element analysis. The contact model involves explicit calculations of the motion of each element in an assembly of discrete finite elements as these elements interact with one another through contact forces, surface friction, cohesion, Walton [2]. As presented in Chapter 3, the finite element solution utilizing constrained individual elements is built upon usage of the explicit time integration scheme, which uses the basic discrete element equation and procedures for its numerical calculation scheme. The progression of the solution scheme from the finite element steps to the discrete element and finite element steps is straightforward.

In this chapter the steps required in the development of discrete element procedures are reviewed. Two basic calculation schemes are required for an effective and robust code development. First it is vital to assimilate and incorporate routines for identifying the location of each discrete element; define, declare, and resolve contact information; and compute contact forces. The second step is to capture the motion of the discrete elements applying contact forces and other applied forces by integrating the equation of motion over time.

The proposed method differs from conventional discrete element analysis in that under the applied forces the element deforms as well as translates and rotates. These translations and rotations result in rigid body motion of the elements and the deformations result in the development of stresses and strains within the elements. This combines the efficacy and accuracy of the finite element method to model deformable bodies with the flexibility of the discrete element method to measure interactions between elements under motion. Standard nonlinear finite element schemes are adopted for analysis and thus the technique neither relies on the decoupling of the deformation modes from the rigid body motion, Shi [3], nor is it based on any modal superposition analysis.

4.2 CONTACT DETECTION

An effective solution of a discrete element problem depends on the computational algorithm used for contact detection and contact resolution. Numerous procedures have been reported in the literature for contact detection, the simplest being to choose any polygon from the flow and then search among all the remaining polygons for contact with the referenced polygon. This procedure is carried out for all the remaining polygons; thus for a system containing N polygons $N^2/2$ searches are required.

Munjiza [4] reported that contact detection takes a considerable proportion of the total CPU time (up to 60% in some cases) required to analyze discrete element problems. In order to reduce the amount of search, the search process for any selected polygon can be done within its immediate neighborhood. Hopkins [5] used a uniform square grid superimposed on the domain of the problem to define a neighborhood for a given polygon. In the present work the same technique is followed, that is, the grid cell size L_c is based on the largest dimension of the largest polygon.

In order to specify the location of each element in a particular cell, the coordinates of the centroid of each element are calculated. These centroidal coordinates are then divided by the length of the cell Lc and the quotient is assigned as the I and J locations in the grid but in integer form for the element, say H. The variables gi and gj are used to compute these values and are then stored in arrays Invx[ ] and Invy[ ] to be recalled during contact processing.

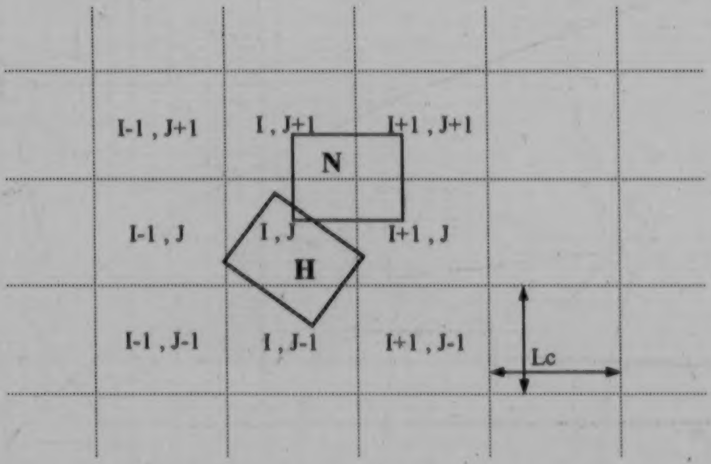

Figure 4.1: Grid cell decomposition of the domain, modified from Hopkins [5]

Counts are made using the array **Ngrid**[ ][ ] to store the total number of elements present in each cell on the grid. A three dimensional array **Grid**[ ][ ][ ] is used to store the element IDs present in each cell.

The structure of the **Grid( )** function used in the computer algorithm developed for the current thesis is as follows:

Grid( )

```
        for (KD = 1 ; KD < = DE ; KD++ )
        {       Ng = DElem[KD] ;
                I = 1 + (int) ( XXAv[Ng] / Lc ) ;
                J = 1 + (int) ( YYAv[Ng] / Lc ) ;
                Ngrid [I] [J] += 1 ;
                tempG = Ngrid [I] [J] ;
                Grid [I] [J] [tempG] = Ng ;
                Invx [Ng] = I ;
                Invy [Ng] = J ;
        }
```

An element from the list of discrete elements **DElem**[ ] is selected and **Grid( )** is used to assign that element to a particular cell.

During contact detection the search is made only in the surrounding eight cells of the cell in which the at hand discrete element is present, as shown in Figure 4.1. Each element present in the neighboring cells is then searched for contacts with the home element (H), the element of concern. An element will be given the status of near element (N) if any of the nodes of this element is located within the home element.

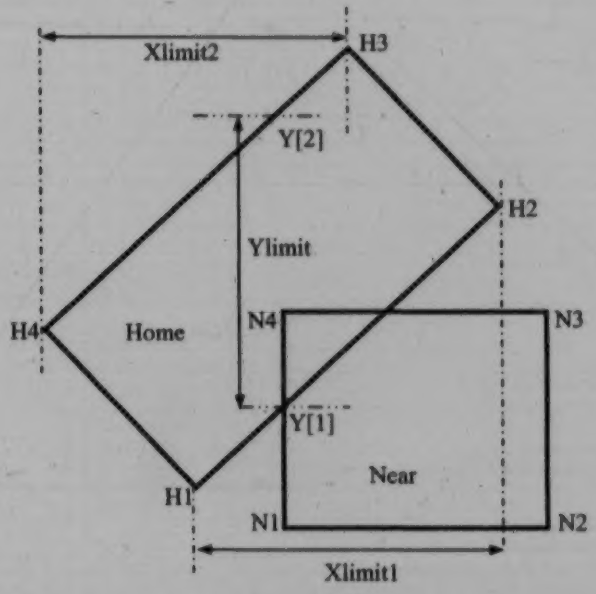

Figure 4.2: Detection of a contacting node N within the home element H

The selection of a contacting node of the near element N with the home element is based on a simple logic. As shown in Figure 4.2, say node N4 is selected in order to check for its presence within the home element H. First it is verified that the X coordinate of node N4 lies within the limits of X coordinates (say Xlimit 1, Xlimit 2) of any two sides of the home element. Then, corresponding to the X coordinate of N4, the Y coordinates on each of these two lines are computed and stored as Y[1] and Y[2]. This defines the values of Ylimit and if the Y coordinate of N4 is within this specified Ylimit then contact is declared and both the element ID N and node ID 4 are stored in the list of the neighbors of home H.

4.3 CONTACT RESOLUTION

After a search for the contacting elements is made for all the discrete elements, the next step is to find the points of intersection on the sides of the home element with the sides of the near element. During contact detection, the node forming the contact is stored and the intersection points are calculated using the two sides around point N4, i.e., the contacting node as shown in Figure 4.2. An algorithm to compute the intersection point of two straight lines is presented in Appendix A and the concepts adopted for the calculation of the respective area of overlap are presented in Appendix B.

4.3.1 Normal Contact Force

In the earlier approaches of Cundall [1] and Barbosa [6] the relative displacement increments are used along with the force-displacement law to calculate the increments in the normal contact forces. Available software packages UDEC and 3DEC use the linear stress-displacement relation in the normal direction to describe the mechanical response at the interface.

Issa [7] based the contact forces on Mindlin's nonlinear theory of frictional contact between elastic bodies. However, the contact forces were still calculated based on the relative motion; i.e., displacements of the centroids of the bodies in the normal direction. The normal force N at the contact point is given by the expression:

$$N = \left[\frac{4R_1R_2}{9\pi^2 \left(\frac{1-\nu^2}{\pi E} \right)^2 (R_1 + R_2)} \right]^{1/2} \delta_N^{3/2} \qquad 4.1$$

where,

δ_N - relative motions of the centroids of the bodies,
ν, E – material constants, and
R_1, R_2 - local radii of curvature of the contacting bodies.

Hopkins [5] implemented an elastic-viscous-plastic normal force contact model in his analysis for sea ice ridges. The elastic components in this model are proportional to the area of intersection and the viscous components are proportional to the rate of change of the area of intersection. A check is provided to ensure that the sum of the elastic and plastic components of the normal force is less than the compressive strength of the material. If the material fails plastically then the plastic components of the normal force will be irrecoverable. Using the soft-particle model and Kelvin-Voit element, Walton [8] calculated the normal contact force as the sum of the linear spring based on displacement and a linear velocity dependent term and expressed it as:

$$N = -Kx - D\dot{x} \qquad 4.2$$

where,

K - spring stiffness, and D - damping coefficient.

Ting et al. [9] also computed the contact forces during any given time step based on contact spring stiffness K and contact dashpot values D for an assembly of ellipse based discrete element models. It is pointed out that summing the incremental contact forces at each time step can result in significant accumulated error, so instead, the total normal overlap at each instant was computed to obtain the total normal contact force.

The relationship between the force F and overlap area A can be described using Hertz's law as implemented by Mirghasemi [10]:

$$F = K\ A \tag{4.3}$$

where, K is the contact stiffness with the dimensionality of Young's modulus and is given by

$$K = \frac{E}{1-\nu^2}\ \frac{\sqrt{2}}{4} \tag{4.4}$$

where,

E = Young's modulus, and

v = Poisson's ratio of the material.

This nonlinear contact law has been modified and implemented in Mirghasemi [10] who defined the area of overlap by defining the area as a product of the depth of penetration δ and a constant d which can be physically interpreted as a diameter of the contact area or as a contact length. Thus:

$$A = d\ \delta \tag{4.5}$$

In the present work, the normal contact force between two interacting polygonal blocks is calculated from the area of overlap or area of intersection and acts at the centroid of this area. For non-triangular overlaps, the area of intersection is computed by dividing the overlap area into triangles.

The quadrilateral elements used in the simulations are free to translate and rotate as their constraints are removed. During their interactions with one another they develop contact forces in normal and tangential directions with respect to the local coordinate framework. The local coordinate system is different for each contact and is based on the position of the intersection points formed. The tangential coordinate t is along the line joining the intersection points and the normal direction n is normal to the tangential coordinate. The position of the intersection points varies with the position of the near element. The intersection points can be formed on one side of the home element or can be along adjacent sides of the home element when there are four or five intersection points. The choice of the local coordinate axis, however, remains independent of the location at which the contact is formed and will always be along the line joining the intersection points, as shown in Figure 4.3. It is oriented such that the positive normal local axis points away from the home polygon.

For calculating the normal contact force an elastic normal force contact model is used. The elastic component of the normal force is proportional to the area of intersection. The normal contact force similar to equation 4.3 for the elastic components can be described as:

$$F_{ne}^{n} = k_{ne} * Area_{e}^{n} \tag{4.6}$$

where,

F_{ne}^{n} = elastic normal force acting on element n,

k_{ne} = elastic normal stiffness, and

$Area_{e}^{n}$ = area of overlap for element n.

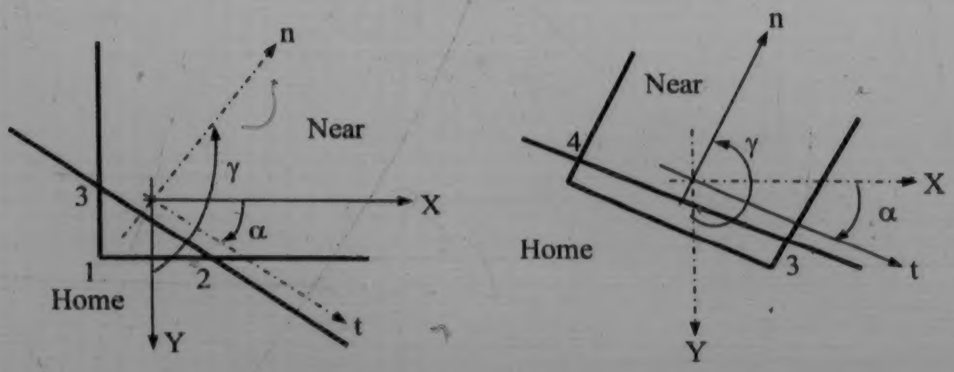

Figure 4.3: Definitions of the angles between the local and global coordinate systems used in the model

In conventional discrete element analysis, the contact forces whether normal or tangential, are applied at the center of the mass of the element along with the resultant moments. In the approach followed here, the normal contact forces developed on the boundary of each element are transformed to the interacting nodes of the elements. The components of the contact force are applied only on the nodes that are a part of the current interaction and not on all the nodes or centre of gravity of the interacting elements.

The normal contact force, computed using the local coordinate system, is transformed to the global coordinate system using the appropriate angle in between the coordinate systems. The angle between the local coordinates and the global coordinates α is first computed based on the points of intersection 2 (or 4) and 3. The resultant angle γ is further computed from α. Based on the direction of approach of the near element toward the home element there can be different combinations for finding the resultant angle γ. These combinations are presented in Appendix C.

The normal contact force is then resolved into horizontal and vertical components in the global coordinate directions. If there is only one node of the element involved in the interaction then the normal contact force is applied on that node. For a two-node interaction, the normal force is distributed proportionally onto the nodes on a weighted basis depending upon the location of the centroid of the area of intersection from each of the nodes of concern. The factors of proportionality are found using Lagrangian interpolation functions for one-dimension, or the interpolation can be based on the coordinates of the nodes and the centroid.

4.3.2 Tangential Contact Model

As reviewed in the literature, the tangential force component increases or decreases because of the incremental slip between elements/particles at the contact surface in the tangential direction. These tangential components T based on normal contact force N can be described by Mindlin's theory as presented in Issa [7] and are computed by the expression:

$$\begin{aligned} T &= \left[1-\left(1-\frac{\delta_T}{K\,f\,N^{2/3}}\right)^{3/2}\right] f\,N && \textit{for}\ \left(|T| \le f\,N\right) \\ |T| &= f\,N && \textit{if}\ \left(|T| > f\,N\right) \end{aligned} \qquad 4.7$$

where,

$$K = \frac{3(2-\nu)}{16\mu\left(\dfrac{6\pi^2 E R_i R_j}{8(1-\nu^2)(R_i+R_j)}\right)^{1/3}} \qquad 4.8$$

f	Friction coefficient between the contacting bodies,
ν, μ, E	Material constants, and
$R_{i/j}$	Average radius of the elements.

Adopting the preferred approach, the tangential force components are based on the relative velocity between the contacting elements. The global velocities are first resolved along the tangential axis of the local coordinate system, then the contact force is computed from the computed relative velocities between home and near elements:

$$T_f = k_{te} * v_X * \Delta t \qquad 4.9$$

where,

T_f - tangential force component,

k_{te} - tangential stiffness,

v_X - relative velocity between home and near elements, and

Δt - time step.

For this tangential model, a check is kept on the magnitude of the tangential force which is not allowed to exceed the maximum developed friction, i.e.:

$$T_f \leq \mu N \qquad 4.10$$

where,

μ - tanϕ, coefficient of friction, and

N - normal contact force.

The tangential components are then resolved back into the global coordinate system and applied on the nodes of concern, with an opposite sense of home with respect to the near element.

A representation of the tangential contact model adopted in this research is shown in Figure 4.4.

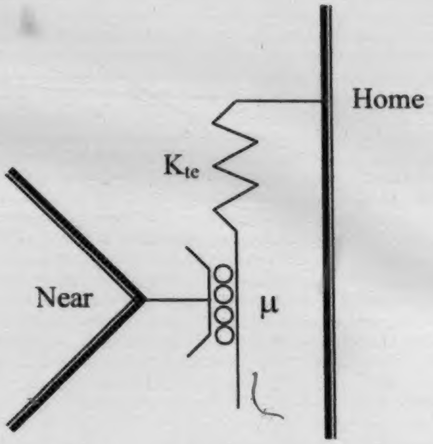

Figure 4.4: Tangential force model

It is very important to resolve the velocities properly along the local tangential axis. The angle γ formed between the local *n* axis and the global Y axis is measured in a counter-clockwise direction. The velocities in the global X or Y direction of the nodes forming the contacting sides are averaged. Then these velocity components are resolved along the *t* axis using the computed angle γ. From the transformed tangential velocities of the near and the home elements, the relative velocity v_X (equation 4.9) between these elements is computed and used to calculate the tangential contact force.

4.4 STRESS CALCULATIONS WITHIN DISCRETE ELEMENTS

In the past, the discrete element model granular materials have been represented by particles of different shapes and sizes. Generally, an explicit central difference scheme is applied to the discrete element method for integrating the equation of motion as opposed to the implicit schemes utilized in continuum mechanics, Jing [11]. The contact forces or stresses acting locally on the boundary or internally within the element are determined at each time step from the known variables on the boundaries of the element considered and its immediate neighbors. For rigid block assemblies of discrete elements, the average stress tensor is computed using an integral along the boundary of the domain, as contributions from contacts inside the domain cancel each other, Cundall [12]. The expression for the average stress tensor is:

$$\bar{\sigma}_{ij} = \frac{1}{V}\sum_{B} x_i T_j \qquad 4.11$$

where,

σ_{ij} - average stress tensor,
V - volume of the domain,
B - integral boundary of the domain,
x - position vector along the boundary, and
T - force at contact.

In comparison to deformable blocks Jing [11] defines the equations of motion for rigid blocks grid points based on the out-of-balance forces and internal stresses developed.

$$f_i = f_i^c + \sum_{k=1}^{N} \sigma_{ij}\left(n_j^k \ \Delta S^k\right) \tag{4.12}$$

where,

f_i	resultant out of balance force,
σ_{ij}	internal stress state,
n^k_j	unit normal,
ΔS^k	length of k^{th} boundary element, and
N	number of different elements connected at a grid point.

At each time step, the accelerations, velocities, and displacements are calculated first, followed by contact forces, stresses, and stresses based on constitutive relations of the contacts.

For the deformable elements considered in this research, the contact forces computed are applied to the contacting node or to the nodes forming the contacting side. These contact forces, along with other external and internal forces, result in the deformation and mobility of the element. As explained in chapter 3, using the net nodal forces (which include self-weight, externally applied forces, the internal resisting force vector, and discrete element contact forces), the incremental displacement vectors are calculated for each node/element over a given time step. These incremental displacements are obtained by direct integration of the equation of motion using an explicit second central difference integration scheme. The incremental displacements and incremental strains are calculated using the element strain displacement matrix **B**. Incremental strains are combined with the constitutive matrix **D** defined for the material concerned to compute the incremental element stresses. However, in chapter 3 the mobility of the elements was not considered and together the quadrilateral elements formed a mesh for finite element analysis.

After applying a suitable disassembly criterion, discussed later, the elements are allowed to move independently and thus can indulge in large rotations and displacements. The definitions for the stresses and strains now need to be handled differently. As described in Bathe [13], for nonlinear analysis involving large displacements and large rotations, total Lagrangian or updated Lagrangian formulations can be adopted. Based on the selected formulation, the stress and strain tensors can be either the 2nd Piola-Kirchoff stress tensor and the Green-Lagrangian strain tensor or the Cauchy stress tensor and the Almansi strain tensor, respectively. These stress and strain measures are energy conjugates of each other. The 2nd Piola-Kirchoff stress tensor is an objective stress tensor with little physical meaning; thus, in general, Cauchy stresses must be calculated. Importantly, the 2nd Piola-Kirchoff stress tensor is invariant under a rigid body rotation.

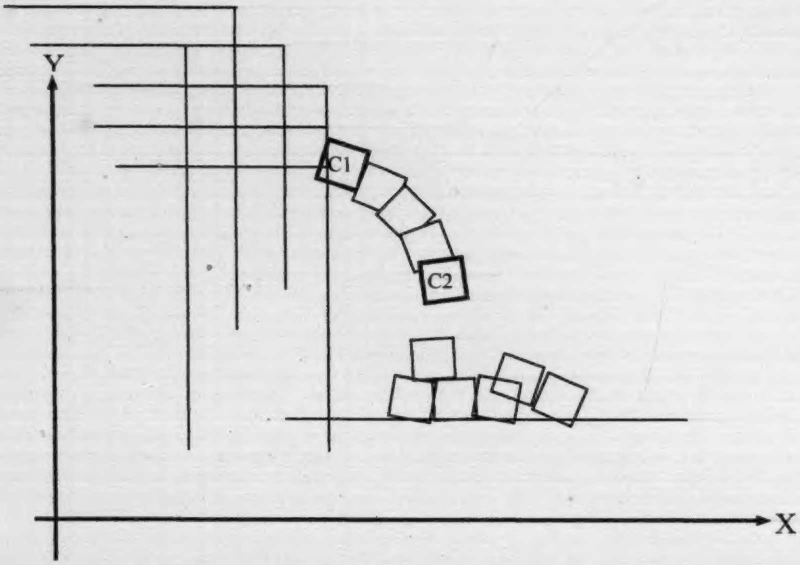

Figure 4.5: Reference configurations representing the motion of a deformable body within a stationary Cartesian coordinate system

As shown in Figure 4.5, as the element displaces from configuration C1 to configuration C2, it may undergo displacements and rotations. Since the configuration of the element at the time corresponding to C2 is unknown, the strain, stresses, and forces are referred to the known configuration C1. Bathe [13] points out that due to a continuous change in the configuration of the element, the Cauchy stresses at time t + Δt cannot be obtained by simply adding the Cauchy stresses at time t.

The Cauchy stress computed at t + Δt must take into account the rigid body rotation of the element as the components of Cauchy stress are not invariants when subjected to rigid body rotation.

The updated Lagrangian method deals with this scenario in an elegant manner by using appropriate stress-strain measures and constitutive relations. This is different from the total Lagrangian method in that all the static and kinetic variables are referred to a known configuration at time t. Using an explicit integration scheme the internal resisting force vector can be written in terms of the element stresses as in Barbosa [14]:

$$\int_V {}^tB_k^T \; {}^t\sigma_k \; dV_k = {}^tI \tag{4.13}$$

where,

${}^tB^T{}_k$ - strain-displacement nodal matrix at time t for element k,

${}^t\sigma_k$ - Cauchy stress for element k at time t, and

V_k - volume of element at deformed configuration.

Equation 4.13 satisfies the principle of virtual work and provides a consistent relation between the nodal forces and the internal stress states.

Once the deformation gradient is known, Cauchy stresses and 2nd Piola-Kirchoff stresses can be evaluated using simple kinematic transformations. The deformation gradient describing the transition from reference configuration C1 to the current configuration C2 is defined as:

$${}_0^tX = \left({}_0\nabla \quad {}^tx^T \right)^T \tag{4.14}$$

where,

$$ {}_0\nabla = \begin{bmatrix} \dfrac{\partial}{\partial x_1} \\ \dfrac{\partial}{\partial x_2} \end{bmatrix} \qquad \text{and} \qquad {}^t x^T = \left\lfloor {}^t x_1 \quad {}^t x_2 \right\rfloor \qquad 4.15 $$

The next step in computing the stress and strain measures corresponding to the current configuration C2 is obtained using the deformation gradient. The stress and strains at configuration C2 are a sum of the stress and strain values of the reference configuration C1 and the additional stress and strain produced during motion from C1 to C2. These stress and strain measures are represented as:

$$ \sigma^{C2^1} = \sigma^{C1} + {}_{C1}^{C2}\sigma \qquad 4.16 $$

$$ \varepsilon^{C2^1} = \varepsilon^{C1} + {}_{C1}^{C2}\varepsilon \qquad 4.17 $$

where,

$\sigma^{C2^1}, \varepsilon^{C2^1}$	Stress and strain measure at configuration C2,
$\sigma^{C1}, \varepsilon^{C1}$	Cauchy stress and strain measure at configuration C1, and
${}_{C1}^{C2}\sigma$, ${}_{C1}^{C2}\varepsilon$	Incremental form of 2nd Piola-Kirchoff stress tensor and Green-Lagrangian strain tensor.

The Cauchy stress and Almansi strain tensors at configuration C2 are calculated using the deformation gradient:

$$ \sigma^{C2} = \frac{1}{\left|{}_1^2X\right|}\,{}_1^2X\,\sigma^{C2^1}\,{}_1^2X^T \qquad 4.18 $$

$$\varepsilon^{C2} = \left|{}^{2}_{1}\overline{X}\right| \; {}^{2}_{1}\overline{X} \; \varepsilon^{C2^{1}} \; {}^{2}_{1}\overline{X}^{T} \qquad 4.19$$

where,

σ^{C2}, ε^{C2} = Cauchy stress and Almansi strain at the new configuration

$$ {}^{2}_{1}\overline{X} = {}^{2}_{1}X^{-1} \qquad 4.20$$

Over time steps, the current configuration moves further away from the reference configuration. Then the current configuration is redefined as the reference configuration and the stress/strain tensors are updated as explained above. Based on the new geometric and material conditions, the strain displacement matrix is recomputed for the new reference configuration. The matrix considered here is the standard form used in linear, finite element analysis, as geometric nonlinearities are accounted for during updating of the configurations and no material nonlinearities are considered in this present work.

The equation of motion for the updated Lagrangian formulation, Bathe [13], in terms of the 2nd Piola-Kirchoff stress tensor can be expressed as:

$$\int_{t}^{t+\Delta t} S_{ij} \left(\delta \; {}^{t+\Delta t}_{t}\Delta\varepsilon_{ij}\right) {}^{t}dA = {}^{t+\Delta t}R \qquad 4.21$$

where,

S_{ij} - 2nd Piola Kirchoff stress tensor,

ε_{ij} - Green-Lagrangian strain tensor,

dA - integration over the area, and

${}^{t+\Delta t}R$ - resultant force vector at time t+Δt.

4.5 DISASSEMBLY CRITERIA

The proposed approach considers discrete elements restrained at nodes to solve for a finite element solution. Progressive fracturing can then be allowed based on some fracturing criterion and the restrained discrete elements are allowed to translate and rotate freely from their specific positions. The motion and stress computations of these discrete elements will be carried out based on various measures as discussed in earlier sections. Remaining discrete elements which do not split from their restraints will continue to be a part of the finite element solution assembly, and further fracturing of this continuum will be carried out as and if required. The disassembly is allowed only along the interfaces and not through the elements.

Munjiza [15] indicated that continuum based models are generalizations of strain rate dependent elasto-plastic models implementing various yield surfaces while keeping the geometry of the problem unchanged. In his work, the finite element model is valid until the load carrying capacity of the localization zone is reduced to zero. Then a crack is assumed to open along the line of localization. A remeshing of the finite elements within every discrete element is performed when the breakage occurs.

The disassembly process adopted in this work is based on the Mohr-Coulomb shear strength yield criteria and the tensile criteria. A search process is carried over all the sides of the element having an interface with it. The internal stress state is transformed to each side, averaged for the neighboring Gauss points and checked for the adopted failure criterion. As presented in Mase [16], the stress tensor can be transformed into the stress vector by applying the following relation:

$$t_i^n = \sigma_{ij} n_j \tag{4.22}$$

or writing explicitly:

$$\left\langle t_1^n \quad t_2^n \quad t_3^n \right\rangle = \left\langle n_1 \quad n_2 \quad n_3 \right\rangle \begin{bmatrix} \sigma_{11} & \sigma_{12} & \sigma_{13} \\ \sigma_{21} & \sigma_{22} & \sigma_{23} \\ \sigma_{31} & \sigma_{32} & \sigma_{33} \end{bmatrix} \tag{4.23}$$

where,

t_i^n = a traction vector on the side having a normal vector n_j to it, and

σ_{ij} = a stress tensor for that element.

At any point on the reference side, the stress vector can be resolved along normal and tangential orthogonal components and the magnitude of these components will be given by:

$$\sigma_N = t_i^n \, n_i = \sigma_{ij} \, n_i \, n_j \qquad 4.24$$

$$\sigma_s^2 = t_i^n \, t_i^n - \sigma_N^2 \qquad 4.25$$

If the normal stress vector on the side is less than the tensile strength of the material, the corresponding elements of that side are separated. The normal stress vector is used in the Mohr-Coulombs criteria to calculate the shear strength on that side of the elements. If the shear stress is greater than or equal to the shear strength acting on that side, a split is declared.

$$\tau \geq \tau_f = c + \sigma_N \tan\phi \qquad 4.26$$

Care is taken to remove the elements from each others' connectivity list, namely **CONNECT[ ]**, as described in chapter 3, or else they will still count in the finite element assembly. This can have effects on the displacement and velocity compatibility constraints of the finite elements assembly. These elements are now free to translate and rotate depending on their neighborhood environment. The contacting forces generated during the motion, including all other external-internal forces, are used to calculate the deformations within these discrete elements and also for the elements in the finite element assembly. The disassembly is carried over along the sides of elements that are constrained only at the nodes. Each element has its own nodes and can thus translate from its present position without the need for remeshing and redefining nodes and elements. The rest of the elements stay connected and follow the scheme for continuum analysis based on described velocity constraints.

The introduction of the Mohr-Coulomb criterion in separating the elements is one of many choices in disassembling. Since there are many models for soil, the shearing or splitting of soils may not necessarily obey the Mohr-Coulomb criteria. Whatever criterion is adopted for element boundaries, it is good practice to be consistent with the continuum yielding models applied inside the element. As presented in chapter 5, the elasto-plastic constitutive relation based on Mohr-Coulomb yield criteria is incorporated in the present research. Element boundaries are introduced mathematical artifacts, however, the soil is one undivided continuum until it starts to separate.

4.6 REDEFINITION OF CONTACTS

As the simulation progresses over time steps, the associations of discrete elements with their neighbors will change. Depending on the amount of translation, rotation, and the magnitude of the time steps, discrete elements can move away from other discrete elements, releasing contacts, and can establish contacts with other discrete elements. If time steps are small, contacts can be redefined after a number of time steps, increasing the computational efficiency. The length of the interval for calling the function **NEIGHBOR ( )** in the code will depend upon the rate of deformation expected for a particular simulation and can be defined effectively after running some trial simulations.

As discussed by Rothenburg [17], the computational effort required for the contact detection process is about half of the overall CPU time required to process a simulation. Thus computational effort can be reduced if the history of the contact position is tracked and continuously updated. Due to potential developments of new contacts and loss of existing contacts, updating schemes need to be carried out after a specific interval. Modifying the approach followed by Cundall [1] of using a mesh overlay to update the contact list, Rothenburg [17] extends the search for potential contacts to second-shell neighbors. These are stored in a data array during the duration of the simulation in order to minimize contact list updating.

4.7 NUMERICAL DAMPING

As presented by Chan [18], global and local dampings are applied in the numerical procedures and implemented on the equation of motion and contact interfaces. Hart [19] discussed that mass-proportional and stiffness-proportional dampings are applied to lower frequency modes and higher frequency inter-block vibrations, respectively. Using both forms of damping in combination is termed Rayleigh damping. It has been pointed out that static solutions require more damping than dynamic solutions. In discontinuum (dynamic) analysis, due to natural energy dissipations such as inter-element sliding or friction, unbalanced vibrations are absorbed.

The equation of motion used to find the velocity at the next time step using the second order central difference method is:

$$\left(\frac{M}{\Delta t^2}+\frac{C}{2\Delta t}\right){}^{t+\Delta t}U = {}^{t}P-\left(K-\frac{2M}{\Delta t^2}\right){}^{t}U-{}^{t-\Delta t}U\left(\frac{M}{\Delta t^2}-\frac{C}{2\Delta t}\right) \qquad 4.27$$

Equation 4.27 contains the mass-proportional damping α within the damping coefficient C as:

$$C = \alpha M \qquad 4.28$$

As discussed in chapter 3, the selection of damping constants cannot be defined with certainty; damping constants must be chosen to provide a solution closer to the critical damping. An adaptive damping scheme that adjusts mass damping coefficients based on rates of energy change has been adopted in 3DEC and

UDEC software. This damping scheme responds like a servo-controlled mechanism.

4.8 SOLUTION STABILITY

Factors that affect the stability of the analysis are discussed in the following sections.

4.8.1 Time Steps

Numerical stability considerations is discussed in Bathe [13]. Explicit integration methods applied are conditionally stable, that is, they are stable if and only if the solution for an initial condition does not grow without bound for any time step and if the time step value is within the stability limits. System equilibrium equations have to be integrated accurately in order to predict the dynamic response of a structure. The time step thus required can be estimated proportionally to the smallest period of the assembly and can be estimated from the equation:

$$\Delta t_n = 2 \min \left| \left(\frac{m}{k} \right)^{1/2} \right| \qquad 4.29$$

where,

m = mass of the associated element, and
k = stiffness of the elements surrounding the node.

The cost of integration analysis is directly proportional to the number of time steps required for the solution. The selection of time steps is important as a time step has to be small enough to obtain an accurate solution but not so small that analysis will be costly.

4.8.2 Contact Formation

Hopkins [5] identified that unobserved contacts can occur if contact detection is not performed as often as required. As the search for contacts is called after a defined number of time steps or a defined interval, some of the contacts are likely to be declared after significant overlap. Due to the quantum nature of the contact detection process, a node can suddenly appear in the interior of another element, Williams [20]. The solution for this problem is to define a fuzzy boundary zone inside and outside the actual boundary. Fuzzy boundaries need to be sufficiently wide that the nodes cannot jump over the contact detection interval. The fuzziness and tolerance for element boundaries complicate the development of geometric rules for interactions. Penalty function schemes can be used to impose contact constraints as the node enters the boundary zone. When it is detected within the zone, the penetrating node is slowed down over some distance by the contact force.

In the code developed here, as neighboring elements approach one another, the velocity of approach of each element is slowed by a small fraction. Based on the time step, if the velocity of approach is large, the overlap computed between elements can be large and can result in a large rebound. In the discrete element procedure damping can help to stabilize the dynamics caused by the delay in contact renewal. In the examples presented, a reduction value of 1% to 2% is applied to the approach velocities of the elements to control contact formation. The values of this fraction are based on the size of the time step increment. As observed during numerous trials conducted to obtain a stable solution, a reduction fraction of 2% or more was suitable for time steps of 0.001 seconds or larger. For smaller time steps, a fractional value of 2% or less was effective. A few iterations of the simulation are required to confirm the value of a reduction fraction.

4.8.3 Memory Allocations

Pointers are used to access a variable in the code. A pointer is a variable that contains a memory address of another variable and points to the value of that variable. The size of a pointer variable is equivalent to that of an integer, i.e., 32 bits. As discussed by Munjiza [21], pointer arithmetic computations are generally faster than those using simple integers. However, pointers may make the computer program difficult to understand.

If computer memory (RAM) is limited, the use of pointers provides a reasonable way to define variables and to store the large quantities of data generated during a calculation cycle for use in the next time steps. The computer language C++ provides system level support for allocating and freeing memory, so it is not necessary to write specific routines for manipulating memory, Ting [22].

4.9 VALIDATION EXAMPLES FOR DISCRETE ANALYSIS

The foregoing computational procedures developed for contact detection and contact force generation were verified by solving three example problems created to check the scheme. The examples presented are related to (1) contact formations, (2) effects of a discrete element contacting a finite element assembly, and (3) combined effects of discrete and finite elements for a multi-block toppling scenario. These examples helped in examining the different functions and models used in the code. The examples are based on the concepts of linear elasticity and no consideration is given to the yielding and development of plastic stress states within these elements. Concepts of elasto-plastic constitutive relations and their applications are presented in chapter 5. Input parameters involved in these examples are given in Table 4.1.

Example	Young's modulus, E kN/m²	Poisson's ratio, ν	Damping coefficient, α	Unit weight, γ kN/m³	Normal stiffness, k_n kN/m²	Tangential stiffness, k_s kN/m	Friction angle, ϕ
1	35000	0.3	3	16.50	2000	500	30
2	50000	0.4	2.5	-----	3000	300	30
3	38000	0.35	3	16.50	7000	700	30

Table 4.1: Input parameters used in the examples

4.9.1 Validation of the Contact Model

Example 1 is used to check the different functions developed for the discrete element analysis zone of the code. The effect of the drop of a quadrilateral element from a height onto two isolate discrete elements lying at the base is examined first, schematic as shown in figure 4.7(a). The elements are idealized as plane strain iso-parametric finite-discrete elements and have eight degrees of freedom as discussed in chapter 3. The standard formulation of finite element analysis is adopted and a two by two numerical integration scheme is used. This example demonstrates the handling of large translations and rotations of discrete elements, which will constitute the motion of discrete elements as these elements disassemble from the finite element assembly.

Figure 4.6 shows the vertical stress distribution and its variations as the element falls under gravity, develops contacts, and loses contacts. As the element falls under gravity, the acceleration, velocity, and displacements at the nodes of the element are equal. Thus no strains and stresses are generated for the time steps from point A to point B.

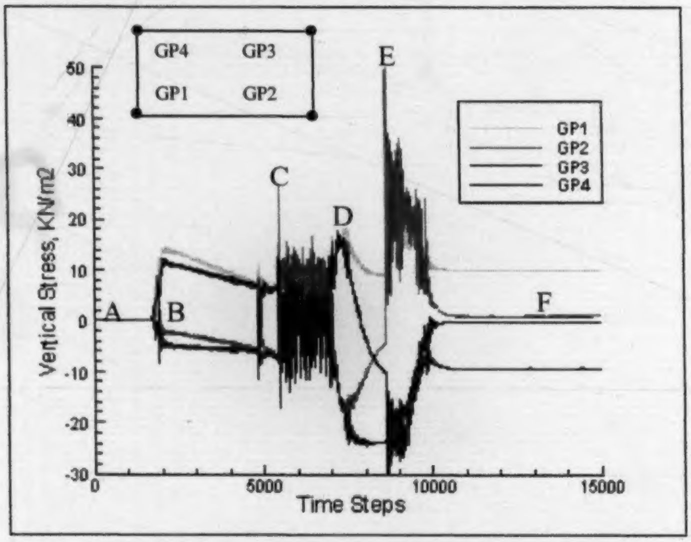

Figure 4.6: Vertical stress distribution of a 2D iso-parametric element falling under gravity (example 1)

As one node of the falling element comes in contact with the element at the base, stress changes takes place at various integration Gauss points, corresponding to point B. This is followed by rotation and translation of the element over the base element until at point C another node of the falling element comes in contact with the base element, making the stress states oscillate toward a different equilibrium state. After some time, contact with the base element is lost and the falling element begins to drop, toppling (at point D) and sliding over the base element. Another contact is formed with a second base element, corresponding to point E, and the stress states begin to fluctuate again. Equilibrium stresses are reached as the element settles down forming contacts with neighboring elements, corresponding to point F in Figure 4.6. Excerpts from the simulation related to points A to F are shown in Figure 4.7.

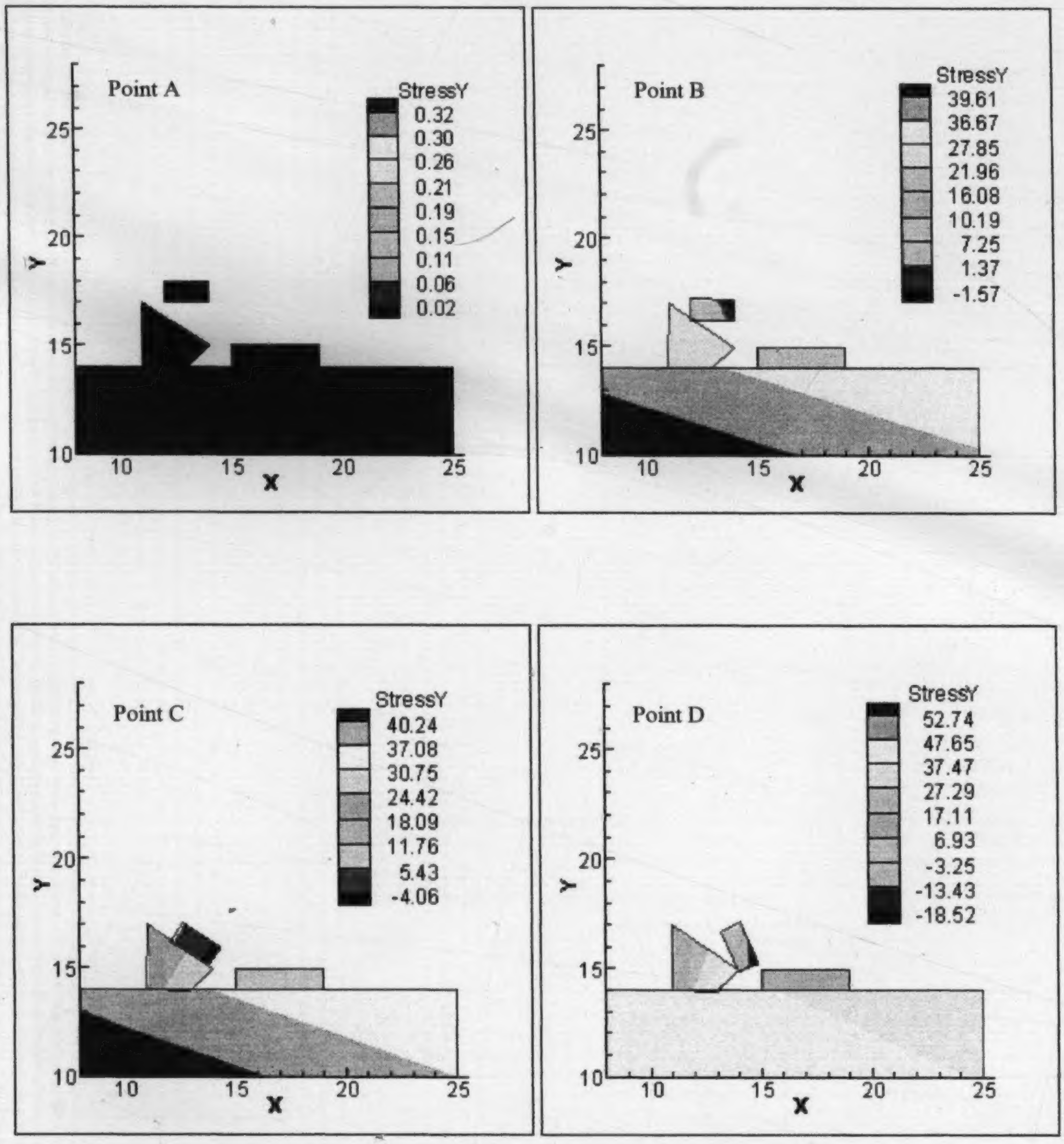

Figure 4.7(a): Simulations of an element falling on base elements at different equilibrium points (example 1, points A, B, C, D)

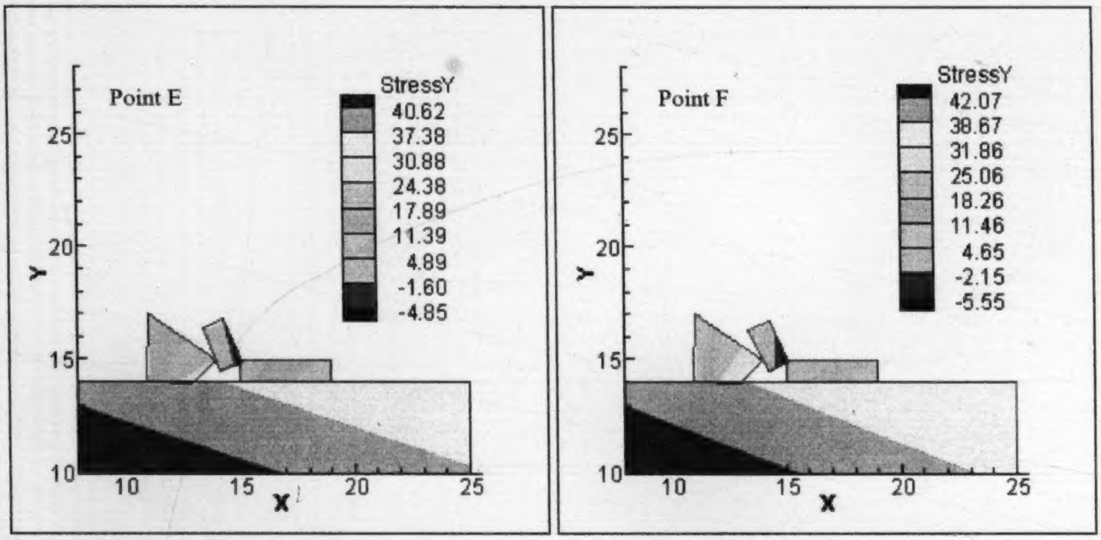

Figure 4.7(b): Simulations of an element falling on base elements at different equilibrium points (example 1, points E, F)

Example 1 is presented in movie format in the attached CD in file Chapter 4/Example 1 Single Block Drop.avi. The video shows the changes in stress contours for vertical stress states produced in the elements when contacts are established and lost.

Example 1 demonstrates a scheme for contact detection and computation of stress states at the integration points of an element falling on other elements. More refined stress states can be achieved in a falling body if it is discretized into more elements.

4.9.2 Discrete Contact Formation with a Finite Element Assembly

The interactions between discrete and finite element assemblies need to be verified for the proper development of a coupled analysis. Example 2 shows the effects of dropping a single element block, carrying a concentrated load at its upper two nodes, on a soil mass represented by an assembly of 100 discrete elements forming a finite element mesh. The results are demonstrated for the effects of concentrated loads only and gravity is turned off during this simulation.

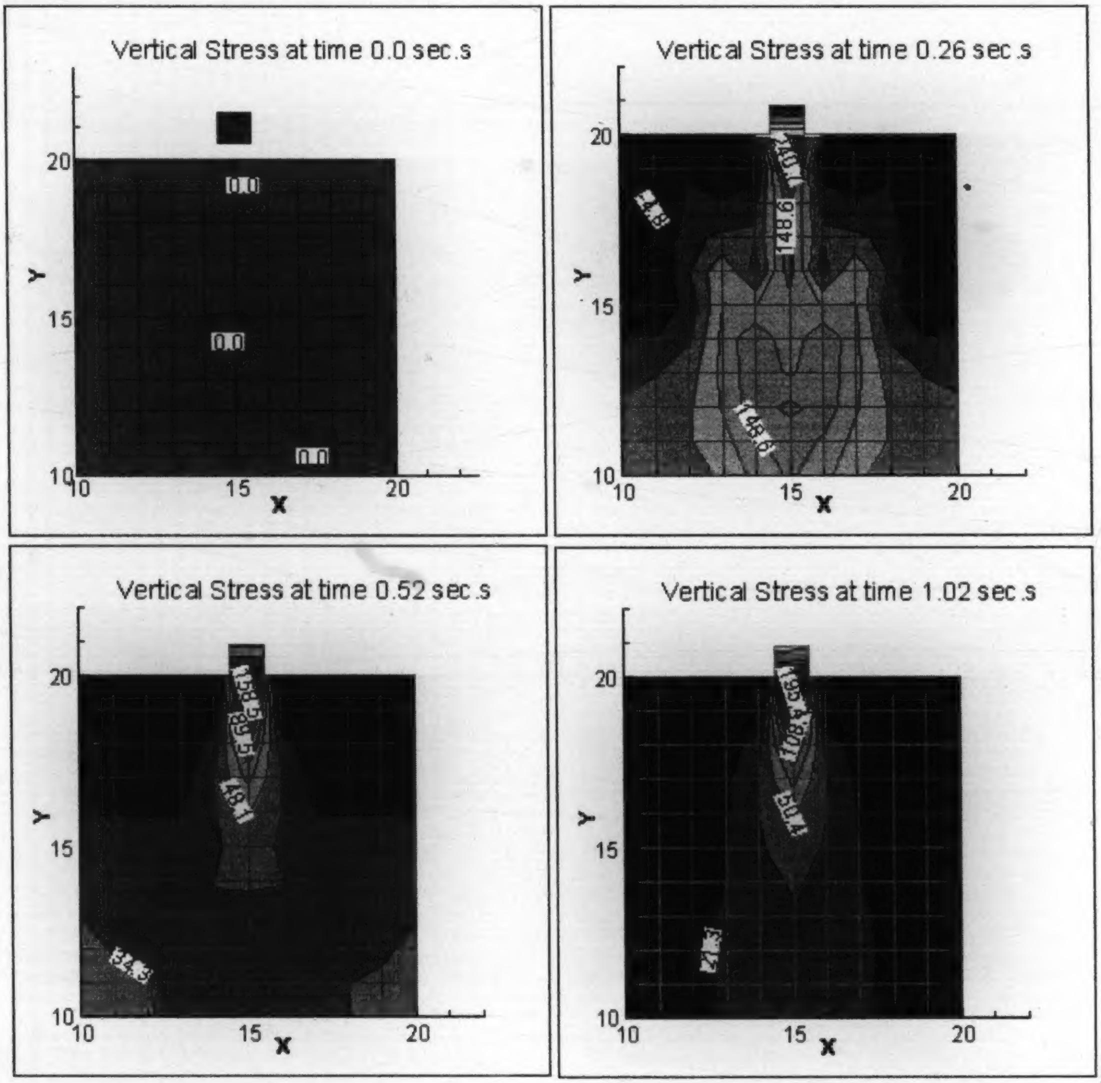

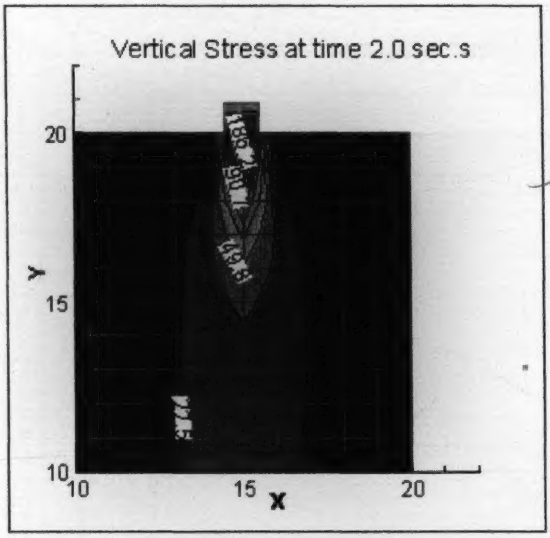

Figure 4.8: Vertical stress developments as discrete-finite elements interact (example 2)

At time 0.0 seconds, a single element block falls under the weight of concentrated loads. The finite element assembly is stress free at this time step.

As contact is established between the dropping element and the element assembly below, stress is generated within the assembly of elements, as shown at time 0.26 seconds. The stress wave propagates and oscillates around equilibrium, through the assembly of elements as shown in simulation extracts at 0.52 and 1.02 seconds. Finally the stress state settles down and attains a final equilibrium value equal to the stress from the element of about 200 kN/m^2 at 2.0 seconds. The variation of the vertical stress with time steps within elements 5 and 6 at Gauss points 3 and 4, respectively, is shown in Figure 4.9.

Slightly lower values of contact normal and tangential stiffness are applied in order to view the overlap of the contacting elements. Updating of the contacts is performed after a specified interval; the simulation movie shows how the elements are affected after contact (see attached CD, file Chapter 4/Example 2 Interaction FE-DE.avi).

Example 2 demonstrates the effectiveness of applying proper values of stiffness and defines the time interval after which the contact list must be updated.

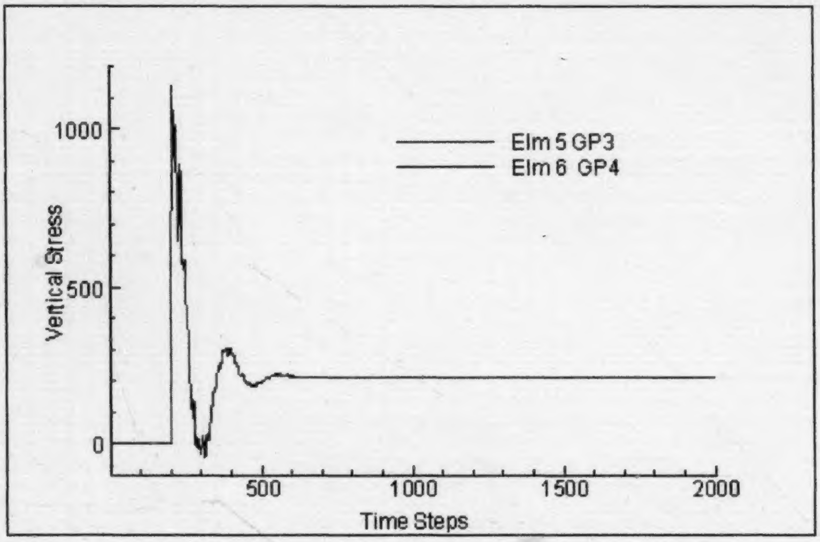

Figure 4.9: Vertical stress and time step plots for elements 5 and 6 in example 2

Excess contact overlap or very high contact stiffness can result in explosion or the contacting element can be pushed too far. The simulation is provided in the attached CD in file Chapter 4/Example 2 Interaction FE-DE.avi.

4.9.3 Toppling of a Block Assembly

The combined usage of discrete and finite element formulations is verified in example 3. A vertical slope comprising 100 iso-parametric quadrilateral block elements is allowed to collapse under the effects of gravity. In the first phase, as the gravity is turned on, the finite element formulation computes the internal principal stresses within the elements, Figure 4.10(a) and (b). Based on a specific split criterion discrete elements are formed. In example 3, a minor principal stress is a basis for split declaration and if its value is negative or equal to zero the split is defined between two neighboring elements. The material is treated as one possessing no tensile strength. These elements then become a part of the discrete element group or remain constrained with the finite element assembly.

The discrete elements formed interact with each other and with other elements in the finite element mesh assembly. This results in disturbance of the equilibrium stress state as the stress wave propagates through all the elements. The stress states within the elements resonate and reach values larger or smaller than the equilibrium values. These internal stress states oscillate over the time steps and damp toward the equilibrium value. Figures 4.10(c) to (f) show the distribution of vertical stresses developed within each of the elements. It is observed that the stresses within individual elements are complex and can be captured even while using a single element to represent a section of the body.

When equilibrium values are reached after the elements undergo translations and rotations, the vertical stress states developed within the elements are due to self-weight at the integration points. These stresses can be depicted as an overall mesh representing a refined geometry. The refinement and the cost of analysis are contingent upon one another, thus the mesh is refined based on the solution requirements. The run time for example 3 up to the point of interest was about 1.5 hours on an IBM Think Pad with an Intel Pentium P II processor and 128 MB of memory (RAM).

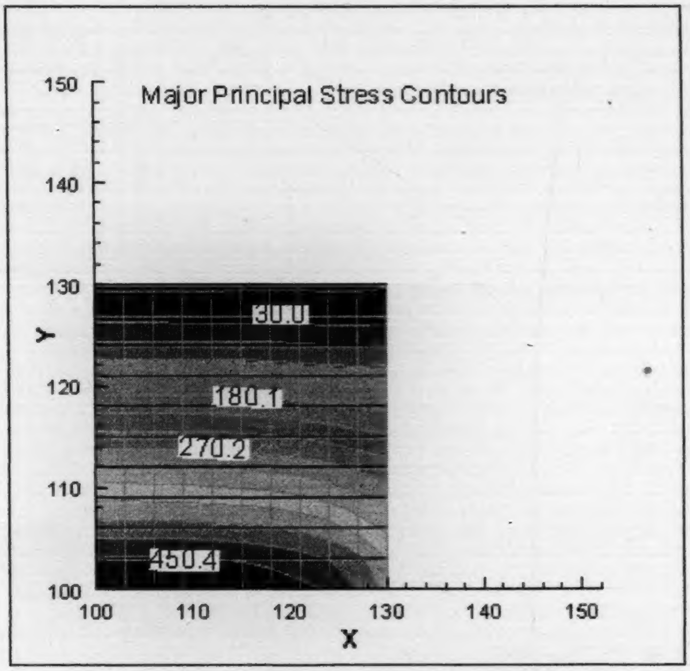

(a) Major principal stress contours

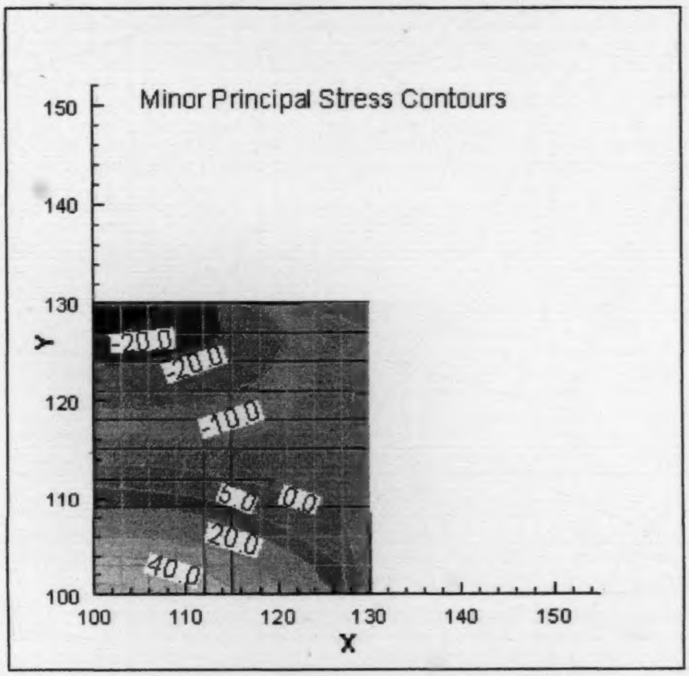

(b) Minor principal stress contours

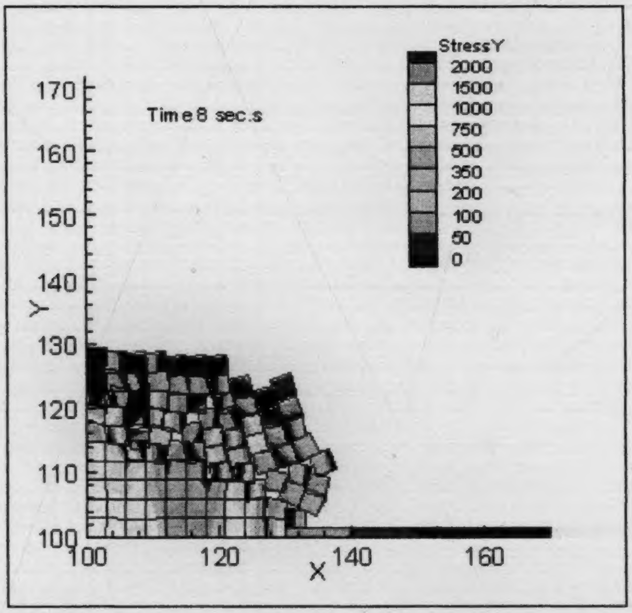

(c) Disassembly of the finite element mesh

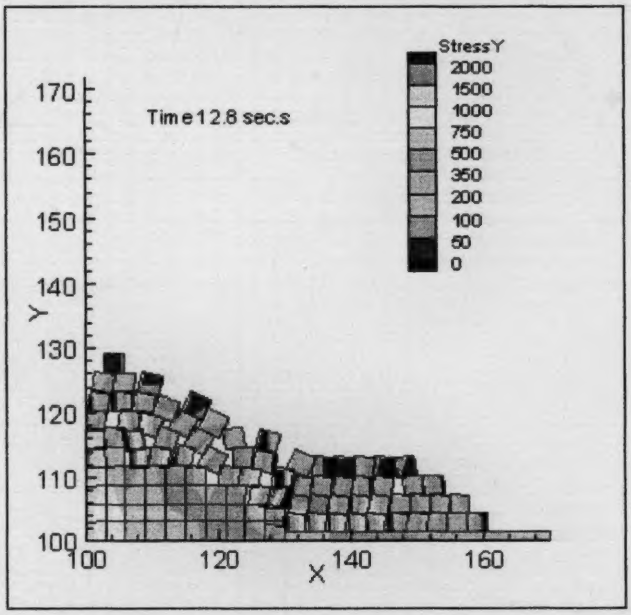

(d) Interaction and vertical stress state after 12.8 seconds

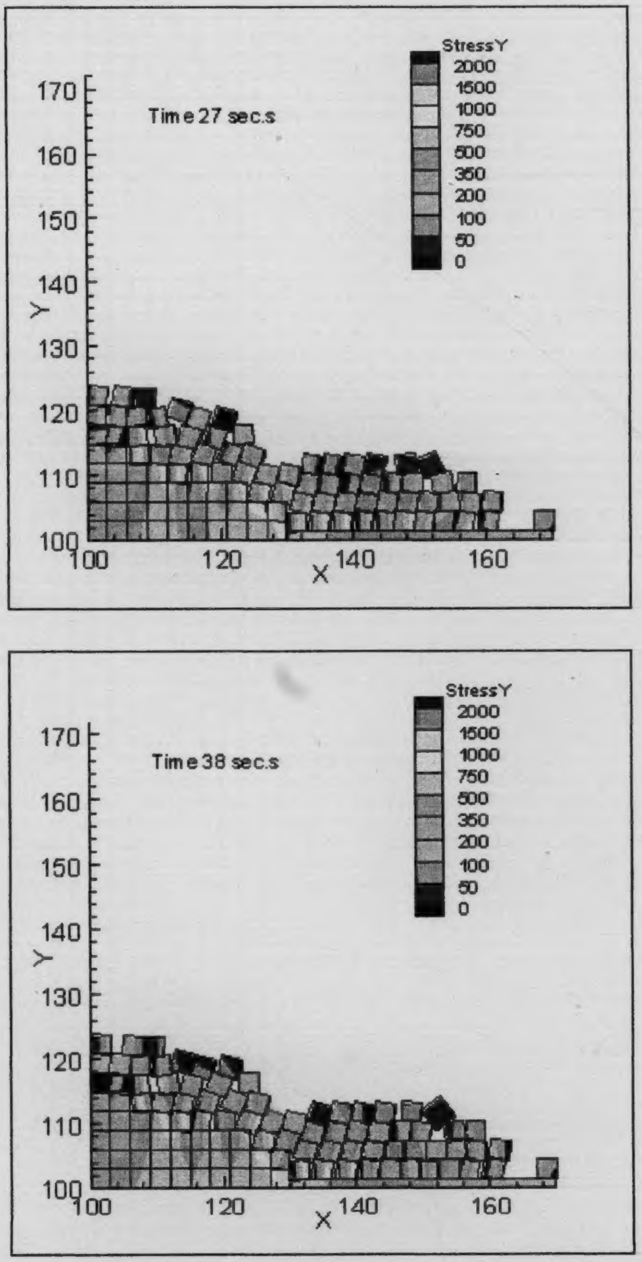

(e) (f) Stress states after 27 and 38 seconds, respectively

Figure 4.10: Multi-block toppling for finite and discrete simulations (example 3)

The example 3 simulation is provided in movie format in the attached CD, in file Chapter 4/Example 3 Multi Block Toppling.avi. The simulation shows the elastic behavior of the elements as they translate, rotate, and interact. As no yield surface is specified for the elastic response, the stress states within the elements reach 10–15 times the equilibrium stresses before they oscillate to equilibrium. Elements subjected to the higher stresses within deform and later regain original shapes and sizes as they equilibrate.

4.10 CONCLUDING REMARKS

A relatively simple discrete element model to analyze the continuum state is presented in this chapter. Nonlinear finite element concepts were incorporated and discrete element formulations were embedded to simulate discontinuum element behavior. Stress-strain states can be determined within elements as they deform, interact, and displace. Each element may undergo large displacements, rotations, and strains. Contact forces are applied along with external and internal forces, and velocities and displacements at the nodes of the elements were obtained by integration of the equation of motion over time. Three validation examples are presented to demonstrate the capability of the proposed method.

BIBLIOGRAPHY

1. Cundall, P. A., and Strack, O. D. L., *A discrete numerical model for granular assemblies*. Geotechnique, 1979. 29(1): p. 47–65.
2. Walton, O. R., *Explicit particle dynamics model for granular materials*. In Proceedings of the 4th International Conference on Numerical Methods in Geomechanics. 1983. Edmonton, Alberta, Canada.
3. Shi, G. H., and Goodman, R. E., *Two dimensional discontinuous deformation analysis*. International Journal for Numerical and Analytical Methods in Geomechanics, 1985. 9: p. 541–556.

4. Munjiza, A., and Andrews, K. R. F., *NBS contact detection algorithm for bodies of similar size*. International Journal for Numerical Methods in Engineering, 1998. 43: p. 131–149.
5. Hopkins, M. A., *Numerical simulation of systems of multidinous polygonal blocks*. 1992, CRREL, U.S. Army Corps of Engineers. p. 74.
6. Barbosa, R., *Discrete element models for granular materials and rock masses in civil engineering*. Ph.D. thesis 1990, University of Illinois: Urbana-Champaign, Illinois USA. p. 140.
7. Issa, J. A., and Nelson, R. B., *Numerical analysis of micromechanical behaviour of granular materials*. Engineering Computations, 1992. 9: p. 211–223.
8. Walton, O. R., *Particle dynamics calculations of shear flow*. Mechanics of Granular Materials: New Models and Constitutive relations, edited by J. T. Jenkins and M. Satake, Elsevier Amsterdam, 1983: p. 327–338.
9. Ting, J. M., Khwaja, M., Meachum, L., and Rowell, J. D., *An ellipse based discrete element model for granular materials*. International Journal for Numerical and Analytical Methods in Geomechanics, 1993. 17: p. 603–623.
10. Mirghasemi, A. A., Rothenburg, L., and Matyas, E. L., *Influence of particle shape on engineering properties of assemblies of two-dimensional polygon shaped particles*. Geotechnique, 2002. 52(3): p. 209–217.
11. Jing, L., *A review of techniques, advances, and outstanding issues in numerical modelling for rock mechanics and rock engineering*. International Journal of Rock Mechanics & Mining Sciences, 2003. 40: p. 283–353.
12. Cundall, P. A., Drescher, A., and Strack, O. D. L. *Numerical experiments on granular assemblies: Measurements and observations*. In the IUTAM Conference on Deformation and Failure of Granular Materials. 1982. Delft, the Netherlands.
13. Bathe, K. J., *Finite element procedures in engineering analysis*. Vol. 1. 1982, New Jersey, USA: Prentice Hall, Inc., 735.
14. Barbosa, R. E., and Ghaboussi, J., *Discrete finite element method*. Engineering Computations, 1992. 9: p. 253–266.
15. Munjiza, A., Owen, D. R. J., and Bicanic, N., *A combined finite-discrete element method in transient dynamics of fracturing solids*. Engineering Computations, 1995. 12: p. 145–174.
16. Mase, G. E., *Continuum mechanics*. Schaum's Outline Series. 1970, New York: McGraw-Hill, 221.
17. Rothenburg, L., and Bathurst, R.J., *Numerical simulation of idealized granular assemblies with plane elliptical particles*. Computers and Geotechnics, 1991. 11: p. 315–329.
18. Chan, D. H., *Course notes of numerical methods in engineering*, Department of Civil Engineering, University of Alberta, 2003.
19. Hart, R. D., *An introduction to distinct element modeling for rock engineering*. Comprehensive Rock Engineering, Ed. Hudson, J. A., 1993. 2: p. 245–261.

20. Williams, J. R., *Contact analysis of large numbers of interacting bodies using discrete modal methods for simulating material failure on the microscopic scale*. Engineering Computations, 1988. no. 5: p. 198–209.
21. Munjiza, A., *Discrete elements in transient dynamics of fractured media*. In the Department of Civil Engineering. Ph.D. thesis 1992, University College of Swansea: Swansea. p. 196.
22. Ting, J. M., and Corkum, B. T., *Computational laboratory for discrete element geomechanics*. Journal of Computing in Civil Engineering, 1992. 6(2): p. 129–146.
23. Munjiza, A., *The combined finite-discrete element method*. 2004, West Sussex: John Wiley & Sons Ltd. 333.

5

ELASTO-PLASTIC CONSTITUTIVE MODEL

Soil behaviour is complex and a single constitutive model capable of capturing the different behaviours of soil does not yet exist, Potts [1]. A constitutive model or a law delineating a mathematical form can describe one's views and ideas about the behaviour of a material. These models are important in providing good results for any solution procedure. The cognizance of the constitutive behaviour of materials devoid of the principles of physics and mathematics is not possible, Desai [2] as mathematics provides a succinct way for expressing physical phenomena. Various subdisciplines of mechanics such as theories of elasticity, hypo-elasticity, and plasticity can also be applied to understand soil behaviour.

Real soils contain a range of particles and their behaviour is dictated by the composition of various fragments. A soil mass is considered failed if it reaches a stress level satisfying an adopted failure criterion. A Mohr-Coulomb failure criterion is commonly used in soil mechanics. Ideally, any adopted constitutive model should be able to capture the behaviour of soil. A few advanced models are able to model soil behaviour, but they require input parameters not easily obtained from site investigations and laboratory tests. Compromise between simplicity and complicity is required in model selection to capture the dominant soil behaviour related to a particular problem, Potts[1].

Chapter 5

5.1 INTRODUCTION

The finite and discrete element solution procedure developed in chapters 3 and 4 assumed a linear elastic material model for computing stresses and an elasto-plastic contact model for part of the discrete analysis. This simple constitutive law is applicable to only a limited class of problems as most materials exhibit nonlinear and more complex responses. If the real behaviour of soil is to be predicted, a more comprehensive constitutive (non-linear) model is required. Nonlinear analysis can be classified into material nonlinearity (associated with material properties, e.g., plasticity) and geometric nonlinearity (associated with changes occurring within the configuration, e.g., as in large movements and deflections), Cook [3]. This research deals with both types of nonlinearity.

In this chapter, a finite element formulation incorporating an elastic, perfectly plastic Mohr-Coulomb model is presented. A brief discussion of the theory of plasticity is presented in this chapter and more details are given in Appendix D. Examples related to the estimation of the bearing capacity of cohesionless soil under a footing and development of active and passive states behind a retaining wall are presented as verification for the model.

5.2 REVIEW OF APPLIED MODELS IN PREVIOUS ANALYSES

In this section several constitutive models used in either discrete or finite element approaches are reviewed. Independent approaches to the finite element method and the discrete element method have been tested and refined over the years. A combined methodology of these two methods has been undergoing development and modification for the last two decades.

The finite element method has found application in a wide range of engineering and medical problems. The theoretical solution obtained using the finite element method satisfies the conditions of equilibrium, compatibility, a material's constitutive behaviour, and the applied boundary conditions. Constitutive behaviour provides appropriate stress-strain properties of the material and links equilibrium and compatibility conditions. It is not possible to obtain a closed form solution incorporating a realistic constitutive model of soil behaviour satisfying the above four conditions, Potts [1].

Various material models and yield criteria have been applied in geotechnical engineering applications within the finite element approach and are not restricted to the following:

a) Drucker and Prager:

$$f = \sqrt{J_2} - \alpha \, I_1 - k \qquad 5.1$$

where α and k are positive material parameters, I_1 is the first invariant of the stress tensor, and J_2 is the second invariant of the deviatoric stress tensor. There is, however, one limitation to the Drucker and Prager model related to the incremental plastic volumetric strains, which are expressed by the equation:

$$d\varepsilon_{ii}^{p} = -3 \, \alpha \, \lambda \qquad 5.2$$

where λ is the positive scalar factor of proportionality of the associated flow rule. As seen, this is a negative volumetric component indicating a volume increase or dilation at failure. However, for loose sands or normally consolidated clays only decreases in volume or compressive deformations occur during shear. This might indicate that normality might not be valid for this case and the model might not be applicable to these materials, Desai [2].

b) Mohr-Coulomb (can be improved to incorporate elastic strain hardening and softening models):

$$F = \sqrt{J_2}\sin\left(\frac{\pi}{3}+\theta\right)-\sqrt{\frac{J_2}{3}}\sin\phi\cos\left(\frac{\pi}{3}+\theta\right)-\frac{I_1}{3}\sin\phi - c\cos\phi = 0 \quad 5.3$$

where c and ϕ are material parameters and θ is the lode angle. This model is applied to the examples studied and presented in this chapter and is explained in detail in Section 5.1. Christian [4] applied an elasto-plastic formulation derived from the Mohr-Coulomb law, with dilatancy removed and a strain hardening model with a capped yield criterion, to analyze problems related to passive earth pressure and the bearing capacity of cohesionless soils.

c) Modified Cam Clay model based on the critical state concept: the yield locus for the modified Cam Clay model takes the form:

$$f = M^2 p^2 - M^2 p_o p + q^2 = 0 \quad 5.4$$

where,

M = slope of critical state line in q-p stress space,
P = normal stress/mean pressure = $I_1/3$,
Q = shear stress = $\sqrt{3J_{2D}}$, and
P_o = pressure corresponding to the intersection of the yield locus with the p-axis in a q-p stress space.

As pointed out by Desai [2], the modified Cam Clay model and various cap models developed by the Cambridge group may be able to successfully simulate a limited number of stress paths for a given material.

Numerous other yield criteria and constitutive relations have been applied for analyzing applications using the finite element method. The most generic for geotechnical engineering applications are discussed above. On the contrary, for discrete element analysis the stress and strain computations are primarily based on the averaging of contact forces and displacements on a specific plane.

The discrete element method as presented by Sawada [5], treats discrete elements as rigid bodies with springs at the contact points to transfer the inter-particle forces. The displacements, rotations, and contact forces involved in discrete element analysis are calculated then converted into macro physical values of stresses and strains.

The PFC^{2D} [6] constitutive model consists of three separate parts: the stiffness model which provides a linear relation between contact force and relative displacement, a slip model which confines the shear force components within the limits of friction coefficients, and a contact-bond model which enforces the bond strength limits. As such, no constitutive relations directly assisting in the computational sequence for stresses and strains are incorporated. This PFC^{2D} constitutive model has been applied to model rock behaviour and to capture the characteristic properties of the rock in terms of elasticity, prefailure micro-cracking, peak strength computations, softening relations of stress-strain in the post peak region, and kinetic energy release from bond breakage, Potyondy [7]. Dorby [8] showed that increments of particle displacements and rotations due to unbalanced forces can be computed from the assembled stiffness matrix of the structure. Stead [9] reported that numerous hybrid methods, a limit equilibrium and finite element analysis, a boundary-finite element and boundary-distinct element method, a particle flow and finite difference, and a finite-distinct element method with adaptive remeshing are being developed to capture the formation of cracks and their propagation.

While for discrete finite element formulations, primarily elastic constitutive laws have been applied, Munjiza [10] assumed a hyperelastic/plastic representation of the constitutive law. The deformation behaviour of the isotropic hyperelastic body was characterized by the strain energy per unit volume in the reference configuration. The constitutive equation for hyperelastic material follows:

$$S = \hat{S}(F,p) = \frac{\partial \hat{\sigma}(F,p)}{\partial F} \qquad 5.5$$

where,

S = the 1st Piola-Kirchhoff stress tensor,
σ = a scalar function, and
F = the deformation gradient.

It is inferred from the work of Barbosa [11] on the discrete finite element method that the matrix of constitutive relations applied to compute the incremental stresses is based on the elasticity parameters of Young's modulus of elasticity E and Poisson's ratio ν. The increment of the Green strain tensor, referring to the base configuration, is used to compute the increment in the symmetric Piola-Kirchhoff stress tensor.

5.3 ELASTO-PLASTIC MODEL

The elasto-plastic model is based on the assumption that a material behaves elastically up to its yield limits or peak strengths and then deforms plastically, Chan [12]. A complete review of the theory of plasticity is available in numerous references. As classified in Desai [2], two categories applicable to the subject of plasticity are the physical theory and the mathematical theory. To understand why a material behaves plastically, the physical theory is studied at a microscopic level. A mathematical formulation of the behaviour is based on experimental observations at a macroscopic level. A brief discussion on the relevant and applied theory of plasticity follows.

For basic plasticity involves four essential ingredients: coincident stress and strain axes, a yield function, a plastic potential function, and a hardening/softening rule, Potts [1]. The basic assumption is that the principal directions of the incremental stress and the incremental plastic strains coincide. The yield criterion can then be defined as a limit to the elastic deformations accumulated and can thus be expressed in terms of the respective stress states. Based on the yield criterion, a yield function separating the purely elastic state from elastic-plastic state can be stated as a scalar function of the stress states. In order to specify the direction of the incremental plastic strain vector for every stress state, it is necessary to define a plastic potential function with an appropriate flow rule. The material is assumed to be a perfectly plastic material for the present research and no hardening or softening rules are applied.

5.3.1 Mohr-Coulomb Yield Criteria

As mentioned earlier, linear elastic-perfectly plastic Mohr-Coulomb yield criteria are incorporated in the present computer code for analysis. The yield surface for this type of material is fixed in the stress space and does not change under loading or unloading conditions. If the stress state is below the yield surface, the behaviour is completely elastic; when the stress state reaches the yield surface plastic straining occurs and a stress state beyond the yield surface is not possible. If the state of stress is maintained at the yield surface, then plastic straining of the material will continue to occur and will eventually lead to the failure of the material. In terms of the shear strength, the Mohr-Coulomb criteria on any failure plane can be represented by the expression:

$$\tau = c + \sigma \tan\phi \tag{5.6}$$

where τ is the shear stress on the failure plane, c is the cohesion of the material of concern, σ is the effective normal stress on the failure surface, and ϕ is the angle of internal friction. The two parameters associated with the criterion can be determined by conducting experiments in the laboratory on the material up to the ultimate or the failure condition.

In terms of the principal stresses, the yield criterion can be expressed by equation 5.7 where the effects of the intermediate principal stress are ignored.

$$F=\frac{\sigma_1+\sigma_3}{2}\sin\phi-\frac{\sigma_1-\sigma_3}{2}-c\cos\phi=0 \qquad 5.7$$

Thus the representation of the projection of the criterion in the stress space on the Π-plane is an irregular hexagonal pyramid, Figure 5.1. The yield strength of the material in compression is higher than the strength in extension, making the hexagon irregular, and shows dependence on the third invariant. It can be expressed in an alternative form of stress invariants including the Lode angle θ, and the invariants of the deviatoric stresses, J_2 and J_3.

$$F=\sqrt{J_2}\sin\left(\frac{\pi}{3}+\theta\right)-\sqrt{\frac{J_2}{3}}\sin\phi\cos\left(\frac{\pi}{3}+\theta\right)-\frac{I_1}{3}\sin\phi-c\cos\phi=0 \qquad 5.8$$

There are two drawbacks to the approach outlined above. First, the magnitude of the plastic volumetric strain, i.e., the dilation, is much larger than that observed for real soils; second, when yielding of the soil is initiated, it will continue to dilate forever. If a non-associated flow rule is adopted, the first drawback can be rectified, Potts [1].

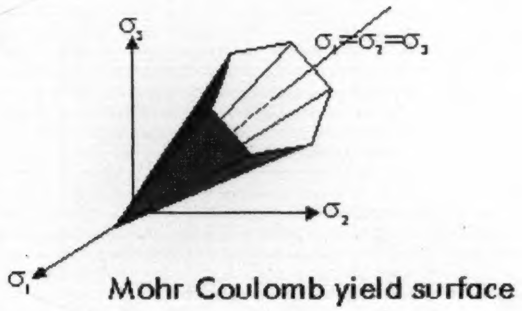

Figure 5.1: Mohr-Coulomb yield surface in principal stress space, Chan, [13]

5.3.2 Finite Element Formulation

The initial steps for the computations of the nodal velocities, nodal displacements, and elemental strains at Gauss points are the same as explained in earlier chapters. The final equilibrium equation over number of timesteps *n* to be attained for a solution procedure utilizing the concepts of velocity constraint is:

$$P_{ext} + \sum_{t=1}^{n} {}_{j}P_{\text{int}}^{t} - \sum_{t=1}^{n} {}_{j}I_{j}^{t} = 0 \qquad 5.9$$

where the net unbalanced force between the externally applied loads and the internal resisting force vectors developed tends to zero as equilibrium is attained. Knowing the nodal displacement values, the strains, stresses, and internal force resisting vectors developed at the Gauss points can be known in incremental form, as described in Appendix D.

The expression for the elasto-plastic constitutive matrix [C^{EP}] can be obtained using the following assumptions:

1) If the present stress state is on the yield surface, then,

$$F = \sqrt{J_2}\sin\left(\frac{\pi}{3}+\theta\right) - \sqrt{\frac{J_2}{3}}\sin\phi\cos\left(\frac{\pi}{3}+\theta\right) - \frac{I_1}{3}\sin\phi - c\cos\phi = 0 \qquad 5.10$$

The variations occurring for the yield function will also be zero,

$$dF = 0 \qquad 5.11$$

The condition

$$F(\sigma_{ij}, \varepsilon_{ij}^{P}) > 0 \qquad 5.12$$

is not permissible. This condition is referred to as a consistency condition, where loading from a plastic state will lead to another plastic state and the yield criterion will be satisfied as long as the material is in the plastic state.

2) The computation progresses over many time steps. The check for plasticity cannot be performed at every time step as it will be too time consuming. The check for the yield surface is carried out when sufficient strain increment has developed, say, over 100 time steps. This continuance of the plastic calculations should be selected with care and after performing certain iterations, such that the strain increment values accumulated over these time steps are not too large as to result in erroneous states.

The accumulated strain or the strain increment over the segment of selected time steps can be expressed in terms of the elastic and the plastic strain components:

$$\sum_{TSC}\{d\varepsilon\} = \sum_{TSC}\{d\varepsilon\}^{E} + \sum_{TSC}\{d\varepsilon\}^{P} \qquad 5.13$$

where TSC is the number of time steps after which the check for plasticity is performed.

In development of the computer code, three separate arrays of pointers are defined for storing the variables of the stress, namely, stress total (σ^T), stress average (σ^A), and stress incremental (σ^I). Similar steps are followed for the strain values.

Before performing the plasticity check, all stress increments over the specified number of time steps are stored commutatively in the stress incremental array. When the check for plasticity is done, the summed stress increments are added to the previous state of stress, stress average (which stores the total stress value after the previous check for plasticity was completed).

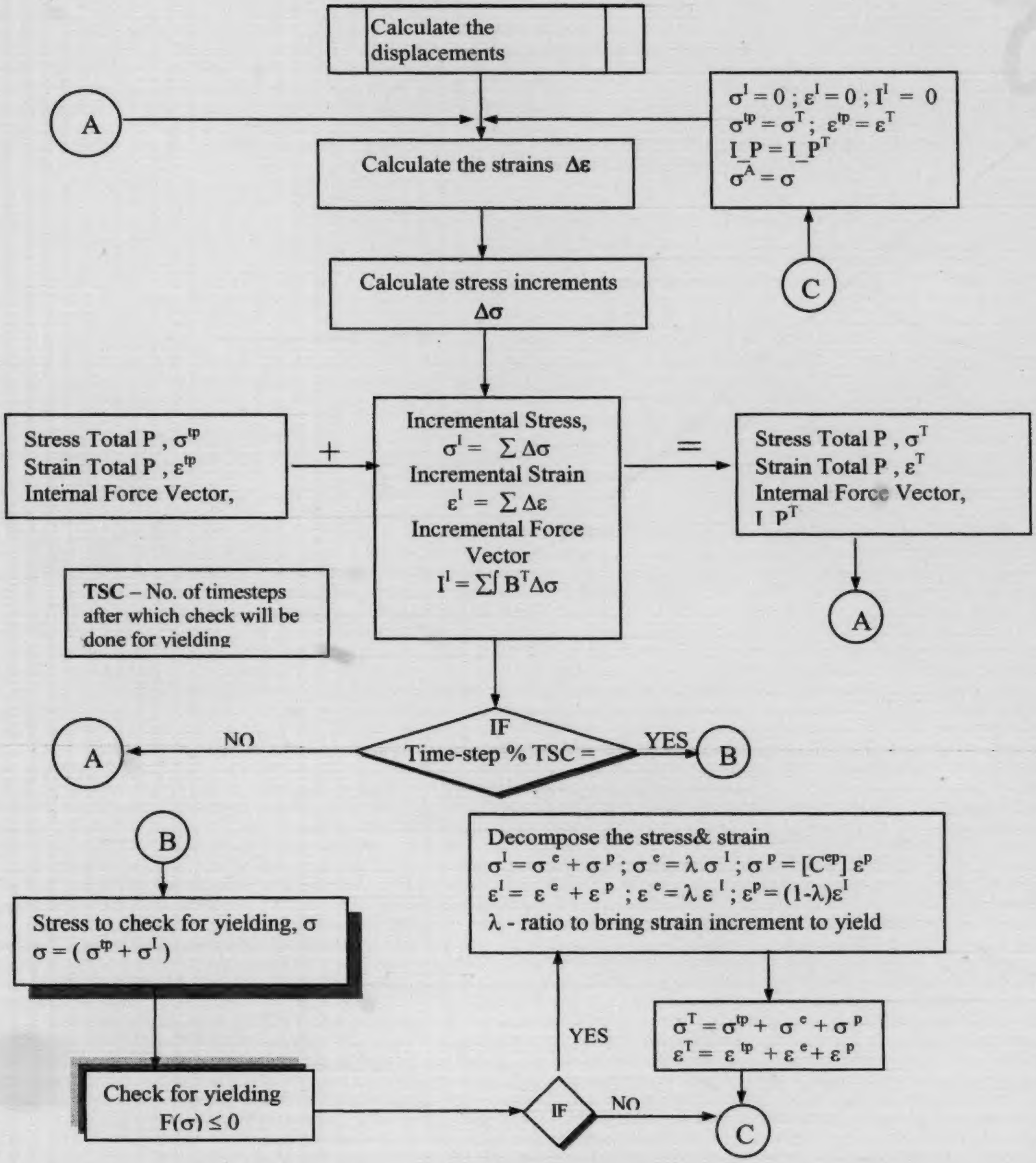

Calculate the displacements
A
Calculate the strains Δε
σ^I = 0 ; ε^I = 0 ; I^I = 0
σ^tp = σ^T ; ε^tp = ε^T
I_P = I_P^T
σ^A = σ
C
Calculate stress increments Δσ
Stress Total P , σ^tp
Strain Total P , ε^tp
Internal Force Vector,
+
Incremental Stress, σ^I = ∑Δσ
Incremental Strain ε^I = ∑Δε
Incremental Force Vector I^I = ∑∫B^TΔσ
=
Stress Total P , σ^T
Strain Total P , ε^T
Internal Force Vector, I_P^T
A
TSC – No. of timesteps after which check will be done for yielding
A
NO
IF Time-step % TSC =
YES
B
B
Decompose the stress& strain
σ^I = σ^e + σ^p ; σ^e = λ σ^I ; σ^p = [C^ep] ε^p
ε^I = ε^e + ε^p ; ε^e = λ ε^I ; ε^p = (1-λ)ε^I
λ - ratio to bring strain increment to yield
Stress to check for yielding, σ
σ = (σ^tp + σ^I)
YES
σ^T = σ^tp + σ^e + σ^p
ε^T = ε^tp + ε^e + ε^p
Check for yielding F(σ) ≤ 0
IF
NO
C

Figure 5.2: Flow chart showing the steps for elasto-plastic computations

This total current stress state is checked for yielding. If the current stress state is still elastic, then the stress increments, stress incremental, are added directly to the stress average value to obtain the total stress up to the current time step and are stored in the stress total array. If yielding occurs, the state of incremental stress needs to be divided into elastic and plastic components. Detailed derivations of the different matrices involved in the above computations are presented in Appendix D. The steps followed in the computation procedure are laid out in the flow chart shown in Figure 5.2. The first step in allocating the stresses into elastic and plastic components is to divide the strain in the elastic and plastic components. This is achieved by using the interval halving and the radial return techniques explained in Appendices E and F.

5.3.3 Displacement Constraints

When computing the elasto-plastic stress states within the elements, the prime concern is the development of excessive strains which could result in largely deformed elements, thus causing numerical instability. Deformed shapes, as shown in Figure 5.3, were observed if the aspect ratio of the elements was not preserved. Another form of instability was observed during the contact detection process of these deformed elements. This resulted from the sharp edges of one excessively deformed element missing contact formation with the sharp edges of another excessively deformed element. Sharp corners may prevent the elements from developing contact forces in the overlap sufficient to provide resistance to the mobility of the elements.

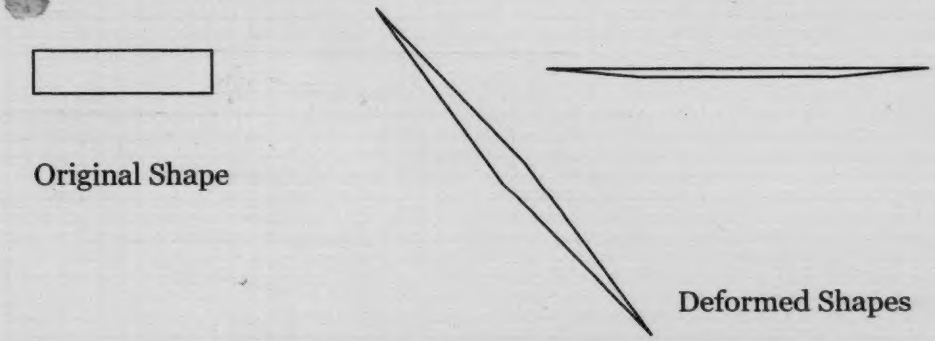

Figure 5.3: Comparison of element shapes

A routine based on the amount of cumulated strains within the elements was developed to control the deformations of the elements. The variable array **ASPECTR[]** was initialized to track these changes in the elements and list the deformed elements in the array. Nodal displacement constraints were applied on the elements stored in this array; element deformations were not applied to individual nodes, the average displacement of all the nodes was applied on the element as a whole. This was achieved and tested in two ways; first, by applying the average of the nodal displacements on each node, and second by the net nodal displacements. Satisfactory results were obtained from both approaches.

5.3.4 Variable Stiffness

In discrete element analysis, it is imperative to provide sufficient normal and tangential stiffness to the contacts developed. As discussed in chapter 4, the stiffness value depends on the time step used in the analysis. For most of the contacts formed between discrete elements, the specified values of normal and tangential stiffness were applied. A different format of applying the stiffness was tested in the developed method for certain types of contacts established during the application of concentrated loads.

As presented in the example of shallow foundation, large concentrated loads may exist on element nodes and the applied values of normal and tangential stiffness may be unable to develop sufficient contact force with the elements in contact. This may lead to excess penetration of one element into another and result in completely losing the contact formed. A very high contact stiffness value would defy the discrete element method's rule to select values of contact stiffness based on the values of time steps; it therefore could not be provided. Applying a high value of contact stiffness also tends to cause numerical instability in terms of blowing up elements at other locations.

As contacts are established between elements below the elements carrying concentrated nodal forces, overlaps between elements increase in order to develop the required contact forces. If a fine mesh is employed to capture failure, then the amount of overlap might not be able to provide the required contact force. Thus values of normal and tangential stiffness need to be modified or amplified by a fraction, to provide the required amount of contact forces.

Two different forms of amplification were tested. The first form of amplification of normal and tangential stiffness $AF_{\alpha 1}$ was applied only to contacts developed with elements carrying concentrated forces. A different range of values from 10 to 100 was applied and the most appropriate value was adopted for the solution based on the final configuration and overlaps achieved. The second form of amplification of normal and tangential stiffness $AF_{\alpha 2}$ was applied to contacts for which the area of contact or overlap exceeded a minimum percentage of the area of either of the elements forming the contact. This value based on percentage of area overlap can be varied depending on the choice of application and the user. A range of values from 1 to 10 was applied and tested for $AF_{\alpha 2}$

5.3.5 Time Steps

The developed code allows the flexibility to define different values of time step to finite element and discrete element sections. Based on different approaches and analysis settings, finite and discrete element analyses may require different time steps. In most cases, the discrete element time step was either the same as the finite element time step or about 3 to 10 times greater or smaller.

5.4 EXAMPLES

The developed model was used to analyze the bearing capacity of a footing and a simple problem of a retaining wall under active and passive earth pressure conditions.

5.4.1 Bearing Capacity of a Footing

Christian [4] points out that the bearing capacity formulae available in the literature are not exact analytical solutions. Numerous assumptions and simplifications are incorporated in their derivations and solutions are verified by small-scale model tests where the point of failure is difficult to identify. Approximate solutions can also be obtained by limit analysis.

A bearing capacity problem described by Desai [2] of a circular footing having a width of 1.2 m is adopted and solved using the proposed discrete finite element approach incorporating the Mohr-Coulomb elasto-plastic constitutive relation. It is presented in two stages: first, the results of the continuum analysis are compared with the available solutions, second, the failure is permitted allowing the elements to split and move. For the first part, two separate meshes are used as shown in Figure 5.4; one is a fine mesh with 800 elements, the other is a less refined 100-element mesh. Different depth or Y range is selected for both cases, as for the discrete element simulation; the finer mesh captures the failure zone more effectively and is discussed later.

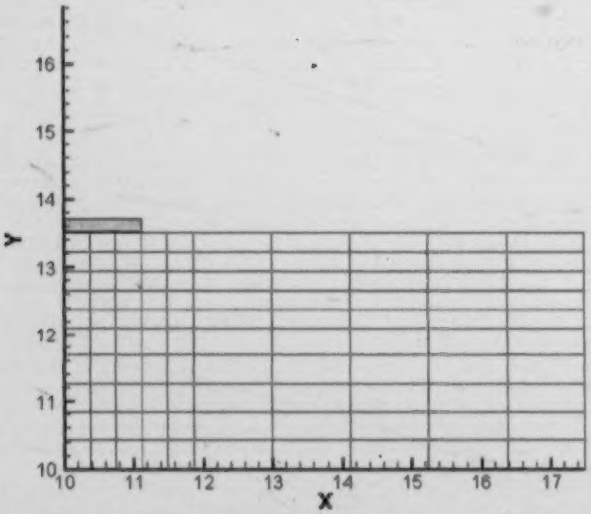

(a)

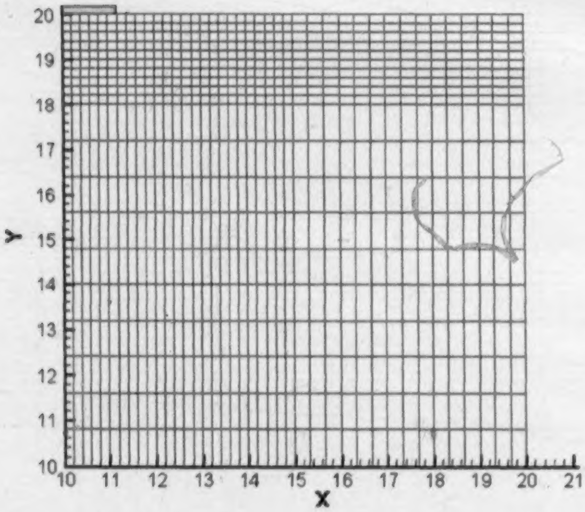
Y
X
10
11
12
13
14
15
16
17
18
19
20
21

(b)

Figure 5.4: (a) 100 element mesh, (b) 800 element mesh

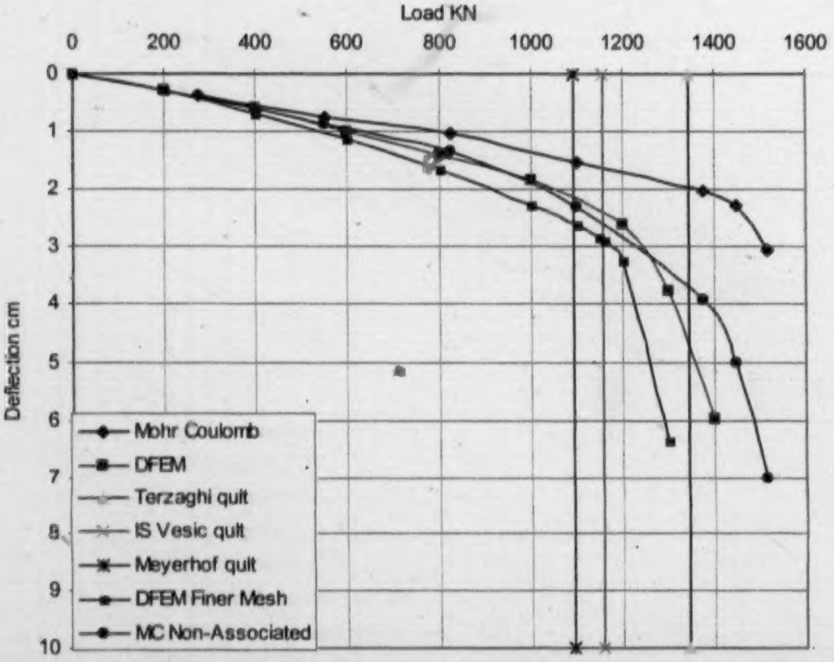

Figure 5.5: Load-Displacement curves for a circular footing

The pressure applied on the footing is converted to equivalent nodal forces. The footing pressures are varied and their corresponding displacements/settlements are plotted until an estimate can be made for the bearing capacity of the footing. The parameters used in the analysis are presented in Table 5.1.

PARAMETER	VALUE
Cohesion (kPa)	69
Angle of Internal Friction	20
Normal Stiffness (kPa)	8000
Tangential Stiffness (kPa)	800
Time Step (sec)	0.0001
Damping Coefficient (sec^{-1})	3

Table 5.1: Parameters used in the analysis of the bearing capacity of a footing

Figure 5.5 shows the predicted load-displacement curves corresponding to the associated Mohr-Coulomb plasticity model. Solution plots are as presented in Desai [2] using associated and non-associated Mohr-Coulomb criteria. The ultimate bearing capacities as estimated from the analytical formulas of Terzhagi, Meyerhoff, and Vesic are plotted with vertical lines. The computed collapse loads are within the range predicted using other methods. Based on the curves, the ultimate/collapse foundation bearing pressure is estimated to be about 1200 kPa. A bearing pressure of 1800 kPa, higher than the ultimate bearing capacity, was used for discrete element analysis and to induce failure.

The displacements of surface nodes under different loading conditions are shown in Figure 5.6. As expected, certain amount of upheaval was obtained outside the limits of the foundation.

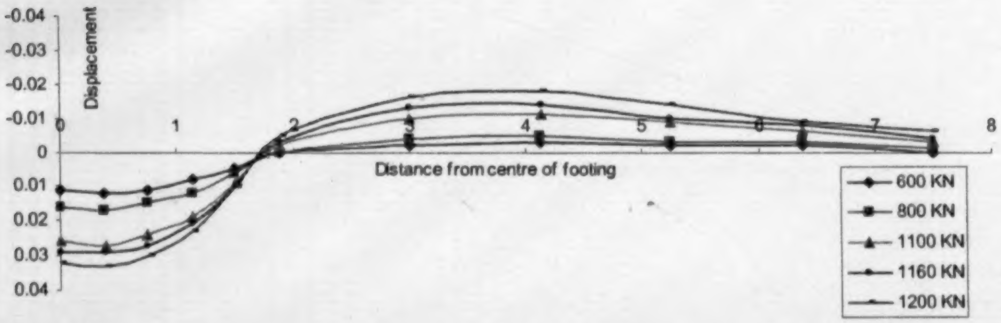

Figure 5.6: Surface displacements for different loading conditions

Figure 5.7 shows the yield pattern and its progression under different loading conditions. Christian [4] showed that a large zone of yielded material occurred at the top of the soil; this was attributed to the analysis method which resulted in a development of tension within this zone. However, in this present analysis, yielding of material was observed near to the ground surface when the external applied foundation pressure was beyond the ultimate bearing capacity of about 1200 kPa.

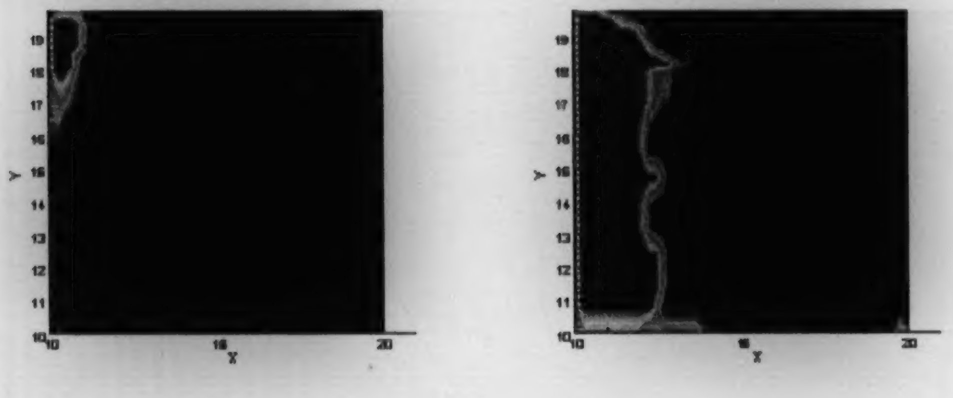

(a) 400 kPa

(b) 800 kPa

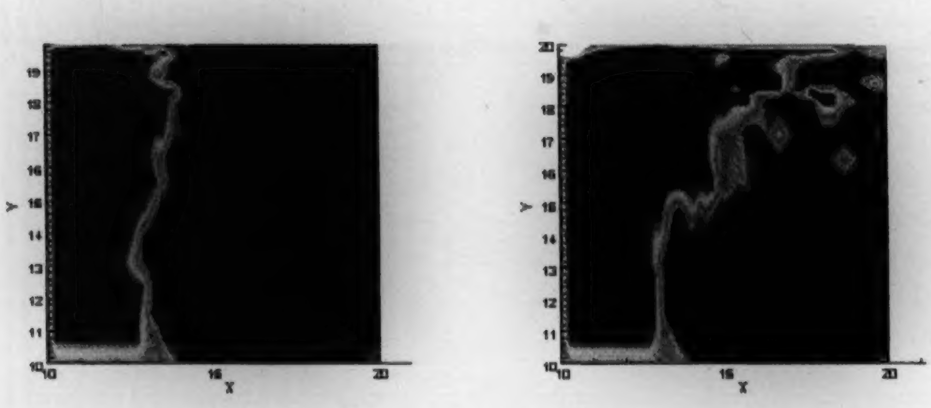

(c) 1200 kPa (d) 1500 kPa

Figure 5.7: Spread of yielded zone under different loading conditions (RED—developed plastic zone; BLUE—no yielding within soil mass)

Results for the second part of the analysis, i.e., the discrete element analysis, are shown in Figure 5.8. In this example, as previously mentioned, the first part of the finite element analysis was carried up to a total time of 2 seconds until equilibrium was obtained, i.e., 20,000 time steps.

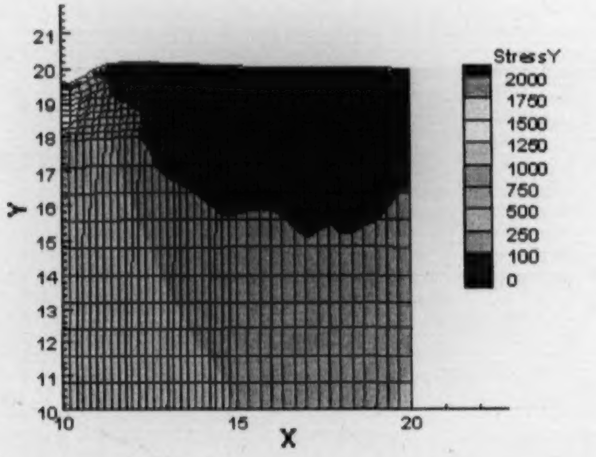

(a) Finite element analysis, time 2.0 seconds

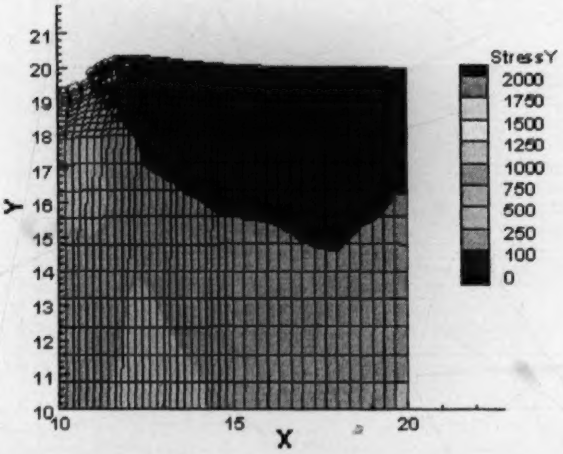

(b) Discrete element analysis; prior to unloading, time 4.5 seconds; failure and split within the elements on the top row can be viewed.

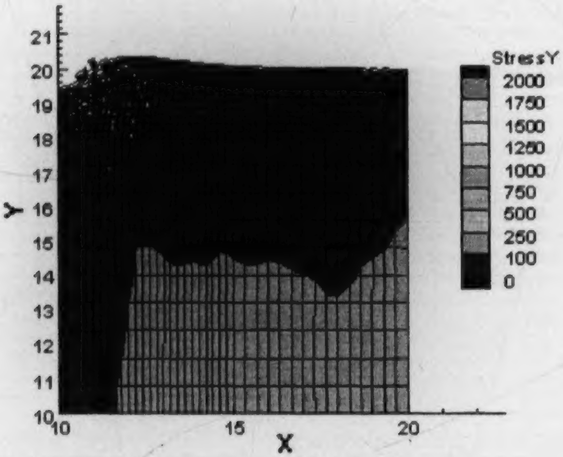

(c) Discrete element analysis after unloading, time 19.0 seconds

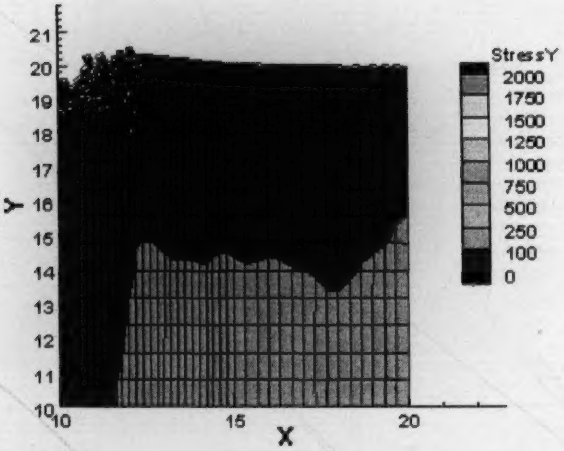

(d) Discrete element analysis, time 34.0 seconds

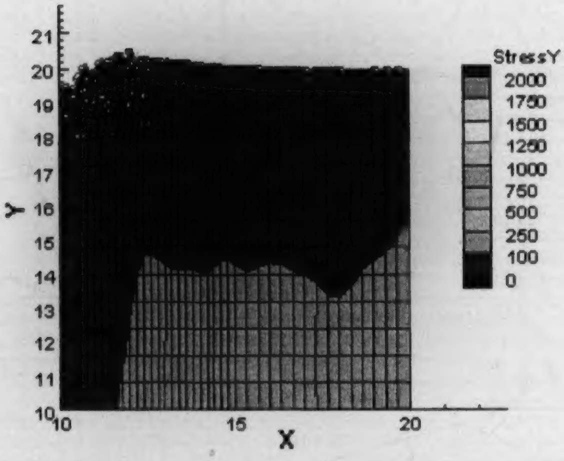

(e) Discrete element analysis, time 49.0 seconds

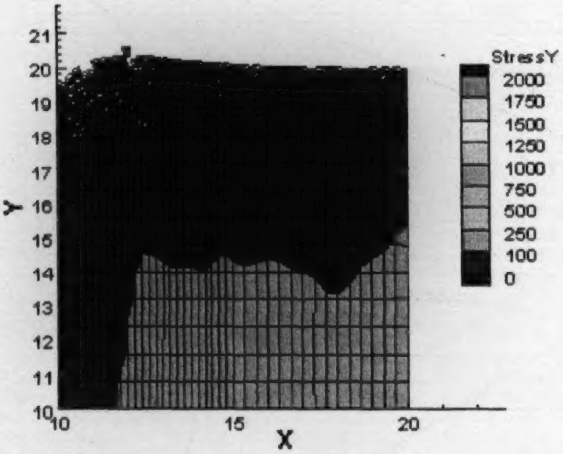

(f) Discrete element analysis, time 56.0 seconds

Figure 5.8: Simulation extracts at different time steps

Based on the failure criteria, the elements are allowed to split and form discrete elements. The mobility of the elements captured at time durations of 1.4, 3.0, 4.0, 5.5, 8.0, 10.5, and 13.5 seconds is shown in Figure 5.8. The simulation movie of the foundation failure is presented in the attached CD in file Example 5.4.1 Foundation Failure. The foundation loads are applied until the total displacement of 0.5 m (assumed) is obtained under the foundation. In real situations, it is expected that as one footing collapses, the structural loads will be distributed over neighboring columns and footings. Thus, in order to capture a realistic simulation, the foundation loads were removed. The analysis was carried out until the elements reached near-equilibrium or were close to stability.

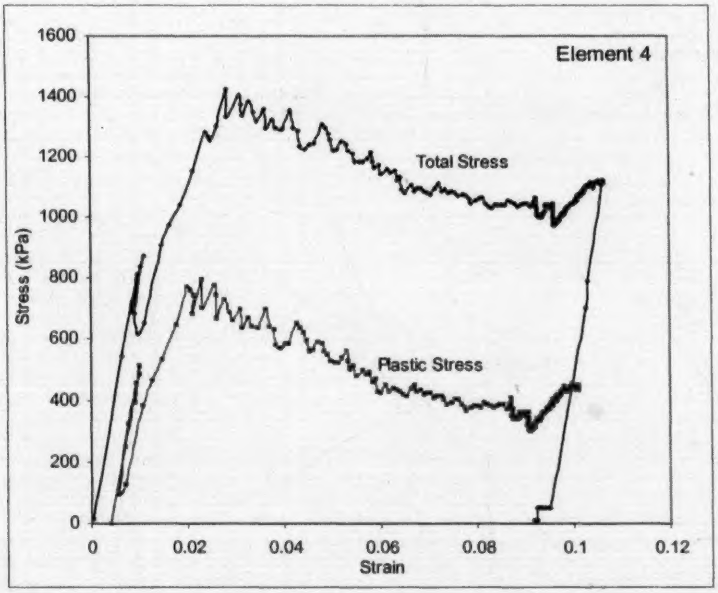

Figure 5.9: Stress-strain variation within an element at the edge of a footing

The computed stress states and their corresponding strain values are plotted in Figures 5.9 and 5.10 for two elements located at the edge of the footing and under the footing at 1.0 m depth, respectively. Curves for total stresses and plastic stresses developed within the elements are shown up to about 4 seconds of simulation. Since the plastic stress-strain curve is plotted on an abscissa of total strain, it is viewed at an offset of about 0.4 percent strain, to account for the initial elastic strain.

Element 4 is located at the edge of the foundation where splitting of the elements loaded with foundation loads occurs and unloading follows. The developed stresses within element 4 dropped to lower values and equilibrated to a stress state of 2.88 kPa (not shown, as this state is reached later), equivalent to the self-weight of the element. Element 77, at a depth of about 0.8 m below the footing, did not feel the unloading instantly, as gradual unloading of the foundation load was applied over a number of time steps. As movement of the element continues, it is interpreted that tension might have developed (represented on the plot with stress values of zero), followed by development of contacts and stresses within the element before it tends to equilibrate toward a stress of about 52.5 kPa (not shown). It can be inferred from Figures 5.9 and 5.10 that for the element directly below the footing, the plastic stress component of the total stress was more than that for the element at the edge of the footing.

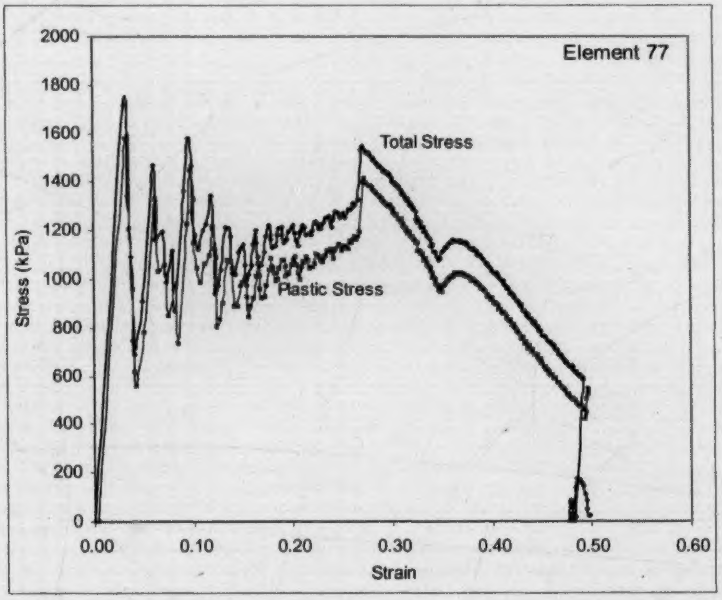

Figure 5.10: Stress-strain variation within an element at 0.8 m depth below a footing

The setup of the computational scheme is such that plastic stresses and strains are computed only if yielding of the element occurs. The check for yielding was done after every 100 time steps and the output was generated. If the stress state is within the yield surface, the calculations would not be done for the plastic stress, thus its value would remain unchanged, and at any stage (as can be inferred from the Figures 5.9 and 5.10), if complete elastic unloading occurs the computed plastic stresses would remain unchanged.

5.4.2 Retaining Wall

Further investigation of the elasto-plastic model was carried out by solving the example of a retaining wall under active and passive earth pressure states. A 520 element mesh was used in the analysis (Figure 5.11).

A 10 m high retaining wall supporting sand, a cohesionless material, as the backfill, is considered. The parameters adopted for the analysis are: modulus of elasticity, 70 MPa; Poisson's ratio, 0.35; unit weight, 16.5 kN/m^3; angle of internal friction, 30°; cohesion, 0 kPa; time step for finite element computation, 0.001 seconds; and damping coefficient, 3 per second.

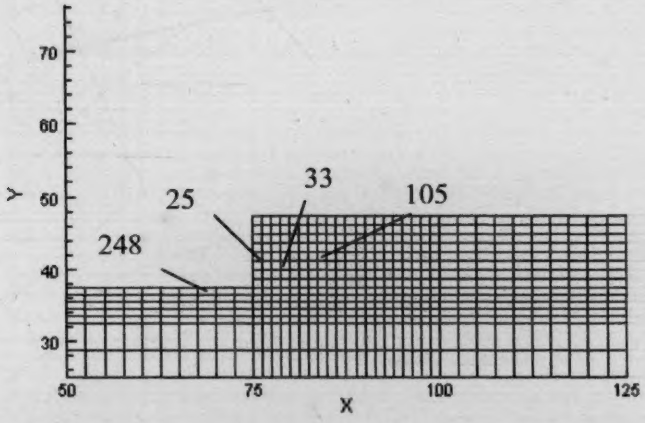

Figure 5.11: Mesh comprised of 520 elements used in retaining wall analysis

Based on Rankine's theory, the active earth pressure coefficient was equal to 0.33 for a 30° angle of internal friction. For a 10 m high retaining wall, the total active earth pressure was 275 kN while the passive earth pressure coefficient was 3, with a total passive earth pressure of 2475 kN acting behind the wall.

Parameters used for discrete element analysis of active and passive earth pressures examples are presented in Table 5.2.

PARAMETER	CASE	
	ACTIVE EARTH PRESSURE	PASSIVE EARTH PRESSURE
Normal Stiffness (kPa)	3000	3000
Tangential Stiffness (kPa)	300	300
Damping Coefficient, α (sec^{-1})	3	5
Time step (sec)	0.0008	0.0009

Table 5.2: Parameters used for discrete element analysis of active and passive earth pressures

The total earth pressures generated behind the retaining wall were computed using two different methods. In the first procedure the stress states of the elements immediately behind the wall were integrated over the height of the wall to obtain the total pressure on the wall. The second method used the element nodal forces to obtain the total pressure on the wall. In both procedures, for varying amounts of displacements, wall earth pressures were calculated and plotted to estimate active and the passive states. Figure 5.12 represents the different load displacement cases and convergence toward the values estimated from analytical formulas.

The available literature on earth pressure theories indicates that for the active stress state, as the wall moves away from the backfill, a portion of the backfill located immediately behind the wall breaks away from the rest of the soil mass. This wedge moves downward and outward for active cases and upward and inward for passive cases. Under these conditions the lateral earth pressure exerted on the wall reaches minimum and maximum values, respectively. Soil failure occurs due to a decrease in lateral stress for active cases and an increase in lateral stress for passive cases. The horizontal strain required to reach an active state of plastic equilibrium is very small. It is inferred based on tri-axial shear test results that a horizontal strain of about 0.5% is required for dense sands. However, a much larger horizontal strain of 5% is required to attain a maximum value of passive earth pressure and the magnitude of strains required in the field may be somewhat different. As presented in Figure 5.12, for the active state a horizontal strain of nearly 0.3% was required to develop the maximum amount of active earth pressure for a 10 m high retaining wall, and a horizontal strain of 1 to 1.5% was required to develop the maximum amount of passive earth pressure for the same wall.

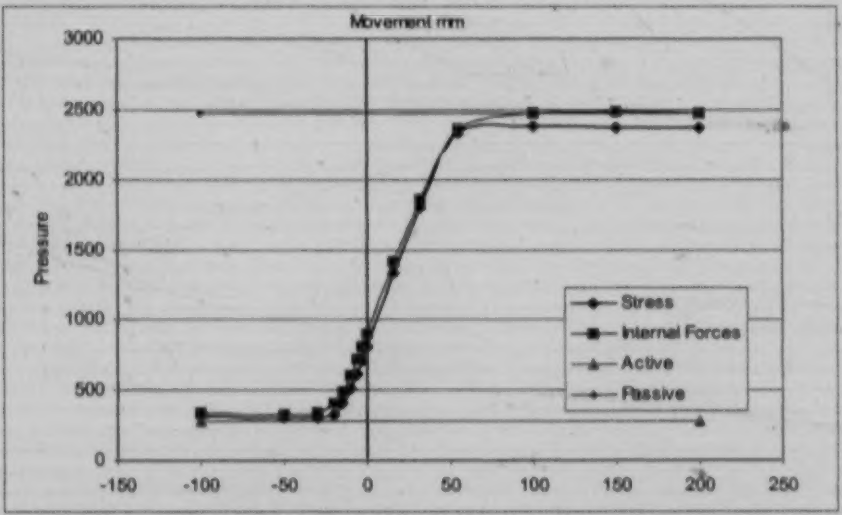

Figure 5.12: Developed pressures for corresponding displacements computed from nodal forces and element stresses.

These two conditions of failure are referred to as the extreme conditions of plastic equilibrium. In intermediate states when the soil is not at plastic equilibrium, it is said to be in *elastic* equilibrium. The developed lateral active and passive earth pressure coefficients are plotted against the corresponding wall translation in

Figure 5.13; the values converge toward the coefficients estimated by the conventional Rankine theory.

The degree of convergence and the accuracy of the method can be judged from Figure 5.14 where the horizontal and the vertical stress states behind the retaining wall are plotted as displacements are applied to the wall.

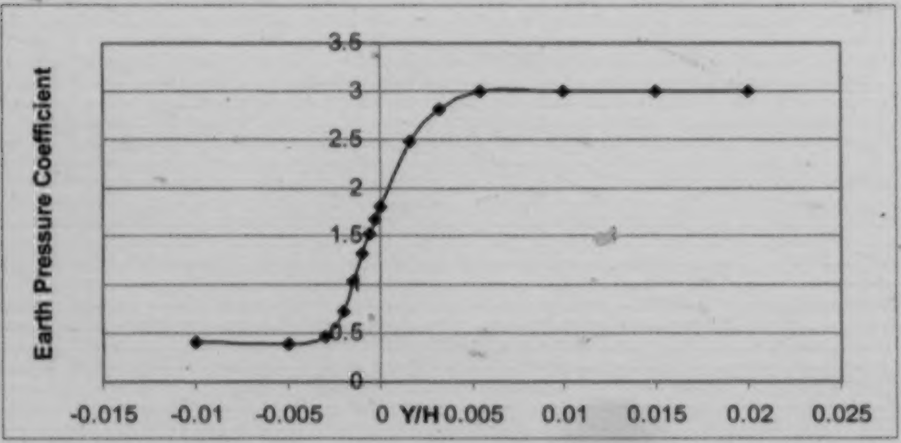

Figure 5.13: Translation of a wall and corresponding earth pressure coefficients

The failure and mobility of elements versus the vertical stress states for different configurations for the active earth pressure case are presented in Figure 5.15. This figure shows that the distribution of stress states within soil (or among the elements) is quite complex. The approach developed here can be used to capture the behaviour of soil mobility. For the simulation, it was assumed that the retaining wall had collapsed; this allowed the elements behind the retaining wall to split and displace. As observed, failure occurred below the toe and extended into the base material. The total run time for this example was about 7 hours on an Intel Centrino processor at 1.88 GHz.

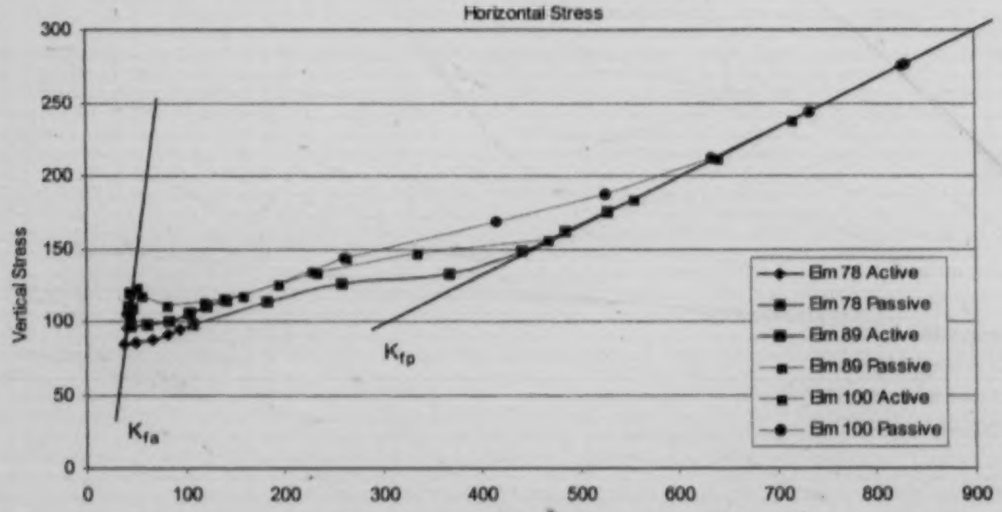

Figure 5.14: Degree of convergence in terms of horizontal and vertical stresses behind a retaining wall.

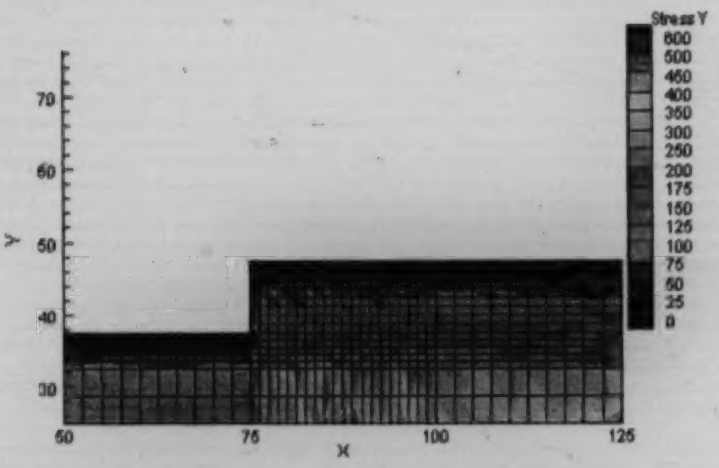

(a) End of finite element analysis (time = 2 secs)

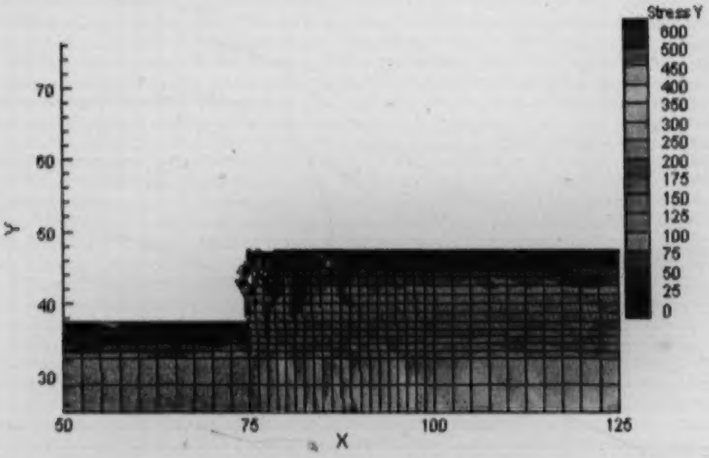

(b) Time 49 seconds

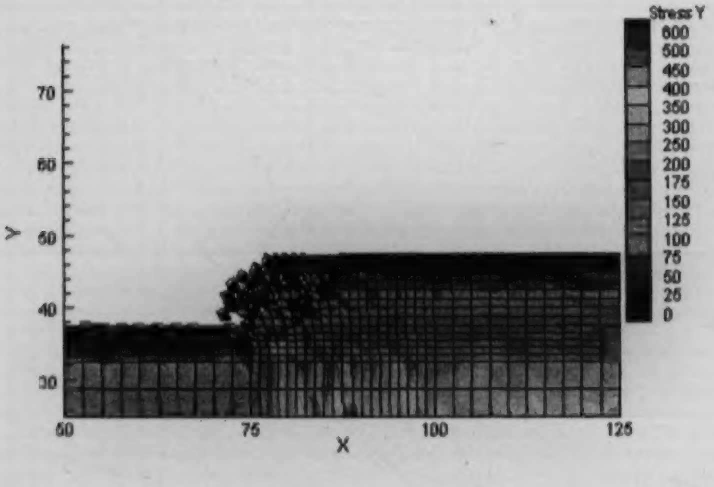

(c) Time 140 seconds

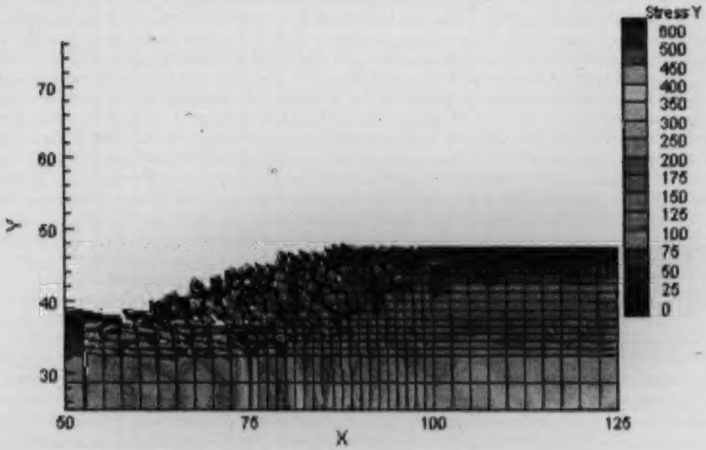

(d) Time 405 seconds

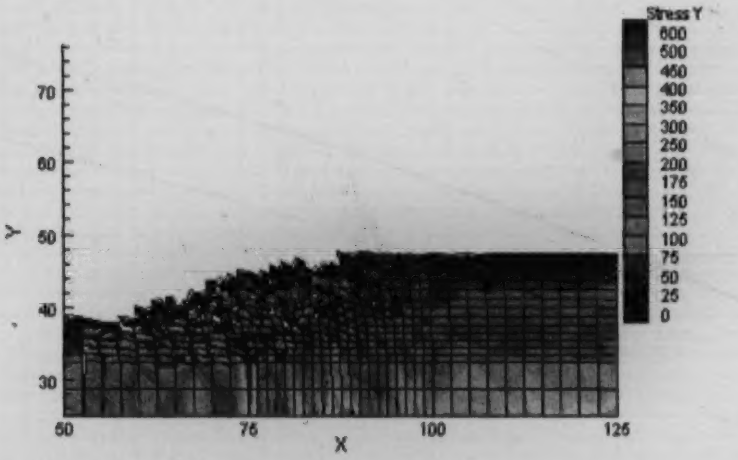

(e) Time 542 seconds

Figure 5.15: Failure for active condition—Simulation with 520 elements

The variation of total stresses and strains over different time steps for finite element analysis and discrete element analysis is shown in Figure 5.16. The plots represent conditions for element 25 behind the retaining wall and for element 248 at the ground surface elevation in front of the retaining wall. It can be inferred from these plots that elements 25 and 248 develop compressive stresses and lose and re-establish contacts. Element 248 shows a strain reversal wherein the element tends to deform along a different direction; this might have occurred during new contact formation.

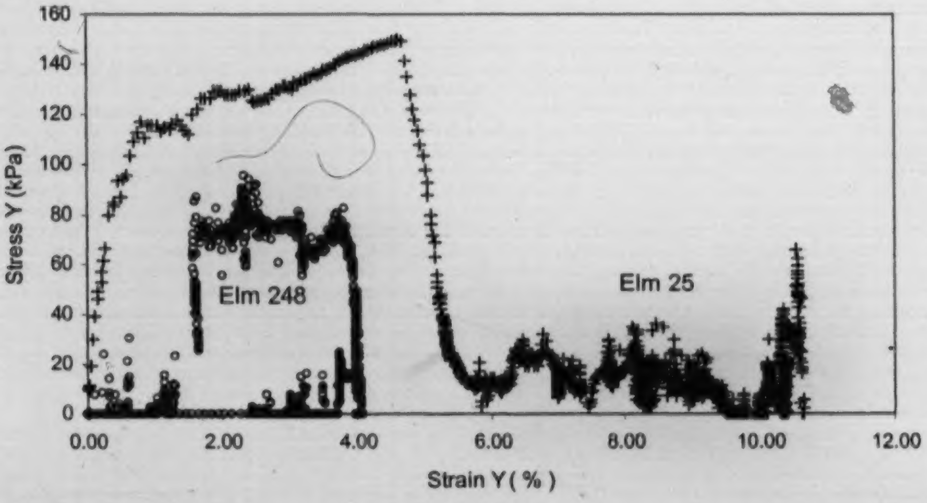

Figure 5.16: Stress-strain plots for elements 25 and 248 during continuum and discontinuum analyses for the active earth pressure case

The same mesh comprising 520 elements was used for the passive earth pressure case. However, the simulation contained another 8 elements in the front acting as a retaining wall to which the prescribed displacement of about 0.3 m was applied to induce failure. These elements were not removed so that lateral strain to the elements representing the backfill is maintained.

The elements that yielded in the active and passive earth pressure cases are shown in Figure 5.17. The computational scheme proceeded in two stages. In the first stage, gravity was switched on and deflections, yielded elements, and the plastic zone were reset to initial values. The prescribed displacements were then applied to the nodes of the presumed retaining wall. The yielding of the elements is recalculated at each Gauss point and the values at the shared nodes are computed as a summation of the values from the neighboring Gauss point. The elements shown in red and yellow are in yielded states.

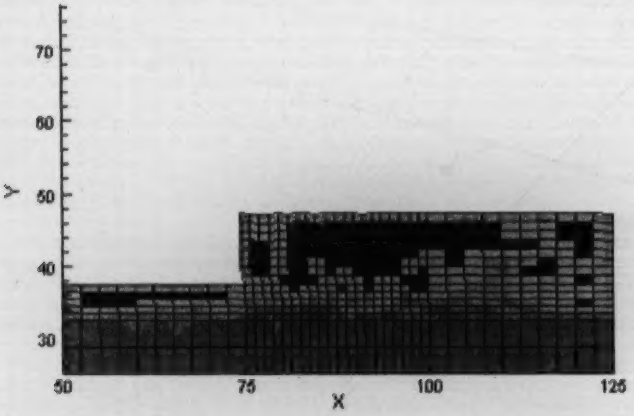

(a) Active earth pressure

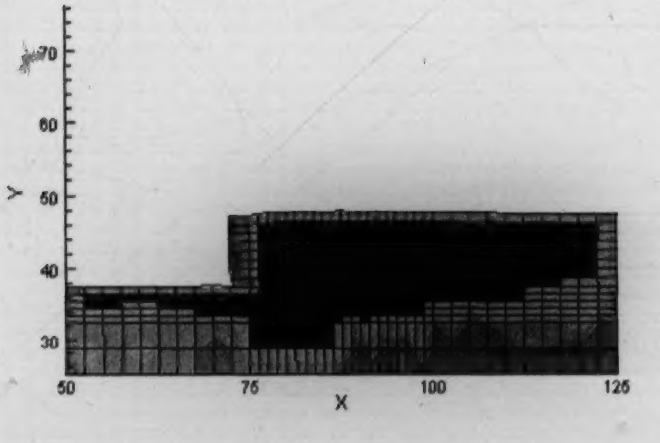

(b) Passive earth pressure

Figure 5.17: Developed plastic zones and yielded elements (RED—Yielded Elements)

Figure 5.18 shows the stress-strain plot in the vertical direction for elements behind the retaining wall. The computation is plotted only up to 5% strain to develop a sense of the variation of stress and strains within the elements. Element 33, just behind the wall, undergoes many loading and unloading phases during the initial state of analysis while element 105, far behind the wall, develops an initial smooth stress state variation. The loading and unloading of the elements occurs whenever new contacts are formed and old contacts are lost. The dynamic nature of the developed scheme causes oscillations in the stress-strain values which are computed based on the rotations and translations generated. The principal stress and strain values may or may not be coincidental.

The output presented was generated at an interval of 100 time steps and after the check for plasticity had been performed. Stress varies in the form of oscillations within the elements over the time steps; when the check for plasticity is performed at the chosen interval of time steps, the stress states are modified to satisfy the yield states.

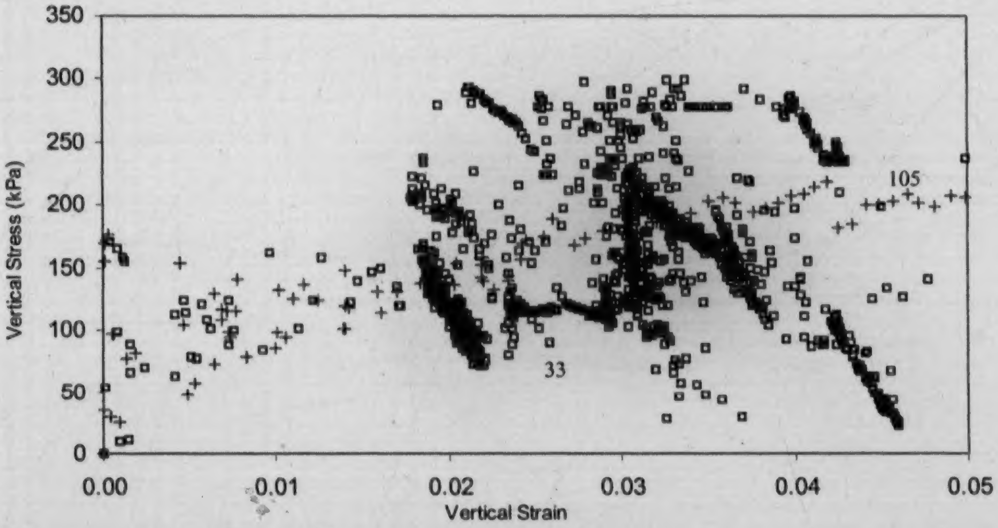

Figure 5.18: Stress-strain plots during finite and discrete analyses for elements 33 and 105

The objective of the simulations was to capture the development of stress and strain states as the elements split, mobilize, and establish contacts. The computational schemes were reliable and could be used for further analysis.

The mobility of the elements and the vertical stress states are presented in Figure 5.19. At the end of the finite element analysis, a time step increment of 0.0009 seconds was used and the analysis was carried out for 800,000 time steps. The stress states show highly compressed zones behind the retaining wall close to the base. As the elements gather motion over time durations of 139 and 274 seconds, few elements appear to be in a state of upheaval. A portion of the soil mass can be viewed as falling over the retaining wall for the configuration at 405 seconds. This movement of discrete elements is anticipated to continue and cause further mobility of the elements. The assembly tends to reach toward a state of equilibrium at about 632 seconds in terms of the distribution and motion of elements and the variation of stress states.

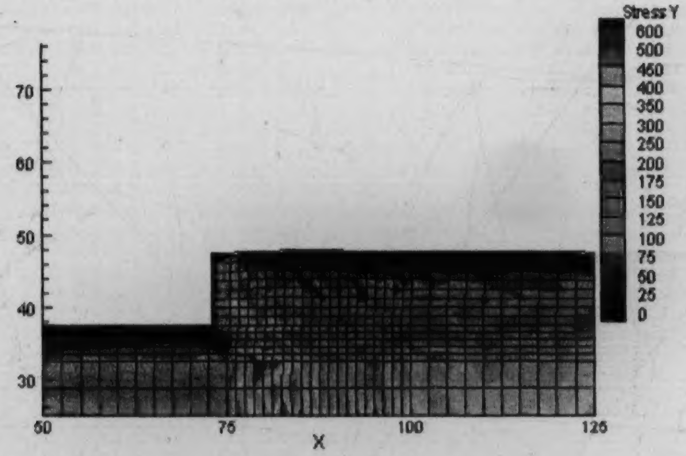

(a) At the end of finite element analysis, time 2 seconds

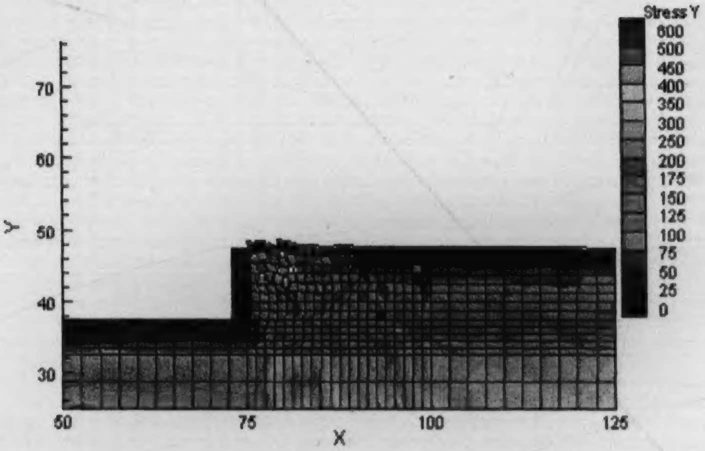

(b) Discrete analysis, time 139 seconds

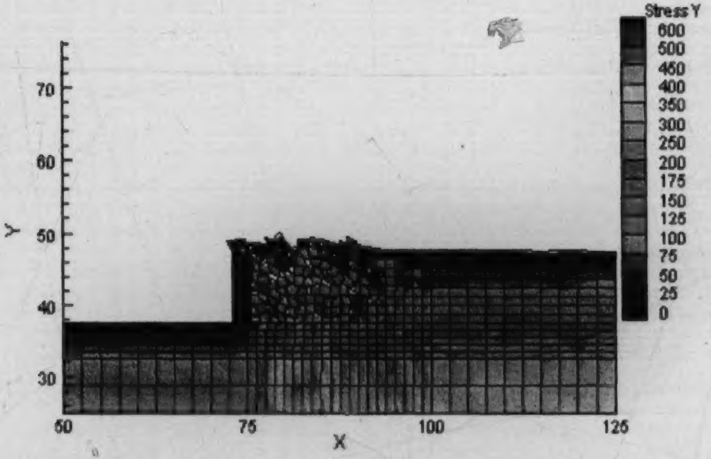

(c) Time 274 seconds

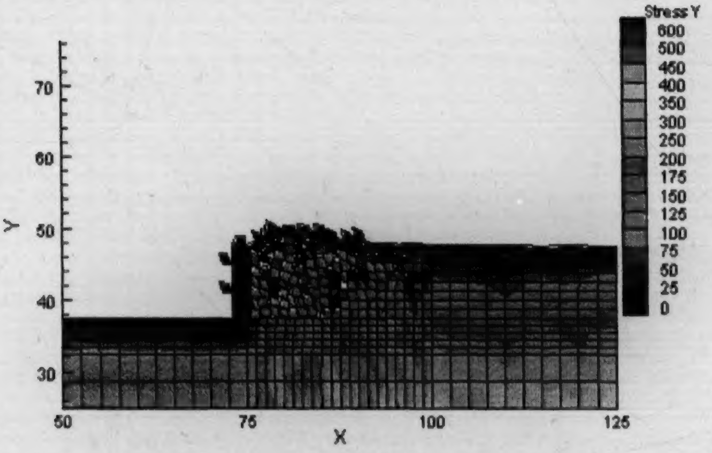

(d) Time 405 seconds

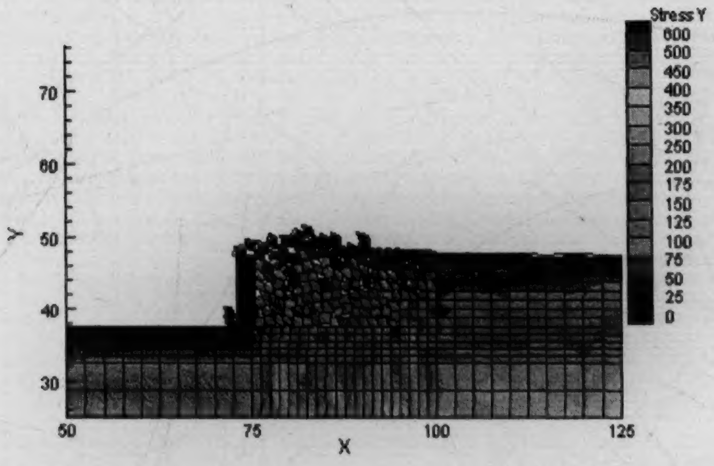

(e) Time 632 seconds

Figure 5.19: Mobility of the elements; Passive earth pressure

The total run time for the simulation was 8 hours using an Intel Centrino 1.88 GHz Processor on a Hewlett Packard Pavilion laptop.

5.5 CONCLUDING REMARKS

The general formulation and material model for the elasto-plastic analysis is introduced for the finite-discrete element analysis attempted in this research. A routine for the plasticity and yield criteria check is developed and presented for the dynamic analysis over numerous time steps. This technique was applied to conventional geotechnical applications of foundation bearing capacity and retaining wall earth pressure problems. The calculations and simulations were further carried out with discrete element analysis and it was shown that stress-strain computations can be performed to acceptable levels of accuracy and convergence by this method.

BIBLOGRAPHY

1. Potts, D. M., and Zdravkovic, L., *Finite element analysis in geo-technical engineering—Theory*. 1999, London, U.K.: Thomas Telford Publishing. 440.
2. Desai, C. S., and Siriwardane, H. J., *Constitutive laws for engineering materials*. 1984: Prentice Hall Inc. 468.
3. Cook, R. D., Malkus, D. S., and Plesha, M. E., Concepts and applications of finite element analysis. 3rd edition. 1989. 630.
4. Christian, J. T., Hagmanni, A. J., and Marr, W. A., *Incremental plasticity analysis of frictional soils*. International Journal for Numerical and Analytical Methods in Geomechanics, 1977. 1: p. 343–375.
5. Sawada, S., and Kishino, Y., *Discrete modeling of granular materials*. In Proceedings of the International Symposium on Deformation and Progressive Failure in Geomechanics. 4–7 October 1997. Nagoya, Japan.
6. Itasca Consulting Group, I., PFC^{2D}, *Particle flow code in two dimensions*, Version 1.1. 1995: Minneapolis, Minnesota: ICG.
7. Potyondy, D. O., Cundall, P. A., and Lee, C. A., *Modelling rock using bonded assemblies of circular particles*. Rock Mechanics, Eds. Aubertin, Hassani and Mitri, 1996: p. 1937–1944.
8. Dobry, R., and Ng, T., *Discrete modeling of stress-strain behaviour of granular media at small and large strains*. Engineering Computations, 1992. 9: p. 129–143.
9. Stead, D., Eberhardt, E., Coggan, J., and Benko, B., *Advanced numerical techniques in rock slope stability analysis—Applications and limitations*.

In Proceedings of Landslides—Causes, Impacts and Countermeasures. 17–21 June 2001. Davos, Switzerland.

10. Munjiza, A., Owen, D. R. J., and Bicanic, N., *A combined finite-discrete element method in transient dynamics of fracturing solids*. Engineering Computations, 1995. 12: p. 145–174.
11. Barbosa, R., *Discrete element models for granular materials and rock masses in civil engineering*, Ph.D. thesis, 1990, University of Illinois: Urbana-Champaign, Illinois USA. p. 140.
12. Chan, D. H., *Finite element analysis of strain softening material*. 1985, Ph.D. thesis, University of Alberta, Edmonton, AB. p. 345.
13. Chan, D. H., *Course notes of numerical methods in engineering*, CIVE 799 notes, Department of Civil Engineering, University of Alberta, Edmonton, AB 2003.

6

CARSINGTON DAM—A CASE STUDY

Lambe [1] in the thirteenth Rankine lecture, specified five different classes of prediction: A, B, B1, C, and C1. It was also indicated that most of the geotechnical literature contained cases and analyses related to C1 predictions and that grade C predictions were autopsies. These classes are shown below:

Grade of Prediction	Time of Prediction	Results at Time of Prediction
A	Before event	—
B	During event	Not known
B1	During event	Known
C	After event	Not known
C1	After event	Known

A slightly different form of defining the gradation was presented by Kennard [2], so that various cases could fit perfectly and to avoid the connotation that a grade A prediction was perfect and accurate. The classes were in the following simpler form:

Grade of Prediction	Time of Prediction
I	Before the event
II	Before the event, so that outcome is known
III	After the event, using information made available after the event

Published Carsington Dam predictions fall in the class C1 or grade III predictions.

6.1 INTRODUCTION

Carsington Dam is situated on Scow Brook near the village of Hognaston in Derbyshire, England. The earth dam had a design height of 35 m, was 1200 m in length, and was comprised of about 2 Mm^3 of clay and mudstone fill. The dam was managed by the British Regional Water Authority and constructed by Shephard Hill & Company Limited from 1981 to 1984, Kennard [2], to increase sources of potable water. Failure of the dam occurred on 05 June 1984 before the full dam height could be achieved, with a massive slide in the upstream direction. The slide was 30 m deep and 500 m long. All installed instruments were read up to the moment of collapse.

The initial report of the investigation, studying the causes of failure, was issued by the Severn Trent Water Authority as "Carsington Dam—The Mechanism of Failure" [3]. It was concluded that the main cause of failure at the initial slip was the foundation yellow clay, which had been weakened by pre-existing shear surfaces. This was coupled with a small amount of progressive failure accounting for about a 10% reduction in the safety factor. Finite element analyses were carried out and documented in the report at two cross-sections to examine and quantify the role played by progressive failure in reducing the average operational strength below the peak strength of the outer yellow clay and Zone II fill. More investigations were later carried out by various authors: Potts [4], Rowe [5], Chen [6], and Skempton [7]. As reported by Rowe [5], failure on the north side commenced on May 21, 1984 and toe displacements and core strains led to the center. Shear planes were developed into the boot of the core and the foundation yellow clay reached a critical state, resulting in a failure of the upstream slope.

The failure of Carsington Dam during construction is here analyzed using the discrete-finite element method presented in earlier chapters. First, the Carsington Dam structure, materials, and the geology of the site will be introduced, followed by the results and discussions of the analysis and a comparison with the findings of previous studies.

6.2 DETAILS OF CARSINGTON DAM

6.2.1 Geology and Site Description

As reported by Skempton [3], the Carsington Dam (Figure 6.1) was being constructed in a broad valley comprised primarily of mudstone belonging to the Namurian Series of the Upper Carboniferous age. The valley was enlarged prior to the last glaciation (Devensian) that had removed most of the glacial deposits present in the valley leaving weathered mudstone. The higher ground surrounding the site was thus covered with boulder clay and glacial gravel, remnants of the penultimate glaciation (Wolstonian).

The mudstones were grey to dark grey or almost black in colour and were weakly calcareous and thinly bedded. Unweathered or slightly weathered mudstone was found in borings at depths greater than about 10 to 15 m below ground level. At shallower depths, the mudstone was brecciated and weathered. Based on the changes made to the fabric and constitution by the weathering, four different types of mudstone were identified: blocky mudstone, brecciated mudstone, dark grey clay, and yellow clay. The material most concerned at this dam site, yellow clay, was the end-product of a long weathering process occurring at depths of about 1 to 2 m below the ground surface. The clay had relatively high moisture content, a high plasticity index, a high clay fraction, and was yellow-brown to mottled grey in colour.

The valley slopes were mantled by the 'head'—a yellow brown mottled clay and topsoil containing scattered angular sandstone fragments and rounded quartz pebbles. This solifluction deposit of clay moved downhill by the freeze-thaw process and created slopes stable for a temperate climate.

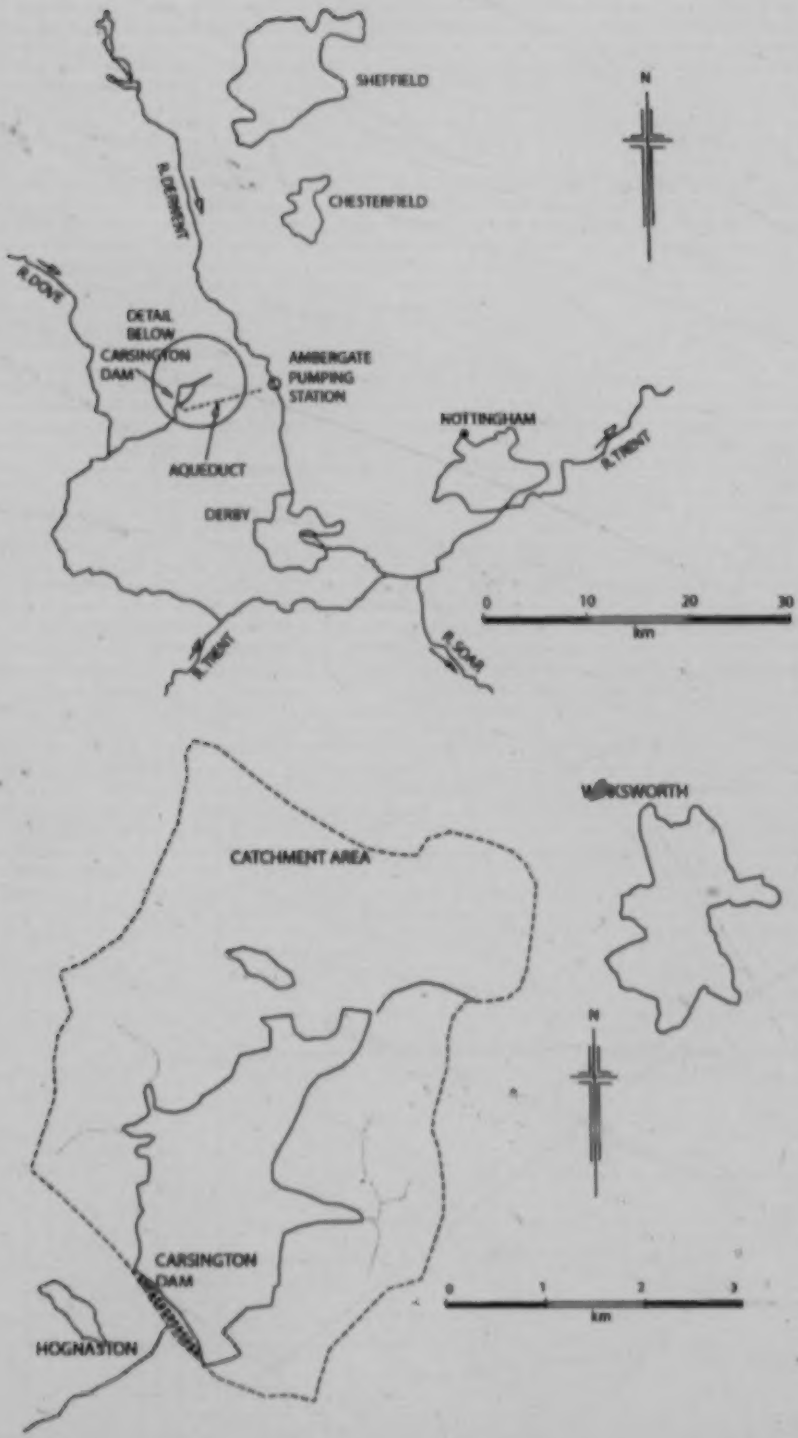
SHEFFIELD
CHESTERFIELD
N
R. DERWENT
R. DOVE
DETAIL BELOW
CARSINGTON DAM
AMBERGATE PUMPING STATION
NOTTINGHAM
R. TRENT
AQUEDUCT
DERBY
0
10
20
30
km
R. TRENT
R. SOAR
W[illegible]KSWORTH
CATCHMENT AREA
N
CARSINGTON DAM
HOGNASTON
0
1
2
3
km

Figure 6.1: Location plans for the Carsington Dam, Skempton [3]

Two different layers were recognized to form within the 'head.' The upper soil was termed subsoil and was silty and had a lower plasticity index relative to the liquid limit. The lower soil was yellow brown and light grey mottled clay and slightly sandy. The Scow Brook flood plain deposit had a maximum thickness of 4 m and consisted of brown-grey sandy clay with occasional gravel.

Professor J. G. Anderson's overview included in the Severn Trent Water Authority report stated that the oxidation of sulphide bearing mudstones had caused weakening and continuous loss of volume. Based on a seismic event 50 km S. E. of Carsington on May 30, 1984, he estimated that the Carsington Dam site lies close to the center of a historically seismic active region.

6.2.2 Construction of the Carsington Dam

The Carsington Dam was an earth embankment with a rolled clay core supported by shoulders of mudstone. The embankment extended for some 1200 meters and had a surface of 1 to 3 upstream and 1 to 2.5 downstream but with slopes modified adjacent to crest and landscaping areas. As reported by Skempton [3], the longitudinal profile of the dam is shown in Figure 6.2 and the longitudinal section of the dam is shown in Figure 6.3.

The foundation of the dam was excavated shallowly with only the topsoil and softer clays being removed from the embankment area. Unfortunately, the yellow clay was not removed completely at the critical section corresponding to chainage (Ch.) 700 to 750 and constituted a weak layer with pre-sheared materials. At the section for the clay core extending upstream like an apron, a key trench was excavated 3 m lower than the level of the general foundation. The foundation below the key trench was stage grouted with the outer rows relatively shallower than the main curtain holes which were sunk up to the same depth as the reservoir. In order to control uplift pressures through the foundation, a series of relief wells set at 10 m to 30 m spacing and discharging into a toe drain were incorporated.

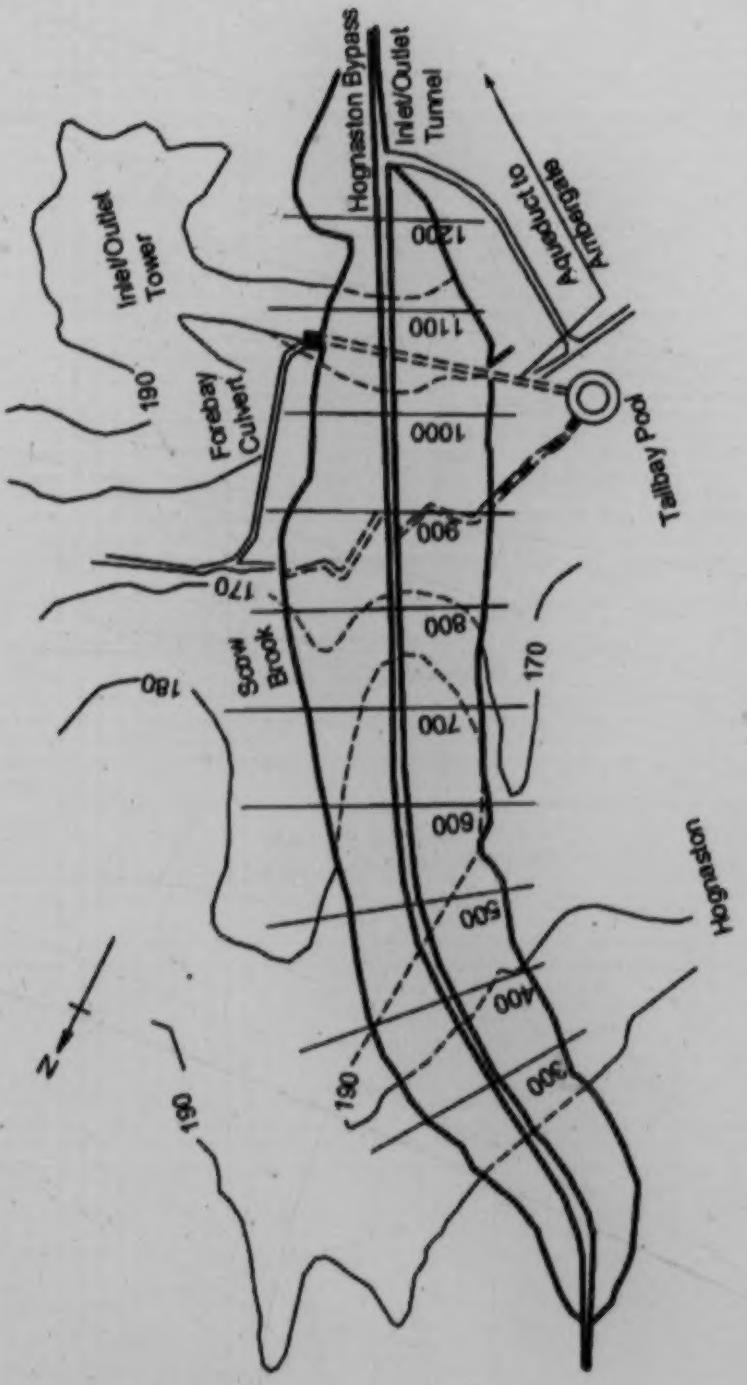
Hognaston Bypass
Inlet/Outlet Tunnel
Aqueduct to Ambergate
Inlet/Outlet Tower
1200
1100
190
Forebay Culvert
1000
Tailbay Pool
900
170
800
Scow Brook
180
170
700
600
500
Hognaston
400
N
190
300
190

Figure 6.2: Plan of the Carsington Dam, Chen [8]

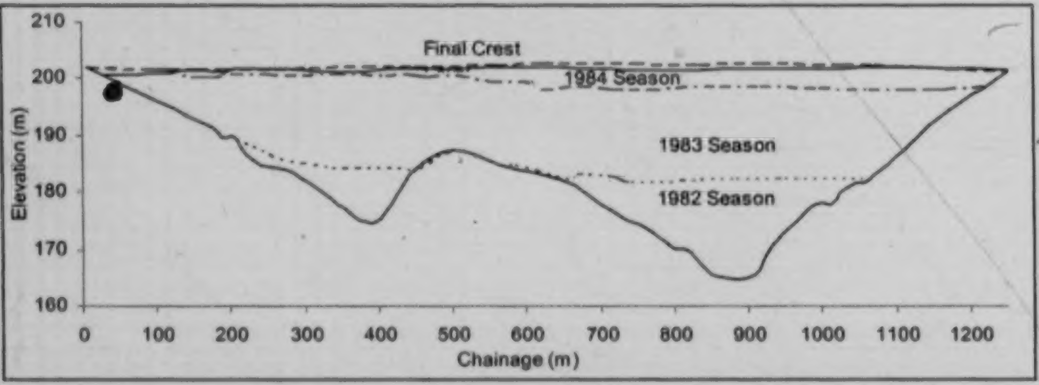

Figure 6.3: Longitudinal profile of the Carsington Dam, Chen [8]

Locally available materials were used in the construction of the dam embankment. A mixture of yellow clay and dark grey clay was used to construct the core and stones greater than 100 mm were removed. The required shear strength of the recovered samples was within 50 to 130 kPa with 80% between 60 to 120 kPa. This required shear strength could be achieved at 95% of Proctor optimum density. Mudstone was selected for the inner shell and was placed in 300 mm thick compacted layers. Relatively unweathered mudstone excavated from deeper depths was used in the outer shell and compacted in 300 mm thick layers with 6 passes using a 7 tonne grid roller. Stones were imported for the construction of drainage layers, beaching, and riprap protection of the upstream face.

After the tender was allocated in May 1981, the following work was completed: preliminary work, pressure grouting in the foundation below the key trench, driving a drainage tunnel, and excavating for an inlet/outlet tower. Diversion of Scow Brook through the diversion tunnel was achieved in July 1982, then embankment work continued through the remainder of 1982 up to Elevation (Elv.) 184 through Ch. 250 to Ch. 450 and up to Elv. 182 from Ch. 650 to Ch. 1000.

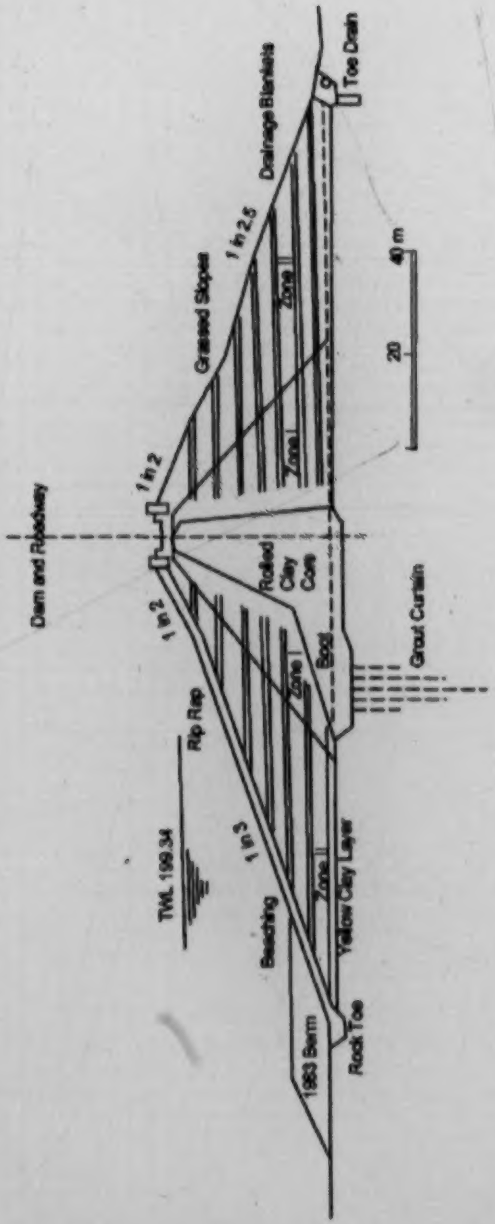
Toe Drain
Drainage Blankets
1 in 2.5
40 m
20
Grassed Slopes
Zone II
Zone I
1 in 2
Dam and Roadway
Rolled Clay Core
Grout Curtain
1 in 2
Boot
Zone I
Rip Rap
TWL 199.34
1 in 3
Zone II
Yellow Clay Layer
Beaching
1983 Berm
Rock Toe

Figure 6.4: Typical cross-section of the Carsington Dam, Chen [8]

The construction work continued rapidly until in July 1983. At elevation 190 m the piezometer readings in the core fill material indicated values high enough to cause concern over the dam's stability. A berm 6 m high and around 240 m long was constructed to a maximum elevation of 175.6 m and the contractor was then allowed to continue with the embankment construction at a controlled rate. In September 1983 earthfill operations were ceased at approximate Elv. 197 m between Ch. 650 and Ch. 1150. Additional filling was allowed to continue to full height north of Ch. 650 to enable work on the crest. The work continued with the remaining earth fill in the center of the dam in early April 1984 at a controlled rise of 0.6 m per week. The final section of the Carsington Dam embankment is shown in Figure 6.4.

6.2.3 Material Properties

6.2.3.1 Yellow Clay

As mentioned in Section 6.2.1, yellow clay is the end-product of a long weathering process occurring at depths of about 1 to 2 m below the ground surface. It is comprised of soft-to-firm yellow-brown and light grey mottled clay. Only a small difference between these two types of clay was found in a large number of tests. Mean values of the index properties reported by Skempton [3] for yellow clay are shown in Table 6.1 and are indicative of inorganic clay with a high plasticity and a moderate amount of kaolinite in the clay fraction. The shear strength parameters of intact yellow clay are shown in Table 6.2.

Test results shown in Figure 6.5 and reported by Skempton [3], show no significant difference between types of test or size of samples. Shear box tests performed on yellow clay samples with a polished and stratified slip surface placed exactly in the separation plane. The relationship between the mobilized strain and the reduction strengths are not well defined for the soil and, as reported, the horizontal pre-existing shear surfaces develop peak strength at about 40 to 50 mm displacements (4% to 5% shear strain) and subsequently fail to the residual after a small further displacement, as shown in Figure 6.6.

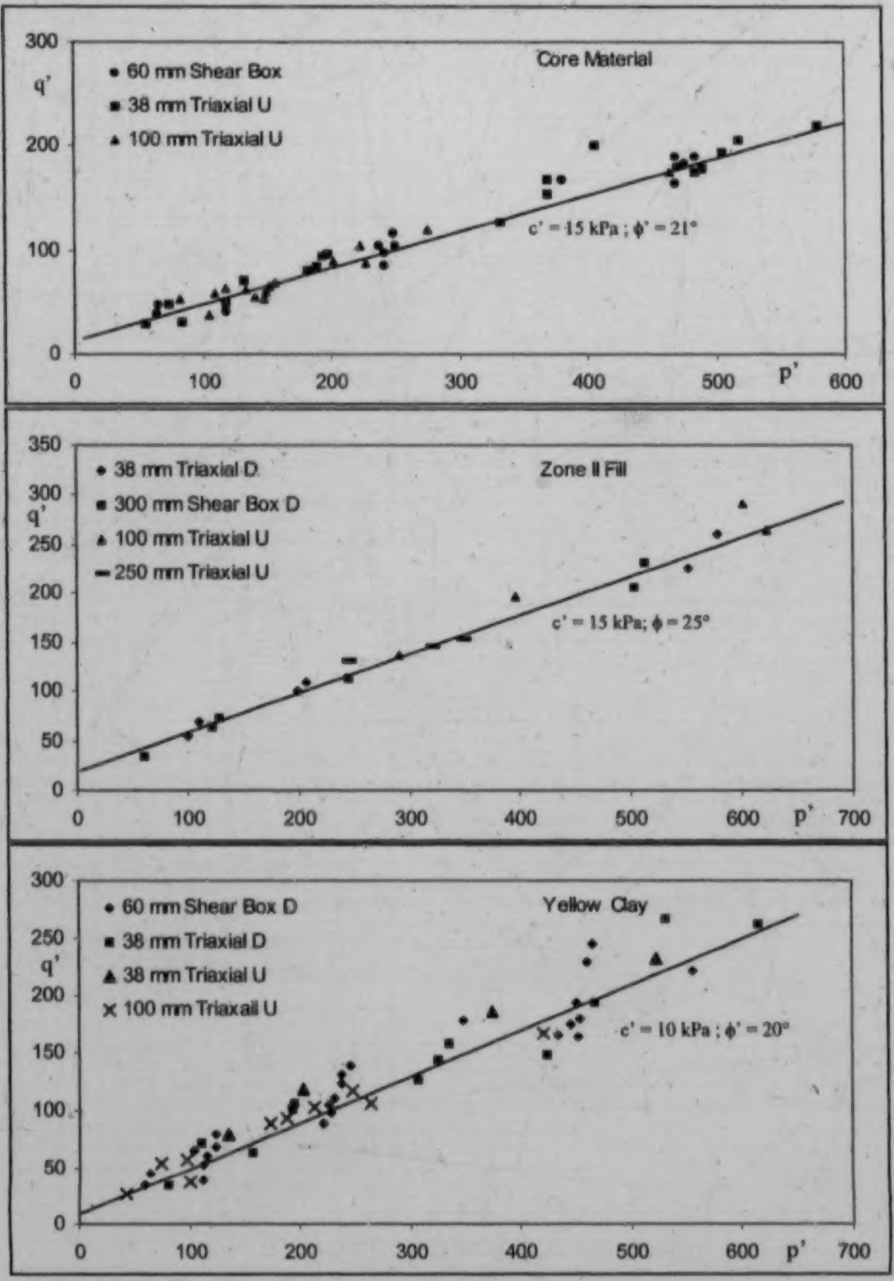

Figure 6.5: Peak shear strength data (Carsington Dam)

$$p' = (\sigma_1' + \sigma_3')/2 \; ; \; q' = (\sigma_1' - \sigma_3')/2 \; kPa$$

Material	Water Content W	Liquid Limit LL	Plastic Limit PL	Plasticity Index PI	Liquidity Index W-PL/PI	Clay Fraction CF	Activity Ratio PI/CF	Specific Gravity G_s
Subsoil	---	69	37	32		30	1.1	---
Yellow Clay	40	75	32	43	0.2	62	0.69	2.67
Dark Grey Clay	30	63	31	32	-0.05	47	0.68	2.70
Brecciated Mudstone	20	43	22	21	-0.1	32	0.65	2.75
Blocky Mudstone	15	44	23	21	-0.4	33	0.64	2.75
Core	33	69	31	38	0.05	56	0.68	2.68
Zone II Fill	14	45	23	22	-0.3	33	0.66	2.75

Table 6.1: Index properties of the materials at the Carsington Dam site

6.2.3.2 Foundation

The foundation was comprised of highly weathered to moderately weathered mudstone. No failure conditions were observed within the foundation; material parameters other than the deformation modulus are not required for analysis. In the finite element analyses carried out by Skempton [3], an equivalent nonlinear deformation modulus was adopted by fitting the observed settlements.

6.2.3.3 Core Material

The core and the boot were comprised of yellow clay and dark grey clay compacted at natural water content. The average values of the material as reported by Skempton [3] are presented in Table 6.1.

6

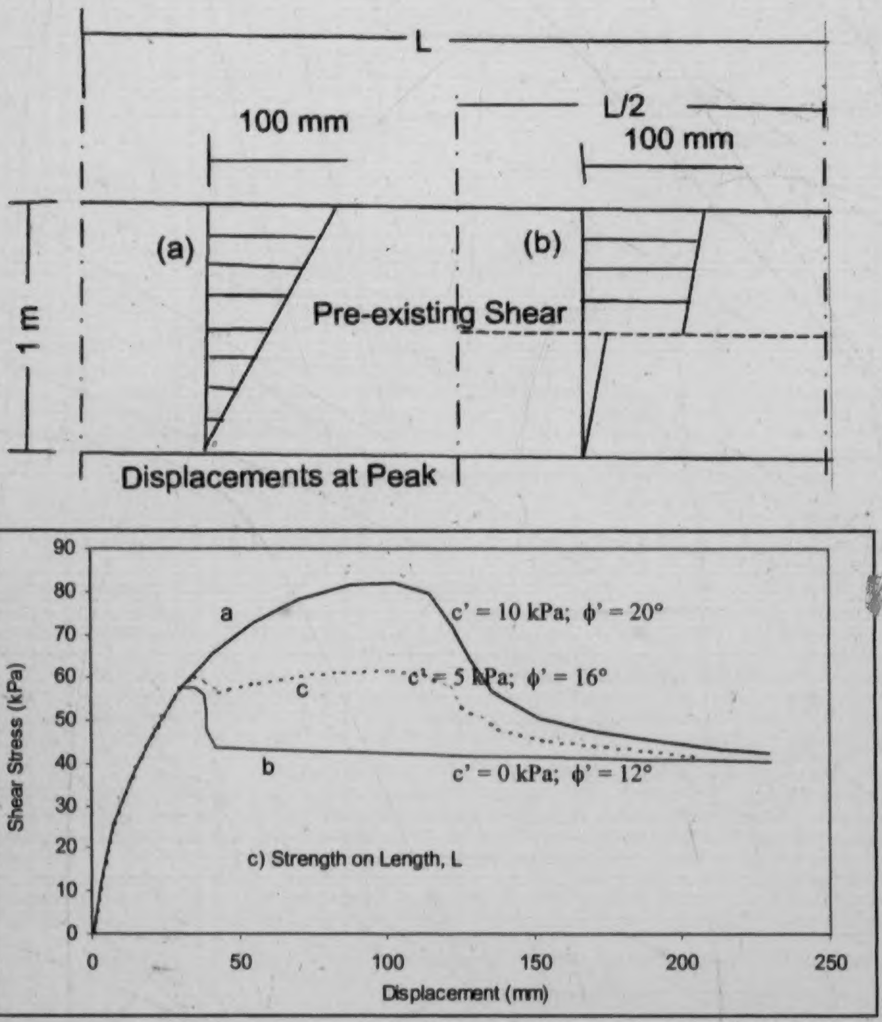

Figure 6.6: Stress-Displacement curves for yellow clay (Carsington Dam), Skempton [3]

Numerous tests conducted during the construction seasons in 1982 and 1983 showed that on average the material as placed had approximately 2% air voids. The end of construction values were controlled largely by the as placed water contents and little decrease occurred as a result of consolidation. Thus the results of the tests conducted in 1984 yielded air voids of 1% and a unit weight of 18.5 kN/m^3. The undrained shear strength measured on 100 mm undisturbed samples by tri-axial shear tests had an average value of 65 kPa. The shear strength parameters of the clay core are given in Table 6.2 and are as shown in Figure 6.7.

Material	Unit Weight γ (kN/m³)	Peak Shear Strength Parameters		Residual Shear Strength Parameters	
		c' (kPa)	ϕ'	c_r' (kPa)	ϕ_r'
Yellow Clay	20	10	20	0	12
Foundation	Strong Base				
Core	20	15	21	0	13
Zone I Fill	20	10	22	---	---
Zone II Fill	21.5	15	27	0	14.5

Table 6.2 : Strength properties of materials at the Carsington Dam site

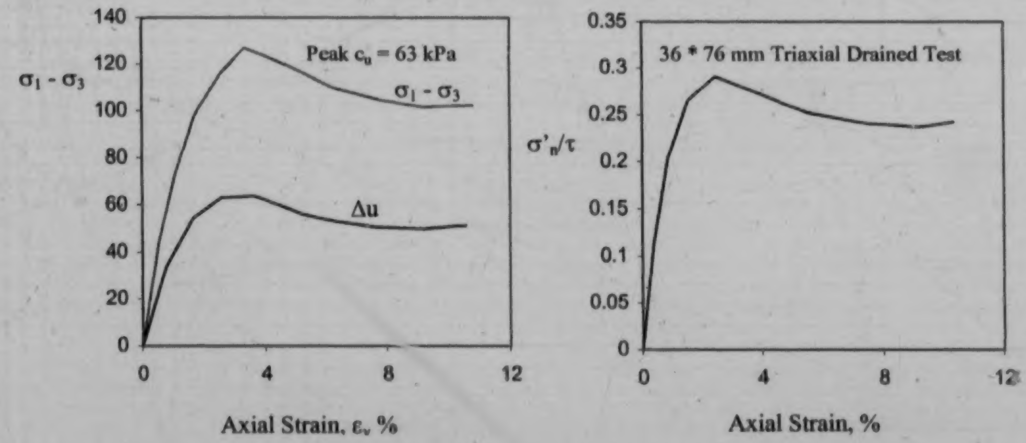

Figure 6.7: Post peak behaviour of the core (Carsington Dam), Skempton [3]

The 250 mm diameter samples recovered from the boreholes showed numerous rutting shears inclined at angles from 0° to 60° to the horizontal throughout the core.

6.2.3.4 Zone I Fill

Zone I fill was constituted of mostly brecciated mudstone with some dark grey clay, compacted at natural water content. As reported by Skempton [3], only a few tests had been conducted on this material. The values of the material properties and strengths for this material determined by tri-axial tests on four 100 mm diameter samples are given in Tables 6.1 and 6.2. As reported by Chen [8], the behaviour of Zone I fill is very similar to that of Zone II fill.

6.2.3.5 Zone II Fill

Zone II fill was also comprised of mudstone compacted at natural water content; the average index properties are presented in Table 6.1. The material consisted of lumps of softened mudstone and a matrix of fragments smaller than 5 mm in size. When immersed in water for 24 hours the lumps broke down to clay slurry. The fill had undergone some weakening compared with the fresh mudstone. This effect was partly due to chemical changes and partly to an increase in water content as discussed in section 6.2.3.6.

In situ density tests, and shear box and tri-axial tests with large samples, showed that the fill above Elv. 170 had an average water content of 14%. Due to slight expansion because of stress relief, the unit weight was 21.5 kN/m^3. Below Elv. 170, three tri-axial samples were found to be fully water saturated and had unit weights of 21 kN/m^3. Strength parameters from tests conducted on undisturbed samples recovered from above Elv. 170 are shown in Table 6.2. Values from tests conducted on recompacted fill in the laboratory were $c' = 10$ kPa and $\phi' = 27^\circ$ at an average initial water content of 17.3%. Zone II samples containing polished and stratified slip surfaces had a residual strength value of $\phi_r' = 14.5^\circ$, as shown in Figure 6.8.

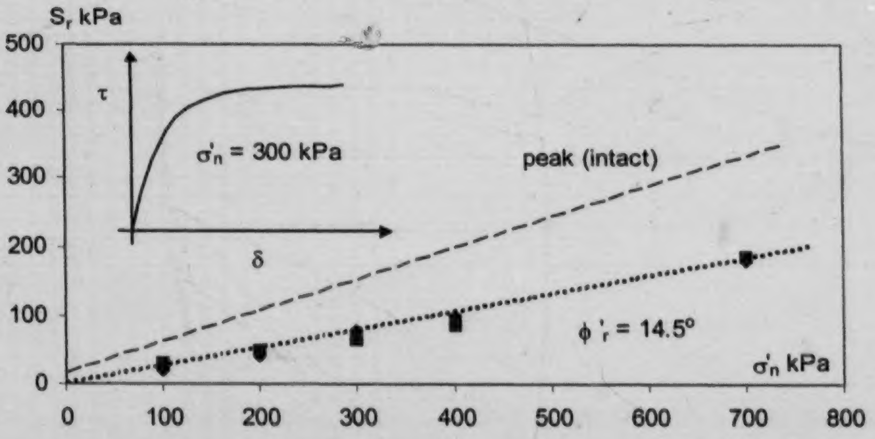

Figure 6.8: Zone II fill strength on slip surfaces (Carsington Dam), Skempton [3]

Compaction surfaces were observed in the Zone II fill and extended for several meters and were nearly horizontal and planar. Small displacements over these surfaces were expected to reduce the strength of the material.

6.2.3.6 Mudstone Deterioration

As referred in Section 6.2.1, the Carsington Dam was built on a site primarily comprised of four types of mudstone. Exposure to the atmosphere caused the mudstone to soften. The reason was attributed to the absorption of water and chemical changes resulting in the release of sulphuric acid and the liberation of Fe, Ca, and other elements into solution. As a consequence, the mudstone used in Zone II fill not only had higher water content than the parent mudstone but may also have been chemically different. Observations made in the field—iron stained water in borrow pits, generation of CO_2 gas from an acid reaction with the limestone drainage blanket, and iron staining at the outer margins of the blankets—lent support to this theory.

Two sets of tests were conducted to verify the geotechnical consequences of the mudstone deterioration. The samples were compacted in the laboratory and tested to find the peak parameters. When the plots were compared, the strength of the fresh mudstone from Zone I fill exceeded that of Zone II fill by about 1° in ϕ'. The second set of tests consisted of alternate leaching and compaction of the mudstone, and the results indicated that full leaching reduced the ϕ' by about 1° below the value for the fill and thus about 2° below the value of fresh material. Although these tests were regarded as more exploratory than definitive, they led to the conclusion that the lowest limit for Zone II materials with water content about 20% can be assumed to be $C' = 15$ *kPa and* $\phi' = 24°$.

Meanwhile, the strength tests conducted on Zone II fill as sampled in July 1984 were related to the time of failure and incorporated the effects of chemical alterations up to that time.

6.2.4 Description of Failure of the Carsington Dam

Construction of the 1200 m long earth embankment began in July 1982. The embankment was to be 37 m in height. By the end of May 1984, the placing of the fill material was almost complete but for the road construction activity which was still to be done. Instrument readings recorded a creep of the upstream peg of the order of 1.5 mm/day and the performance of the dam was observed to be normal.

Heavy rainfall amounting to approximately 40 mm fell during the period from June 1 to June 3, 1984. This brought earthmoving to a standstill. The wet conditions did not allow work to commence until Monday June 4, 1984 when a longitudinal crack was reported on the dam crest at 7:30 hrs. The first report recorded that the crack in the crest was approximately 50 mm wide between Ch. 675 and Ch. 740 and extended 50 m on each end but with diminishing width. Additional monitoring pegs were installed to measure the rate of widening of this crack. At this time, no noticeable differential vertical movement was apparent. Monitoring of existing survey pegs, piezometers, and other instruments was intensified to obtain detailed information about the event particularly at the four-instrumented sections in the dam.

A sudden increase in movement was observed at the upstream peg, with a creep rate as high as about 30 mm/day. Piezometers in the upstream part of the core and foundation, between Ch. 600 and Ch. 800, showed marked increases in levels. It was clear that the movements were mainly representative of a horizontal translation of the core and the upstream shoulder in the upstream direction. An extension to the existing upstream berm between Ch. 650 and Ch. 950 commenced at about 15.40 hours on June 4, along with the weather sealing of the crack on the dam crest, as in Figure 6.9. By Monday evening the crack width had reached 130 mm maximum but with little vertical differential movement

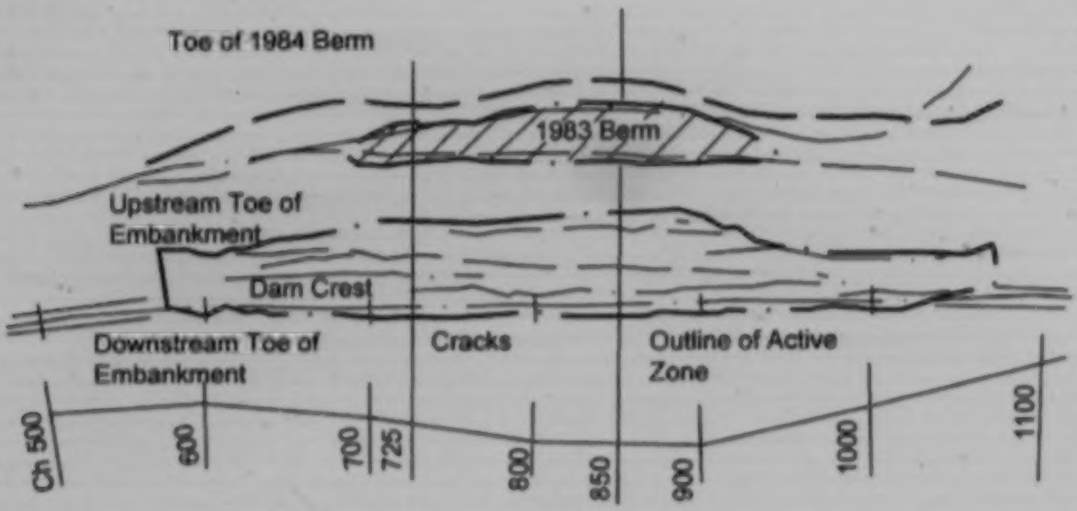
Toe of 1984 Berm
1983 Berm
Upstream Toe of Embankment
Dam Crest
Downstream Toe of Embankment
Cracks
Outline of Active Zone
Ch 500
600
700
725
800
850
900
1000
1100

Figure 6.9: Plan of the Carsington Dam during failure, Skempton [3]

By Tuesday, June 5, 1984, the crack width was increasing at a much greater rate (150 mm per hour) with an accompanying drop in level of the upstream side. A family of longitudinal cracks developed with intermittent droppings of wedges into the openings. By late afternoon, the crevasse had extended from Ch. 590 to Ch. 1050 with a maximum drop of the upstream side in the order of 3 m between Ch. 650 m to Ch. 800 m. Cracks had opened up on the upstream slope allowing beaching to drop into the voids formed. A second crack 2 m downstream of the original crack opened rapidly and the wedge between these cracks collapsed. Work on the berm extension continued throughout the day. No instrument readings were taken overnight but the piezometers at Ch. 700 showed drops in levels whereas at Ch. 850 levels still increased.

By the end of the day, the creep rate of upstream peg movement reached as high as 310 mm/day. A maximum total movement of 620 mm at the most critical section Ch. 725 was reported. The pore pressures dropped rapidly as shown in Figure 6.10 and as reported by Skempton [3].

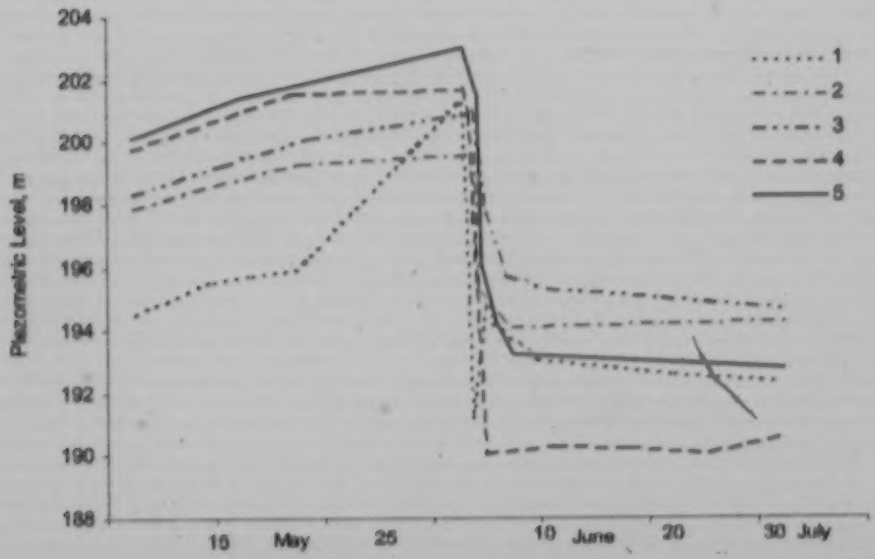

Figure 6.10: Sudden reduction of pore pressure in the Carsington Dam after failure, Skempton [3]

Inspections done on Wednesday, June 6, 1984 revealed large movements overnight, with a drop of 10 m within the crest. The upstream toe moved 13 m laterally and at Ch. 725 a graben 8 m wide by 2 m wide had formed within the riprap surface protection. Although movement of the dam virtually stopped on June 6, 1984, berm construction continued for few days. A channel was formed through the berm to release water trapped in the upstream toe drain. Piezometer readings at sections within the core and upstream zones were recorded and showed a considerable fall in pressure by about 10 m. The upstream part of the dam before and after failure is illustrated in Figure 6.11 for Ch. 725 (Skempton [3]).

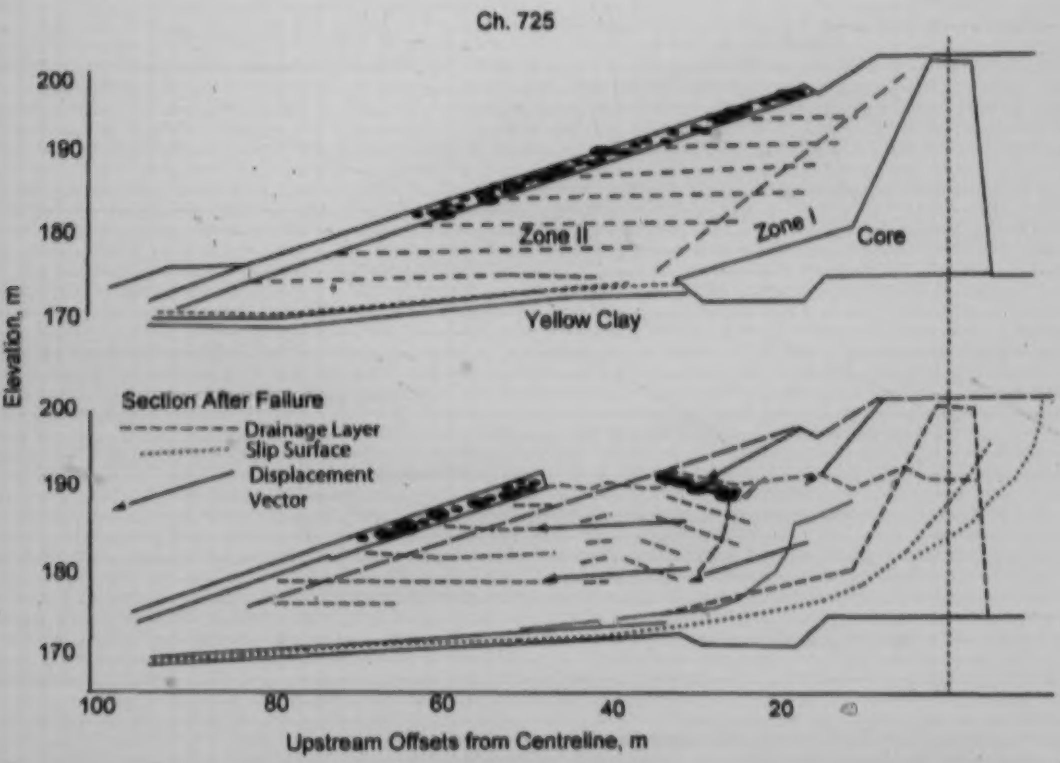
Ch. 725
200
190
180
170
Zone II
Zone I
Core
Yellow Clay
Elevation, m
Section After Failure
Drainage Layer
Slip Surface
Displacement Vector
200
190
180
170
100
80
60
40
20
Upstream Offsets from Centreline, m

Figure 6.11: Investigative section at Ch. 725 of the Carsington Dam, Skempton [3]

The position and nature of the slip surface were explored by means of trial pits, shafts excavated through the upstream shoulder of dam, and by large diameter borings through the core. Part of the main slip surface was highly polished and striated, passing through the yellow clay into the boot in the most critical section.

6.2.5 Material Models

The failure of the upstream side of the Carsington Dam in Derbyshire, England just prior to completion in 1984 was reviewed, analyzed, and examined by Skempton [3], Potts [4], Chen [6, 8], and Rowe [5]. Finite element analyses were performed to capture the progressive failure assuming strain-softening properties for non-uniformly loaded brittle soils.

Skempton [3], used limit equilibrium analyses to calculate the factor of safety (FOS) against failure on a potential slip surface, as:

$$F = \frac{\sum c'.l + \sum(\sigma_n - u)\tan\phi'.l}{\sum \tau.l} \qquad 6.1$$

In general, c' and ϕ' were assigned parameters less than the peak strength of the intact material due to the presence of pre-existing shears and nonuniform strains acting on the strain softening materials. Three different types of FOS were computed based on intact peak strength, peak strength with pre-existing shears and with strength reduced by shears, and progressive failure. Analysis of the section at Ch. 725 yielded that the three FOS thus established were 1.41, 1.21, and 1.0, respectively, reflecting a reduction of 14% and 29% of the FOS. Thus, pre-existing shears and progressive failure contribute in equal parts to the total reduction of 29%.

Finite element analyses were carried out by Skempton [3] and Potts [4] to examine and quantify the role of progressive failure in reducing the average operational strength below the peak strength of the outer part of the failure through the yellow clay and the Zone II fill. The failure surface passed through the core and the top of the core extension and through the yellow clay of the foundation to the toe. The Imperial College finite element program (ICFEP) was used by both authors. The program was developed at Imperial College for geotechnical analysis of soil structures and soil structure interactions. Skempton [3] used nonlinear elastic and strain hardening/softening Mohr-Coulomb models for analysis (Figure 6.12) while Potts [4] adopted an elasto-plastic soil model with pre-failure and unloading-reloading behaviour modeled by isotropic elastic theory, and failure and post-failure strain softening were modeled by plasticity using Mohr-Coulomb failure criteria (equation 6.2) as shown in Figure 6.12.

$$F(\sigma) = J/(p' + \alpha)G(\theta) - 1 \qquad 6.2$$

where,

$$J^2 = \left[(\sigma_1' - \sigma_2')^2 + (\sigma_2' - \sigma_3')^2 + (\sigma_3' - \sigma_1')^2\right]/6 \qquad 6.3$$

$$p' = (\sigma_1' + \sigma_2' + \sigma_3')/3 \qquad 6.4$$

$$G(\theta) = \sin\phi' / \left(\cos\theta + \sin\theta \sin\phi' / \sqrt{3}\right) \qquad 6.5$$

$$\theta = \tan^{-1}\left[\left(2\left((\sigma_2' - \sigma_3')/(\sigma_1' - \sigma_3')\right) - 1\right)/\sqrt{3}\right] \qquad 6.6$$

$$\alpha = c'/\sin\phi' \qquad 6.7$$

The program SAGE developed at the University of Alberta was used by Chen [8], for two dimensional analysis of sections of the Carsington Dam. The linear elastic modulus before the peak and associated flow rules were adopted for all nonlinear models in trial analysis. Strength reduction due to the geological pre-shears and construction defects was taken into account in determining the strength parameters. For the core material, the von-Mises yield criterion was adopted with a hyperbolic softening model, while for yellow clay and Zones I and II materials, a brittle elasto-plastic model with Mohr-Coulomb failure criteria and associated flow rules was employed.

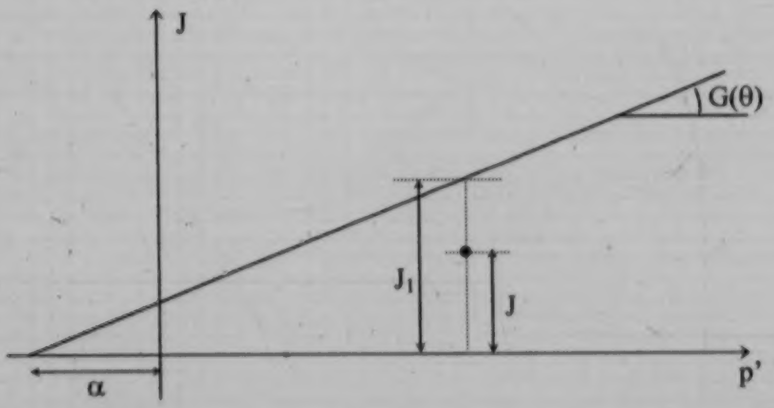

Figure 6.12: Yield criteria and definition of terms (Carsington Dam), Potts [4]

The material model adopted in the present study is based on Mohr-Coulomb yield criteria with non-associated flow rule and has been discussed in chapter 5. The material parameters considered for the present analysis are summarized in Table 6.3 and are near the representative values adopted by Skempton [3] for analysis of failure modeling post peak loss of strength based on plastic undrained states. As specified by Skempton [3], no mathematical model for soil behaviour using a single set of deformation parameters can deal realistically with all types of loading. Parameters can be derived from tests or field observations which match as far as possible the type of loading being modeled.

In the present work, an undrained total stress analysis was carried out and compared with the effective stress analysis presented in Skempton [3]. Since the core was partly saturated, it was expected there would be some undrained contraction and gain in the undrained strength with increasing average stress. At the lower part of the core and boot, the average total stress would produce near saturation and ϕ = 0 behaviour. Perfect plasticity was assumed at and after failure, with a zero dilation angle and associated flow rule for Mohr-Coulomb's criteria. This means that no volume change due to shear occurs after undrained failure.

MATERIAL **PROPERTY**	**FOUNDATION**	**YELLOW CLAY**	**CORE**	**ZONE I**	**ZONE II**
Cohesion (kPa)	STRONG BASE	15	52	13.5	13.5
Angle of Internal Friction		0	0	24	24
Young's Modulus (kPa)	125,000	3,000	2,500	60,000	60,000
Poisson's Ratio	0.35	0.42	0.43	0.38	0.38
Density (kN/m³)	20.00	19.50	18.50	21.00	21.00

Table 6.3: Material parameters used in analysis of the Carsington Dam failure

The real soil behaviour for conditions related to stress rotations during loading and stiff boundary conditions can be better predicted using soil models with plasticity.

6.2.6 Mesh used in Analysis of the Carsington Dam Failure

The mesh used in the present analysis is shown in Figure 6.13. The total number of elements in the mesh used was 1061, with 441 elements in the foundation, 101 elements in Zone I, 319 elements in Zone II, 18 elements in the yellow clay, and 182 elements in the clay core. A finer mesh was applied to the upstream Zone II clay core and yellow clay layers. As discussed in chapter 3, the defined mesh has to be regular and symmetric. Each element should have four nodes; if an element is in the middle, each of the element's nodes should be connected to nodes of exactly three other elements; otherwise the mesh becomes irregular and the routines developed will result in incorrect displacements and velocity constraints. If refinement is carried out in one zone, a corresponding refinement is needed in other zones within the same range of coordinates. The drawback of this technique is that a refined mesh needs to be defined for areas where a coarser mesh would suffice.

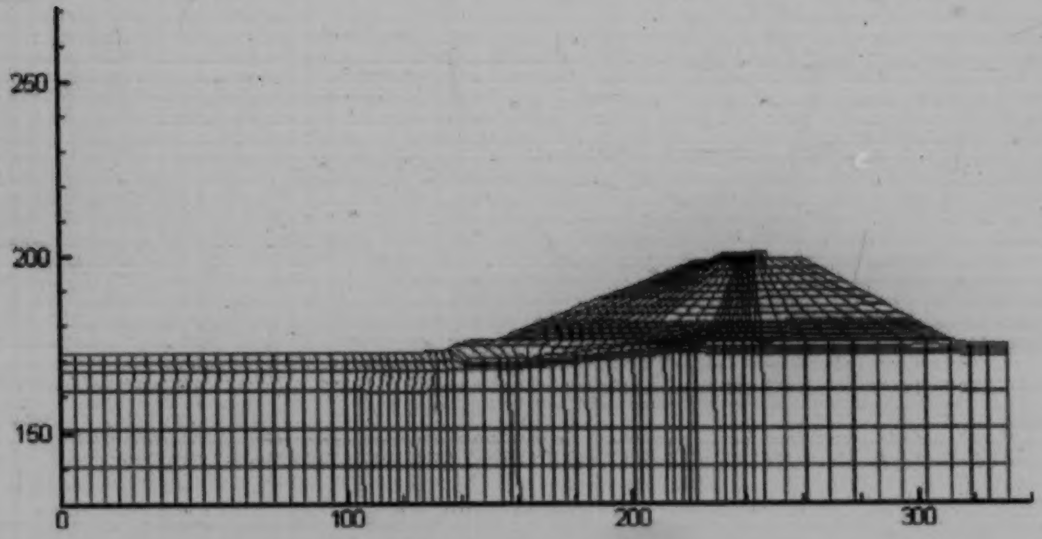

Figure 6.13: Mesh used in the analysis of the Carsington Dam failure, chainage 725.

6.3 RESULTS AND DISCUSSION

Results of the present analysis were compared in two parts to corresponding analyses in the available literature. In the first part outputs of finite element analysis are discussed; in the second part the discussion is extended to results obtained from the discrete finite element method developed in this research program.

As presented by Skempton and Vaughan [7], the initial slip occurred through the core which previously had contemporary shear surfaces due to rutting, and through the yellow clay which contained solifluction shears. During design, the factor of safety (FOS) was estimated at about 1.4 which was further reduced to 1.2 to allow for shear. The presence of brittle materials and the development of progressive failure further reduced the FOS to 1.0. The contribution of progressive failure to a reduction in the FOS varied from 21% to 26%. Finite element analyses and limit equilibrium analyses have indicated that the FOS just before collapse was about 1.1.

Previously reported analyses showed that failure occurred when the dam reached an elevation 0.5 m lower than the final height. The present analysis was carried out at the maximum design height of the Carsington Dam. The mesh used for the analysis is based on a section at chainage 725. The mesh is described in section 6.2.6 and consisted of 4-node quadrilateral elements with independent nodes.

6.3.1 Finite Element Analysis of the Carsington Dam

6.3.1.1 Staged Construction

An advantage of the developed dynamic solution scheme for finite element analysis is the ease with which elements can be added and removed. Analyses related to excavations and construction of embankments can be sequentially modeled and solved. This benefit can be achieved because each element of the mesh is prescribed independent matrices for various components in the computational cycles. The effects and interactions between elements as originally presented are based on the connectivity and restraints of one element with another. For example, the matrices of constitutive relations, displacement constraints, strains, and stresses are stored individually for each element and are at no point assembled as global matrices.

The Carsington Dam simulation was carried out in stages to simulate the staged construction of the dam. A total of six construction stages were used. For the first stage, the elements of the foundation were initialized, the gravity switched on, and the stress computations preformed until equilibrium was reached. The coordinates of the mesh were then reset to the initial coordinates. The computation for the first stage elements comprised 30,000 time steps of 0.0001 seconds. For each subsequent stage, the simulation was carried out for about 10,000 time steps and the equilibrium was checked within the duration of the time defined before elements for the next stage were added.

The results of the vertical stresses developed after the first, third, and fifth stages are shown in Figure 6.14. Due to the intensity of the mesh used in the analysis, the mesh is not shown in the figures below. As reported by Chen [8], there is little difference between the results of the effective and total stress analyses because the vertical load is the same for both cases.

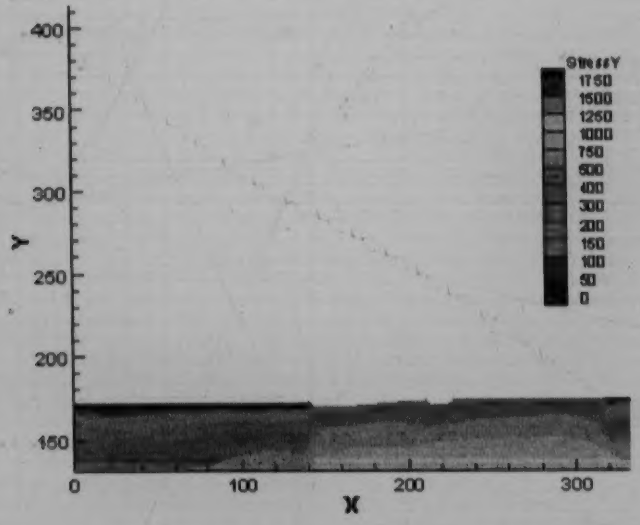

(a) First stage, foundation elements

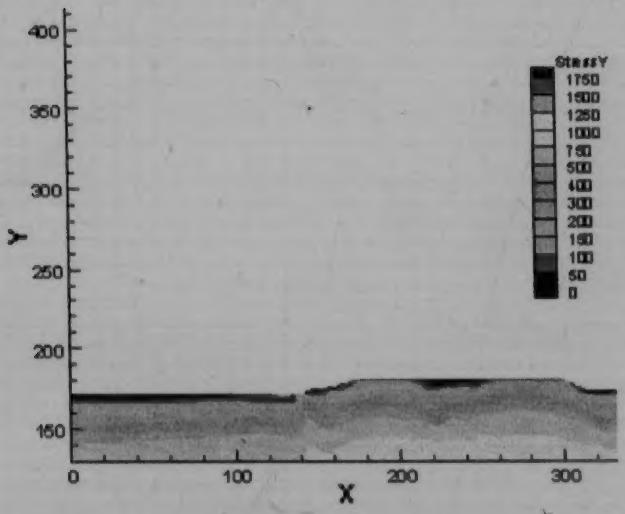

(b) Third stage elements added

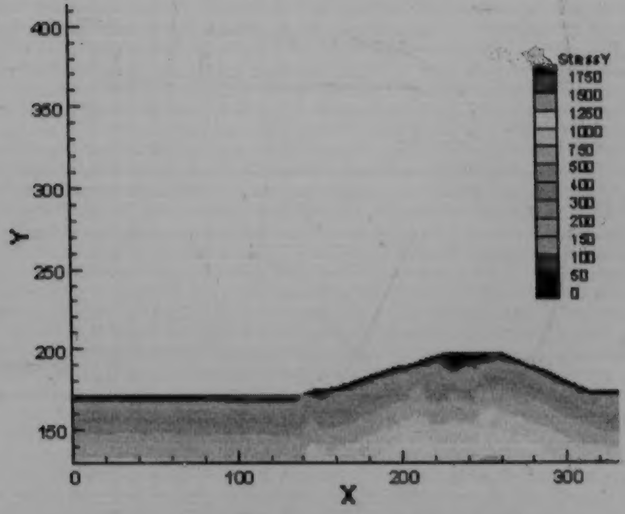

(c) Fifth stage elements added

Figure 6.14: Vertical stress contours as different stages of elements are added to the Carsington Dam

The computed stress states matches with the values computed and are presented for elevations of 160 and 190 m. In view of the results from various runs, it is concluded that reasonable values of parameters will yield similar distributions of vertical displacements and stresses. Variation of the stress states in the horizontal and the vertical directions at the end of the loading stage or when all the elements are considered is shown in Figure 6.15.

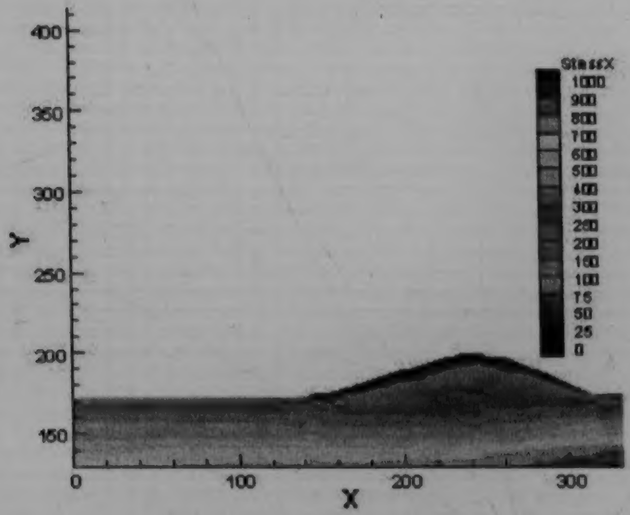

(a) Horizontal stress distribution

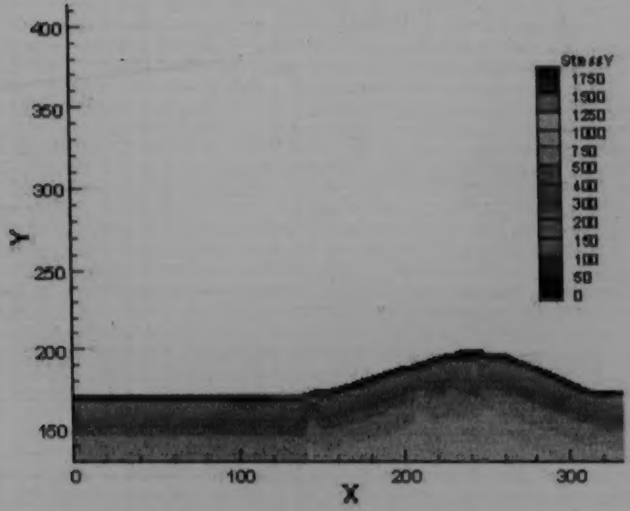

(b) Vertical stress distribution

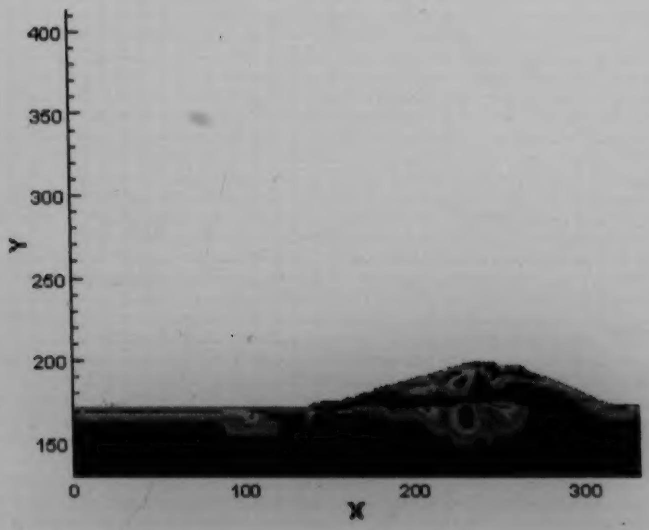

(c) Developed plastic zones within the Carsington Dam

[RED—plastic zones; BLUE—elastic zones]

Figure 6.15: Contour plots of the Carsington Dam at the end of construction

The vertical stress plot at the end of the loading stage within the dam is shown in Figure 6.15(b). An arching action within Zone I and Zone II can be observed due to a higher elastic modulus. A similar observation was made by Chen [8] and the use of a nonlinear elastic modulus compatible with the observed settlements was recommended. In the current analysis even with the use of an elasto-plastic constitutive relation, similar behaviour was observed. Figure 6.15(c) shows the yielded elements when the last stage of elements was added. The elements in the vicinity of and in the boot of the clay core and all the elements comprising the yellow clay soil show yielding. At the top of the dam and along Zone I and Zone II side slopes, yielding or failure of the material can be seen. The top of the dam and elements closer to the surface might be developing tensile stresses or tension cracks. In the present analysis the material in the model has been defined as a no-tension material, and thus will tend to show yielding.

6.3.1.2 Displacement Profiles

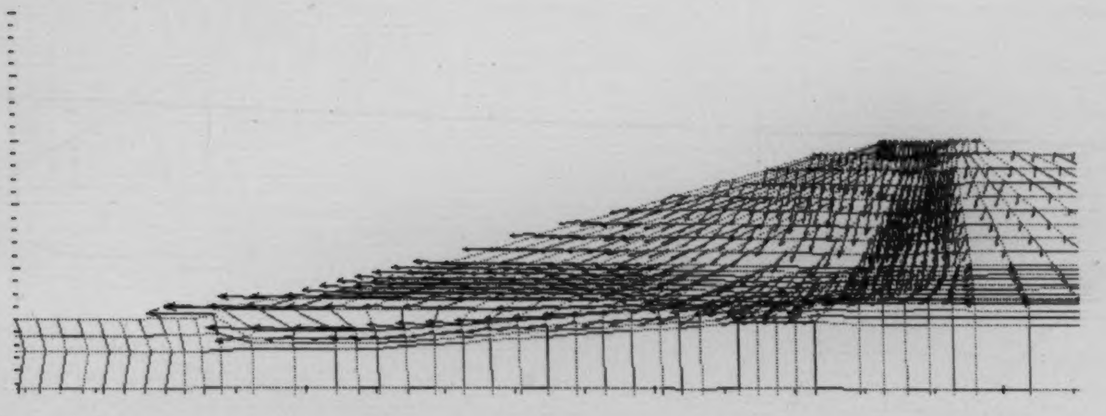

Figure 6.16: Displacement vectors over the upstream slope (Carsington Dam)

Rowe [5] reported that the first visual evidence of impending collapse was the formation of tension cracks at Ch. 707 m on June 4, 1984; this was followed by a total collapse of the dam across the valley by June 6, 1984. The toe displacements and core strains led to the center, dragging the side with extensive shear planes and with failure occurring within the boot and the foundation yellow clay.

The vectors of total displacement just prior to failure are shown in Figure 6.16. As presented by Skempton [3] and also visualized in this figure, there is a significant component of settlement relative to the horizontal movement. The core shows slightly more settlement than the shoulders. The horizontal movement is slightly toward the upstream and a tilt was observed at the crest of the dam during the 1983-84 winter season.

As for the vertical displacement distribution within the main dam just before failure, the calculated values compare well with those computed by models reported by Chen [8]. The vertical displacement profile is shown in Figure 6.17. Even with the use of models for the core and shell different from those applied by other authors, the foundation material seems to play a significant part in controlling the settlements as it tends to provide a vertical constraint to the dam materials. As shown in Table 6.3, a high elastic modulus of 125,000 kPa is used for the foundation material.

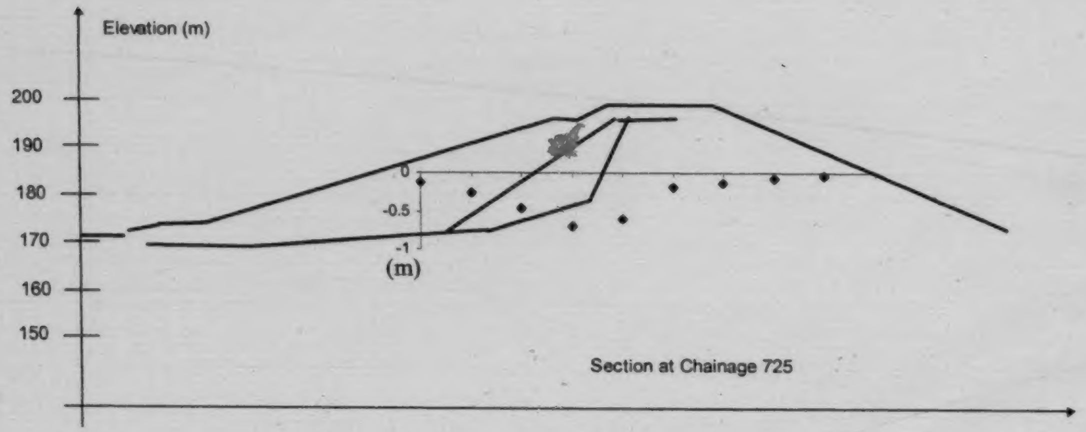

Figure 6.17: Vertical displacements (in meters) (Carsington Dam)

As there are no constraints on the horizontal directions, as discussed above for the vertical direction, the results of horizontal displacements just before dam failure show large differences among the various models studied so far.

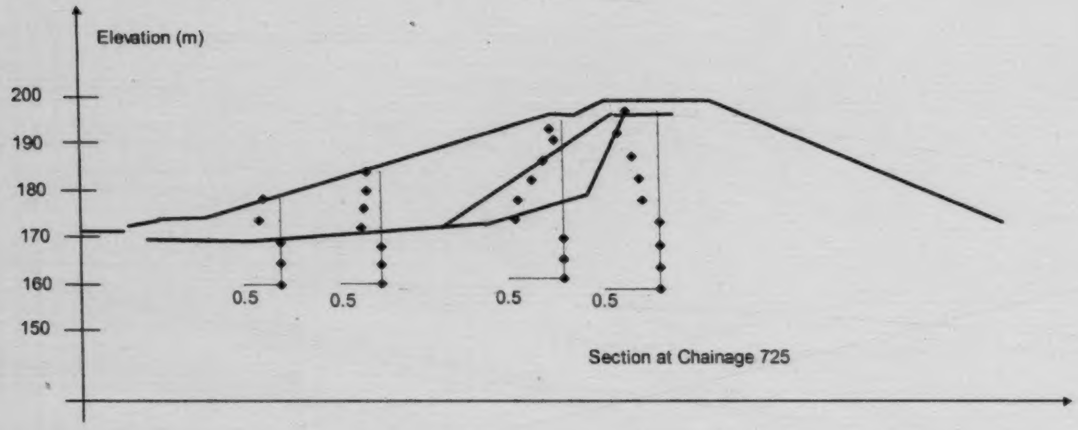
Elevation (m)
200
190
180
170
160
150
0.5
0.5
0.5
0.5
Section at Chainage 725

Figure 6.18: Horizontal displacements (in meters) (Carsington Dam)

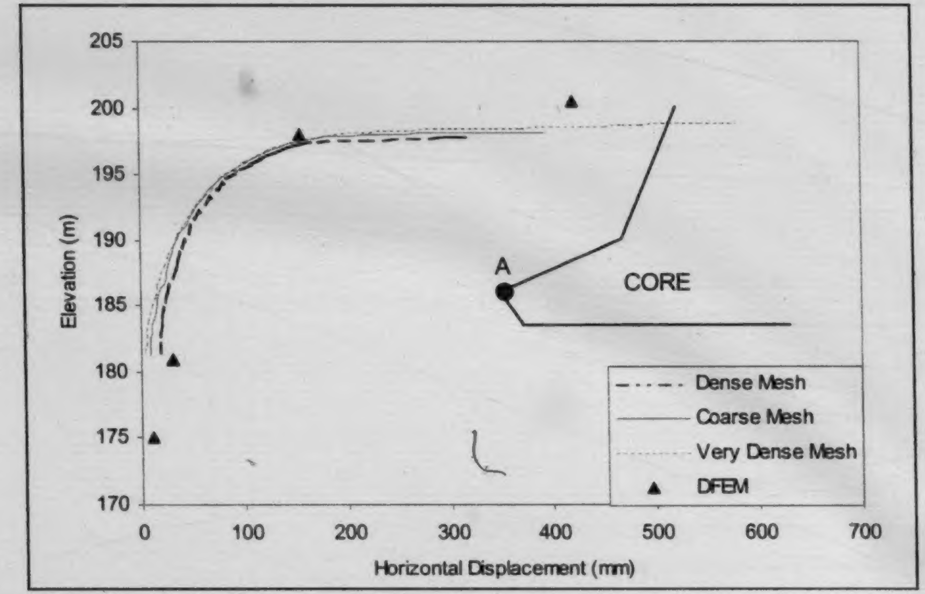

Figure 6.19: Horizontal displacement in the core versus elevation (Carsington Dam)

There are difficulties in predicting deformation quantities. As presented in Figure 6.18, larger horizontal deformations are initiated along the yellow clay layer (not shown) which reflects a high shear deformation of this material. The observed horizontal deflections within the core at the base are in the range of 200 to 275 mm. This analysis revealed horizontal deflections of about 150 mm up to the construction elevation of 198 m and within the range of 400 to 450 mm for the construction height of 200.5 m. As reported by the analysis carried out by Chen [8], horizontal deflections were 100 to 150 mm. The horizontal displacement of node A in the core in comparison to the height of the construction of Carsington Dam is presented in Figure 6.19 and it is comparable with values reported by Chen [8] using coarse, dense, and very dense meshes. Distribution patterns revealed similar variations but the quantitative values were different. The different results can be attributed to differences in analysis types and models used for the materials.

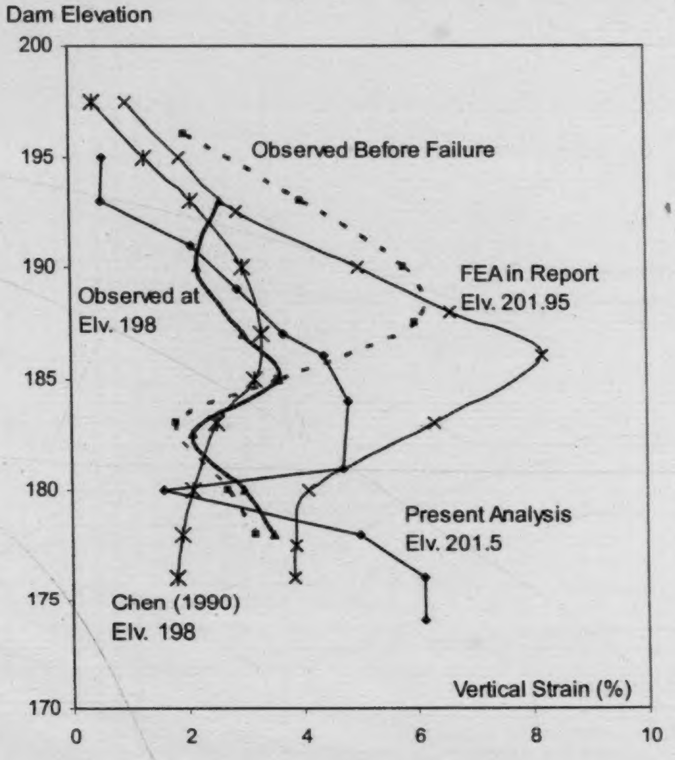

Figure 6.20: Comparison of vertical strains in the core (Carsington Dam)

Figure 6.20 shows the vertical strains measured in the field at settlement gauge BS1 and the strains predicted by various authors. Reasonable agreement is achieved between observed and predicted strains. The core settlements and the strains are primarily controlled by the strength of the core. The predicted values are higher than observed values indicating that the predicted spread of the core due to shear is more than what is observed. Thus, the vertical strain distribution is acceptable in the average sense of the analysis.

As quoted by Chen [8], finite element analysis produces a relative error of at least 50% to 100%, even in the average sense. Analytical predictions of horizontal and vertical deformations will improve with the advance of field investigations and laboratory techniques. Currently, the predicted deformation patterns reflect the field conditions with reasonable input information. This instills confidence in the use of these methods for back analyzing failure mechanisms.

6.3.2 Discrete Finite Element Analysis of the Carsington Dam

In his thesis, Chen [8] discussed the feasibility of formulating problems in plasticity and by use of shear band and localization. In dam engineering the main concern is with the working performance of the dam and predictions about the stability of the dam. Prior to the initiation of failure of the Carsington Dam, creep rates of less than 1.5 mm per day were observed resulting in quasi-static loading conditions. Thus, the process before failure can be formulated within the framework of plasticity with assumptions of small strain and small deformation. At critical state, significant increase in creep rates results in progressive failure due to disturbances in highly strained areas. The failure proceeds to a new equilibrium state that involves large deformations, a total break down of materials, and motion of separated wedges. The discussion in Chen [8] is extended by the present approach in which a post failure state is achieved, i.e., the post failure behaviour of the dam is modeled.

Discrete element analysis of the Carsington Dam failure was carried out with a time step of 0.001 seconds and a damping coefficient of 3. The simulation was computed up to 4.0 million time steps over 167 hours (~ 7 days). Failure was initiated or the elements were allowed to split up based on a specified strength criterion. As shown in Figure 6.21(a), failure begins at the top of the dam or within the yellow clay layer. The crack that develops on the top of the dam extends downward and causes the elements to further split and start displacing. Positions of the elements at time intervals of 500, 1000, 1500, 2000, 2500, 3000, 3500, and 4000 seconds, along with the vertical stress states are shown in Figure 6.21. As represented by the white spaces in the figures, the cracks can be visualized as growing and causing failure of the upstream slope.

In Figure 6.21(c) a large failure surface has developed along the interface of Zone I and the clay core. The break up of elements occurs and the slope failure takes place. This failure further progresses toward the downstream slope and compares reasonably well with the final attained configuration of the failed dam section in Figure 6.11.

A simulation movie of the Carsington Dam failure is presented in the attached CD as Example 6.1 Carsington Dam.avi.

One observes that the method of analysis developed in this thesis is capable of modelling the complex behaviour of a failed soil mass by coupling the two independent techniques of finite element and discrete element methods.

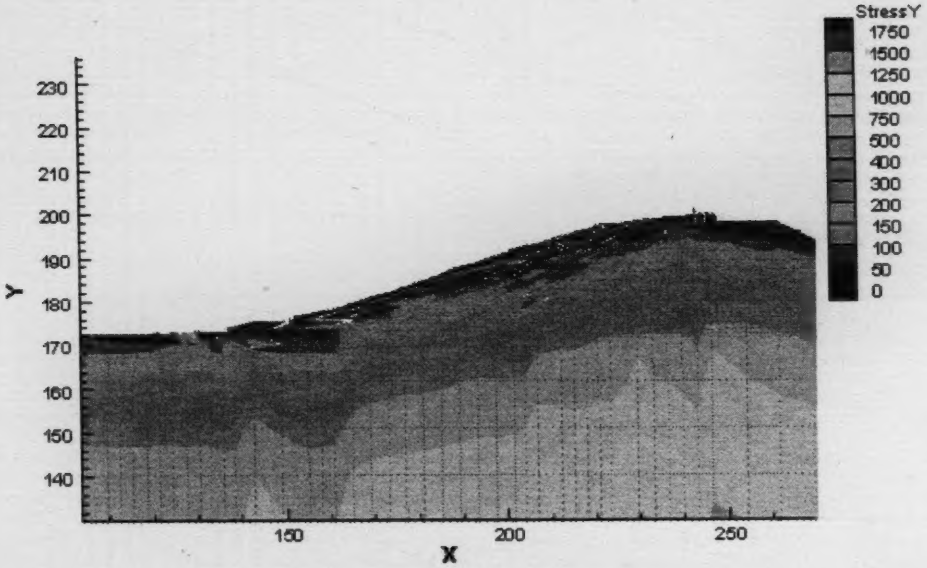

(a) After 500 seconds

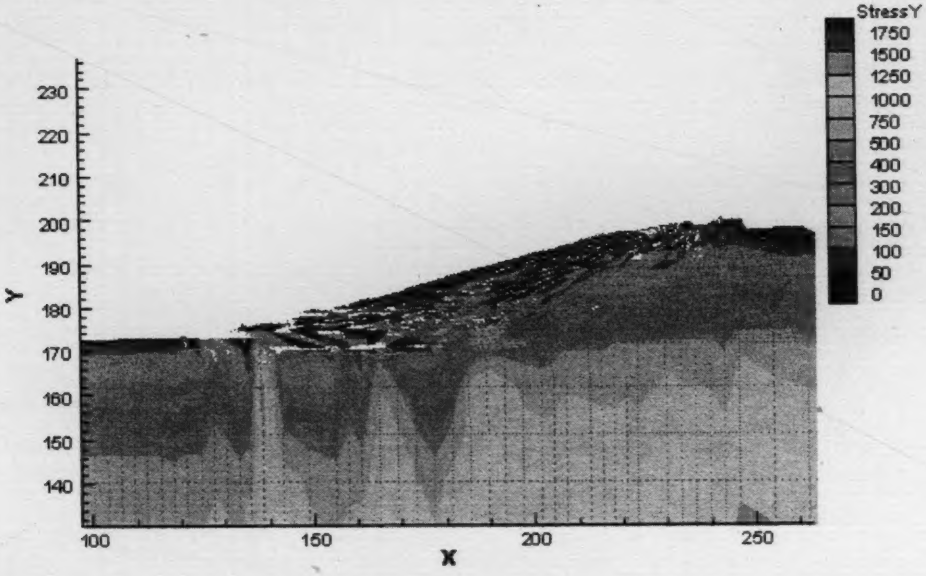

(b) After 1000 seconds

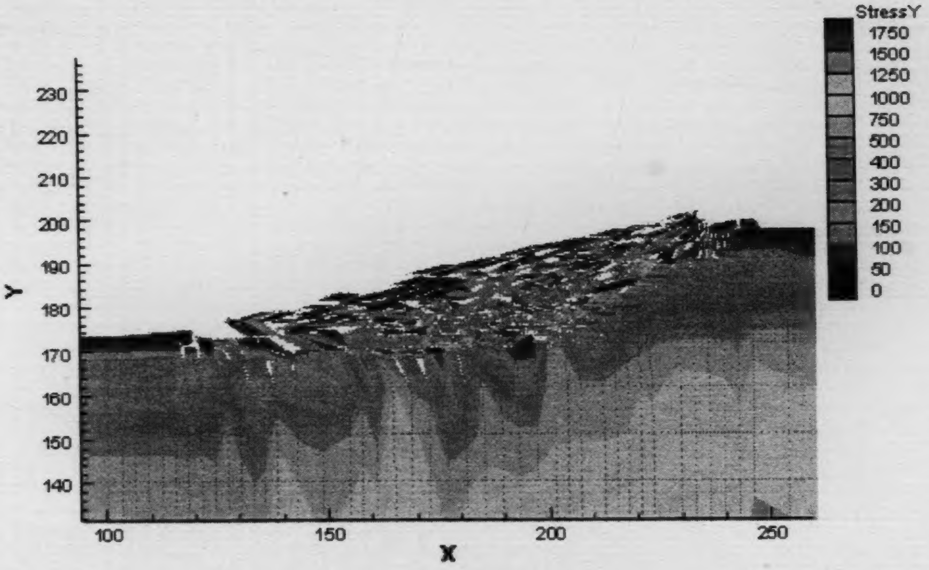

(c) After 1500 seconds

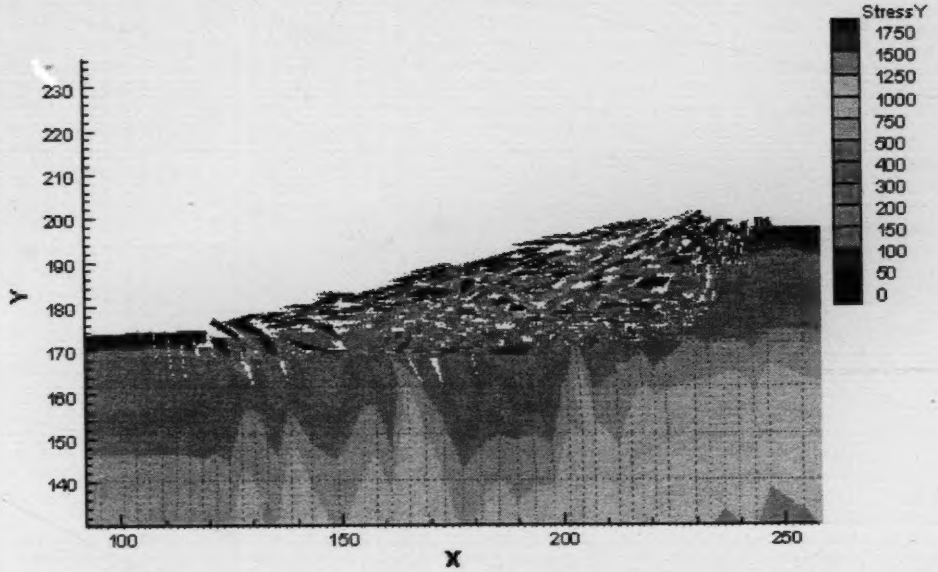

(d) After 2000 seconds

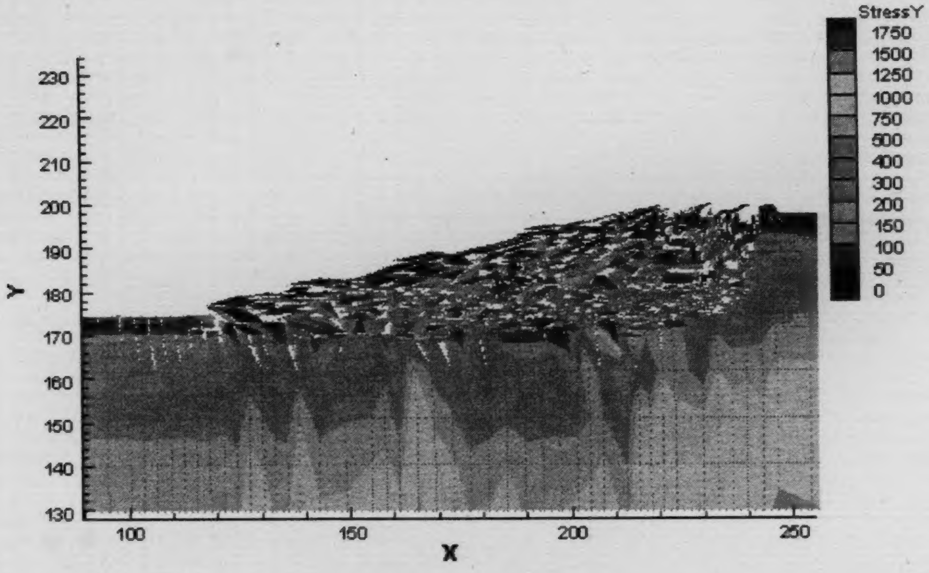

(e) After 2500 seconds

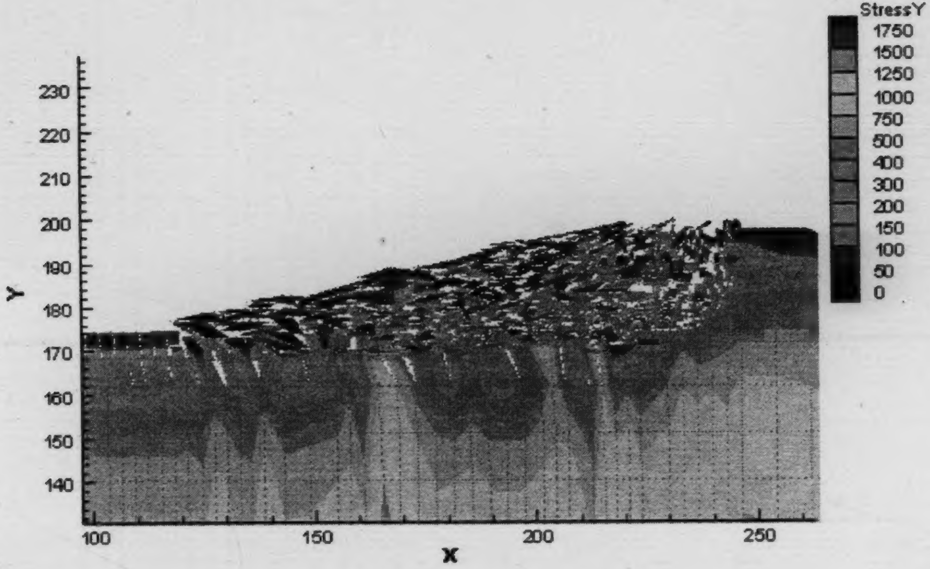

(f) After 3000 seconds

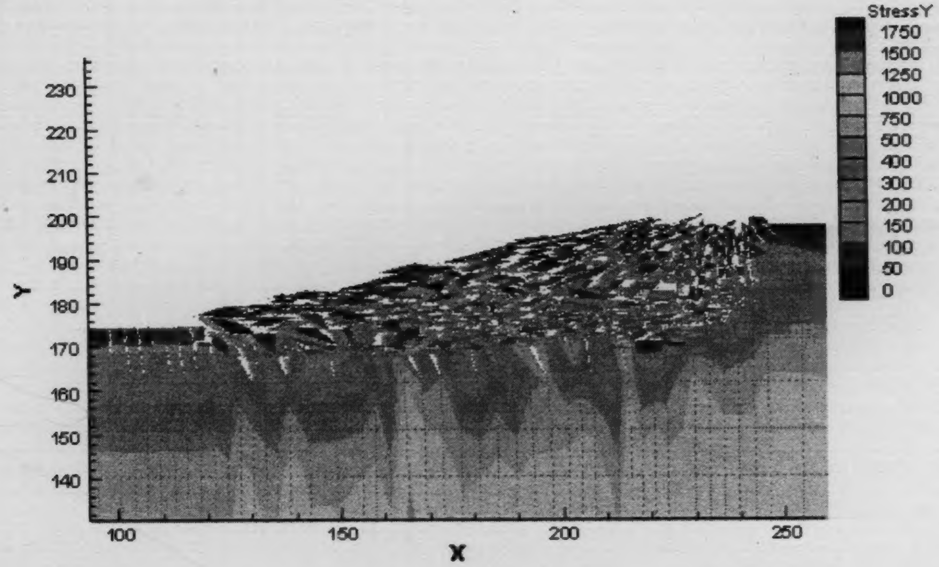

(g) After 3500 time steps

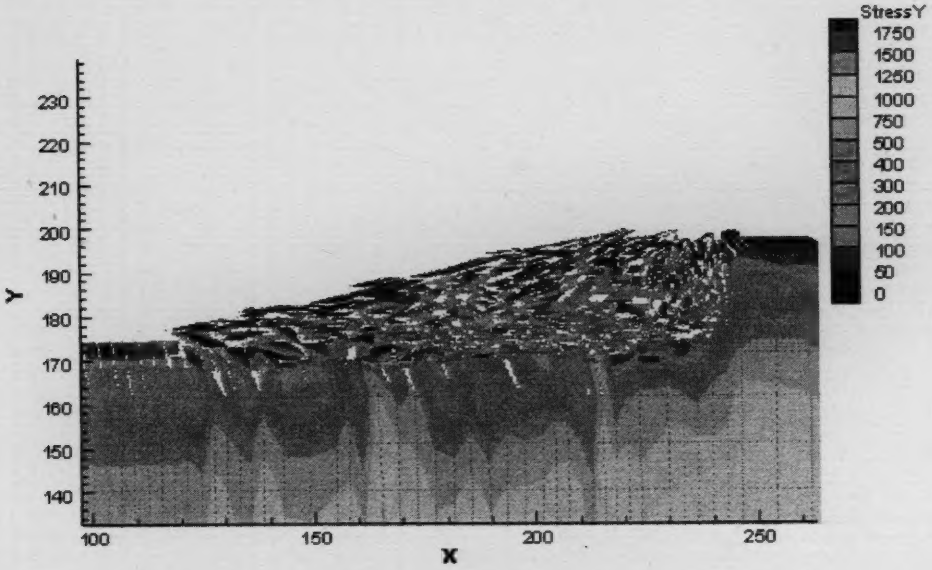

(h) After 4000 time steps

Figure 6.21: Stages of failure of the Carsington Dam

6.4 CONCLUDING REMARKS

The computer model developed for analyzing the failure of soil mass was tested in this chapter by back analyzing the case history of the Carsington Dam failure. The method combines the capabilities of the versatile finite element method and the flexible discrete element method to model interactions among multiple bodies. Several authors have shown that the failure of the Carsington Dam was promoted by strain softening, starting within the highly strained boot. This behaviour is captured by allowing the elements to split based on a strength criterion, and displace, resulting in the development of failure surfaces. The pattern resulting from the present analysis can be considered a good approximation to that observed in the field.

BIBLIOGRAPHY

1. Lambe, T. W., *Predictions in soil engineering*. Geotechnique, 1975. 23: p. 149-202.
2. Kennard, M. F., and Bromhead, E. N., *Carsington Dam—The near miss which became a bulls-eye*. Forensic Engineering, May 21–23, 2000. Proceedings of the Second Congress, San Juan, Puerto Rico: p. 102–111.
3. Morton, B. S., and Skempton, A. W., *Carsington Dam—The mechanism of failure*. Report submitted to Severn Trent Water Authority, *U.K.* 1986.
4. Potts, D. M., Dounias, G. T., and Vaughan, P. R., *Finite element analysis of progressive failure of Carsington embankment*. Geotechnique, 1990. 40(1): p. 79–101.
5. Rowe, P. W., *A reassessment of the causes of the Carsington embankment failure*. Geotechnique, 1991. 41(3): p. 395–421.
6. Chen, Z., Morgenstren, N. R., and Chan, D. H., *Progressive failure of Carsington Dam: A numerical study*. Canadian Geotechnical Journal, 1992. 29: p. 971–988.
7. Skempton, A.W.a.V., P.R., *The failure of Carsington Dam*. Geotechnique, 1993. 43(1): p. 151–173.
8. Chen, Z., *Analysis of progressive failure of Carsington Dam*. Department of Civil Engineering. 1990, PhD thesis, University of Alberta: Edmonton. p. 340.

7 CONCLUSIONS

7.1 SUMMARY AND CONCLUDING REMARKS

The objective of this research is to realistically model the behaviour of geological materials and their failure states. The work here couples the versatile finite element method with the discrete element method to model the hybrid continuum/discontinuum properties of geotechnical structures such as soil and rock in order to predict and control their behavior. Steps taken to develop a 'discrete finite element method' were: (1) an equivalent finite element solution was generated using discrete individual elements with separate nodes, (2) appropriate time steps and damping criteria were selected, (3) suitable nodal restraints were determined, (4) different aspects of the discrete element formulation were modeled, and (5) an elasto-plastic constitutive model was validated. The developed method was tested for practical use by simulating a classic geo-engineering problem, the Carsington Dam failure. The conclusions and implications of this research are presented in this section. It is expected that the developed discrete finite element method will be useful in solving a broad range of geo-material problems.

In Chapter 3, a two-dimensional new finite element method is proposed for analyzing geotechnical structure. In this method, the problem is represented by individual 2D quadrilateral discrete elements with eight independent degrees of freedom. Different types of restraints were explored to maintain effective coordination between the elements at shared nodes. The solution scheme developed is based on the solution of the equation of motion derived from Newton's second law. This solution scheme enabled the concepts of discrete element analysis to be incorporated at a later stage. Stress distributions within a uniformly loaded soil mass, a slope, and a foundation have been examined. The analysis demonstrates the capability and effectiveness of the usage of restrained discrete elements in capturing the results for a continuum.

The discrete element method is discussed in Chapter 4. After a review of available discrete element approaches, the relevant and most applicable concepts are included in the presently developed method. This includes the concept of using a grid for contact detection, computation of contact forces based on overlap areas, and the direction of application of these contact forces satisfying specified criteria. Models of these contacts are discussed and verified. New schemes for the creation of discrete elements from the finite element assembly are developed in order to create a discontinuum from a specified continuum. These are based on normal and tangential stress states that exist at the boundaries of the elements. Computational aspects of the method related to the numerical stability and data structure have been discussed. Simulations based on the proposed method predict real world behavior reasonably well.

The proposed method combines the capabilities of the finite element method to model a continuum and the flexibility of the discrete element method to model interactions in an array of discrete elements which may undergo large displacements, rotations, and strains. Contact stresses between elements are transformed into equivalent nodal forces and are incorporated in the net force for each element. Suitable stress-strain measures are included to determine realistic stress and strain values. The model of deformable elements, the contact model, and the stress states were verified. Examples illustrating the application of the method for studying geotechnical problems related to large movements are presented.

In Chapter 5, a suitable elasto-plastic constitutive relation representative of geotechnical behaviour was researched. An elastic perfectly-plastic Mohr-Coulomb criterion based on a flow rule accounting for representative soil behaviour was selected. In accordance with the dynamic solution scheme, the duration/time intervals when yield criteria need to be checked were identified. A subroutine was developed to identify the elements in the yielding state and to preserve the aspect ratio of each element for numerical stability, without interfering with the amount of deformation/strains accumulated. The developed method was applied to conventional geotechnical problems related to the estimation of bearing capacity of soil under a footing and the amount of earth pressure developed behind a retaining wall under active and passive states. The analyses were carried out beyond failure, further than many common solutions for these problems, to examine post failure behaviour.

At the design stage, it is important that the conditions of small strain and deformation are satisfied. However, when failure occurs and the magnitude of the impact of the failure is to be identified, the method should present sufficient insight into the sequence of events occurring over time. Even with the use of a simple soil behavioural model, it was possible to get a preferred slip plane based on the splitting of the elements. However in order to capture the post failure plane, a suitably refined mesh needs to be applied and better element shapes need to be selected.

A case history of the Carsington Dam failure that occurred in 1984 was back analyzed to capture the post failure deformations and the suitability of the developed method.

The discrete finite element method developed here is robust in modeling post failure deformation, can use continuum material properties, and can incorporate realistic in situ stress conditions. It has the ability to calculate stresses and strains that are difficult to determine using discrete element techniques.

7.2 SUGGESTIONS FOR FURTHER RESEARCH

The computer code developed here is based on two-dimensional quadrilateral elements. The code could be modified to include a variety of element shapes, for instance, triangular elements or elements with more degrees of freedom. A mesh with fewer numbers of elements would be suitable for the analysis of triangular elements or elements with higher degrees of freedom. The developed code could be further modified to a three dimensional state, but it is anticipated that due to the imbedded discrete element routines related to contact formations and detections, a realistic analysis would be very demanding on computer time and memory.

Routines based on the presence and effects of groundwater can be included to perform effective stress analysis. The effects of groundwater would have to be modeled to capture the situation anticipated as failure occurs and the elements displace and produce corresponding changes to the hydrostatic stress states. It can be inferred from field observations that as failure occurs the hydrostatic levels in the soil tend to drop significantly. Is this the real condition for simulation? Or as elements collide are there local increases in pore pressures in individual elements? How should the corresponding values of stress states be determined? How would this affect the stability and the progression of stresses within the elements? These are some of the issues that will have to be addressed when water is included in the analysis.

For each element in the presented model the computations are based on independent matrices for mass, constitutive relations, etc. The developed code can include different materials with variable properties. Problems related to soil structure and particle interactions could be modeled using transition zones for different properties in order to avoid numerical instability. Numerous applications related to the construction of pile walls, retaining walls, anchors, soil nails, reinforcements, and others can then be simulated with ease.

In order to allow for the fragmentation through the elements, each element can be further divided into number of sub-elements. As the splitting occurs through the element, the number of elements and other related matrices of the elements can be updated. This would help in capturing more smooth failure planes for any geotechnical geometry and problem.

APPENDIX A
INTERSECTION POINTS

The steps involved in the calculations of intersection points are:

i. The node forming the contact with the home element is recalled from the array it is stored in, i.e., CNODE [ ].
ii. The search for intersection points is carried out using the contacting node N4 and its two adjacent nodes.
iii. The first intersection point is computed with the line joining the contact node N4 and one of its adjacent nodes, preferably the one in the counterclockwise direction.
iv. A search is made for the intersection point between the contacting side and all the sides of the home element, moving in a counterclockwise direction and storing the intersection points calculated.
v. The process is continued with the next adjacent node of the contacting node, the one in the clockwise direction. A search is made for an intersection with the line joining this adjacent node and a contacting node on all the sides of the home element in a counterclockwise direction.
vi. If there is more than one contacting node of the near element, then the search process will comprise the second contacting node and the adjacent node in a clockwise direction.
vii. All intersection points and contacting nodes are stored in an array IP [ ] to be recalled later to find the areas of overlap between the home and near elements.

Intersection points are computed using the following algorithm adopted from the Internet site http://astronomy.swin.edu.au/~pbourke/geometry/lineline2d/, retrieved 15 March 2004:

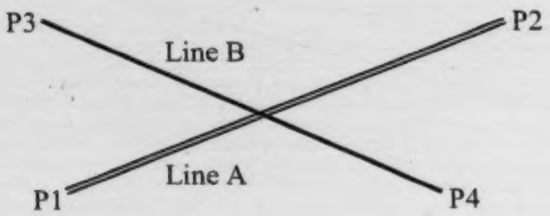

Figure A-1: Illustration of the calculation of the intersection point between two lines

A line can be described by equation A-1:

$$\begin{aligned} P_a &= P_1 + u_a(P_2 - P_1) \\ P_b &= P_3 + u_b(P_4 - P_3) \end{aligned} \qquad \text{A-1}$$

where,

P_a = X (or Y) coordinate of line A,

P_b = X (or Y) coordinate of line B,

P_i = X (or Y) coordinate of any point i on line A or B, and

u_a or u_b = two unknowns for these equations.

Solving for the intersection point where $P_a = P_b$, these two unknowns can be computed.

$$X_1 + u_a(X_2 - X_1) = X_3 + u_b(X_4 - X_3) \qquad \text{A-2}$$

$$Y_1 + u_a(Y_2 - Y_1) = Y_3 + u_b(Y_4 - Y_3) \qquad \text{A-3}$$

Solving simultaneous equations A-2 and A-3 for u_a and u_b, gives:

$$u_a = \frac{(X_4 - X_3)(Y_1 - Y_3) - (Y_4 - Y_3)(X_1 - X_3)}{(Y_4 - Y_3)(X_2 - X_1) - (X_4 - X_3)(Y_2 - Y_1)} \qquad \text{A-4}$$

$$u_b = \frac{(X_2 - X_1)(Y_1 - Y_3) - (Y_2 - Y_1)(X_1 - X_3)}{(Y_4 - Y_3)(X_2 - X_1) - (X_4 - X_3)(Y_2 - Y_1)} \qquad \text{A-5}$$

The values of u_a and u_b obtained from equations A-4 and A-5 are used to find the coordinates of the intersection point:

$$X = X_1 + u_a(X_2 - X_1) \qquad \text{A-6}$$

$$Y = Y_1 + u_a(Y_2 - Y_1) \qquad \text{A-7}$$

Before calculating the intersection points using equations A-6 and A-7, the lines are checked to see whether they intersect, as these lines can be parallel or coincident. If the denominators for the expressions of u_a and u_b are zero, the lines are parallel; if the numerator and the denominator of these expressions are both zero, the lines are coincident.

Another check is made to find out whether the intersection point lies within the limit range of coordinates for these two lines. If the values of u_a and u_b lie within 0 and 1, the lines intersect within the range of their respective coordinates; otherwise, the intersection point lies outside the limits of these lines.

The coordinates of the intersection point are computed if all the above checks are satisfied.

This is followed by contact resolution in which the overlapping areas are computed from the available intersection points. Corresponding normal contact forces are generated and applied on the elements' nodes along with already acting internal and external forces.

APPENDIX B
AREAS OF OVERLAP

The calculations for the normal force are done from the area of overlap or area of intersection between the home and the near polygons. In traditional discrete element analysis the contact forces are calculated from the depth of penetration of one element into another, Barbosa [1]. In Figure B-1 it can be seen that for the same penetration, there can be different areas of overlap, thus one can have different normal contact forces for the same amount of penetration, Williams [2]. It was pointed out in Munjiza [3] that if the contact kinematics is based on depth of penetration, then energy imbalance can be produced. The node of the near element can enter from one side of the home element and exit at the other side of the home element. Depending on the amount of the depth of penetration relative to each side, spurious energy can develop. The potential energy possessed is proportional to:

$$\text{Potential Energy} \propto \delta^2 \qquad \text{B-1}$$

where δ is the depth of penetration. This potential energy is in fact the kinetic energy that is transformed to potential energy on contact. Thus, as the node enters the home element from one side it has a penetration of δ_a and the kinetic energy transformed to potential energy is proportional to:

$$\text{Kinetic Energy} \cong \text{Potential Energy} \propto \delta_a^2 \qquad \text{B-2}$$

As the contact is lost through the other side of the home element, the total amount of kinetic energy recovered is proportional to:

$$\text{Kinetic Energy} \propto \delta_b^2 \qquad \text{B-3}$$

which is greater than the initial total energy of the system, thus spurious energy is generated within the contact kinematics. Based on the area of overlap, the normal contact force will be able to overcome this problem.

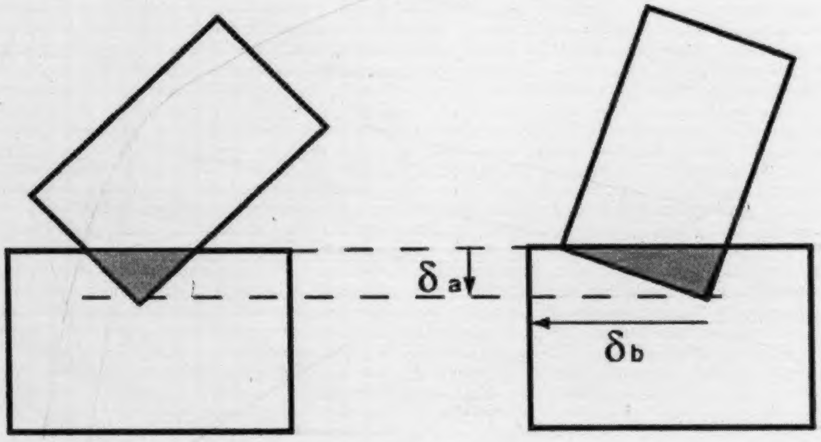

Figure B-1: Comparison of area of overlap and depth of penetration

In this formulation the contact force calculations are based on the area of overlap between elements in contact.

After computing the intersection points, the areas of overlap are calculated using three points at a time, i.e., by forming a triangle. If the area of overlap is in the shape of a polygon with more than three sides, it can be subdivided into triangles and the areas of individual triangles are added together to provide the cumulative area of the polygon. From the three intersection points for a given triangle, the area of overlap can be calculated using the equation:

$$\mathit{Area\,of\,Triangle} = 0.5 * \left(X_1Y_2 + X_2Y_3 + X_3Y_1 - X_1Y_3 - X_2Y_1 - X_3Y_2\right) \quad \text{B-4}$$

BIBLIOGRAPHY

1. Barbosa, R., *Discrete element models for granular materials and rock masses in civil engineering*. Ph.D. thesis 1990, University of Illinois: Urbana-Champaign, Illinois USA. p. 140.

2. Williams, J. R., *Contact analysis of large numbers of interacting bodies using discrete modal methods for simulating material failure on the microscopic scale*. Engineering Computations, 1988. no. 5: p. 198–209.

3. Munjiza, A., *The combined finite-discrete element method*. 2004, West Sussex: John Wiley & Sons Ltd. 333.

APPENDIX C
RESOLVING CONTACT FORCES IN THE GLOBAL COORDINATE SYSTEM

The forces developed between elements forming contacts are initially computed in the local coordinate system. The local coordinate system is defined as shown in Figure C-1, with the local X axis t parallel to the line joining the intersection points (shown by crosses) and the local Y coordinate n perpendicular to the local X axis in a counter-clockwise direction pointing toward the near element.

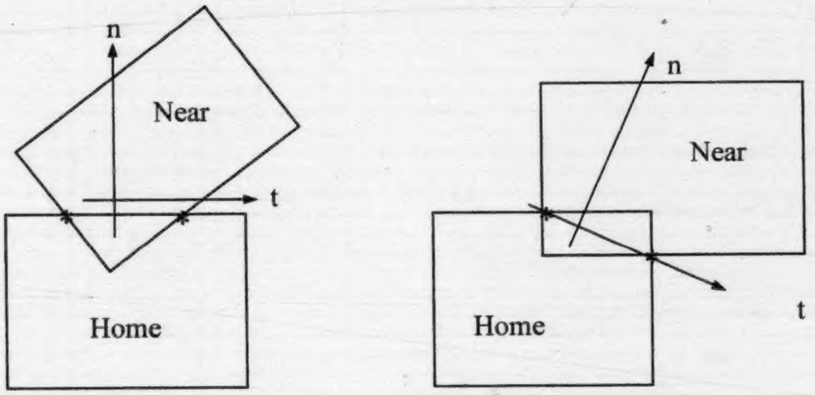

(a) 3 Intersection Points (b) 4 Intersection Points

Figure C-1: Definition of local coordinate system

Based on directions of the contact between the home and near elements, the angles used to calculate the contact forces are computed as described below. The angles used in the computations are:

α =angle between the local and global X axis,

γ = angle between the local and global Y axis, measured in a counter clockwise direction from the global Y axis.

CASE A: Contact with home element as near element penetrates from above.

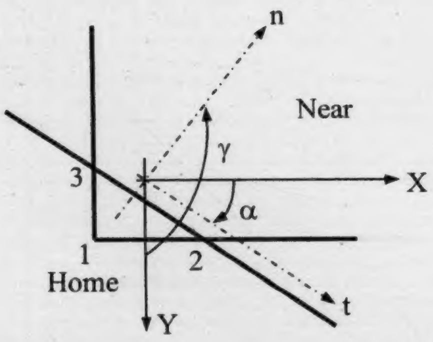

Figure C-2: Near element approaching from top right direction

The value of angle α is calculated as the slope of the line joining intersection points 2 and 3 and will be negative for this case. The intersection points are calculated in a counter clockwise sense.

$$\alpha = \tan^{-1}\left(\frac{YY[2]-YY[3]}{XX[2]-XX[3]}\right) \qquad \text{C-1}$$

The angle γ will be given by (90 – α). Using the obtained value of γ, the normal contact force acting between the home and near elements can be resolved into the global coordinate system. The resolved force components will be:

$$F_x = F_n n_x \qquad \text{C-2}$$

$$F_y = F_n n_y \qquad \text{C-3}$$

where $n_x = \cos\gamma$ and $n_y = \sin\gamma$ are the direction functions. However, for the near element the direction of the forces is reversed and applied at the respective node(s).

CASE B: **Contact of home element with near element approaching from bottom.**

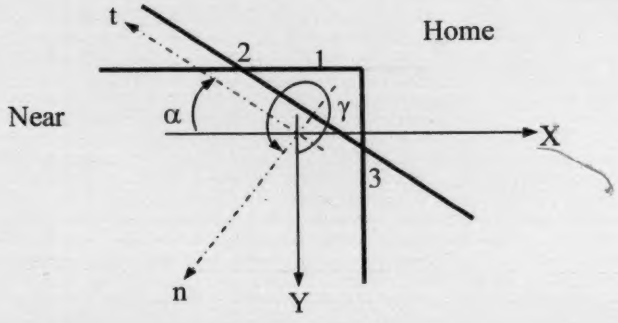

Figure C-3: Near element approaching from bottom left side

The value of angle α is calculated as the slope of the line joining intersection points 2 and 3 and will be negative for this case. The angle γ will be given by (270 – α).

CASE C: **Contact with home element and near element from top but with home element on right.**

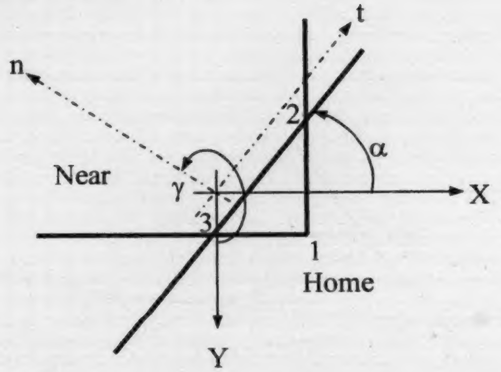

Figure C-4: Near element approaching from top left direction

The value of angle α is calculated as the slope of the line joining intersection points 2 and 3, with α being positive. The angle γ is given by (90 – α) but the normal to the near element points at an angle of (270 – α). If the value is assigned as (90 – α), the direction of normal contact force on the home element remains the same; if (270 – α) is assigned, the direction for the home element needs to be reversed. In the Visual C++ code, keeping the logic based on the X coordinates of the intersection points, the angle is assigned a value of (90 – α).

CASE D: Contact with home element and near element from bottom but with home element on left.

The value of angle α is calculated as the slope of the line joining intersection points 2 and 3, with α being positive. The angle γ will be given by (270 – α) but the normal to the near element points at an angle of (90 – α). If the value is assigned as (270 – α), the direction of normal contact force on the home element remains the same; if (90 – α) is assigned, the direction for the home element needs to be reversed. In the code, keeping the logic based on the X coordinates of the intersection points, the angle is assigned a value of (270 – α).

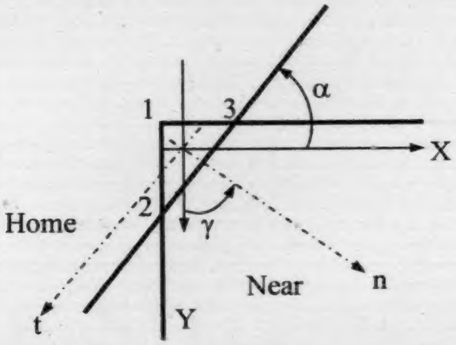

Figure C-5: Near element approaching from bottom right direction

CASES E, F, G, H: Special cases for horizontal and vertical intersection planes.

For special cases the definition of the angle γ is slightly modified. It is computed and defined based on the direction of the normal contact force required to act on the home and near elements. For these cases the angle γ is measured with respect to the positive global X axis in a counter clockwise direction.

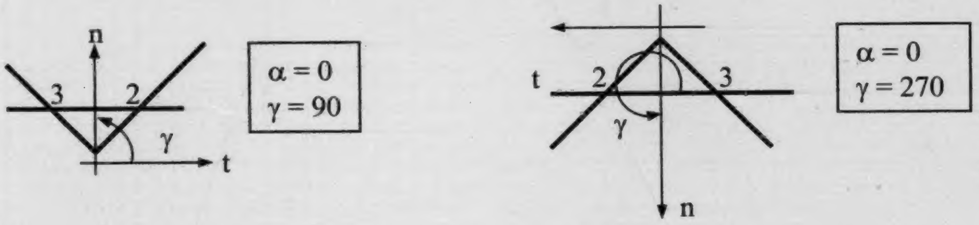
n
3
2
γ
t
α = 0
γ = 90
t
2
3
γ
n
α = 0
γ = 270

CASE: E (XI(2) > XI(3)) CASE: F (XI(2) < XI(3))

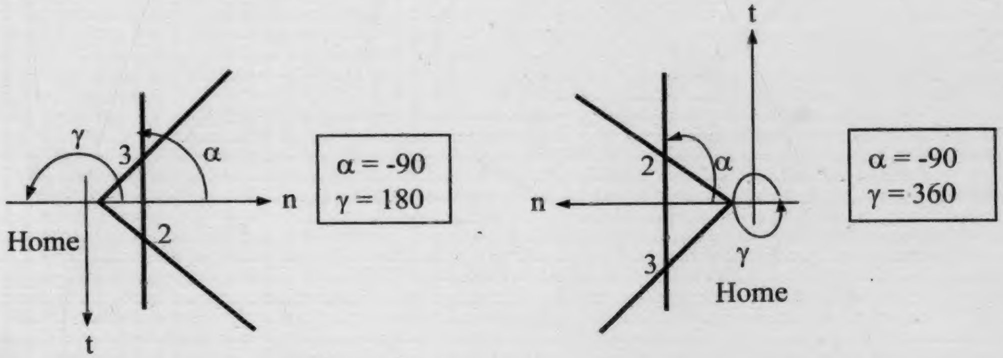
γ
3
α
n
Home
2
t
α = -90
γ = 180
t
2
α
n
3
γ
Home
α = -90
γ = 360

CASE: G (YI(2) < YI(3)) CASE: H (YI(2) > YI(3))

Figure C-6: Special cases for the calculation of angle γ

CASES I, J: Definitions for four intersection points.

If there are 4 intersection points, the local axis will be defined along intersection point 2 and 4 (case I) and between intersection points 3 and 4 (case J).

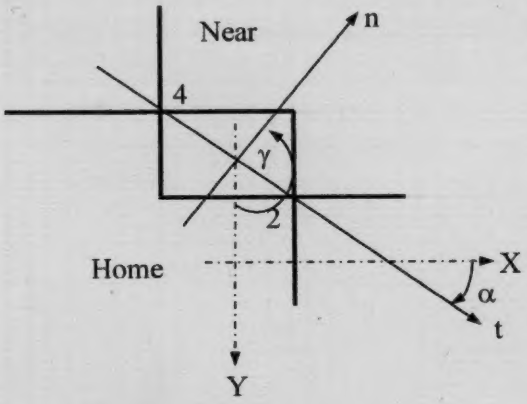

Case I: Local system defined by the line joining intersection points ‘2’ & ‘4’.
If X[2] > X[4]; $\gamma = 90 - \alpha$
Else $\gamma = 270 - \alpha$

Case J: Local system defined by the line joining intersection points 3’ & ‘4’.
If X[3] > X[4]; $\gamma = 90 - \alpha$
Else $\gamma = 270 - \alpha$

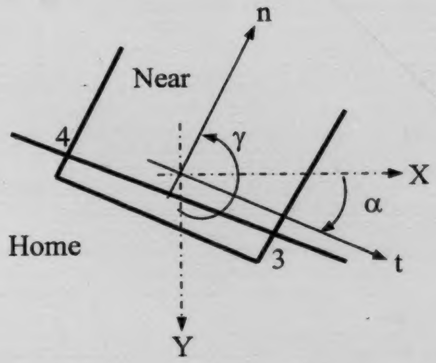

Figure C-7: Local coordinate system for 4 intersection points

The resolution of the force components and the velocities follows the same pattern as defined above.

APPENDIX D
MOHR-COULOMB ELASTO-PLASTIC MODEL

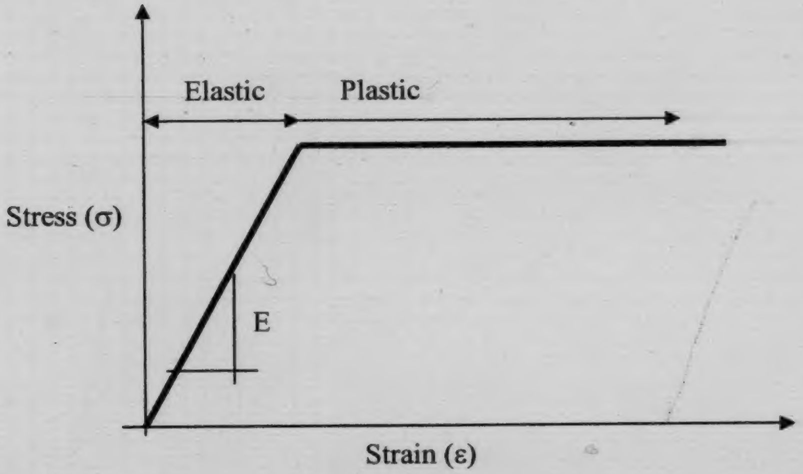

Figure D-1: Elastic perfectly-plastic Mohr-Coulomb constitutive relationship

The incremental strain can be divided into an elastic component and a plastic component.

$$\{d\varepsilon\} = \{d\varepsilon^e\} + \{d\varepsilon^p\} \text{ or} \qquad \text{D-1}$$

$$\{d\varepsilon^e\} = \{d\varepsilon\} - \{d\varepsilon^p\} \qquad \text{D-2}$$

Only elastic strain increments $d\varepsilon^e$ will cause stress changes; as a result the stress increments can be written as:

$$\{d\sigma\} = [C_e]\{d\varepsilon^e\} \text{ or} \qquad \text{D-3}$$

$$\{d\sigma\} = [C_e](\{d\varepsilon\} - \{d\varepsilon^p\}) \qquad \text{D-4}$$

The yield function F describes the locus of the yield point. When the stress state is on the plastic yield point, the consistency condition is met and no stress state is possible beyond the yielding limits. The consistency condition is:

$$dF = \left\langle \frac{\partial F}{\partial \sigma} \right\rangle \{d\sigma\} = 0 \qquad \text{D-5}$$

The plastic component of the strain is computed from:

$$\{d\varepsilon^{p}\} = \lambda \left\{ \frac{\partial G}{\partial \sigma} \right\} \qquad \text{D-6}$$

where G is a plastic potential function and λ is a plastic scaling factor.

The plastic scaling factor λ is derived from:

$$\lambda = \frac{\left\langle \frac{\partial F}{\partial \sigma} \right\rangle [C_e]}{\left\langle \frac{\partial F}{\partial \sigma} \right\rangle [C_e] \left\{ \frac{\partial G}{\partial \sigma} \right\}} \{d\varepsilon\} \qquad \text{D-7}$$

The incremental stress equation now becomes:

$$\{d\sigma\} = [C_e]\{d\varepsilon\} - [C_e]\lambda \left\{ \frac{\partial G}{\partial \sigma} \right\} \text{ or} \qquad \text{D-8}$$

$$\{d\sigma\} = \left([C_e] - [C_p]\right) \{d\varepsilon\} \qquad \text{D-9}$$

where,

$$[C_p]=\frac{[C_e]\left\{\frac{\partial G}{\partial \sigma}\right\}\left\langle\frac{\partial F}{\partial \sigma}\right\rangle[C_e]}{\left\langle\frac{\partial F}{\partial \sigma}\right\rangle[C_e]\left\{\frac{\partial G}{\partial \sigma}\right\}} \qquad \text{D-10}$$

The next step is to choose any yield criteria and its corresponding yield function and the plastic potential function to find the matrix. The yield function of the Mohr-Coulomb yield criterion is defined as:

$$F=\frac{\sigma_1+\sigma_3}{2}\sin\phi-\frac{\sigma_1-\sigma_3}{2}-c\cos\phi=0 \qquad \text{D-11}$$

An alternative form of the invariants can also be used to define failure and yield criteria. This alternative set of invariants includes I_1, I_2, J_1, J_2, and a quantity θ known as the lode angle. The yield function F can now be written as:

$$F=\frac{I_1}{3}\sin\phi+\sqrt{J_2}\cos\theta-\frac{\sqrt{J_2}}{\sqrt{3}}\sin\phi\sin\theta-c\cos\phi=0 \qquad \text{D-12}$$

where,

$I_1=\sigma_x+\sigma_y+\sigma_z$ is the first strain invariant, D-13

$J_2=\frac{1}{6}\left[(\sigma_x-\sigma_y)^2+(\sigma_y-\sigma_z)^2+(\sigma_z-\sigma_x)^2\right]+\tau_{xy}^2$ is the second deviatoric stress invariant, D-14

$J_3=\sigma_x^d\,\sigma_y^d\,\sigma_z^d-\sigma_z^d\,\tau_{xy}^2$ is the third deviatoric stress invariant, D-15

$\theta=\frac{1}{3}\sin^{-1}\left(-\frac{3\sqrt{3}}{2}\frac{J_3}{J_2^{3/2}}\right)$ with $-\frac{\pi}{6}\le\theta\le\frac{\pi}{6}$ is the lode angle, D-16

where c is the cohesion and ϕ is the angle of internal friction.

The value of the term within the arcsine of the lode angle has to be within the limits of −1 and 1, otherwise, arcsine calculations will give errors. When the value of the term comes close to −1 or 1, it should be assigned a value slightly higher or lower, respectively, to avoid calculation errors.

The deviatoric stress component σ_i^d in any direction can be defined as:

$$\sigma_i^d = \sigma_i - \frac{I_1}{3} \qquad \text{D-17}$$

where i can be x, y, or z.

The plastic potential function G has the same form as the yield function F except the internal friction angle ϕ is replaced by the dilation angle ψ. Thus the plastic potential function takes the form:

$$G = \frac{I_1}{3}\sin\psi + \sqrt{J_2}\cos\theta - \frac{\sqrt{J_2}}{\sqrt{3}}\sin\psi\sin\theta - c\cos\psi = 0 \qquad \text{D-18}$$

The derivatives of the yield function in terms of the stress invariants are computed using the chain rule of differentiation.

$$\left\langle \frac{\partial F}{\partial \sigma} \right\rangle = \frac{\partial F}{\partial I_1}\left\langle \frac{\partial I_1}{\partial \sigma} \right\rangle + \frac{\partial F}{\partial J_2}\left\langle \frac{\partial J_2}{\partial \sigma} \right\rangle + \frac{\partial F}{\partial J_3}\left\langle \frac{\partial J_3}{\partial \sigma} \right\rangle \qquad \text{D-19}$$

The derivatives of the Mohr-Coulomb yield function, with respect to the stress invariants, can be written as follows:

$$\frac{\partial F}{\partial I_1} = \frac{\sin\phi}{3} \qquad \text{D-20}$$

Before doing the derivation of the yield function F with respect to J_2 and J_3, a small differential is done to ease the way for doing the differentiation.

The derivative of θ with respect to the any of the variables can be taken as:

$$\sin(3\theta)=\left(-\frac{3\sqrt{3}}{2}\frac{J_3}{J_2^{\frac{3}{2}}}\right)=X(say) \qquad \text{D-21}$$

Note that:

$$\frac{d}{dx}\left(\sin^{-1}(X)\right)=\frac{1}{\sqrt{1-X^2}}\frac{dX}{dx} \qquad \text{D-22}$$

$$\frac{1}{\sqrt{1-X^2}}=\frac{1}{\sqrt{1-(\sin(3\theta))^2}}=\frac{1}{\sqrt{1-\sin^2(3\theta)}}=\frac{1}{\sqrt{\cos^2(3\theta)}}=\frac{1}{\cos(3\theta)} \qquad \text{D-23}$$

Now the derivatives are continued from above:

$$\frac{\partial F}{\partial J_2}=\left(\frac{1}{2\sqrt{J_2}}\cos\theta+\sqrt{J_2}\frac{\partial}{\partial J_2}\cos\theta\right)-\frac{\sin\phi}{\sqrt{3}}\left(\frac{\sin\theta}{2\sqrt{J_2}}+\sqrt{J_2}\frac{\partial}{\partial J_2}\sin\theta\right) \qquad \text{D-24}$$

$$\frac{\partial}{\partial J_2}\cos\theta=-\sin\theta\frac{\partial}{\partial J_2}\left(\frac{1}{3}\sin^{-1}\left(\frac{-3\sqrt{3}}{2}\frac{J_3}{J_2^{3/2}}\right)\right)=\frac{1}{2J_2}\left(\frac{\sin\theta}{\cos 3\theta}\left(-\frac{3\sqrt{3}}{2}\frac{J_3}{J_2^{3/2}}\right)\right) \qquad \text{D-25}$$

$$\frac{\partial}{\partial J_2}\sin\theta=\cos\theta\frac{\partial}{\partial J_2}\left(\frac{1}{3}\sin^{-1}\left(\frac{-3\sqrt{3}}{2}\frac{J_3}{J_2^{3/2}}\right)\right)=\frac{1}{2J_2}\left(\frac{-\cos\theta}{\cos 3\theta}\left(-\frac{3\sqrt{3}}{2}\frac{J_3}{J_2^{3/2}}\right)\right) \qquad \text{D-26}$$

$$\frac{\partial F}{\partial J_2}=\left(\frac{1}{2\sqrt{J_2}}\cos\theta+\frac{1}{2\sqrt{J_2}}\left(\frac{\sin\theta}{\cos 3\theta}\left(-\frac{3\sqrt{3}}{2}\frac{J_3}{J_2^{3/2}}\right)\right)\right) \qquad \text{D-27}$$

$$-\frac{\sin\phi}{\sqrt{3}}\left(\frac{\sin\theta}{2\sqrt{J_2}}-\frac{1}{2\sqrt{J_2}}\left(\frac{\cos\theta}{\cos 3\theta}\left(-\frac{3\sqrt{3}}{2}\frac{J_3}{J_2^{3/2}}\right)\right)\right)$$

Let:

$$\sin\beta = -\frac{3\sqrt{3}}{2}\frac{J_3}{J_2^{3/2}} \qquad \text{D-28}$$

then,

$$\frac{\partial F}{\partial J_2} = \frac{\cos\theta}{2\sqrt{J_2}}\left\{\left(1+\frac{\sin\theta\sin\beta}{\cos 3\theta\cos\theta}\right)+\frac{\sin\phi}{\sqrt{3}}\left(\frac{\sin\beta}{\cos 3\theta}-\frac{\sin\theta}{\cos\theta}\right)\right\} \qquad \text{D-29}$$

$$\frac{\partial F}{\partial J_3} = \sqrt{J_2}\,\frac{\partial}{\partial J_3}\cos\theta-\frac{\sqrt{J_2}}{\sqrt{3}}\sin\phi\,\frac{\partial}{\partial J_3}\sin\theta \qquad \text{D-30}$$

$$\frac{\partial}{\partial J_3}\cos\theta = -\sin\theta\,\frac{\partial}{\partial J_3}\left(\frac{1}{3}\sin^{-1}\left(\frac{-3\sqrt{3}}{2}\frac{J_3}{J_2^{3/2}}\right)\right)=\frac{\sqrt{3}\sin\theta}{2\cos 3\theta\, J_2^{3/2}} \qquad \text{D-31}$$

$$\frac{\partial}{\partial J_3}\sin\theta = \cos\theta\,\frac{\partial}{\partial J_3}\left(\frac{1}{3}\sin^{-1}\left(\frac{-3\sqrt{3}}{2}\frac{J_3}{J_2^{3/2}}\right)\right)=\frac{\sqrt{3}\cos\theta}{2\cos 3\theta\, J_2^{3/2}} \qquad \text{D-32}$$

Substituting the values of these derivatives :

$$\frac{\partial F}{\partial J_3} = \frac{\sqrt{3}\sin\theta}{2J_2\cos 3\theta}+\frac{\cos\theta}{2J_2\cos 3\theta}=\frac{\sqrt{3}\sin\theta+\cos\theta}{2J_2\cos 3\theta} \qquad \text{D-33}$$

The derivatives of the stress invariants with respect to the stresses are:

$$\left\langle\frac{\partial I_1}{\partial\sigma}\right\rangle = \langle\ 1\ \ 1\ \ 1\ \ 0\ \rangle \qquad \text{D-34}$$

$$\left\langle \frac{\partial J_2}{\partial \sigma} \right\rangle = \left\langle \ \sigma_x^d \quad \sigma_y^d \quad \sigma_z^d \quad 2\tau_{xy} \right\rangle \tag{D-35}$$

The first component of the above matrix was obtained by:

$$\frac{\partial J_2}{\partial \sigma_x} = \frac{1}{6}\left[2(\sigma_x - \sigma_y) + 2(\sigma_z - \sigma_x)(-1)\right] \tag{D-36}$$

$$\frac{\partial J_2}{\partial \sigma_x} = \frac{2}{3}\sigma_x - \frac{1}{3}\sigma_y - \frac{1}{3}\sigma_z \tag{D-37}$$

Adding and subtracting $\frac{1}{3}\sigma_x$ on the left hand side of equation D-37:

$$\frac{\partial J_2}{\partial \sigma_x} = \left(\sigma_x - \frac{\sigma_x + \sigma_y + \sigma_z}{3}\right) = \sigma_x^d \tag{D-38}$$

$$\frac{\partial J_3}{\partial \sigma_x} = \frac{\partial}{\partial \sigma_x}\left(\sigma_x^d \, \sigma_y^d \, \sigma_z^d - \sigma_z^d \, \tau_{xy}^2\right) \tag{D-39}$$

$$\frac{\partial J_3}{\partial \sigma_x} = \frac{\partial}{\partial \sigma_x}\left[\left(\sigma_x - \frac{I_1}{3}\right)\left(\sigma_y - \frac{I_1}{3}\right)\left(\sigma_z - \frac{I_1}{3}\right) - \left(\sigma_z - \frac{I_1}{3}\right)\tau_{xy}^2\right] \tag{D-40}$$

$$\frac{\partial J_3}{\partial \sigma_x} = \left[\left(1 - \frac{1}{3}\right)\sigma_y^d \, \sigma_z^d + \sigma_x^d\left(0 - \frac{1}{3}\right)\sigma_z^d + \sigma_x^d \, \sigma_y^d\left(0 - \frac{1}{3}\right) - \left(0 - \frac{1}{3}\right)\tau_{xy}^2\right] \tag{D-41}$$

$$\frac{\partial J_3}{\partial \sigma_x} = \frac{2}{3}\sigma_y^d \, \sigma_z^d - \frac{1}{3}\sigma_x^d \, \sigma_z^d - \frac{1}{3}\sigma_x^d \, \sigma_y^d + \frac{1}{3}\tau_{xy}^2 = \sigma_y^d \, \sigma_z^d - \frac{1}{3}\sigma_y^d \, \sigma_z^d - \frac{1}{3}\sigma_x^d \, \sigma_z^d - \frac{1}{3}\sigma_x^d \, \sigma_y^d + \frac{1}{3}\tau_{xy}^2 \tag{D-42}$$

$$\frac{\partial J_3}{\partial \sigma_x} = \sigma_y^d \, \sigma_z^d + \frac{1}{3}\left(-\sigma_y^d \, \sigma_z^d - \sigma_x^d \, \sigma_z^d - \sigma_x^d \, \sigma_y^d + \tau_{xy}^2\right) \tag{D-43}$$

$$\frac{\partial J_3}{\partial \sigma_x}=\sigma_y^d\,\sigma_z^d+\frac{1}{3}\left[-(\sigma_y-p)(\sigma_z-p)-(\sigma_x-p)(\sigma_z-p)-(\sigma_x-p)(\sigma_y-p)+\tau_{xy}^2\right]$$

D-44

where $p=\frac{I_1}{3}$, and

$$\frac{\partial J_3}{\partial \sigma_x}=\sigma_y^d\,\sigma_x^d+\frac{1}{3}\left[p(2\sigma_x+2\sigma_y+2\sigma_z)-\sigma_y\sigma_z-\sigma_x\sigma_z-\sigma_x\sigma_y-3p^2+\tau_{xy}^2\right]$$

D-45

Expanding for p and solving:

$$\frac{\partial J_3}{\partial \sigma_x}=\sigma_y^d\sigma_z^d+\frac{1}{3}\left[\frac{1}{3}\left(\sigma_x^2+\sigma_y^2+\sigma_z^2-\sigma_y\sigma_z-\sigma_x\sigma_z-\sigma_x\sigma_y\right)+\tau_{xy}^2\right] \qquad \text{D-46}$$

$$\frac{\partial J_3}{\partial \sigma_x}=\sigma_y^d\sigma_z^d+\frac{1}{3}\left[\frac{1}{6}\left(2\sigma_x^2+2\sigma_y^2+2\sigma_z^2-2\sigma_y\sigma_z-2\sigma_x\sigma_z-2\sigma_x\sigma_y\right)+\tau_{xy}^2\right] \qquad \text{D-47}$$

Rearranging equation D-47 gives:

$$\frac{\partial J_3}{\partial \sigma_x}=\sigma_y^d\sigma_z^d+\frac{1}{3}\left[\frac{1}{6}\left((\sigma_x-\sigma_y)^2+(\sigma_y-\sigma_z)^2+(\sigma_z-\sigma_x)^2\right)+\tau_{xy}^2\right] \qquad \text{D-48}$$

$$\frac{\partial J_3}{\partial \sigma_x}=\sigma_y^d\sigma_z^d+\frac{J_2}{3} \qquad \text{D-49}$$

Thus, differentiating J$_3$ with all components of the stress states gives the matrix:

$$\left\langle\frac{\partial J_3}{\partial \sigma}\right\rangle=\left\langle \sigma_y^d\sigma_z^d+\frac{J_2}{3} \quad \sigma_x^d\sigma_z^d+\frac{J_2}{3} \quad \sigma_x^d\sigma_y^d+\frac{J_2}{3}-\tau_{xy}^2 \quad -2\sigma_z^d\tau_{xy}\right\rangle \qquad \text{D-50}$$

The terms of the matrix are the derivatives of the yield function with respect to the stress states. The components of the matrix are:

$$\begin{aligned}\frac{\partial F}{\partial \sigma_x}=\frac{\sin\phi}{3}+\left(\frac{\cos\theta}{2\sqrt{J_2}}\left\{\left(1+\frac{\sin\theta\sin\beta}{\cos 3\theta\cos\theta}\right)+\frac{\sin\phi}{\sqrt{3}}\left(\frac{\sin\beta}{\cos 3\theta}-\frac{\sin\theta}{\cos\theta}\right)\right\}\right)\sigma_x^d+ \\ \left(\frac{\sqrt{3}\sin\theta+\cos\theta}{2J_2\cos 3\theta}\right)\left(\sigma_y^d\sigma_z^d+\frac{J_2}{3}-\frac{3J_3}{2J_2}\sigma_x^d\right)\end{aligned} \tag{D-51}$$

$$\begin{aligned}\frac{\partial F}{\partial \sigma_y}=\frac{\sin\phi}{3}+\left(\frac{\cos\theta}{2\sqrt{J_2}}\left\{\left(1+\frac{\sin\theta\sin\beta}{\cos 3\theta\cos\theta}\right)+\frac{\sin\phi}{\sqrt{3}}\left(\frac{\sin\beta}{\cos 3\theta}-\frac{\sin\theta}{\cos\theta}\right)\right\}\right)\sigma_y^d+ \\ \left(\frac{\sqrt{3}\sin\theta+\cos\theta}{2J_2\cos 3\theta}\right)\left(\sigma_x^d\sigma_z^d+\frac{J_2}{3}-\frac{3J_3}{2J_2}\sigma_y^d\right)\end{aligned} \tag{D-52}$$

$$\begin{aligned}\frac{\partial F}{\partial \sigma_z}=\frac{\sin\phi}{3}+\left(\frac{\cos\theta}{2\sqrt{J_2}}\left\{\left(1+\frac{\sin\theta\sin\beta}{\cos 3\theta\cos\theta}\right)+\frac{\sin\phi}{\sqrt{3}}\left(\frac{\sin\beta}{\cos 3\theta}-\frac{\sin\theta}{\cos\theta}\right)\right\}\right)\sigma_z^d+ \\ \left(\frac{\sqrt{3}\sin\theta+\cos\theta}{2J_2\cos 3\theta}\right)\left(\sigma_x^d\sigma_y^d+\frac{J_2}{3}-\tau_{xy}^2-\frac{3J_3}{2J_2}\sigma_z^d\right)\end{aligned} \tag{D-53}$$

$$\begin{aligned}\frac{\partial F}{\partial \tau_{xy}}=\frac{\sin\phi}{3}+\left(\frac{\cos\theta}{2\sqrt{J_2}}\left\{\left(1+\frac{\sin\theta\sin\beta}{\cos 3\theta\cos\theta}\right)+\frac{\sin\phi}{\sqrt{3}}\left(\frac{\sin\beta}{\cos 3\theta}-\frac{\sin\theta}{\cos\theta}\right)\right\}\right)2\tau_{xy}+ \\ \left(\frac{\sqrt{3}\sin\theta+\cos\theta}{2J_2\cos 3\theta}\right)\left(-2\sigma_z^d\tau_{xy}-\frac{3J_3}{J_2}\tau_{xy}\right)\end{aligned} \tag{D-54}$$

In order to find the matrix containing the derivatives of the plastic potential function G with respect to the stresses, the angle of internal friction ϕ is replaced with the dilation angle ψ in the above equations.

The Mohr-Coulomb model can be reduced to Tresca yield criteria by making the angle of internal friction ϕ equal to zero. This helps in checking the gradients of the yield function with respect to the stresses.

$$Max\left(\frac{1}{2}|\sigma_1-\sigma_2|,\frac{1}{2}|\sigma_2-\sigma_3|,\frac{1}{2}|\sigma_3-\sigma_1|\right)=k \qquad \text{D-55}$$

When the shearing stresses are zero the values of the normal stresses in any direction are the same as the principal stress value. So the derivative of the Tresca yield criteria with respect to the stresses gives:

$$\frac{\partial}{\partial\sigma_1}\left(\frac{1}{2}|\sigma_1-\sigma_3|\right)=\frac{1}{2} \quad and \quad \frac{\partial}{\partial\sigma_3}\left(\frac{1}{2}|\sigma_1-\sigma_3|\right)=-\frac{1}{2} \qquad \text{D-56}$$

This helps to check whether the calculations done for the above equations for derivatives of yield function F are correct.

Once the gradients have been calculated, it is possible to find the elasto-plastic constitutive matrix, [C_{ep}].

APPENDIX E
INTERVAL HALVING TECHNIQUE

The interval halving technique is a simple and effective way to obtain a solution for any equation of the type:

$$f(x) = 0 \qquad \text{E-1}$$

The objective is to find a value of $x = x_0$ such that the above equation is satisfied. In order to obtain a solution, the following conditions must be satisfied:

- *$f(x)$ must be continuous in x,*
- *extreme values of the function are known for which $f(x_1) < 0$ and $f(x_2) > 0$.*

This function f(x) is the yield function and x is the value of α for which the yield criteria is always met. The value of α lies between 0 and 1 and can be determined from the following steps:

1. *Determine the mid-point x_m between x_1 and x_2:*

$$x_m = \frac{x_1 + x_2}{2} \qquad \text{E-2}$$

2. *If x_m satisfies the function $f(x_m) = 0$ within tolerable limits, assign $x_0 = x_m$; otherwise, proceed to the next step.*
3. *If $f(x_m) < 0$, assign x_m to x1 and repeat steps 1 and 2 until the criteria or the tolerance limits are met. If $f(x_m) > 0$, assign x_m to x2 and repeat steps 1 and 2.*

The procedure is shown in Figure E-1.

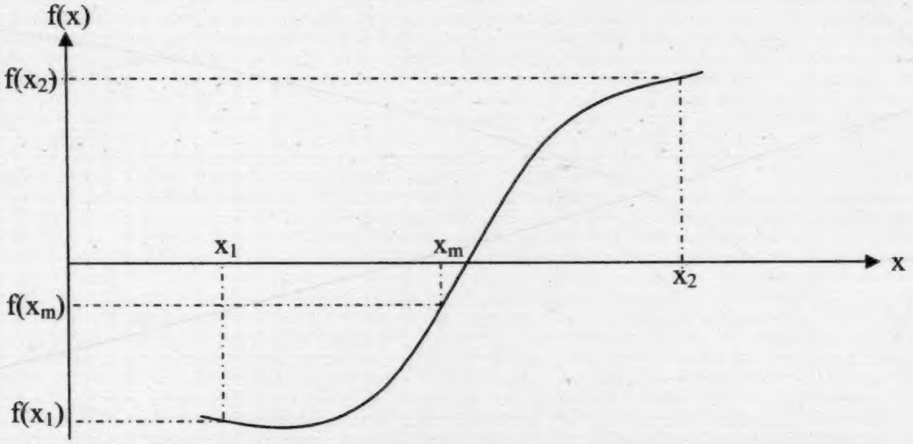

Figure E-1: Solution procedure for interval halving technique, Chan [1]

The convergence rate of this method is slower than other methods and the number of iterations required is given approximately by:

$$n = \log_2(m+1) \qquad \text{E-3}$$

where,

n = the number of iterations required, and
m = the number of significant digits of x.

An advantage of this method is that it is not necessary to require the derivatives of f to be continuous; therefore, the yield surfaces with corners can be solved without difficulty.

BIBLIOGRAPHY

1. Chan, D. H., *Finite element analysis of strain softening material.* 1985, Ph.D. thesis, University of Alberta, Edmonton, AB. p. 345.

APPENDIX F
RADIAL RETURN METHOD

The iterative techniques of the Newton-Raphson method or the modified Newton-Raphson method are applied to find solutions for the behaviour of nonlinear material. As described in previous sections, the calculation algorithm revolves around the current estimation of the incremental displacements based on the resultant forces on the nodes of the elements. These displacements are further used to evaluate the incremental strains at each integration point. The integration of the constitutive model is then performed along the incremental strain path to estimate changes in the stress states, Potts [1]. These stress changes are incorporated into the stress states at the beginning of the increment and used to evaluate the net nodal equivalent forces.

The constitutive model matrix for the elasto-plastic Mohr-Coulomb criteria is dependent on the current state of stress, thus, care must be taken when integrating the constitutive equation to obtain stress changes. The two methods primarily employed in the finite element method are the substepping algorithm and the radial return algorithm, both part of the stress point algorithms. In the substepping approach, the incremental strains are divided into a number of substeps wherein the strains are a proportion of the incremental strains. The constitutive equations are then integrated numerically over each substep using the Euler, the modified Euler, or the Runge-Kutta approach. The radial stress return algorithm (Chan, [2]) is incorporated into the developed method as explained below.

The condition for an admissible stress state is:

$$F(\sigma) \leq 0 \qquad \text{F-1}$$

If the stress state lies on the yield surface,

$$F\left(\sigma^{*}\right) = 0 \tag{F-2}$$

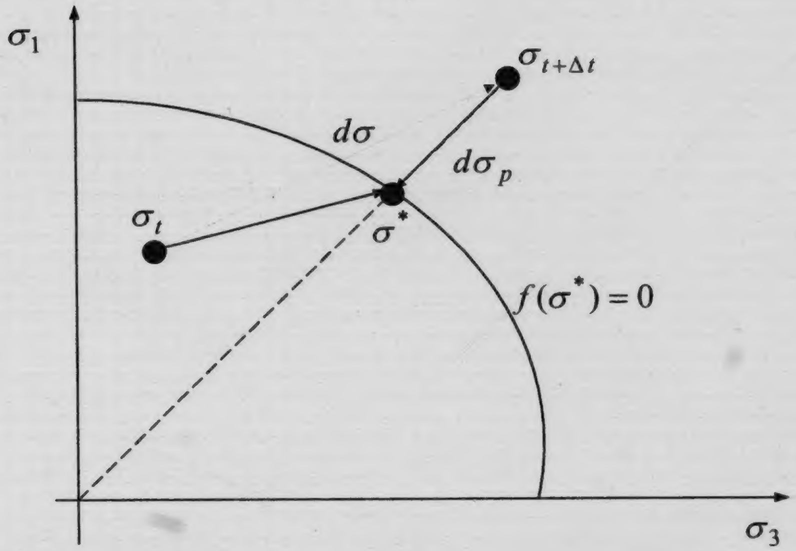
σ_1
$\sigma_{t+\Delta t}$
$d\sigma$
$d\sigma_p$
σ_t
σ^*
$f(\sigma^*) = 0$
σ_3

Figure F-2: Radial return for Mohr-Coulomb plasticity, two dimensional stress space

$$dF = \frac{\partial F}{\partial \sigma_p}\, d\sigma_p \tag{F-3}$$

where $\frac{\partial F}{\partial \sigma_p}$ is the gradient of the yield surface.

Let the stress change $d\sigma_p$ be perpendicular to the yield surface, and let:

$$d\sigma_p = \lambda \frac{\partial F}{\partial \sigma_p} \tag{F-4}$$

where λ is a proportionality constant.

$$F(\sigma) + dF = F\left(\sigma^{*}\right) = 0 \tag{F-5}$$

$$F(\sigma) + \frac{\partial F}{\partial \sigma_p} d\sigma_p = 0 \qquad \text{F-6}$$

The value for $d\sigma_p$ is substituted from Equation F-4,

$$F(\sigma) + \frac{\partial F}{\partial \sigma_p} \lambda \frac{\partial F}{\partial \sigma_p} = 0 \qquad \text{F-7}$$

or

$$\lambda = \frac{-F(\sigma)}{\frac{\partial F}{\partial \sigma_p} \frac{\partial F}{\partial \sigma_p}} \qquad \text{F-8}$$

Finally,

$$d\sigma_p = -\left(\frac{F(\sigma)}{\frac{\partial F}{\partial \sigma_p} \frac{\partial F}{\partial \sigma_p}} \right) \frac{\partial F}{\partial \sigma_p} \qquad \text{F-9}$$

Update the stresses and iterate until $F(\sigma^*) = 0$ or is within the defined tolerance criteria.

BIBLIOGRAPHY

1. Potts, D. M., and Zdravkovic, L., *Finite element analysis in geo-technical [illegible]gineering—Theory*. 1999, London, U.K.: Thomas Telford Publishing. 440.
2. Chan, D. H., *Course notes of numerical methods in engineering*, CIVE 799 notes, Department of Civil Engineering, University of Alberta, Edmonton, AB 2003.